NATIONAL TECHNICAL UNIVERSITY OF ATHENS
SCHOOL OF APPLIED SCIENCES
DEPARTMENT OF PHYSICS
HIGH ENERGY PHYSICS LABORATORY

Characterization of semiconductor detectors and test beams with high-rate telescopes for the Tracker upgrade of the CMS experiment

A dissertation presented by

Patrick Asenov

to
The Department of Physics
for the degree of Doctor of Philosophy
in the subject of Physics

The research presented here was conducted at the
Detector Instrumentation Lab
at the Institute of Nuclear and Particle Physics,
NCSR "Demokritos"

November 2020

Characterization of semiconductor detectors and test beams with high-rate telescopes for the Tracker upgrade of the CMS experiment

Ph.D THESIS

Patrick Asenov

Advisors: Theodoros Alexopoulos, Professor, NTU-Athens
Dimitrios Loukas, Director of Research, NCSR "Demokritos"

Exam committee:

....

Theodoros Alexopoulos

Professor, NTUA

....

Jérémy Andrea

Researcher, IPHC-CNRS

....

Costas Foudas

Professor, UoI

....

Michael Kokkoris

Professor, NTUA

....

Aristotelis Kyriakis

Director of Research, NCSR "Demokritos"

....

Dimitrios Loukas

Director of Research, NCSR "Demokritos"

....

Nikos Manthos

Professor, UoI

Athens, November of 2020

....
Patrick Asenov

H.F.R.I.
Hellenic Foundation for Research & Innovation

ΕΘΝΙΚΟ ΜΕΤΣΟΒΙΟ ΠΟΛΥΤΕΧΝΕΙΟ
ΣΧΟΛΗ ΕΦΑΡΜΟΣΜΕΝΩΝ ΜΑΘΗΜΑΤΙΚΩΝ
ΚΑΙ ΦΥΣΙΚΩΝ ΕΠΙΣΤΗΜΩΝ

Χαρακτηρισμός ημιαγώγιμων ανιχνευτών και δοκιμαστικές δέσμες με τηλεσκόπια υψηλού ρυθμού για την αναβάθμιση του Tracker του πειράματος CMS

ΔΙΔΑΚΤΟΡΙΚΗ ΔΙΑΤΡΙΒΗ

Πάτρικ Ασένοβ

Διπλωματούχος ΣΗΜΜΥ Ε.Μ.Π.

ΕΠΙΒΛΕΠΟΝΤΕΣ :

Θ. ΑΛΕΞΟΠΟΥΛΟΣ Δ. ΛΟΥΚΑΣ
Καθηγητής Ε.Μ.Π. Διευθυντής Ερευνών ΕΚΕΦΕ "Δημόκριτος"

ΑΘΗΝΑ, Νοέμβριος 2020

ΕΘΝΙΚΟ ΜΕΤΣΟΒΙΟ ΠΟΛΥΤΕΧΝΕΙΟ
ΣΧΟΛΗ ΕΦΑΡΜΟΣΜΕΝΩΝ ΜΑΘΗΜΑΤΙΚΩΝ ΚΑΙ ΦΥΣΙΚΩΝ ΕΠΙΣΤΗΜΩΝ

Χαρακτηρισμός ημιαγώγιμων ανιχνευτών και δοκιμαστικές δέσμες με τηλεσκόπια υψηλού ρυθμού για την αναβάθμιση του Tracker του πειράματος CMS

ΔΙΔΑΚΤΟΡΙΚΗ ΔΙΑΤΡΙΒΗ

Πάτρικ Ασένοβ

Διπλωματούχος ΣΗΜΜΥ Ε.Μ.Π.

ΤΡΙΜΕΛΗΣ ΣΥΜΒΟΥΛΕΥΤΙΚΗ ΕΠΙΤΡΟΠΗ:

1. Θεόδωρος Αλεξόπουλος, Καθ. ΕΜΠ
2. Μιχαήλ Κόκκορης, Καθ. ΕΜΠ
3. Δημήτριος Λουκάς, Διευθ. Ερευνών ΕΚΕΦΕ ¨Δημόκρητος¨

ΕΠΤΑΜΕΛΗΣ ΕΞΕΤΑΣΤΙΚΗ ΕΠΙΤΡΟΠΗ:

1. Θεόδωρος Αλεξόπουλος, Καθ. ΕΜΠ
2. Ζερεμί Οντρεά, Ερ. IPHC-CNRS
3. Κώστας Φουντάς, Καθ. ΠΙ
4. Μιχαήλ Κόκκορης, Καθ. ΕΜΠ
5. Αριστοτέλης Κυριάκης, Διευθ. Ερευνών, ΕΚΕΦΕ ¨Δημόκρητος¨
6. Δημήτριος Λουκάς, Διευθ. Ερευνών, ΕΚΕΦΕ ¨Δημόκρητος¨
7. Νίκος Μάνθος, Καθ. ΠΙ

ΑΘΗΝΑ, Νοέμβριος 2020

....

Πάτρικ Ασένοβ

ΕΛ.Ι.Δ.Ε.Κ.
Ελληνικό Ίδρυμα Έρευνας & Καινοτομίας

To Gulnara,
for all the love, patience and support a man could get.

Περίληψη στα ελληνικά

Για να αποκαλύψουν τα μυστήρια του σύμπαντος, οι φυσικοί υψηλών ενεργειών θα πρέπει να ενισχύσουν την ικανότητα για ανακαλύψεις του ισχυρότερου επιταχυντή συγκρούσεων σωματιδίων στον κόσμο. Ο Μεγάλος Αδρονικός Επιταχυντής Υψηλής Φωτεινότητας (High Luminosity Large Hadron Collider, HL-LHC) αποτελεί μια τρέχουσα αναβάθμιση του Μεγάλου Αδρονικού Επιταχυντή (Large Hadron Collider, LHC) η οποία στοχεύει στην αύξηση της φωτεινότητας του επιταχυντή κατά έναν παράγοντα 10, παρέχοντας καλύτερη δυνατότητα για παρατηρήσεις σπάνιων φαινομένων και για βελτιώσεις στατιστικά οριακών μετρήσεων. Προκειμένου να αντιμετωπίσει τις προκλήσεις της πρωτοφανούς φωτεινότητας πρωτονίων-πρωτονίων, η Συνεργασία Συμπαγές Μιονικό Σωληνοειδές (Compact Muon Solenoid, CMS) θα πρέπει να αντεπεξέλθει στη γήρανση του παρόντος ανιχνευτή και να προωθήσει τις μεθόδους που χρησιμοποιούνται για την απομόνωση και την ακριβή μέτρηση των προϊόντων των πιο σημαντικών συγκρούσεων.

Για να προσδιοριστούν οι συνθήκες των πιο σημαντικών συμβάντων, είναι κρίσιμο να υπολογιστεί η ορμή των σωματιδίων παρακολουθώντας τις τροχιές τους δια μέσου του μαγνητικού πεδίου του ανιχνευτή. Όσο πιο καμπυλωτή η διαδρομή ενός σωματιδίου, τόσο λιγότερη ορμή είχε αρχικά. Οι διαδρομές φορτισμένων σωματιδίων καταγράφονται στο εσώτερο μέρος του ανιχνευτή CMS, του Τροχιοδεικτικού ανιχνευτή (Tracker), βρίσκοντας τις θέσεις των σωματιδίων σε διάφορα σημεία-κλειδιά. Ο Τροχιοδεικτικός ανιχνευτής είναι ικανός να ανακατασκευάσει τα μονοπάτια υψηλής ενέργειας μιονίων, ηλεκτρονίων και αδρονίων, καθώς και να καταχωρήσει τροχιές που προέρχονται από τη διάσπαση των βραχύβιων b κουαρκ που θα χρησιμοποιηθούν για τη μελέτη των διαφορών μεταξύ ύλης και αντιύλης. Η ακρίβεια της θέσης στον Τροχιοδεικτικό ανιχνευτή χρειάζεται να είναι της τάξης των 10 μικρομέτρων, ενώ το υλικό του να αντέχει σε δριμεία ακτινοβολία. Ο αναβαθμισμένος Τροχιοδεικτικός ανιχνευτής για την εποχή του HL-LHC θα κατασκευαστεί εξ ολοκλήρου από αισθητήρες πυριτίου, θα έχει βελτιωμένες δυνατότητες σκανδαλισμού και θα αποτελείται από δύο υπο-ανιχνευτές: έναν ανιχνευτή κορυφής κυψελίδων που θα καταλαμβάνει την εσωτερική περιοχή και έναν Εξωτερικό Τροχιοδεικτικό ανιχνευτή (Outer Tracker, OT) που θα αποτελείται από δομικές μονάδες μικρολωρίδων.

Τα δισκίδια όλων των πρότυπων αισθητήρων μικρολωρίδων πυριτίου τύπου p που μελετήθηκαν στο πλαίσιο της Αναβάθμισης Φάσης-2 του Τροχιοδεικτικού ανιχνευτή του CMS περιείχαν μισοφέγγαρα (half-moons) με δομές δοκιμών. Ήταν απαραίτητο να εκτελεστούν ηλεκτρικός χαρακτηρισμός και δοκιμές ακτινοβόλησης στις δομές δοκιμής αποκομμένες από αυτά τα δισκίδια, προκειμένου να προσδιοριστούν η ποιότητα του υλικού και η συμπεριφορά των εξαρτημάτων που εμπεριέχονται στις δομές δοκιμής. Τα αποτελέσματα αυτών των δοκιμών αναλύονται στο παρόν έργο.

Από την άλλη πλευρά, κατά τη διάρκεια της περιόδου έρευνας και ανάπτυξης οι δοκιμές υπό δέσμη είναι ένας ισχυρός τρόπος για να εξεταστεί η συμπεριφορά των αισθητήρων πυριτίου σε ρεαλιστικές συνθήκες. Τα τηλεσκόπια που χρησιμοποιούνταν στο παρελθόν διέθεταν ηλεκτρονικά ανάγνωσης αργά για τις ανάγκες του αναβαθμισμένου πειράματος CMS. Νέα τηλεσκόπια κυψελίδων σχεδιάστηκαν, κατασκευάστηκαν και τέθηκαν σε λειτουργία για δοκιμές με δέσμες υπό τον ονομαστικό ρυθμό του LHC με πρότυπες δομικές μονάδες για την Αναβάθμιση Φάσης-2 του Τροχιοδεικτικού ανιχνευτή του CMS. Οι πτυχές σχεδιασμού και λειτουργίας δύο τέτοιων τηλεσκοπίων υψηλού ρυθμού, καθώς και τα αποτελέσματα των πρώτων δοκιμών με δέσμες μαζί τους, περιγράφονται επίσης σε αυτή τη διατριβή.

Στο Κεφάλαιο 1 γίνεται ιστορική ανασκόπηση των επιταχυντών και περιγράφονται οι βασικές κατηγορίες τους, όπως ο γραμμικός επιταχυντής, το κύκλοτρο και το σύγχρωτρο. Στη συνέχεια παρουσιάζεται ο Μεγάλος Αδρονικός Επιταχυντής που βρίσκεται στο ευρωπαϊκό κέντρο πυρηνικών ερευνών στη Γενεύη. Αυτός αποτελείται από ένα δακτύλιο περιφέρειας 27 χιλιομέτρων από υπεραγώγιμους μαγνήτες και είναι μια διαδοχή διατάξεων που επιταχύνουν σωματίδια, κυρίως πρωτόνια, σε όλο και υψηλότερες ενέργειες. Κάθε διάταξη ενισχύει την ενέργεια της δέσμης σωματιδίων πριν από την έγχυση της δέσμης στην επόμενη διάταξη στη σειρά. Η αλυσίδα περιέχει τον Γραμμικό Επιταχυντή 2 που επιταχύνει τα πρωτόνια στην ενέργεια των 50 MeV, τον Αρωγό Σύγχρωτρο Πρωτονίων που επιταχύνει τα πρωτόνια στα 1.4 GeV, το Σύγχρωτρο Πρωτονίων που επιταχύνει τα πρωτόνια στα 25 GeV, και το το Σούπερ Σύγχρωτρο Πρωτονίων που επιταχύνει τα πρωτόνια στα 450 GeV, Τα πρωτόνια μεταφέρονται τελικά στον Μεγάλο Αδρονικό Επιταχυντή όπου οι δέσμες επιταχύνονται ως την ενέργεια των 6.5 TeV, ανά δέσμη. Από τον Ιούνιο του 2018 έχει αρχίσει η αναβάθμιση του Μεγάλου Αδρονικού Επιταχυντή στον Μεγάλο Αδρονικό Επιταχυντή Υψηλής Φωτεινότητας που θα επιτρέψει νέες ανακαλύψεις στη φυσική από το 2027 και έπειτα. Η αναβάυμιση στοχεύει στην αύξηση της φωτεινότητας της μηχανής κατά συντελεστή 10 ως τα $10^{35}\,\mathrm{cm}^{-2}\mathrm{s}^{-1}$, παρέχοντας μεγαλύτερη ευκαιρία να παρατηρηθούν σπάνια φαινόμενα και να βελτιωθούν στατιστικά οριακές μετρήσεις. Αντίστοιχα θα αναβαθμιστούν και τα μεγάλα πειράματα του επιταχυντή ALICE, ATLAS, CMS, LHCb (Fig. 1).

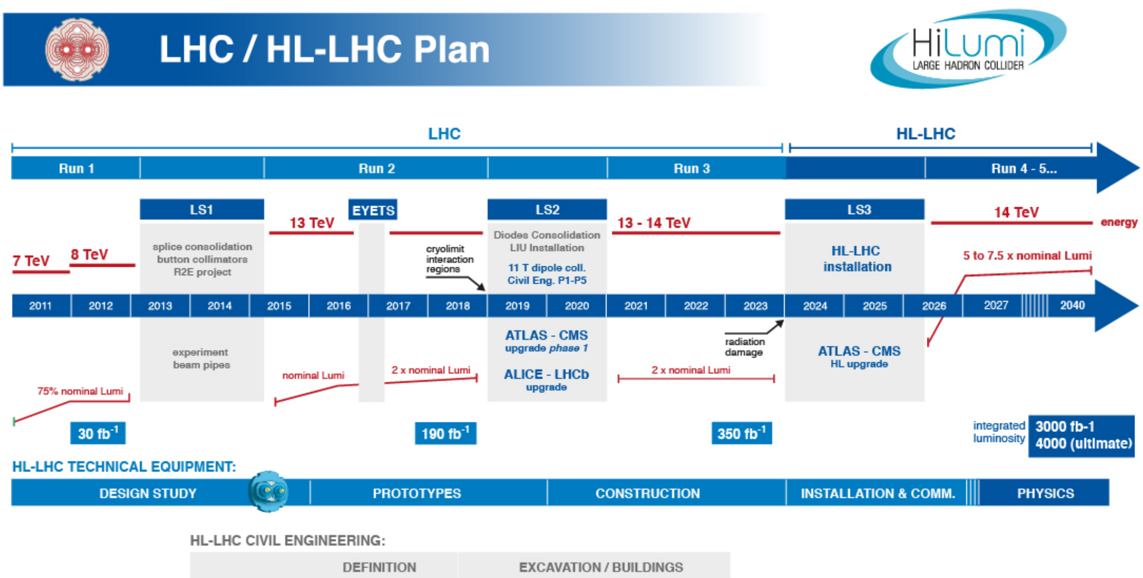

Figure 1: Το βασικό σχέδιο λειτουργίας για τον Μεγάλο Αδρονικό Επιταχυντή για την επόμενη δεκαετία και ύστερα, όπου φαίνονται η ενέργεια των συγκρούσεων (άνω κόκκινη γραμμή) και η φωτεινότητα (κάτω γραμμές).

Στο Κεφάλαιο 2 πραγματοποιείται ενδελεχής παρουσίαση όλων των τμημάτων του ανιχνευτή CMS (Fig. 2) τα οποία αντιπροσωπεύουν διαφορετικά στρώματα που περικλείουν τον άξονα της δέσμης. Αναλύονται ο σκοπός και η λειτουργία του υπεραγώγιμου σωληνοειδούς μαγνήτη μήκους 13 μέτρων που παράγει το μαγνητικό πεδίο έντασης 3.8 T το οποίο κάμπτει τις τροχιές των φοριστμένων σωματιδίων επιτρέποντας το διαχωρισμό τους, τον τροχιοδεικτικό ανιχνευτή από πυρίτιο, τον ηλεκτρομαγνητικό θερμιδομετρητή που αποτελείται από κρυστάλλους από κράμα μολύβδου-βολφραμίου, τον αδρονικό θερμιδομετρητή που αποτελείται από παρεμβαλλόμενα στρώματα πυκνού ορείχαλκου ή χάλυβα εναλλασσόμενα με πλαστικούς σπινθηριστές ή κρυσταλλικές ίνες, και τους απομακρυσμένους από το σημείο σύγκρουσης θαλάμους αερίων που ανιχνεύουν τα μιόνια. Κατά την Αναβάθμιση Φάσης-2 ο Εξωτερικός τροχιοδεικτικός ανιχνευτής θα περιέχει ως βασική δομική μονάδα τη μονάδα $\mathrm{p_T}$. Θα υπάρχουν δύο τύποι μονάδων $\mathrm{p_T}$, η μονάδα 2S και η μονάδα PS. Και οι δύο απαρτίζονται από ζεύγη αισθητήρων πυριτίου, αλλά ενώ οι μονάδες 2S αποτελούνται από δύο αισθητήρες μικρολωρίδων, οι μονάδες PS αποτελούνται από έναν αισθητήρα μικρολωρίδων και έναν αισθητήρα κυψελίδων. Η λειτουργικότητά τους στηρίζεται στη συσχέτιση επιτυχιών (μετρημένων χτυπημάτων από σωματίδια) στους δύο αισθητήρες της κάθε μονάδας, με την απόρριψη σημάτων από σωματίδια με εγκάρσια ορμή μικρότερη από ένα δεδομένο κατώφλι p_T. Ένα ολοκληρωμένο κύκλωμα λαμβάνει τις θέσεις των χτυπημάτων από φορτισμένα σωματίδια που κάμπτονται στο εγκάρσιο επίπεδο κατά μια γωνία εξαρτώμενη από την p_T, μετρά την απόσταση σε τοπικές συντεταγμένες και τη συγκρίνει με ένα προκαθορισμένο παράθυρο αποδοχής για την επιλογή υποψηφίων με υψηλή p_T. Τα στελέχη τροχιάς (το στέλεχος είναι τύπος τοπικού τμήματος τροχιάς που πρέπει να αντιστοιχεί σε ζευγάρι επιτυχιών στους δύο αισθητήρες μιας μονάδας για ένα δεδομένο παράθυρο αποδοχής) σχηματίζονται και ωθούνται στο σύστημα σκανδαλισμού σε κάθε διασταύρωση δεσμών (Fig. 3). Ένα σύστημα εξεύρεσης τροχιών λαμβάνει δεδομένα στελεχών από μεμονωμένες δομικές μονάδες $\mathrm{p_T}$, και ύστερα πραγματοποιεί εξεύρεση έγκυρων τροχιών.

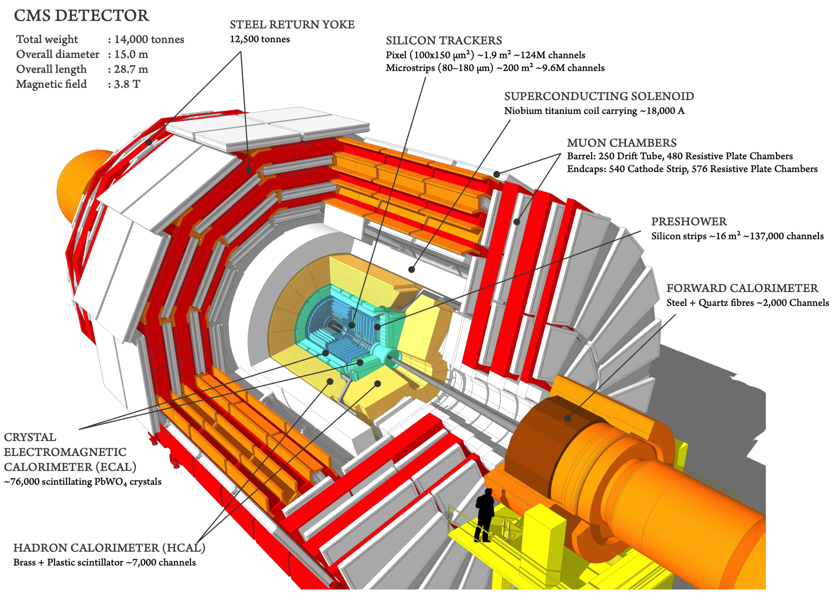

Figure 2: Τμηματική προβολή του ανιχνευτή CMS. Οι δέσμες του LHC κινούνται σε αντίθετες κατευθύνσεις, κατά μήκος του κεντρικού άξονα του κυλίνδρου του CMS, και συγκρούονται στο μέσο του ανιχνευτή CMS. (Εικόνα: CMS-OUTREACH-2019-001.)

Το Κεφάλαιο 3 κάνει μια ολοκληρωμένη σύνοψη της θεωρίας ημιαγωγών, και παρουσιάζει τους αισθητήρες ημιαγωγών και την αλληλεπίδραση της ιονίζουσας ακτινοβολίας μαζί τους. Ξεκινάει από τις φυσικές ιδιότητες του πυριτίου, αναλύει την επίδραση των προσμείξεων στις ημιαγώγιμες ιδιότητές του, περιγράφει τη λειτουργία της διόδου p-n υπό διαφορετικές συνθήκες πόλωσης

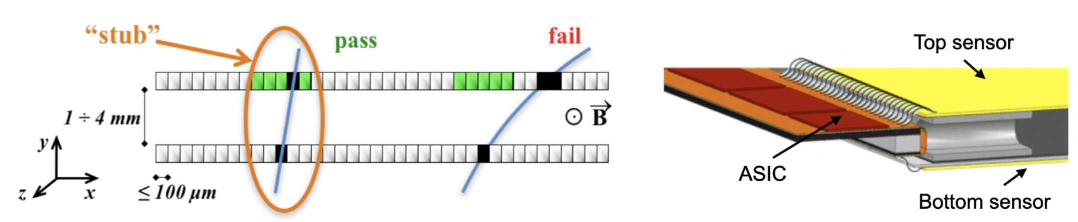

Figure 3: Σκίτσο για την αρχή εύρεσης στελέχους από τροχιά (αριστερά) και του γενικού σχεδίου για δομική μονάδα p_T (δεξιά). Μια τροχιά διαπερνά και τους δύο αισθητήρες μιας δομικής μονάδας. Μια άλλη τροχιά χαμηλής ορμής πέφτει έξω από το παράθυρο αποδοχής και δεν παράγει στέλεχος. (Εικόνα: CERN-LHCC-2017-009.)

(δίνοντας έμφαση στα φαινόμενα ολίσθησης και διάχυσης), περιγράφει τη λειγουργία του πυκνωτή δομής Μέταλλο-Οξείδιο-Ημιαγωγός με έμφαση στη συμπεριφορά του φορτίου στις τρεις περιοχές λειτουργίας του (συσσώρευση, απογύμνωση, αναστροφή, όπως φαίνονται στη Fig. 4) και την αντίστοιχη χαρακτηριστική καμπύλη χωρητικότητας-τάσης (Fig. 5), επεξηγεί τις βλάβες από διαφορετικούς τύπους ακτινοβολίας, και τέλος περιγράφει τις αρχές λειτουργίας των ανιχνευτών πυριτίου, και ειδικότερα των δύο βασικών τύπων τους, μικρολωρίδων και μικροκυψελίδων.

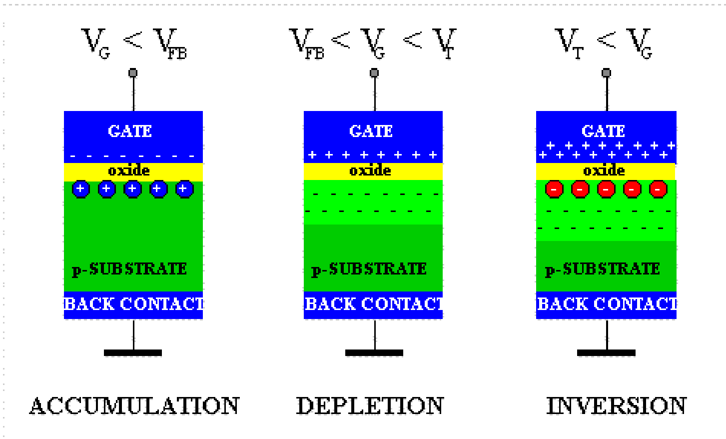

Figure 4: Φορτία σε δομή Μέταλλο-Οξείδιο-Ημιαγωγός υποστρώματος πυριτίου τύπου p υπό συνθήκες συσσώρευσης, απογύμνωσης και αναστροφής. (Εικόνα: Bart V. Van Zeghbroeck, Principles Of Semiconductor Devices And Heterojunctions, Prentice Hall, December 1st 2009.)

Στο Κεφάλαιο 4 γίνεται περιγραφή των διαδικασιών ηλεκτρικού χαρακτηρισμού και κλιματικών δοκιμών δομών πυριτίου τύπου p από τα ίδια δισκίδια με τους αισθητήρες που θα αποτελέσουν τη βάση για συναρμολόγηση για τις 2S δομικές μονάδες του τροχιοδεικτικού ανιχνευτή. Οι δομές παρασκευάζονται από την HPK και περιέχουν μεταξύ των άλλων διόδους και πυκνωτές σε διάταξη Μέταλλο-Οξείδιο-Ημιαγωγός. Από τις καμπύλες ρεύματος διαρροής-τάσης πόλωσης των διόδων εξάγεται η τιμή της τάσης απογύμνωσης, καθώς και το συμπέρασμα αν εμφανίζεται φαινόμενο κατάρρευσης στην εκάστοτε δίοδο ή όχι. Από τις καμπύλες χωρητικότητας-τάσης στους πυκνωτές δομής Μέταλλο-Οξείδιο-Ημιαγωγός εξάγεται η τιμή της τάσης επίπεδης ζώνης (η τάση στην οποία ο πυκνωτής αλλάζει συμπεριφορά και περνάει από την περιοχή συσσώρευσης στην περιοχή απογύμνωσης), καθώς και άλλες πολύτιμες παράμετροι. Οι δοκιμές στον κλιματικό θάλαμο λαμβάνουν χώρα σε υψηλές τιμές υγρασίας και σε υψηλές και χαμηλές τιμές θερμοκρασίας, για να ελεγχθεί η συμπεριφορά των διόδων σε ακραίες συνθήκες λειτουργίας. Σημαντικές πληρο-

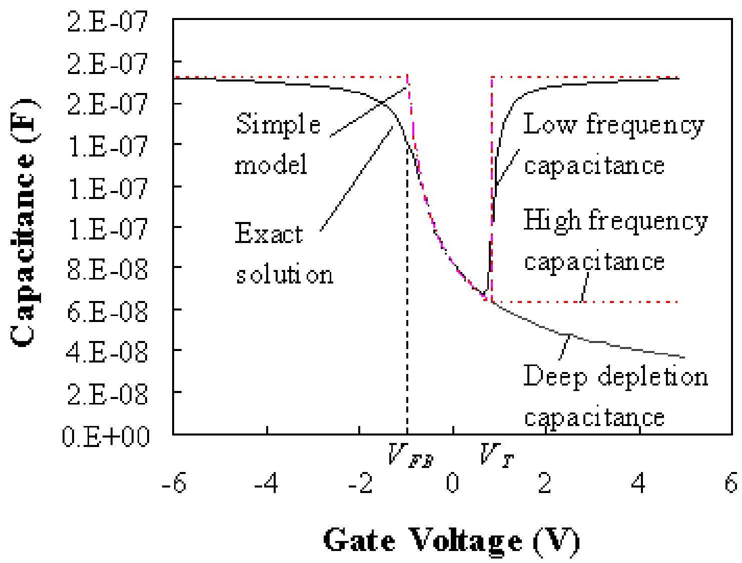

Figure 5: Χωρητικότητα χαμηλής συχνότητας πυκνωτή σώματος τύπου p. Εμφανίζεται η ακριβής λύση για τη χωρητικότητα χαμηλής συχνότητας (σταθερή γραμμή) και τις χωρητικότητες χαμηλής και ψηλής συχνότητας που ελήφθησαν με απλό μοντέλο τομής ευθειών (διακεκκομμένες γραμμές). $N_A = 10^{17}\,\mathrm{cm}^{-3}$ και $t_{ox} = 20\,\mathrm{nm}$. (Εικόνα: Bart V. Van Zeghbroeck, Principles Of Semiconductor Devices And Heterojunctions, Prentice Hall, December 1st 2009.)

φορίες για τις δομές με διόδους και πυκνωτές δίνει και η μελέτη τους κατά την ακτινοβόληση με γ-φωτόνια από πηγή κοβαλτίου-60 σε ολικές δόσεις ισοδύναμες με τις δόσεις που θα απορροφήσουν οι μονάδες του Εξωτερικού τροχιοδεικτικού ανιχνευτή στο αναβαθμισμένο πείραμα CMS σε όλη τη διάρκεια της λειτουργίας του. Οι ακτινοβολήσεις έλαβαν χώρα στην Ελληνική Επιτροπή Ατομικής Ενέργειας (ΕΕΑΕ) με πηγή ενεργότητας 11 TBq και ρυθμό δόσης 0.96 kGy/h. Το σύστημα ψύξης αποτελείτο από θερμοηλεκτρικό ψύκτη, πλάκα αλουμινίου και ανεμιστήρα για απαγωγή θερμότητας, ενώ ένας μικροελεγκτής χρησιμοποιήθηκε για τη σταθεροποίηση της θερμοκρασίας (Fig. 6, αριστερά). Η ισορροπία φορτισμένων σωματιδίων επιτεύχθηκε χάρη σε ένα δοχείο από μόλυβδο με εσωτερική επένδυση αλουμινίου μέσα στο οποίο διατηρήθηκαν τα δείγματα κατά τη διάρκεια των ακτινοβολήσεων που πραγματοποιήθηκαν σε απόσταση 4 μέτρων από την πηγή (Fig. 6, δεξιά). Στις διόδους δεν παρατηρήθηκε φαινόμενο κατάρρευσης ακόμα και για τάσεις της τάξης των $-1000\,\mathrm{V}$. Στις καμπύλες χωρητικότητας-τάσης των πυκνωτών διάταξης Μέταλλο-Οξείδιο-Ημιαγωγός παρατηρήθηκε μετατόπιση της τάσης επίπεδης ζώνης προς υψηλότερες απόλυτες τιμές συναρτήσει της δόσης ακτινοβολίας και για μικρές δόσεις, λόγω του επαγόμενου θετικού φορτίου στο οξείδιο μετά την έκθεση σε γ-φωτόνια (Fig. 7).

Στο Κεφάλαιο 5 περιγράφονται οι διαδικασίες βαθμονόμησης και η προσομοίωση του τηλεσκοπίου CHROMIE, καθώς και τα αποτελέσματα των σχετικών δοκιμών με δέσμες 120 GeV πιονίων. Το CHROMIE βρίσκεται στο CERN και είναι ένα από τα τηλεσκόπια που σχεδιάστηκαν και συναρμολογήθηκαν προκειμένου να δοκιμαστούν υπό δέσμη οι δομικές μονάδες p_T Φάσης-2 ως προς την αποδοτικότητα των καναλιών ανάγνωσης και το μέγεθος των συμπλεγμάτων από επιτυχίες (χτυπήματα). Τα οχτώ επίπεδα του τηλεσκοπίου περιέχουν αισθητήρες κυψελίδων που χρησιμοποιούνται στην ανακατασκευή τροχιών με υψηλή ακρίβεια. Όλα τα τηλεσκόπια που χρησιμοποιούνταν μέχρι πρότεινος από τη συνεργασία CMS διέθεταν τσιπ με συχνότητα ανάγνωσης 4600 φορές μικρότερη από την ονομαστική συχνότητα του Μεγάλου Αδρονικού Επιταχυντή (40 MHz), γεγονός που καθιστούσε αδύνατη τη δοκιμή των νέων δομικών μονάδων υπό τις ονομαστικές συνθήκες λειτουργίας τους. Το CHROMIE, όμως, αποτελεί τηλεσκόπιο υψηλού ρυθμού που

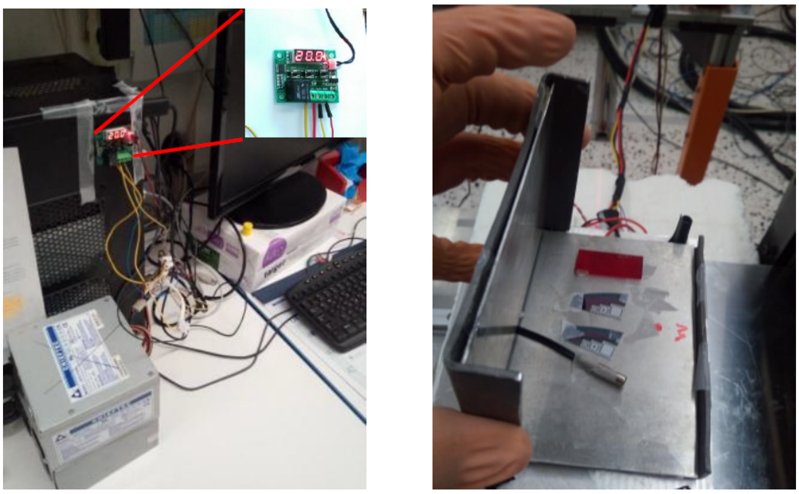

Figure 6: Αριστερά: Ο μικροελεγκτής και τα τροφοδοτικά της πειραματικής εγκατάστασης. Δεξιά: Το δοχείο μολύβδου-αλουμινίου για ισορροπία φορτισμένων σωματιδίων.

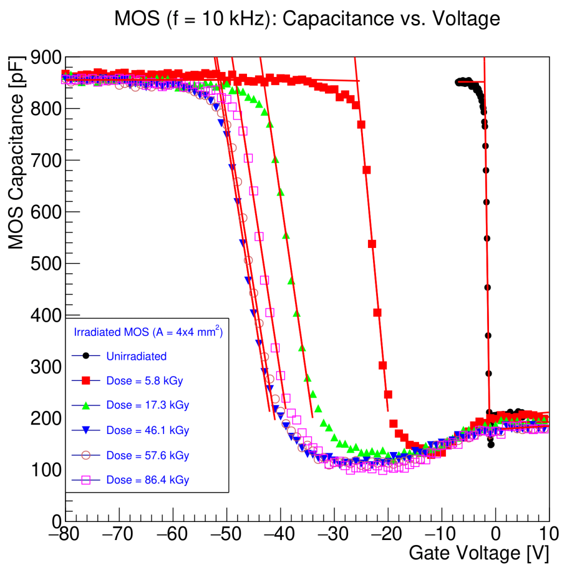

Figure 7: Καμπύλες χωρητικότητας-τάσης για πυκνωτή δομής Μέταλλο-Οξείδιο-Ημιαγωγός για διάφορες δόσεις. Συχνότητα μέτρησης = 10 kHz.

μπορεί και ανταποκρίνεται στον ονομαστικό ρυθμό των 40 MHz, και διαθέτει συμβατά υλικό και λογισμικό με τα υπάρχοντα στο πείραμα CMS, ενώ έχει ευκρίνεια της τάξης των 10 μm. Ένα αυτόνομο πρόγραμμα για την προσομοίωσή του βασισμένο στο λογισμικό Geant4 έχει αναπτυχθεί παράλληλα με τη συναρμολόγηση του τηλεσκοπίου (Fig. 8). Το πρόγραμμα αυτό μεταξύ των άλλων μπορεί να προβλέπει την ενέργεια που εναποθέτουν τα πρωτογενή σωματίδια σε κάθε επίπεδο της διάταξης (Fig. 9), την ευκρίνεια του τηλεσκοπίου, το μέγεθος των συμπλεγμάτων στα διάφορα επίπεδα (σε αριθμό κυψελίδων/μικρολωρίδων) και το συνολικό φορτίο του κάθε συμπλέγματος.

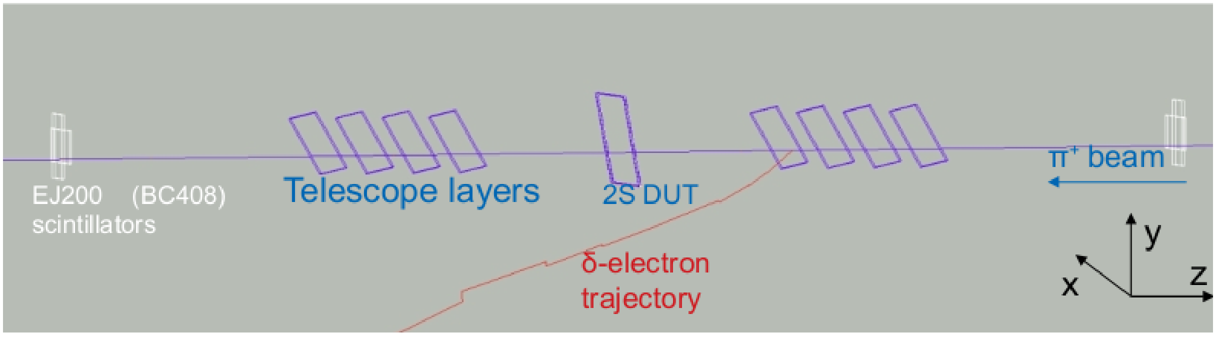

Figure 8: Οπτικοποίηση της γεωμετρίας προσομοίωσης με Geant4 του CHROMIE σε λειτουργία υπό δέσμη. Η διάταξη προς δοκιμή είναι μια μονάδα 2S: 2 αισθητήρες πυριτίου (102700 μm × 94108 μm × 320 μm), με απόσταση μεταξύ των αισθητήρων: περίπου 2 mm, απόσταση μεταξύ κέντρων γειτονικών μικρολωρίδων: 90 μm, ενεργό βάθος: 240 μm.

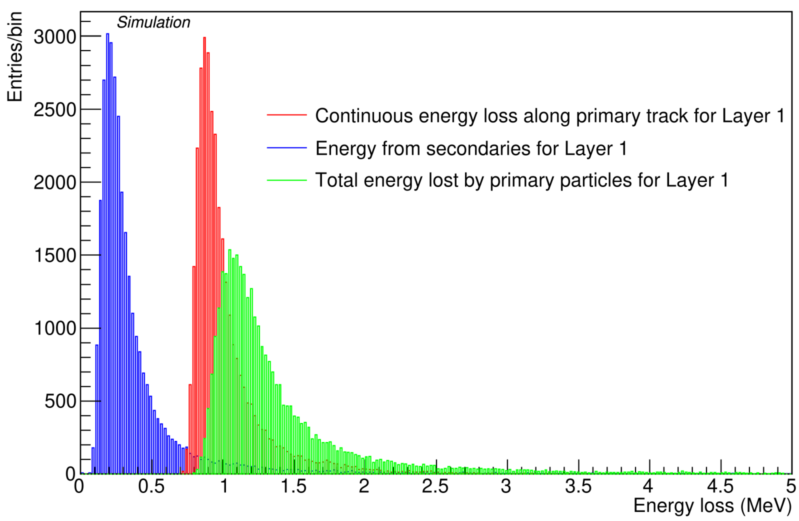

Figure 9: Απωλεσθείσα ενέργεια από τα πρωτογενή σωματίδια (120 GeV π^+) στο Επίπεδο 1 του CHROMIE (προσομοίωση).

Το Κεφάλαιο 6 έχει ως θέμα το σχεδιασμό και την προσομοίωση με το πρόγραμμα Geant4 του τηλεσκοπίου CHROMini, το οποίο βρίσκεται στο IPHC στο Στρασβούργο, ενώ γίνεται και σύγκριση με τα αποτελέσματα της πρώτης δοκιμής με δέσμες 25 MeV πρωτονίων προερχόμενες από το κύκλοτρο CYRCé. Το κύκλοτρο παρέχει μια παλμική δέσμη με συχνότητα 85 MHz η οποία μπορεί να μειωθεί με ειδική διάταξη σε συχνότητα παραπλήσια με τον ονομαστικό ρυθμό του Μεγάλου

Αδρονικού Επιταχυντή. Η διάταξη του CHROMini είναι παραπλήσια με εκείνη του CHROMIE, αλλά απαρτίζεται από μόνο δύο επίπεδα με αισθητήρες κυψελίδων (Fig. 10). Το πρόγραμμα προσομοίωσης χρησιμοποιήθηκε για τη σχεδίαση του τηλεσκοπίου (πάχη εξαρτημάτων, μέγεθος κυψελίδων) και για την εκτίμηση της απόδοσής του ως προς την εναπόθεση ενέργειας στον ανιχνευτή, την πολλαπλή σκέδαση των πρωτονίων, τη χωρική ευκρίνεια (Fig. 11), το προφίλ της δέσμης και την πολλαπλότητα επιτυχίας (Fig. 12).

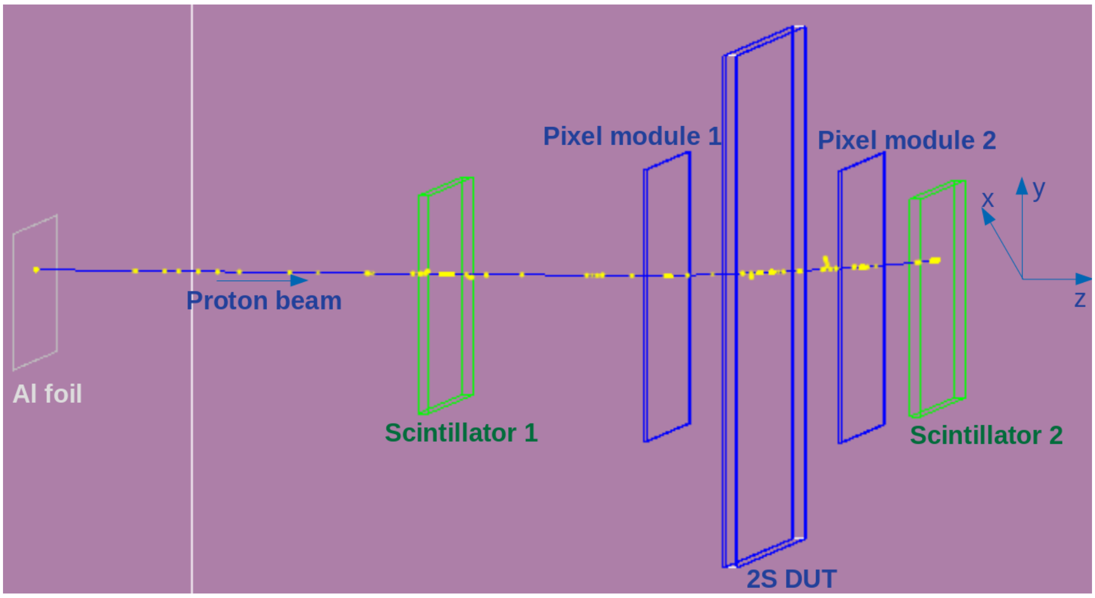

Figure 10: Οπτικοποίηση της προσομοιωμένης γεωμετρίας του τηλεσκοπίου CHROMini και μιας διάταξης προς δοκιμή (2S δομική μονάδα).

Στο Κεφάλαιο 7 περιγράφεται μια δοκιμή με δέσμες 4 GeV ηλεκτρονίων με το τηλεσκόπιο DATURA και με μονάδα 2S ως διάταξη υπό δοκιμή, στην περιοχή δοκιμών TB21 του DESY (Fig. 13). Το DATURA είναι ένα τηλεσκόπιο τύπου EUDET. Περιέχει έξι επίπεδα αισθητήρων κυψελίδων με χωρική ευκρίνεια της τάξης των λίγων μικρομέτρων, ψηφιακή απόδοση και προγραμματιζόμενη μονάδα λογικής σκανδαλισμού. Η μετέπειτα ανάλυση των δεδομένων από τη δοκιμή με δέσμες είχε ως στόχο τον υπολογισμό της απόδοσης εύρεσης στελεχών για διαφορετικές γωνίες περιστροφής της 2S μονάδας (Fig. 14). Στο κεφάλαιο αυτό σκιαγραφούνται τα τεχνικά χαρακτηριστικά του DATURA, το στήσιμο και η εξέλιξη της δοκιμής με δέσμες, τα διαφορετικά πλαίσια για την ανάλυση των δεδομένων (βασισμένα στα scope2s, EUTelescope) και οι διάφορες σαρώσεις της διάταξης υπό δοκιμή (γωνιακή σάρωση, σάρωση κατά μήκος των μικρολωρίδων, γωνιακή σάρωση κατά μήκος των μικρολωρίδων).

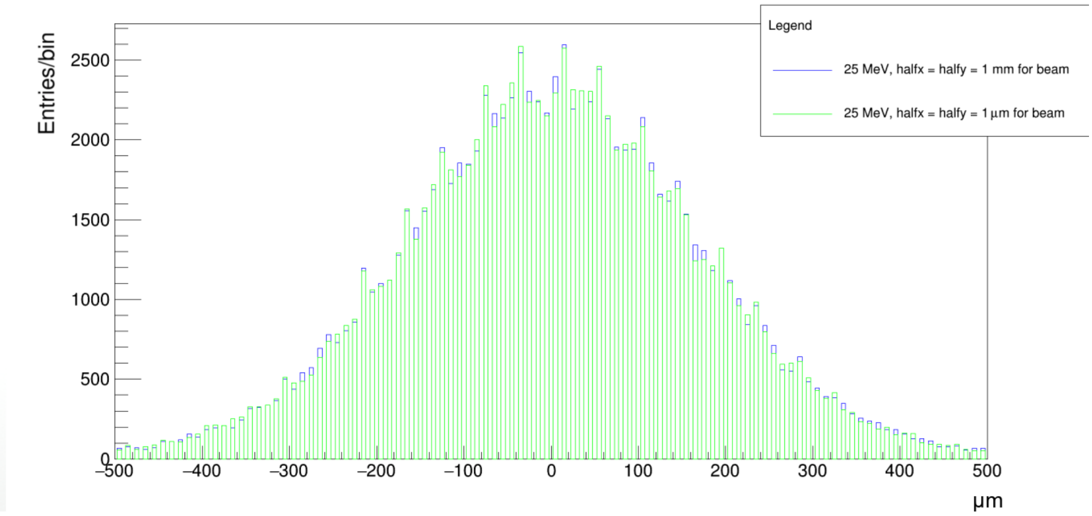

Figure 11: Υπολείμματα-Υ ($C^{'}C_y$) για τον δεύτερο 2S αισθητήρα κατά μήκος της δέσμης: σύγκριση ανάμεσα σε κυκλική δέσμη διαμέτρου 1 μm και σε κυκλική δέσμη διαμέτρου 1 mm (προσομοίωση).

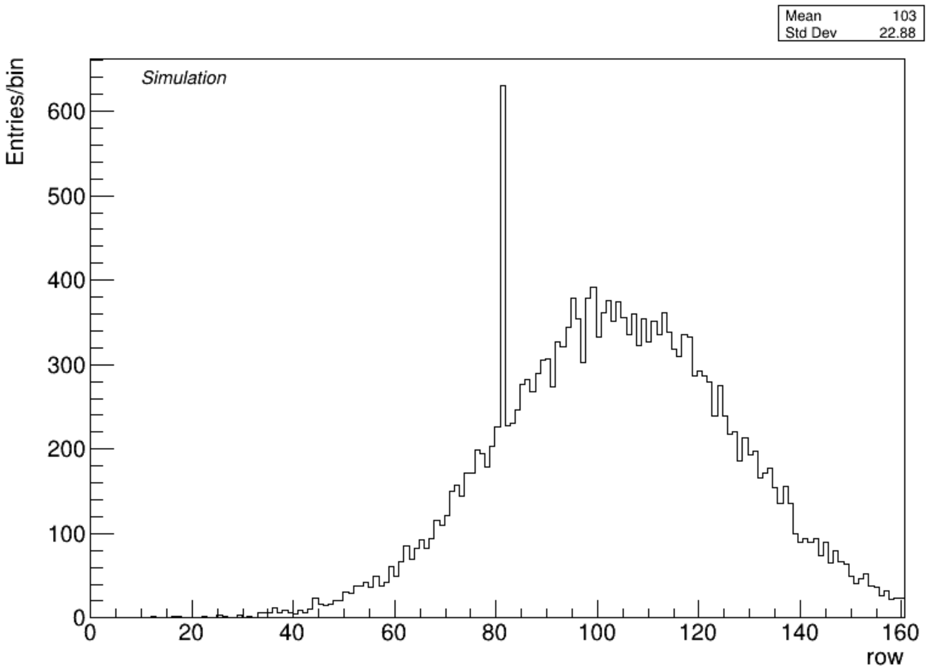

Figure 12: Χάρτης επιτυχίας κατά μήκος των σειρών για χτυπημένη δομική μονάδα του δεύτερου επιπέδου κυψελίδων κατά μήκος της δέσμης (προσομοίωση). Η κορυφή αντιστοιχεί σε περισσότερες επιτυχίες στο μέσο της δομικής μονάδας όπου οι κυψελίδες έχουν διπλάσιο πλάτος σε σχέση με τις υπόλοιπες.

Figure 13: Φωτογραφία της περιοχής δοκιμών TB21 όπου επισημαίνονται ο διπολικός μαγνήτης και το τηλεσκόπιο DATURA.

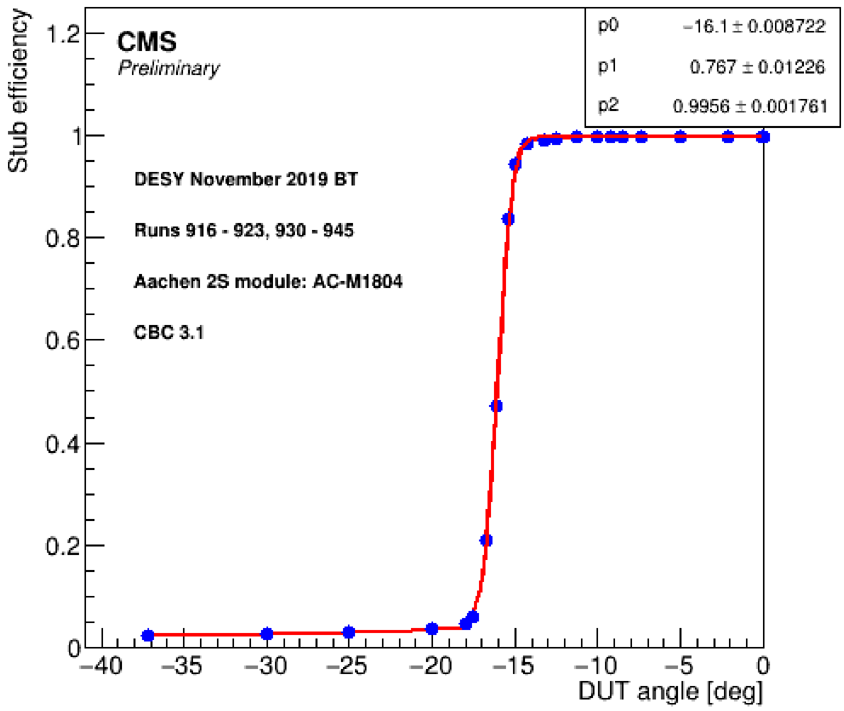

Figure 14: Αποδοτικότητα στελέχους της δομικής μονάδας 2S συναρτήσει της γωνίας στροφής της διάταξης υπό δοκιμή από δοκιμή με δέσμες στο DESY.

Στο πλαίσιο αυτής της διδακτορικής διατριβής έχουν προκύψει οι ακόλουθες δημοσιεύσεις και παρουσιάσεις:

P. Asenov, Commissioning and simulation of CHROMIE, a high-rate test beam telescope, JINST 15 (2020) 02, C02003.

P. Asenov, P. Assiouras et al., Cobalt-60 gamma irradiation of silicon test structures for high-luminosity collider experiments, PoS Vertex2019 (2020) 061.

P. Assiouras, P. Asenov et al., A program for fast calculation of capacitances, in planar pixel and strip silicon sensors, PoS Vertex2019 (2020) 059.

CMS collaboration, The phase-2 upgrade of the CMS tracker, CERN, Geneva, Switzerland, Rep. CERN-LHCC-2017-009.

W Adam et al., P-type silicon strip sensors for the new CMS Tracker at HL-LHC, JINST 12 (2017) 06, P06018.

W Adam et al., Characterisation of irradiated thin silicon sensors for the CMS phase II pixel upgrade, Eur.Phys.J.C 77 (2017) 8, 567.

W Adam et al., Beam test performance of prototype silicon detectors for the Outer Tracker for the Phase-2 Upgrade of CMS, JINST 15 (2020) 03, P03014.

P. Asenov, Test beam facility at CYRCé for high particle rate studies with a CMS upgrade module: design and simulation, 7th Beam Telescopes and Test Beams Workshop, 14-18 January 2019, CERN.

P. Asenov, Contribution of INPP to the CMS Phase-2 Upgrade, HEP 2019 - Conference on Recent Developments in High Energy Physics and Cosmology 17-20 April 2019, NCSR "DEMOKRITOS", Athens, Greece.

P. Asenov, Performance of a simple 2-plane telescope (CHROMini) and a CMS 2S module in a 25 MeV proton beam: Comparison between data and Geant4 simulation, 8th Beam Telescopes and Test Beams Workshop, 27-31 January 2020, Tbilisi State University.

Abstract

In order to unveil the mysteries of the universe the high energy physicists will need to boost the world's most powerful particle collider's potential for discoveries. The High Luminosity Large Hadron Collider (HL-LHC) is an ongoing upgrade of the Large Hadron Collider (LHC) which aims at increasing the luminosity of the accelerator by a factor of 10, providing a better opportunity to observe rare processes and meliorating statistically marginal measurements. To face the challenges of the unprecedented p-p luminosity, the Compact Muon Solenoid (CMS) collaboration will need to cope with the aging of its present detector and to advance the methods used to isolate and measure accurately the products of the most significant collisions.

To determine the conditions of the most important events it is critical to calculate the momentum of particles by tracking their paths through the magnetic field of the detector. The more curved the path of a particle, the less momentum it had. The charged particle paths are recorded in the innermost part of the CMS detector, the Tracker, by finding the positions of particles at several key points. The Tracker is capable of reconstructing the paths of high-energy muons, electrons and hadrons, as well as of registering tracks coming from the decay of the short-lived b quarks that will be used to study the differences between matter and antimatter. The position accuracy in the Tracker needs to be of the order of 10 micrometers, while its material to be able to withstand severe radiation. The upgraded Tracker detector for the HL-LHC era will be made entirely of silicon sensors, will have improved trigger capabilities and will be composed of two sub-detectors: a Pixel vertex detector occupying the inner region and an Outer Tracker (OT) consisting of microstrip modules.

The wafers of all the microstrip prototype p-type silicon sensors which were studied in the framework of the CMS Phase-2 Tracker Upgrade contained half-moons with test structures. It was necessary to perform electrical characterization and irradiation tests on the test structures diced from these wafers, in order to determine the material quality and the behavior of the components on the test structures. The results of these tests are analyzed in this work.

On the other hand, during the research and development period, tests performed under beam are a powerful way to examine the behavior of the silicon sensors in realistic conditions. The telescopes used in the past had a slow readout for the needs of the upgraded CMS experiment. New pixel telescopes were designed, built and commissioned for beam tests under the LHC nominal rate with prototype modules for the CMS Phase-2 Tracker Upgrade. The design and operation aspects of two such high-rate telescopes, as well as the results of the first beam tests with them, are also described in this dissertation.

This doctoral dissertation comes along with the following publications and presentations that have emerged during its course:

P. Asenov, Commissioning and simulation of CHROMIE, a high-rate test beam telescope, JINST 15 (2020) 02, C02003.

P. Asenov, P. Assiouras et al., Cobalt-60 gamma irradiation of silicon test structures for high-luminosity collider experiments, PoS Vertex2019 (2020) 061.

P. Assiouras, P. Asenov et al., A program for fast calculation of capacitances, in planar pixel and strip silicon sensors, PoS Vertex2019 (2020) 059.

CMS collaboration, The phase-2 upgrade of the CMS tracker, CERN, Geneva, Switzerland, Rep. CERN-LHCC-2017-009.

W Adam et al., P-type silicon strip sensors for the new CMS Tracker at HL-LHC, JINST 12 (2017) 06, P06018.

W Adam et al., Characterisation of irradiated thin silicon sensors for the CMS phase II pixel upgrade, Eur.Phys.J.C 77 (2017) 8, 567.

W Adam et al., Beam test performance of prototype silicon detectors for the Outer Tracker for the Phase-2 Upgrade of CMS, JINST 15 (2020) 03, P03014.

P. Asenov, Test beam facility at CYRCé for high particle rate studies with a CMS upgrade module: design and simulation, 7th Beam Telescopes and Test Beams Workshop, 14-18 January 2019, CERN.

P. Asenov, Contribution of INPP to the CMS Phase-2 Upgrade, HEP 2019 - Conference on Recent Developments in High Energy Physics and Cosmology 17-20 April 2019, NCSR "DEMOKRITOS", Athens, Greece.

P. Asenov, Performance of a simple 2-plane telescope (CHROMini) and a CMS 2S module in a 25 MeV proton beam: Comparison between data and Geant4 simulation, 8th Beam Telescopes and Test Beams Workshop, 27-31 January 2020, Tbilisi State University.

Preface

Purpose of this dissertation is to introduce and demonstrate the basic components of the LHC complex, the need for the HL-LHC Upgrade and the upgraded CMS detector, alongside with its detection technologies. It focuses mainly on the Phase-2 Upgrade of the Outer Tracker, with special emphasis on the semiconductor technology used there. Furthermore, the characterization of the related test structures and the respective laboratory equipment are described. Finally, in this dissertation the test beam and simulation results of the test beams with prototype modules and the high-rate telescopes used there are discussed. The arrangement of the manuscript is described below, providing a brief summary of the chapter's content.

- **Chapter 1**: The introductory chapter, with a retrospect of the most powerful particle colliders, with a main focus on the Large Hadron Collider (LHC) complex and a brief presentation of the physics motivation behind its upgrade to the High Luminosity Large Hadron Collider (HL-LHC).

- **Chapter 2**: An in-depth overview of the CMS detector, shedding light on all its aspects, focusing mainly on the Tracker and its Phase-2 Upgrade.

- **Chapter 3**: A comprehensive review on semiconductor theory, semiconductor sensors and the interaction of ionizing radiation with them.

- **Chapter 4**: A summary of the electrical characterization, the climate tests and irradiation with cobalt-60 gamma photons of Hamamatsu p-type silicon test structures.

- **Chapter 5**: A description of the calibration procedures and the Geant4 simulation of the CMS High Rate telescOpe MachInE (CHROMIE) at CERN, and the results of a test beam with 120 GeV pions.

- **Chapter 6**: A presentation of the design and the Geant4 simulation of the CHROMini telescope at IPHC-Strasbourg, along with the results of its first test beam with 25 MeV protons.

- **Chapter 7**: The final chapter dedicated to a beam test of modules with two strip sensors at DESY, emphasizing the calculation of the stub efficiency for tracks inclined along the strips and for various rotation angles of a given module.

This dissertation is submitted for the degree of Doctor of Philosophy in Physics at the National Technical University of Athens. The research described herein was conducted at the facilities of the National Centre for Scientific Research (NCSR) "Demokritos", the European Organization for Nuclear Research (CERN), the Greek Atomic Energy Commission (GAEC), the Karlsruhe Institute of Technology (KIT), the German Electron Synchrotron (DESY) and the Hubert Curien Pluridisciplinary Institute (IPHC), and it is to the best of my knowledge original, except where references and acknowledgments of other works are provided.

During the research described herein I was a member of the NCSR "Demokritos" team.

Acknowledgments

This dissertation has been accomplished due to the guidance and support of several people. Over a span of nearly 4 years and during the experimental activities conducted in four countries, I had the opportunity to meet and collaborate with wonderful persons and to experience some of the best time of my life.

First of all, I would like to express my sincere gratitude to my supervisor Dr. Dimitris Loukas who gave me the opportunity to work on the upgrade of one of the biggest experiments in the world. He persistently encouraged me to seek answers even to the toughest questions and was a fathomless source of ideas and advice throughout the whole duration of my PhD.

I would also like to denote my deep appreciation to Dr. Aris Kyriakis, a highly experienced researcher who passed me a large portion of his rich knowledge on both hardware and data analysis. Many aspects of the work presented here wouldn't have been realized without him.

I wish to show my gratitude to Dr. Theodoros Alexopoulos and Dr. Michail Kokkoris for accepting to be part of my advisory committee and their continuous support throughout the years.

Furthermore, I would like to thank two more people from our group: Panos Assiouras for the effective teamwork on the characterization of silicon test structures and for the shifts we shared during the irradiation campaign, and Yiannis Kazas - our talented engineer who would always come up with bright solutions when things would go awry in the lab, and would make all devices work again. Thank you for making me feel at home in the workplace.

I am indebted to Dr. Alexander Dierlamm, Dr. H.J. Simonis, Dr. A.M. Nürnberg and the doctoral and non-doctoral students of the CMS hardware group at KIT, especially Marius Metzler, for assisting me in my first steps in sensor characterization during my internship in Karlsruhe.

I acknowledge the contribution of Konstantinos Filippou to the electrical measurements on MOS capacitors and diodes, and to Argiro Boziari and Panagiota Konstantinou to the setup of the cobalt-60 and related shifts during the irradiation campaign at GAEC. Credits for the design of the irradiated test structures go to all members of the CMS OT Sensor Working Group.

I am profoundly thankful to Dr. Stefano Mersi and Dr. Nikkie Deelen for introducing me to the CHROMIE telescope at CERN and giving me the opportunity to work on its implementation and testing. The CHROMIE telescope was developed by the CHROMIE team: B. Akgün, J. Andrea, C. Collard, N. Deelen, A. Di Mattia, G. Hugo, T. Kiss, A. Kyriakis, D. Loukas, S. Mersi, N. Siegrist, T. Tölyhi, A. Tsirou, V. Veszprémi and myself, with the support of I. Ahmed, E. Albert, J. Fulcher, D. Gigi, J.-F. Pernot, H. Postema and P.G. Verdini. In particular, I would like to give credits to Dr. Jérémy Andrea, Dr. Caroline Collard and Dr. Aris Kyriakis for their contribution to the analysis program.

I would like to pay my special regards to Dr. Jérémy Andrea and Dr. Ulrich Goerlach for their meticulous guidance through the development of the simulation program for the CHROMini telescope at IPHC. The CHROMini telescope was developed by the CHROMini team: J. Andrea, C. Bonnin, J.-M. Brom, L. Charles, C. Collard, N. Deelen, A. Dierlamm, A. Droll, T. Goeltzenlichter, U. Goerlach, C. Grimault, L. Gross, C. Haas, G. Heitz, D. Kotlinski, M. Krauth, U. Langenegger, D. Loukas, S. Maier, E. Nibigira, N. Ollivier-Henry, C. Ruescas, J. Sonneveld and S. Veeramootoo and myself. In particular, I would like to give credits to Clément Grimault for his contribution to the comparison between the simulation output and test beam data.

I am deeply grateful on the one hand to Dr. Daniel Pitzl and Chun (Ginger) Cheng, and on the other hand to Dr. A.M. Nürnberg, for the fact that I had all the help I needed in setting up and comprehending scope2s and the EUTelescope framework's analysis program, respectively.

Some of the conference presentations, notes and publications in journals accompanying this dissertation were edited by Dr. Katja Klein and Dr. Panja Luukka. I warmly thank them both for the fruitful discussions and comments.

In addition, for the fulfillment of my doctoral research work I would like to acknowledge financial support from the Hellenic Foundation for Research and Innovation (HFRI).

I would like to thank my family for being next to me during this important stage of my life and for teaching me to pursue my dreams. I would also like to thank my friends who have shared travels, holidays, walks, meals, conversations and beautiful moments with me in the past four years.

My biggest and wholehearted acknowledgment goes to my partner in life Gulnara. Words cannot describe how much I appreciate her kindness, affection and love towards me, and how much I am grateful about her endurance during my stressful days (and nights) of writing this dissertation. To her I dedicate this work.

The possession of knowledge does not kill the sense of wonder and mystery. There is always more mystery.
Anaïs Nin

Adopt the pace of nature: her secret is patience.
Ralph Waldo Emerson

Contents

Chapter 1

Introduction

This chapter presents a retrospect of the most powerful particle accelerators, with a main focus on the Large Hadron Collider (LHC) complex and a brief presentation of the physics motivation behind its upgrade to the High Luminosity Large Hadron Collider (HL-LHC).

1.1 History of particle accelerators

Particle accelerators are among the main tools used in high energy physics for basic research. They are powerful machines which use electromagnetic fields to propel charged particles to very high energies, and to contain them in well-defined beams. There are two basic classes of accelerators: electrostatic and electrodynamic (or electromagnetic) accelerators. Electrostatic accelerators use static electric fields to accelerate particles (e.g. the Cockcroft-Walton generator and the Van de Graaff generator) where the achievable kinetic energy for particles is determined by the accelerating voltage, which is limited by electrical breakdown. Electrodynamic accelerators, on the other hand, use changing electromagnetic fields (magnetic induction or oscillating radio frequency fields) to accelerate particles which can pass through the same accelerating field multiple times, and so the output energy is not limited by the strength of the accelerating field. Most modern large-scale accelerators are electrodynamic, and their development in the 20th century introduced humanity to a new era of scientific and technological achievements.

However, we can trace the origins of the predecessor of the modern accelerators much earlier, in the 18th century. The electrophorus is a manual capacitive electrostatic generator used to produce electrostatic charge via the process of electrostatic induction. Italian scientist Alessandro Volta improved and popularized the device in 1775, which was invented by Johan Carl Wilcke in 1762 (Fig. 1.1). The electrophorus consists of a dielectric plate (originally a resinous material, but plastic in modern versions) and a metal plate with an insulating handle. The dielectric plate is first charged through the triboelectric effect by rubbing it with fur. The metal plate is then placed onto the dielectric plate, and then the electrostatic field of the charged dielectric causes the charges in the metal plate to separate [1].

British inventor James Wimshurst developed another electrostatic generator between 1880 and 1883 which separates electric charges through electrostatic induction (or *influence*) not depending on friction for its operation. Two contra-rotating insulated discs mounted with metal sectors in a vertical plane, two crossed metal neutralizer bars with metallic brushes, and a spark gap formed by two metal spheres placed near the surfaces of each disc, mounted on insulating supports and connected to the output terminals, constitute the Wimshurst influence machine

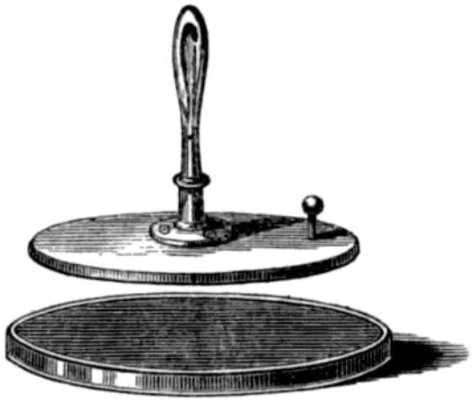

Figure 1.1: Volta's electrophorous, a simple manual capacitive electrostatic generator.

(Fig. 1.2). During the rotation of the discs an imbalance of charges is induced, amplified, and collected by the metal spheres which act like collectors. The positive feedback increases the accumulating charges exponentially until the dielectric breakdown voltage of the air is reached and an electric spark jumps across the gap [2].

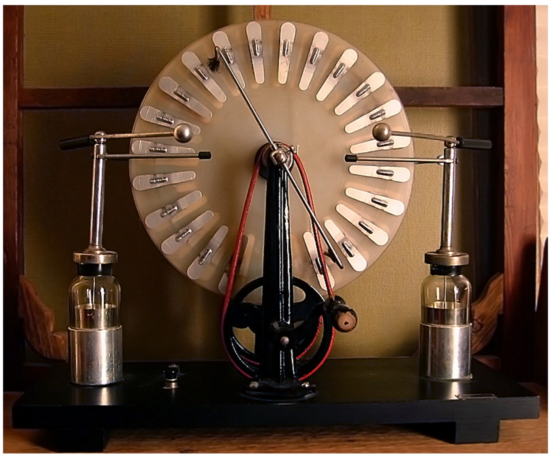

Figure 1.2: The Wimshurst influence machine for generating high voltages.

By the end of the 19th century cathode rays had already been discovered by Plücker and Hittorf. Arthur Schuster had demonstrated that cathode rays could be deflected by electric fields, and William Crookes had showed they could be deflected by magnetic fields. At that time, in 1897, J. J. Thomson succeeded in measuring the mass of cathode rays, and thus showed that they consisted of negatively charged particles smaller than atoms. These were the first known "subatomic particles", which were later named electrons. The device used in the experiment was a cathode-ray tube (CRT) consisting of a vacuum sealed tube, a negatively charged conductor called cathode on one side of the inside of the tube and a positively charged conductor on the opposite side of the inside of the tube (Fig. 1.3). A small hole in the anode was allowing some electrons to pass through it, creating a beam of electrons. On the opposite side of the tube there was a coating that was glowing when struck by the electrons. This allowed J. J. Thomson to see where the electron beam was hitting. CRTs were later used in monitors, oscilloscopes and even memory devices [3]. Wilhelm Conrad Röntgen used a similar tube, which was filled with low-pressure gas, in his experiments. He wrapped some black cardboard around the tube where the repeated electrical pulses produced electric discharges in the gas. After turning off the lights in the room, Röntgen noticed that some photographic plates near his equipment were glowing. He concluded that the tube was producing invisible radiation of an unknown nature, which he called an X-ray, and that this was causing the fluorescence he had observed. The field of radiography for material and structure analysis emerged after the development of the X-ray tubes (Fig. 1.4) in which the X-ray spectrum depends entirely on the anode material and the accelerating voltage [4].

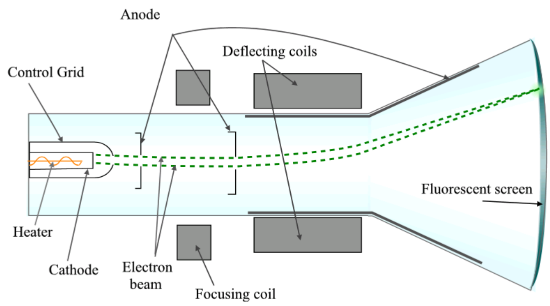

Figure 1.3: The cathode-ray tube used to display images.

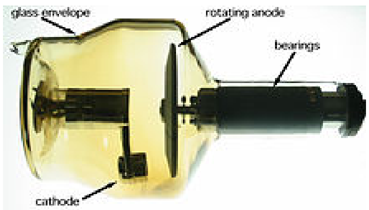

Figure 1.4: The X-ray tube, a vacuum tube that converts electrical input power into X-rays.

The first "high-energy" accelerators were designed and built in the 20th century. In 1932 John Douglas Cockcroft and Ernest Thomas Sinton Walton performed the first artificial nuclear disintegration in history using their device (Fig. 1.5, left) to accelerate protons produced by a discharge in H gas. The accelerator was powered by an electric circuit that generated a high DC voltage from a low-voltage AC (or pulsing DC) input. This electric circuit is now called a Cockcroft-Walton (CW) generator or multiplier and is widely used in everyday electronic devices that require high voltages, like microwave ovens and photocopiers, since it is built of low-cost components and is easy to insulate. It comprises a voltage multiplier ladder network of capacitors and diodes to generate high voltages. The voltage across each stage of the cascade is equal to only twice the peak input voltage in a half-wave rectifier and three times the input voltage in a full-wave rectifier (Fig. 1.5, right) [5].

In the 1930s another type of accelerator emerged that soon dominated the field. The Van de Graaff generator is an electrostatic generator which uses a moving belt to accumulate electric charge on a hollow metal globe on the top of an insulated column, creating very high electric potentials (Fig. 1.6). It can produce very high voltage direct current electricity at low current levels. Modern Van de Graaff generators can achieve potentials of several megavolts [6]. Particle-beam Van de Graaff accelerators are often used in a tandem configuration, in which negatively charged ions are injected at one end towards the high potential terminal, where they are accelerated by attractive force towards the terminal (Fig. 1.7). When the ions reach the

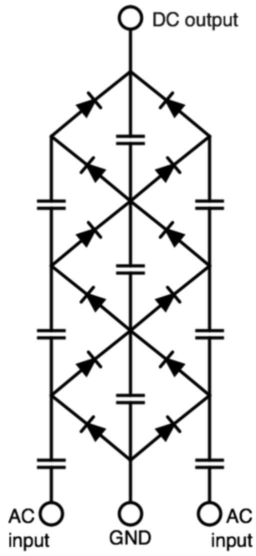

Figure 1.5: Left: The Cockcroft-Walton voltage multiplier which was part of one of the early particle accelerators. Right: A three-stage full-wave Cockcroft-Walton multiplier.

terminal, some of their electrons are subtracted to make them positively charged and are subsequently accelerated by repulsive forces away from the terminal. Thus, two accelerations take place at the cost of one generator [7].

In 1940, a new model of particle accelerator, the betatron, was completed at the University of Illinois, under the direction of the American physicist Donald W. Kerst. The betatron (Fig. 1.8) is an accelerator that uses the electric field induced by a varying magnetic field from a primary coil to accelerate electrons (beta particles) injected into a vacuum torus to high speeds, causing them to circle around the torus in the same manner as current is induced in the secondary coil of a transformer (Faraday's Law). Nowadays s are used to produce high-energy X-ray beams for multiple applications [8].

During these decades, an advancement in the technology of an accelerator which could produce higher particle energies than the previous electrostatic particle accelerators (the Cockcroft-Walton accelerator and Van de Graaff generator) took place. The linear particle accelerator (linac) can accelerate charged subatomic particles or ions to a high speed by subjecting them to a series of oscillating electric potentials along a linear beamline. The first such operational machine (based on the principles proposed by Gustav Ising) was constructed by Rolf Widerøe at the RWTH Aachen University. A linac consists of a straight hollow pipe vacuum chamber which contains the other components, the particle source at one end of the chamber which produces the charged particles which the machine accelerates, a series of open-ended cylindrical electrodes whose length increases progressively with the distance from the source extending along the pipe from the source, a target with which the particles collide located at the end of the accelerating electrodes and an electronic oscillator and amplifier which generate a radio frequency AC voltage of high potential, which is applied to the cylindrical electrodes. This RF AC voltage is the accelerating voltage which produces the electric field which accelerates the parti-

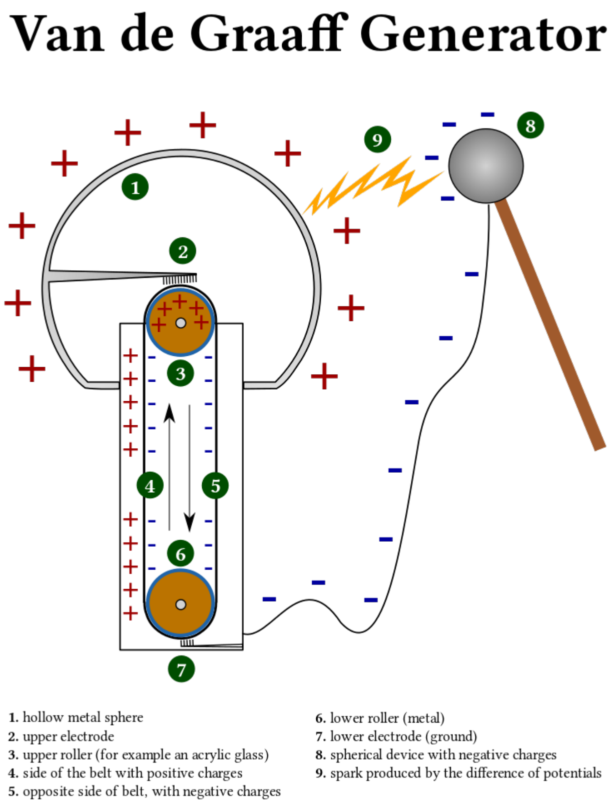

Figure 1.6: A Van de Graaff generator which produces very high voltage direct current electricity at low current levels. It consists of a belt of rubber moving over two rollers of differing material, one of which is surrounded by a hollow metal sphere. Due to the triboelectric effect, simple contact of dissimilar materials causes the transfer of some electrons from one material to the other. That's why the rubber of the belt will become negatively charged while the acrylic glass of the upper roller will become positively charged.

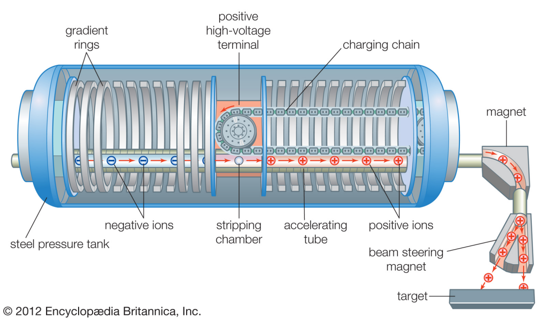

Figure 1.7: A two-stage tandem particle accelerator. A beam of negative ions enters from the top and is accelerated toward the positive terminal at the center. There it passes through carbon foil in a stripping chamber, where many of the negative ions lose electrons and emerge as positive ions. The beam is then accelerated away from the positive terminal, and the positive ions are separated by magnets and steered toward the target.

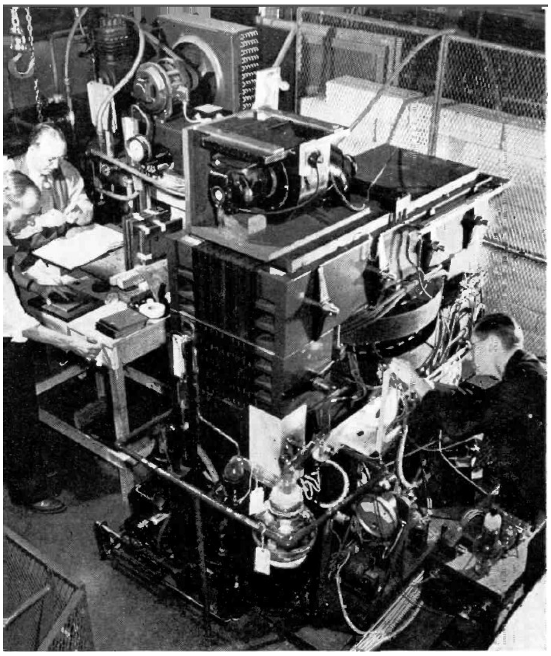

Figure 1.8: A betatron, the first machine capable of producing electron beams at energies higher than could be achieved with a simple electron gun.

cles, while opposite phase voltage is applied to successive electrodes. In the linac, the particles are accelerated multiple times by the applied voltage, so the particle energy is not limited by the accelerating voltage [9]. Linacs have many applications in radiation therapy, serve as particle injectors for higher-energy accelerators (Fig. 1.9), and are used directly to achieve the highest kinetic energy for light particles for particle physics, like in the case of the 3.2-kilometre-long linac at the SLAC National Accelerator Laboratory in California [7].

Another type of widely used modern particle accelerator is the cyclotron invented by Ernest Lawrence in 1929-1930 at the University of California, Berkeley. A cyclotron consists of a metal cylinder divided into two hollow "D"-shaped sheet metal electrodes called "dees" enclosed in a vacuum chamber. The dees are located between the poles of a large electromagnet and are placed face to face with a narrow gap between them (Fig. 1.10). Charged particles are injected into the center of this space and accelerated outwards from the center. The particles are held to a spiral trajectory by the static magnetic field applied perpendicular to the electrode plane by the electromagnet. A radio frequency (RF) alternating voltage of several thousand volts is applied between the dees. This voltage creates an oscillating electric field in the gap between the dees that accelerates the particles [10]. Apart from particle physics applications, cyclotrons are used in nuclear medicine for the production of radionuclides. The accelerator at IPHC-Strasbourg which was used for some of the test beams described in this dissertation is a cyclotron.

In 1945, Robert Lyster Thornton at Ernest Lawrence's Radiation Laboratory led the construction of a 470 cm cyclotron. In 1946, this cyclotron was converted to a novel type of particle accelerator based on a design by Edwin McMillan. This was the first synchrocyclotron which could produce 195 MeV deuterons and 390 MeV α-particles. In the synchrocyclotron the frequency of the driving RF electric field is varied to compensate for relativistic effects as the particles' velocity begins to approach the speed of light, contrary to the classical cyclotron, where this frequency is constant. In the synchrocyclotron, only the one dee retains its classical shape, while the other pole is open (Fig. 1.11). In addition, the frequency of oscillating electric

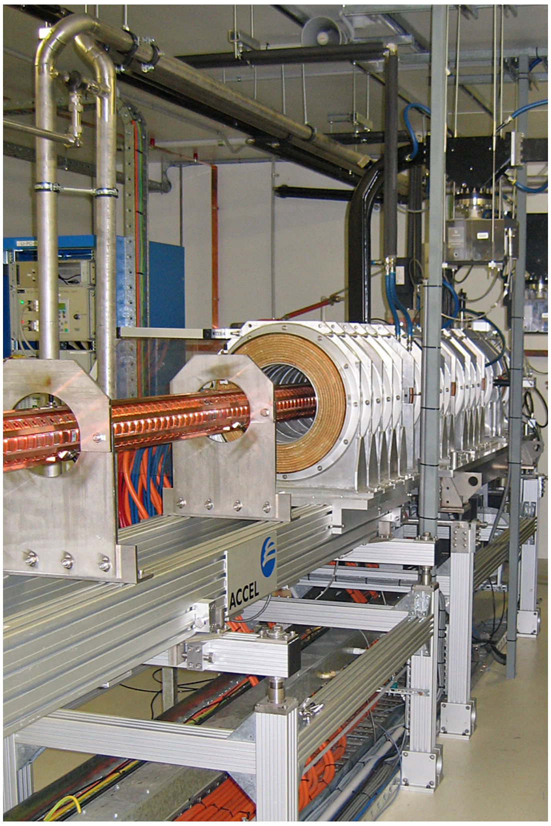

Figure 1.9: The linac within the Australian Synchrotron uses radio waves from a series of RF cavities at the start of the linac to accelerate the electron beam in bunches to energies of 100 MeV.

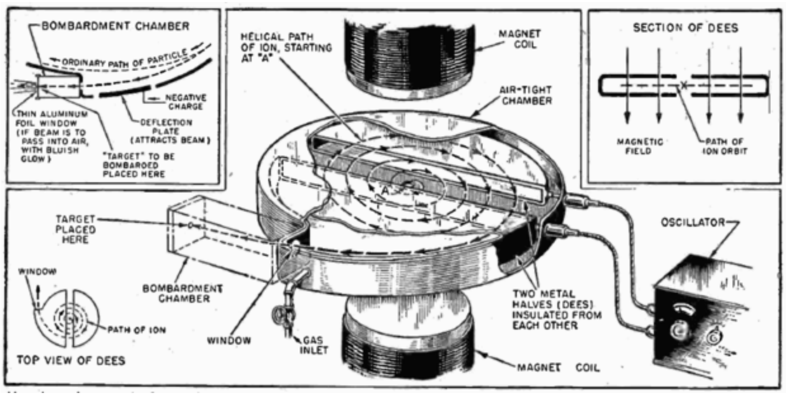

Figure 1.10: A cyclotron accelerates charged particles outwards from the center along a spiral path. The particles are held to a spiral trajectory by a static magnetic field and accelerated by a rapidly varying (radio frequency) electric field.

field in a synchrocyclotron is decreasing continuously instead of kept constant so as to maintain cyclotron resonance for relativistic velocities. One terminal of the oscillating electric potential varying periodically is applied to the dee and the other terminal is grounded. The ions to be accelerated are forced to move in circles of increasing radius and their acceleration takes place as they enter or leave the dee. The main advantage of the synchrocyclotron is that the potential difference applied between the dees can be smaller, since it is not necessary anymore to restrict the number of revolutions executed by the ion before its exit [11].

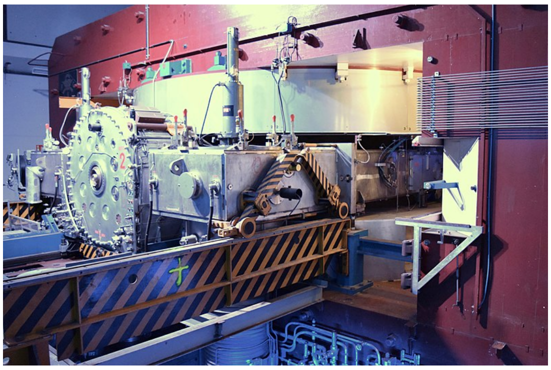

Figure 1.11: A synchrocyclotron, in which the frequency of the driving RF electric field is varied to compensate for relativistic effects as the particles' velocity begins to approach the speed of light.

In 1945 the first electron synchrotron was constructed by Edwin McMillan (while its principle was earlier invented by Vladimir Veksler independently) and in 1952 the first proton synchrotron (designed by Sir Marcus Oliphant) was built. The synchrotron revolutionized the progress in accelerator technology, as in such a system the bending (with dipole magnets), the beam focusing (with quadrupole/sextupole magnets) and the direct acceleration (with radio frequency cavities) can be separated into different components. Some of the first large-scale accelerator facilities were based on the synchrotron design, and until today the most powerful accelerators are of this type (Fig. 1.12) [7], [12].

Figure 1.12: The Tevatron, a synchrotron collider type particle accelerator at Fermi National Accelerator Laboratory (Fermilab), Batavia, Illinois, USA. Shut down in 2011, until 2007 it was the most powerful particle accelerator in the world, accelerating protons to an energy of over 1 TeV. Beams of circulating protons in the two circular vacuum chambers in the two rings visible collided at their intersection point.

In the synchrotron the accelerating particle beam travels around a fixed closed-loop path.

The magnetic field which bends the particle beam into its closed path increases with time during the accelerating process, being synchronized to the increasing kinetic energy of the particles. For low-energy particles, the frequency of the applied electromagnetic field may also change to follow their non-constant circulation time. By modifying these parameters accordingly as the particles gain energy, the circulation path can be held constant as they are accelerated. However, the maximum energy that a cyclic accelerator can convey is limited by the maximum strength of the magnetic fields and the maximum curvature of the particle path (and by the synchrotron radiation for electron/positron beams). So, for increasing the energy limit superconducting magnets (which are not limited by magnetic saturation) should be used [7], [12].

Due to their geometry synchrotrons are unable to accelerate particles from zero kinetic energy (since the closed particle path would have to be cut by a particle emitter). That's why pre-accelerated particle beams need to be injected into a synchrotron. A linac or another synchrotron, fed by a particle source comprising a simple high voltage power supply, could be used for the pre-acceleration [7], [12].

The accelerators at CERN (SPS) and DESY which were used for some of the test beams described in this dissertation are synchrotrons.

1.2 The Large Hadron Collider (LHC)

The Large Hadron Collider (LHC) is the world's largest and highest-energy particle accelerator, as well as the largest machine in the world. It was built by the European Organization for Nuclear Research (CERN) between 1998 and 2008 in collaboration with over 10000 scientists and hundreds of universities and laboratories from more than 100 countries. It first commenced operation on 10 September 2008, and remains the latest addition to CERN's accelerator complex. The LHC consists of a 27-kilometre ring of superconducting magnets with a number of accelerating structures to boost the energy of the particles along the way [13].

The accelerator complex at CERN is a succession of machines which accelerate particles, mainly protons, to increasingly higher energies. Each machine boosts the energy of a beam of particles, before injecting the beam into the next machine in the sequence. The proton source is a simple bottle of hydrogen gas and an electric field is used to strip hydrogen atoms of their electrons to yield protons. Linac 2, the first accelerator in the chain, accelerates the protons to the energy of 50 MeV. The beam is afterwards injected into the Proton Synchrotron Booster (PSB), which accelerates the protons to 1.4 GeV, followed by the Proton Synchrotron (PS), which pushes the beam to 25 GeV, and the Super Proton Synchrotron (SPS), where the protons reach the energy of 450 GeV. The protons are finally transferred to the LHC - the last element in this chain, where particle beams are accelerated up to the record energy of 6.5 TeV per beam (Fig. 1.13) [13].

Inside the accelerator, two high-energy particle beams travel (in opposite directions in separate beam pipes) at close to the speed of light before they are forced to collide. The beam pipes are actually two tubes kept at ultrahigh vacuum. The beams are guided around the accelerator ring by a strong magnetic field maintained by superconducting electromagnets which are built from coils of special electric cable. The cable operates in a superconducting state, which allows the efficient conducting of electricity without resistance or loss of energy. Since this requires chilling the magnets to -271.3 °C, part of the accelerator is connected to a distribution system of liquid helium, which cools the magnets [13].

Thousands of different magnets of various sizes are used to direct the beams around the accelerator. These include 1232 dipole magnets, each 15 metres long and weighing in at 35 tonnes, which bend the beams, and 392 quadrupole magnets, each 5-7 metres long, which

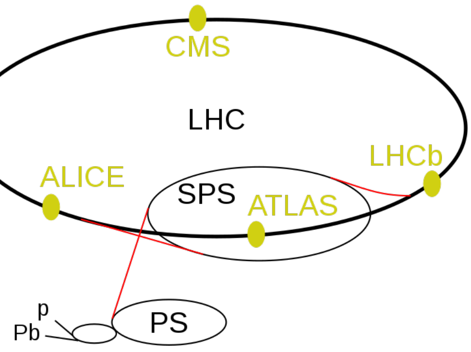

Figure 1.13: The crossing points of the LHC which correspond to its main experiments.

help to keep the particles in a tight beam. The quadrupoles have four magnetic poles arranged symmetrically around the beam pipe to squeeze the beam either vertically or horizontally. Just before collision, another type of magnet - the insertion magnet - is used to "squeeze" the particles closer together, thus increasing the chances of collisions. Making the tiny particles to collide can be compared to firing two needles 10 km apart with such precision that they meet halfway. The control systems, the services and technical infrastructure for the accelerator are housed under one roof at the CERN Control Center. From there, the beams inside the LHC are guided to collide at four locations around the accelerator ring, corresponding to the positions of the four major particle detectors of LHC - ALICE, ATLAS, CMS and LHCb (Fig. 1.13, 1.14) [13].

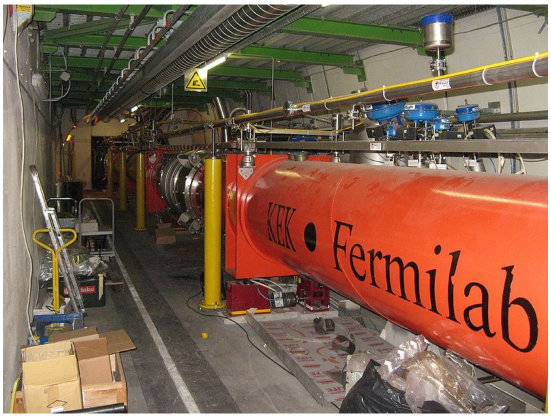

Figure 1.14: Superconducting quadrupole electromagnets are used to direct the beams to four intersection points, where interactions between accelerated protons will take place.

Three quadrupoles are used to create a system called an inner triplet and there are eight inner triplets, two of which are located at each of the four large LHC detectors. Inner triplets perform the squeezing of the beam mentioned above, by making it 12.5 times narrower - from 0.2 millimetres down to 16 micrometres across. After the collisions in a detector, huge magnets assist the measurement of particles. Charged particles are deflected by the magnetic field in a detector, and their momentum can be calculated from the amount of deflection, thus helping physicists to determine the identity of the particles. After the collisions, the particle beams are separated again by dipole magnets, while other magnets minimize the spread of the particles from the collisions. When it is time to dispose of the particles, they are deflected from the LHC towards the beam dump. Finally, a "dilution" magnet decreases the beam intensity by a factor of 100000 before the beam collides with a block of concrete and graphite composite for its final stop [13].

The LHC has been built in the same tunnel (Fig. 1.15) as its predecessor - the Large Electron-Positron (LEP) collider, which consisted of 5176 magnets and 128 accelerating cavities. The LEP was - and still is - the largest electron-positron accelerator ever built. For the alignment of the LHC components the best reference geometry in the tunnel was provided by the position of the LEP quadrupole alignment targets [14].

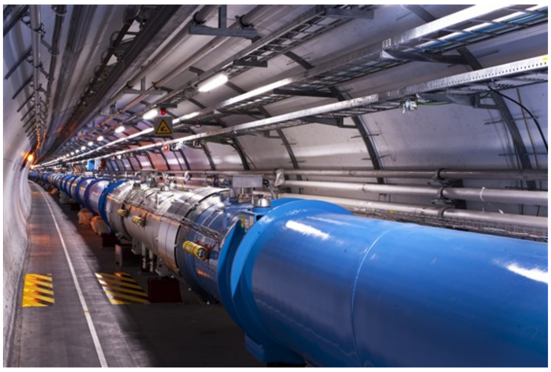

Figure 1.15: Inside the LHC tunnel.

It should be noted that apart from the proton-proton collisions, the LHC is occasionally colliding protons with lead ions (Pb). The injector chain which boosts and delivers the lead ions is different than the one for the protons. For the lead ions, the chain is Linac 3, the Low Energy Ion Ring (LEIR), the PS and the SPS [15].

The main aim of the LHC detectors was to allow physicists to test the predictions of different theories of particle physics in accordance with the Standard Model (SM), and especially to discover the long-sought Higgs boson [16]. The Standard Model is the most established and well-tested physics theory so far to encapsulate the behavior of the building blocks of the universe - the fundamental particles, which are governed by four fundamental forces - and how these particles and three of the forces are related to each other. According to the SM, all matter particles occur in two basic types called quarks and leptons. Each of these groups consists of six particles, which are related in pairs, also called generations. The lightest and most stable particles constitute the first generation of which all stable matter in the universe is made of, whereas the heavier and less-stable particles (which quickly decay to more stable ones) belong to the second and third generations. The six quarks are paired in three generations - the up quark and the down quark form the first generation, followed by the charm quark and strange quark which form the second generation, and then finally the top quark and bottom (or beauty) quark which form the third generation. Quarks appear as well in three different colors and only mix in such ways as to form colorless objects. The six leptons are likewise arranged in three generations - the electron and the electron neutrino, the muon and the muon neutrino, and the tau and the tau neutrino (Fig. 1.16). The electron, the muon and the tau all have an electric charge and a significant mass, whereas the neutrinos are electrically neutral and have very little mass [17].

The fundamental forces in the universe are the strong force, the weak force, the electromagnetic force, and the gravitational force. Each of them works over different ranges with a different strength. Gravity is the weakest but it has an infinite range. On the other hand, the electromagnetic force also has infinite range but is many times stronger than gravity. Finally, the weak and strong forces are effective over a very short range and dominate only at the level

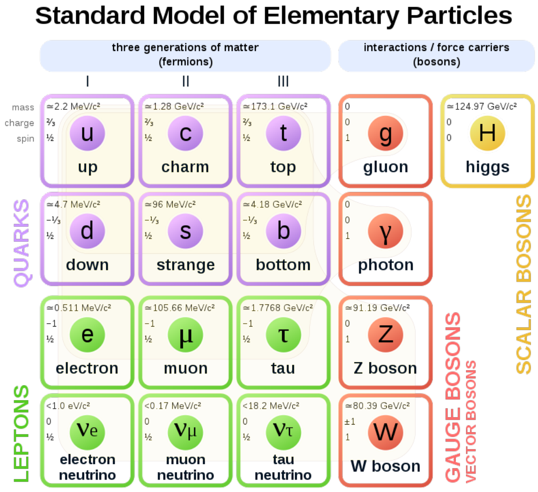

Figure 1.16: Standard model of elementary particles: the 12 fundamental fermions and 5 fundamental bosons.

of subatomic particles. The weak force is much stronger than gravity (despite its name) but is indeed the weakest of the other three. The strong force is the strongest of all four fundamental interactions. The weak, the electromagnetic and the strong forces result from the exchange of force-carrier particles, which belong to a broader group called bosons. Particles of matter may transfer discrete amounts of energy by exchanging bosons with each other. Each fundamental force has its own corresponding boson: the weak force is carried by the W and Z bosons, the electromagnetic force is carried by the photon and the strong force is carried by the gluon (Fig. 1.16). It is hypothesized that the graviton should be the corresponding force-carrier of gravity, however it has not been discovered yet. The SM includes the weak, electromagnetic and strong forces and all their carrier particles, and explains sufficiently how these forces act on all of the matter particles. As the quantum theory used to describe the micro world and the general theory of relativity used to describe the macro world are difficult to fit into a single framework, gravity hasn't been incorporated into the SM. No one has achieved so far to make the two theories mathematically compatible in the context of the SM, but luckily, at the minuscule scale of fundamental particles (which is much smaller than the scale of human bodies or planets), the effect of gravity is so weak that it can be considered negligible. So the SM is an excellent theory when describing this immensely small scale [17].

In the 1970s, physicists realized that there are very close ties between the weak force and the electromagnetic force. The two forces can be described within the same theory and this unification implies that electricity, magnetism, light and some types of radioactivity are all manifestations of a single underlying force known as the electroweak force. The basic equations of the unified theory correctly describe the electroweak force and its associated force-carriers - the photon, and the W and Z bosons - but unfortunately all of these particles emerge without a mass. While this is valid for the photon, it is known that the W and Z bosons have mass, nearly 100 times that of a proton. To solve this problem, theoretical physicists Robert Brout, François Englert and Peter Higgs made a proposal. According to it, the now so-called Brout-Englert-Higgs mechanism gives mass to the W and Z bosons when they interact with an invisible field, now called the Higgs field, which pervades the universe (Fig. 1.17, 1.18) [18]. Right after the Big Bang, the Higgs field was zero, but as the universe cooled and the temperature fell below a critical value, the field grew spontaneously so that any particle interacting with it could acquire a mass. The more a particle interacts with this field, the heavier it is. Nevertheless, particles like the photon that do not interact with the Higgs field are left without any mass. Like all fundamental fields, the Higgs field has an associated particle, which is called the Higgs boson and is the "visible" manifestation of the Higgs field, compared to a wave at the surface of the sea [18].

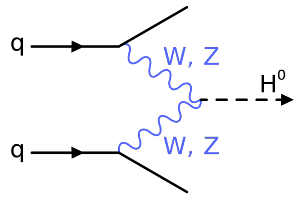

Figure 1.17: Feynman diagram of Higgs production through W/Z-boson fusion.

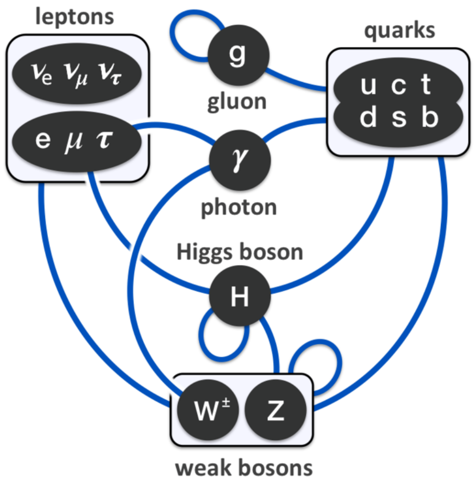

Figure 1.18: Summary of interactions between particles described by the Standard Model

For many decades no experiment had ever observed the Higgs boson to confirm the theory. On 4 July 2012, the CMS [19] and ATLAS [20] experiments at CERN's Large Hadron Collider announced that they had each observed a new particle in the mass region around 125 GeV, consistent with a Higgs boson predicted by the SM. It should be mentioned that the Higgs boson, as proposed within the Standard Model, is the simplest manifestation of the Brout-Englert-Higgs mechanism, but other types of Higgs bosons are predicted by other theories that go beyond the SM. On 8 October 2013 the Nobel prize in physics was awarded jointly to François Englert and Peter Higgs "for the theoretical discovery of a mechanism that contributes to our understanding of the origin of mass of subatomic particles, and which recently was confirmed through the discovery of the predicted fundamental particle, by the ATLAS and CMS experiments at CERN's Large Hadron Collider".

1.3 The High Luminosity Large Hadron Collider (HL-LHC)

Even though the Standard Model is currently the best existing description of the subatomic world, it does not explain the complete picture. The theory incorporates only three out of the four fundamental forces and there are also important questions that the SM does not answer: What is the nature of dark matter? What is the nature of dark energy? What happened to the antimatter after the big bang? Why are there three generations of quarks and leptons with such a different mass scale? Why does quantum chromodynamics (QCD) seem to preserve CP-symmetry? What is the mechanism through which neutrinos obtain their mass? Can the mathematical framework of the SM become consistent with general relativity within spacetime singularities like the Big Bang and black hole event horizons? Are there extra dimensions and can we detect them? What are the nature and properties of quark-gluon plasma, thought to have existed in the early universe? The answers to these questions along with the discoveries of new exotic particles are expected to come in the upcoming years (Fig. 1.19) [21], [22], [23]. Various extensions of the standard model through supersymmetry (SUSY), like the Minimal Supersymmetric Standard Model (MSSM) and Next-to-Minimal Supersymmetric Standard Model (NMSSM), as well as completely new theories, such as string theory and M-theory (brane theory) tend to explain the entirety of current phenomena and to proceed one step towards a Theory of Everything. Most of these theories are about to be tested by the CMS and ATLAS experiments in the near future [23] and are some of the most active areas of research in both theoretical and experimental physics.

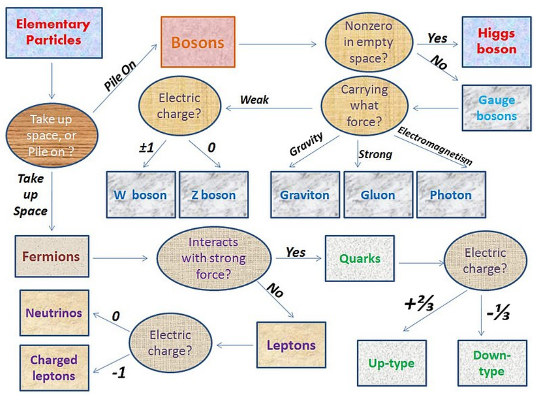

Figure 1.19: Standard Model and Beyond particles in a glimpse.

The High-Luminosity Large Hadron Collider (HL-LHC) project aims to step up the performance of the LHC in order to boost the potential for discoveries after 2027, and thus to give physicists the opportunity to give answers to the unsolved mysteries in physics which were mentioned above. The objective is to increase the luminosity of LHC by a factor of 10 beyond its initial design value, thereby enabling the experiments to enlarge their data sample by an order of magnitude compared with the LHC baseline program. Following several years of design study, we are going through a total of ten years of developments, prototyping, testing and implementation for this challenging project, most of which lie ahead (Fig. 1.20). Operation is expected to start around 2027 and the timeline of the project is dictated by the fact that soon many critical components of the accelerator will reach the end of their lifetime due to radiation damage and will thus need to be replaced. The upgrade phase is therefore indispensable not only for the complete exploitation of the LHC physics potential, but also to enable operation of the accelerator beyond 2026 [24], [25].

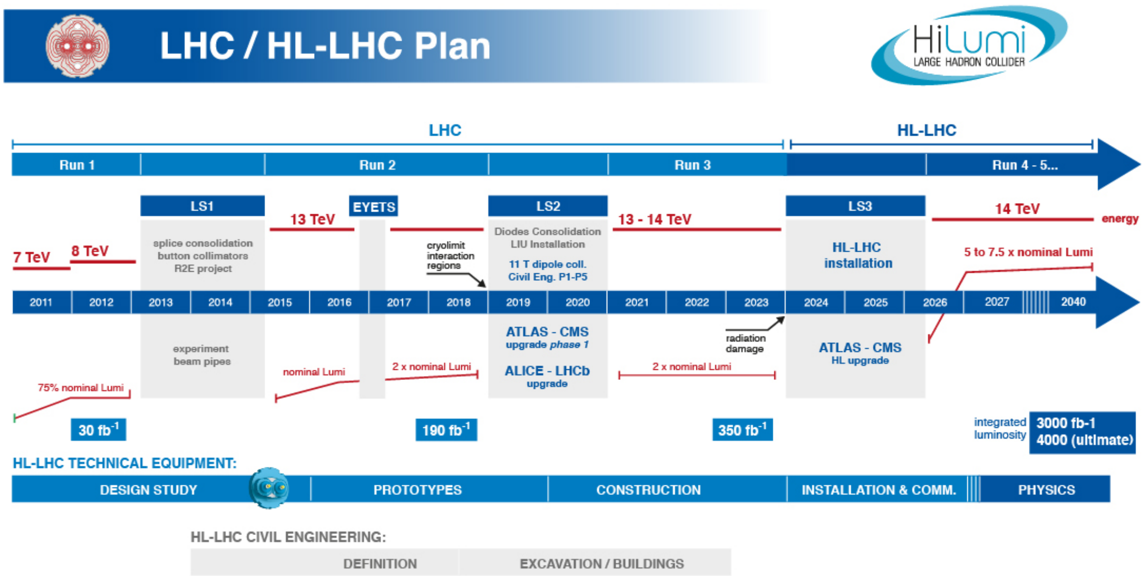

Figure 1.20: LHC baseline plan for the next decade and beyond showing the energy of the collisions (upper red line) and luminosity (lower lines).

As luminosity is proportional to the number of collisions that occur in a given amount of time, it is an important parameter indicating the performance of an accelerator. I.e. the higher the luminosity, the more data the experiments of a collider can gather to allow them to observe rare processes. The HL-LHC, a project which was announced as the top priority of the European Strategy for Particle Physics in 2013, will of course allow physicists to study known mechanisms in greater detail, such as the Higgs boson, but also to observe infrequent new phenomena that might reveal themselves. It is remarkable how the HL-LHC will produce at least 15 million Higgs bosons per year, compared to around three million which came from the LHC in 2017 [24], [25].

The first phase of the project began in 2011 and was partly financed by the European Commission's seventh framework programme (FP7). The design study came to a close in October 2015 with the publication of a technical design report, marking the start of the construction phase for the project, while the civil-engineering work started in April 2018. The project is led by CERN with the support of an international collaboration of 29 institutions in 13 countries (mostly CERN member states, as well as Russia, Japan and USA). The upgraded hadron collider will rely on novel technologies, including cutting-edge 11-12 Tesla superconducting magnets, compact superconducting crab cavities with ultra-precise phase control for beam rotation, new technology for beam collimation and 300 meter-long high-power, loss-less superconducting links [24], [25].

The instantaneous luminosity L can be expressed as:

$$L = \gamma \frac{n_b N^2 f_{rev}}{4\pi\beta^* \epsilon_n} R; \; R = \frac{1}{\sqrt{1 + \frac{\theta_c \sigma_z}{2\sigma}}} \tag{1.1}$$

where γ is the proton beam energy in unit of rest mass; n_b is the number of bunches in the machine: 1380 for 50 ns spacing and 2808 for 25 ns; N is the bunch population ($N_{nominal\ 25\ ns}$: 1.15×10^{11} p ($\Longrightarrow$ 0.58 A of beam current at 2808 bunches); f_{rev} is the revolution frequency (11.2 kHz); β^* is the beam beta function (focal length) at the collision point (nominal design 0.55 m); ϵ_n is the transverse normalized emittance (nominal design: 3.75 μm); R is a luminosity geometrical reduction factor (0.85 at 0.55 m of β^*, down to 0.5 at 0.25 m of β^*); θ_c is the full crossing angle between colliding beam (285 μrad as nominal design); σ, σ_z are the transverse and longitudinal r.m.s. size, respectively (16.7 μm and 7.55 cm) [24].

A milestone was achieved on 2 November 2017 when stable beams were declared with a peak luminosity of 2.05×10^{34} cm^{-2}s^{-1}, more than twice the design luminosity. The total integrated luminosity of 66 fb^{-1} recorded in 2018 was more than the 60 fb^{-1} forecasted. This record integrated luminosity was achieved thanks to the high machine availability and the stable beam ratio. The graphs of the possible evolution of peak and integrated luminosity as predicted when the Preliminary Design Report for the HL-LHC was written are shown in Fig. 1.21 [24].

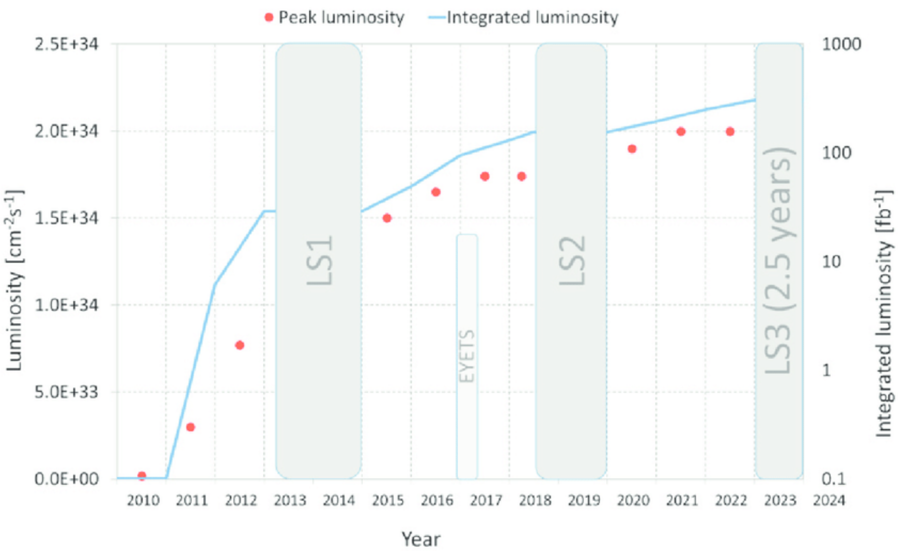

Figure 1.21: LHC luminosity plan for the ongoing decade, both peak (red dots) and integrated (blue line). Main shutdown periods are indicated.

To achieve their objectives the physicists working on the High Luminosity LHC will have to determine a set of beam parameters and the hardware configuration that will enable the LHC to reach: *1.* A peak luminosity of 5×10^{34} cm^{-2}s^{-1} with leveling, allowing: *2.* An integrated luminosity of 250 fb^{-1} per year, enabling the goal of 3000 fb^{-1} in a dozen years after the upgrade (which is about ten times the luminosity reach of the first twelve years of the LHC lifetime). Since the significant energy deposition by collision debris in the interaction region magnets and the necessity to limit the peak pileup impose a priori a limitation of the peak luminosity, the HL-LHC operation will have to rely on luminosity leveling. The luminosity profile without leveling (Fig. 1.22, left) quickly decreases from the initial peak value, due to protons consumed in collisions. But by designing the collider to operate with a constant luminosity, i.e. "leveling" it and suppressing its decay for a significant portion of the fill, the average luminosity is more or less the same as the one of a run without leveling (Fig. 1.22, right), however with the advantage that the maximum peak luminosity is smaller [24].

Due to the fact that the maximum leveled luminosity is limited, in order to maximize the integrated value one needs to maximize the run length, which can be obtained by filling the

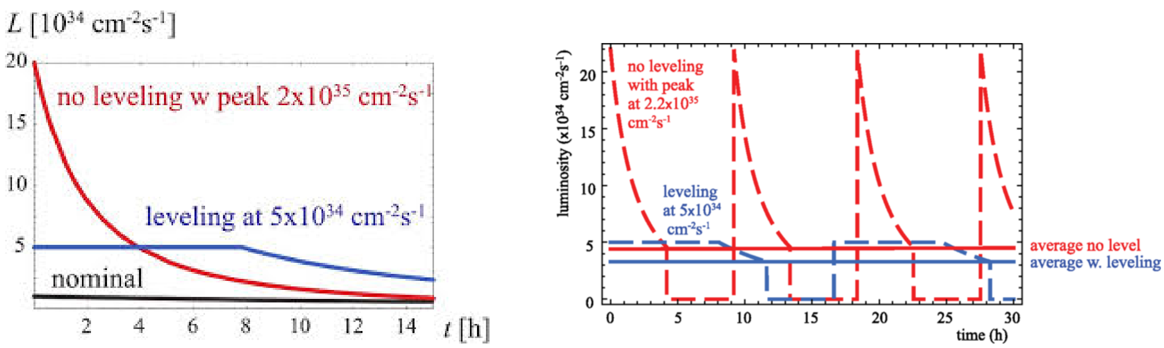

Figure 1.22: Left: Luminosity profile for a single long fill: starting at nominal peak luminosity (black line), with upgrade no leveling (red line), with leveling (blue line). Right: Luminosity profile with optimized run time, without and with leveling (blue and red dashed lines), and average luminosity in both cases (solid lines).

maximum number of protons, i.e. by maximizing the beam current ($I_{beam} = n_b N$). Other key factors for optimizing the integrated luminosity and obtaining the preset goal of 3 fb^{-1}/day (Fig. 1.23) are a short average machine turnaround time and a good overall machine efficiency, where the efficiency is defined as the ratio between actual time spent in physics production and the physics time of the ideal cycle. HL-LHC with 150 days of physics needs an efficiency of approximately 40%. During past LHC runs the efficiency varied, without luminosity leveling and the added system complexity of the HL-LHC (e.g. Crab Cavity operation), between 20% and 40%. Requiring a much higher efficiency than the one of the present LHC, with a (leveled) luminosity five times the nominal one and additional technically demanding hardware, will be a real challenge [24].

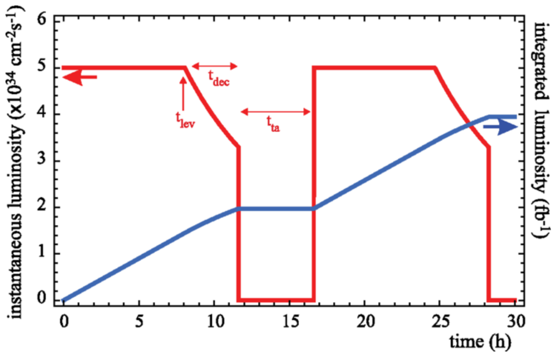

Figure 1.23: Luminosity cycle for HL-LHC with leveling and a short decay (optimized for integrated luminosity).

The total beam current in the LHC may be a hard limit since many systems are affected by this parameter. Radiofrequency (RF) power system and RF cavity, Collimation, Cryogenics, Kickers, Vacuum, beam diagnostics, Quench Protection System (QPS), various controllers, etc. Radiation effects put aside, all systems have been designed in principle for $I_{beam} = 0.86\ A$, which is the so-called "ultimate" beam current [24]. For HL-LHC it is needed to increase the beam brightness. The beam brightness is a global property since it must be maximized at the beginning of the beam generation and subsequently to be preserved throughout the entire injector chain and LHC itself. It is the main goal of the LHC Injectors Upgrade (LIU) Project at CERN to increase the brightness at the LHC injection, basically by increasing the number of protons per bunch by a factor two above what we have today while maintaining the emittance at the present low value [24]. A classical approach to the luminosity upgrade is to reduce β^*, the optical function at the Interaction Points (IPs), by means of stronger and larger aperture low-β triplet quadrupoles. However, this would imply an increase of beam sizes inside the low-β triplet quadrupoles and a wider crossing angle, which both require in turn larger aperture low-β triplet quadrupole magnets, a larger first separation/recombination dipole and some alterations in the matching section. As stronger chromatic deviations coming from the larger β-functions inside the triplet magnets may exceed the strength of the existing correction circuits, a novel scheme called Achromatic Telescopic Squeeze (ATS) uses the adjacent arcs as enhanced matching sections and the increase of the β-functions in those arcs to boost at constant strength the efficiency of the lattice sextupoles. For the reduction of β^* the quadrupole magnets need to double the aperture, with a peak field 50% above the present LHC, requiring more advanced superconductors based on Nb_3Sn [24]. Nonetheless, the very small β^* requires larger crossing angle, which implies a mitigation of the geometrical luminosity reduction factor R, as defined in (1.1). An elegant solution for compensating the geometric reduction factor is the use of special superconducting RF crab cavities, capable to generate transverse electric field to rotate each bunch by $\theta_c/2$, such as they collide effectively head on, overlapping perfectly at the collision point (Fig. 1.24). Crab cavities make then accessible the full performance reach of the small β^*: their primary function is to boost the virtual peak luminosity for attaining the full HL-LHC performance [24].

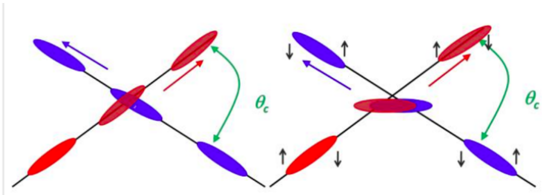

Figure 1.24: Effect of the crab cavity on the beam (small arrows indicate the torque on the bunch generated by the transverse RF field).

Some of the systems that need to be changed or improved, just because they become more vulnerable to breakdown and accelerated wearing out are mentioned below: *1.* Inner Triplet Magnets: At about 300 fb^{-1} some components of the low-beta triplet quadrupoles (Fig. 1.25) and their corrector magnets will have received a dose of 30 MGy, causing thus radiation damage. Some corrector magnets of nested type are likely to wear out and damage is expected because the most likely way of failing is through sudden electric breakdown That is why replacement of the triplet must be envisaged before damage. *2.* Cryogenics: To increase flexibility of intervention and then availability (i.e. integrated luminosity) a new cryo-plant for a full separation between Superconducting Radiofrequency (SRF) and Magnets cooling is planned to be installed. *3.* Collimation: The collimation system has been designed for the first phase of LHC operation, but will certainly need a renovation plan mainly concerning momentum and betatron cleaning, as well as the tertiary collimators protecting the triplets. An improvement of the collimation system will be the use of new material for the jaws, in order to decrease the impedance (half of the LHC impedance is attribute to collimators). A molybdenum-graphite composite, coated with molybdenum, is considered the optimal solution, capable to reduce the impedance of factor five to ten, keeping the robustness of the present design. *4.* Radiation To Electronics (R2E) and SC links for remote cold powering: A considerable effort is under way to study how to replace the radiation sensible electronic boards with radiation hard cards. For some special zones removal

of the power supplies and associated digital field boards (DFBs) are foreseen to be removed out of the tunnel, possibly on the surface. Displacement of power converter to a faraway distance or surface is possible only thanks to a novel technology - the Superconducting links (SCLs) made out of high-temperature superconductors (YBCO or BSCCO) or MgB_2 superconductors.
5. QPS, machine protection and remote manipulation: These systems will become a bottleneck along with aging of the machine and higher performance of 40 to 60 fb^{-1} per year [24].

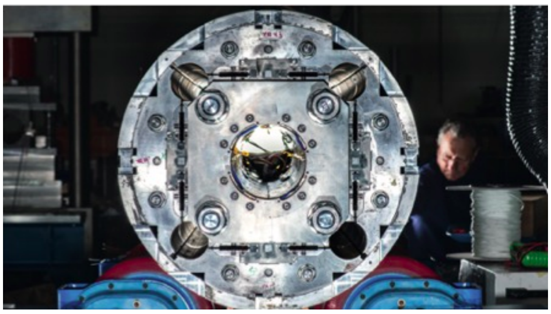

Figure 1.25: View of the cross-section of a short-model magnet for the High Luminosity LHC quadrupole, with three coils manufactured at CERN and one coil made in the US. (Image: Robert Hradil, Monika Majer/ProStudio22.ch).

Bibliography

[1] Pancaldi, Giuliano (2003). *Volta, Science and Culture in the Age of Enlightenment*. Princeton University Press. ISBN 0-691-12226-1., pp. 73-105 *Volta's 'invention' of the electrophorus*.

[2] *History of Electrostatic Generators*, Hans-Peter Mathematick Technick Algorithmick Linguistick Omnium Gatherum.

[3] *History of the Cathode Ray Tube*, About.com. Retrieved 27 November 2019.

[4] Behling, Rolf (2015), *Modern Diagnostic X-Ray Sources, Technology, Manufacturing, Reliability*, Boca Raton, FL, USA: Taylor and Francis, CRC Press. ISBN 9781482241327.

[5] Kleppner, Daniel; Kolenkow, Robert J. (1973), *An Introduction to Mechanics* (2nd ed.), Boston: McGraw-Hill. p. 498. ISBN 0-07-035048-5.

[6] Van de Graaff, R. J.; Compton, K. T.; Van Atta, L. C. (February 1933), *The Electrostatic Production of High Voltage for Nuclear Investigations*, Physical Review. 43 (3): 149-157.

[7] *Particle accelerator | instrument*, Encyclopædia Britannica. Retrieved 27 November 2019.

[8] *Betatron | particle accelerator*, Encyclopædia Britannica. Retrieved 27 November 2019.

[9] G. Ising, *Prinzip einer Methode zur Herstellung von Kanalstrahlen hoher Voltzahl*. In: Arkiv för Matematik, Astronomi och Fysik. Band 18, Nr. 30, 1924, S. 1-4.

[10] U.S. Patent 1,948,384 Lawrence, Ernest O. *Method and apparatus for the acceleration of ions*, filed: January 26, 1932, granted: February 20, 1934

[11] US patent 2615129, Edwin McMillan, *Synchro-Cyclotron*, issued 1952-10-21.

[12] *Design Report Tevatron 1 project*, TeVI Group, Sep 1984 - 518 pages, FERMILAB-DESIGN-1984-01.

[13] *LHC Design Report. 1. The LHC main ring*, Buning, O. et al. CERN-2004-003-V-1, CERN-2004-003.

[14] *LHC Design Report. 2. The LHC infrastructure and general services*, Buning, O. et al. CERN-2004-003-V-2, CERN-2004-003.

[15] *LHC Design Report. 3. The LHC injector chain*, Benedikt, M. et al. CERN-2004-003-V-3, CERN-2004-003.

[16] J. Baglio, A. Djouadi, *Higgs production at the LHC*, Journal of High Energy Physics 1103 (3): 055 (2011).

[17] A. Salam (1968). N. Svartholm (ed.). *Elementary Particle Physics: Relativistic Groups and Analyticity*, Eighth Nobel Symposium. Stockholm: Almquvist and Wiksell. p. 367.

[18] P.W. Higgs (1964). *Broken Symmetries and the Masses of Gauge Bosons*, Physical Review Letters. 13 (16): 508-509.

[19] CMS collaboration (2012), *Observation of a new boson at a mass of 125 GeV with the CMS experiment at the LHC*, Physics Letters B. 716 (1): 30-61.

[20] ATLAS collaboration (2012), *Observation of a New Particle in the Search for the Standard Model Higgs Boson with the ATLAS Detector at the LHC*, Physics Letters B. 716 (1): 1-29.

[21] J. D. Lykken (2010), *Beyond the Standard Model*, CERN Yellow Report. CERN. pp. 101-109. CERN-2010-002.

[22] S. Sekmen, *Beyond the Standard Model Physics at the High Luminosity LHC*, PoS ICHEP2018 (2018) 283.

[23] ATLAS, CMS Collaborations, *Report on the Physics at the HL-LHC and Perspectives for the HE-LHC*, CERN-LPCC-2019-01, CMS-FTR-19-001, ATL-PHYS-PUB-2019-006.

[24] G. Apollinari et al, *High-Luminosity Large Hadron Collider (HL-LHC): Technical Design Report V. 0.1*, CERN Yellow Rep.Monogr. 4 (2017) 1-516 CERN-2017-007-M.

[25] G. Apollinari, O. Bruening, T. Nakamoto, L. Rossi, *High Luminosity Large Hadron Collider HL-LHC*, CERN Yellow Report CERN-2015-005, pp. 1-19.

Chapter 2

The CMS experiment

This chapter aims to present a comprehensive overview of the CMS detector, putting emphasis on its Tracker and its Phase-2 upgrade.

2.1 Detector design and detection of particles

The CMS detector [1], one of the two experiments which discovered the Higgs boson in 2012 [2] is 21 m long, 15 m wide and 15 m high. It is located in a cavern, that could contain hundreds of thousands of people, at Cessy in France, just across the border from Geneva. The detector resembles a giant filter shaped as a cylindrical onion, with several concentric layers of components around the interaction point of the collisions between the two counter-rotating proton beams of the LHC (Fig. 2.1). Each layer is designed to stop, track or measure a different type of particle manifesting itself from proton-proton and heavy ion collisions. Finding the energy and momentum of a particle gives clues to its identity. In addition, particular patterns of particles might be indications of undiscovered and exciting physics [1].

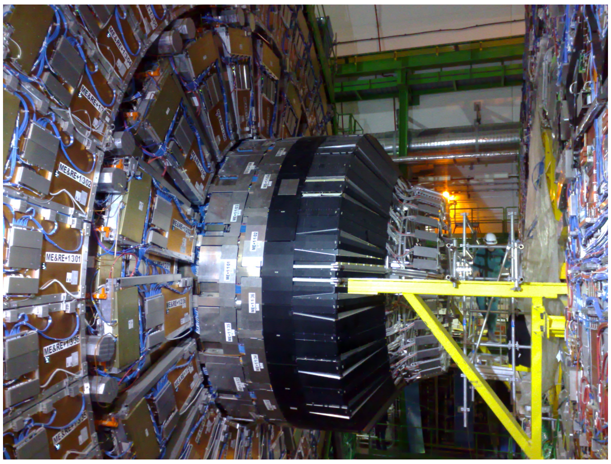

Figure 2.1: An overall view of the CMS detector. (Image: CMS/CERN.)

The initial requirements for the CMS detector included: a high-quality central tracking system to give accurate momentum measurements, a high-resolution method to detect and measure electrons and photons (an Electromagnetic Calorimeter), a "hermetic" Hadron Calorimeter which should entirely surround the collisions and prevent particles from escaping, and a high-performance system to detect and measure muons (Muon Chambers). Taking into consideration these priorities, the first essential item was a very strong magnet to allow physicists to accurately measure even particles with very high momentum, such as muons. A large magnet also allowed a number of muon detector layers to be contained within the magnetic field, so that momentum could be measured both inside the coil by the tracking system and outside of the coil by the Muon Chambers (Fig. 2.2) [1].

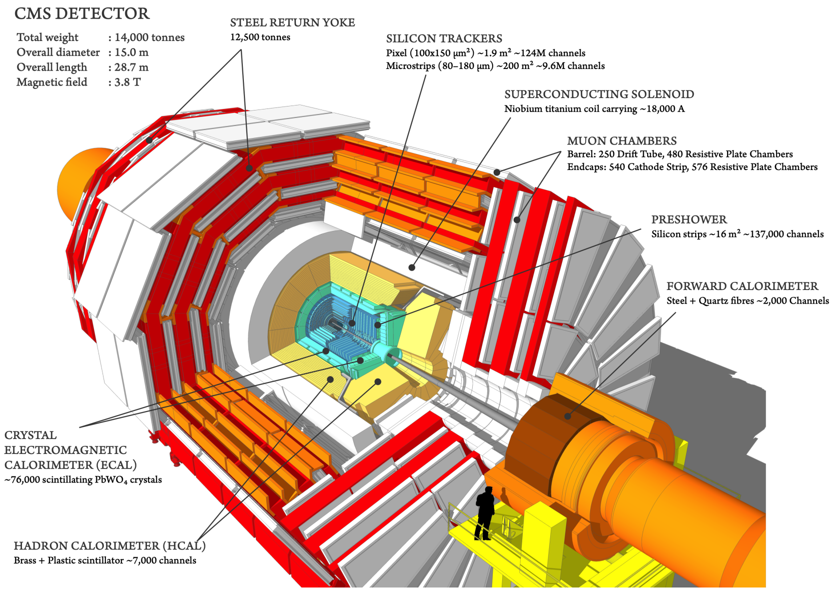

Figure 2.2: Sectional view of the CMS detector. The LHC beams travel in opposite directions along the central axis of the CMS cylinder colliding in the middle of the CMS detector. (Image: CMS-OUTREACH-2019-001.)

The solenoid magnet is a coil of superconducting wire, cooled to -268.5 °C, that produces a magnetic field when electricity flows through it, with an overall length of 13 m and a diameter of 7 m (inner diameter of 5.9 m), and a magnetic field of 4 T, about 100000 times stronger than that of the Earth. It is the largest magnet of its type ever built and allows the Tracker and Calorimeters to be placed inside the coil, resulting in a detector that is regarded as compact, compared to other detectors of similar mass. Technical expertise from past CERN experiments at LEP (the Large Electron Positron Collider) was crucial for determining that constructing sections above ground (rather than building them directly in the cavern where additional access and safety issues would have to be considered) saved significant amount of time. Also, it was decided that work on building the detector sections should be performed in parallel with the excavation of the cavern for saving more time. It was furthermore concluded that sub-detectors should be made easily accessible to allow for easier and more efficient maintenance. Thus, CMS was designed in fifteen separate slices, that after having been built on the surface were lowered down into the cavern. This slicing, thanks to the careful design of cabling and piping, ensures that the sections can be fully opened and closed with minimum disruption, and each distinct segment of the CMS detector remains accessible within the cavern (Fig. 2.3) [1].

Different particles that emerge from LHC collisions break at different distances from the beam axis as they travel away from the collision. Each particle leaves a trace in the detector and the CMS detector gathers up information about every one of these tracks so that physicists

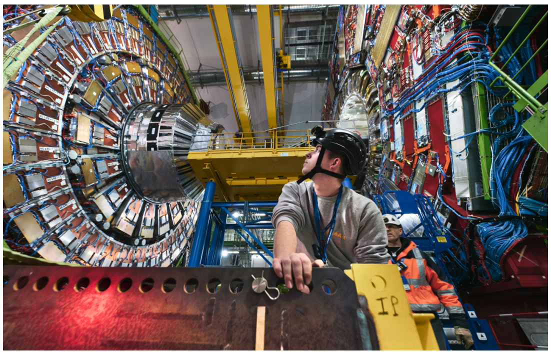

Figure 2.3: Removal of the CMS beam pipe. (Image: Maximilien Brice/Julien Ordan/CERN.)

can solve the puzzle and see the complete picture of what happened at the heart of the collision. New particles discovered in CMS will be usually unstable and will quickly convert into a cascade of lighter, more stable and better-known particles. Each layer of CMS consists of different material(s) that exploit the different properties of the final better-known particles to measure the energy or momentum of each one [1].

A particle emerging from a collision will travel outwards and will first come up against the Tracker made of silicon pixel and strip modules. The pixels and strips accurately measure the positions of passing charged particles allowing a precise track reconstruction. The momenta of charged particles are revealed through the curvature of their spiraling paths in the CMS magnetic field. The next layers of the detector, the calorimeters, will stop electrons, photons and sprays of particles produced by quarks called jets, thus allowing the measurement of the energies of the particles. The first calorimeter layer, the Electromagnetic Calorimeter (ECAL) is designed to measure the energies of electrons and photons (particles which interact electromagnetically) with huge precision, after stopping them. On the other hand, the hadrons (particles that interact by the strong force) will deposit most of their energy in the next layer, the Hadron Calorimeter (HCAL). The only known particles to voyage beyond the HCAL are muons and weakly interacting particles (like neutrinos). Muons are charged particles, which are afterwards tracked further in the dedicated Muon Chambers, while their momenta are also measured from the bending of their paths in the magnetic field. Neutrinos, however, will escape detection, as they have neutral charge and hardly interact at all. Their presence and location can be deduced by adding up the momenta of all the detected particles, and assigning the missing momentum to the neutrinos. From all of the above it is clear that particles traveling through CMS leave behind characteristic signatures in the different layers, allowing them to be identified (Fig. 2.4). The collision data is transferred from CERN to centers around the world where physicists will reconstruct each event and the presence of any new particles can be inferred [1].

The CMS Collaboration has acquired many intriguing physics results thanks to its detector. Indicatively, CMS observed for the first time ever that the excited, loosely-bound Υ states disappear relative to the more tightly-bound ground-state Υ [3]. Moreover, CMS measured the rare $B_s^0 \to \mu^+\mu^-$ decay which allowed to define constraints on the models of physics beyond the Standard Model [4].

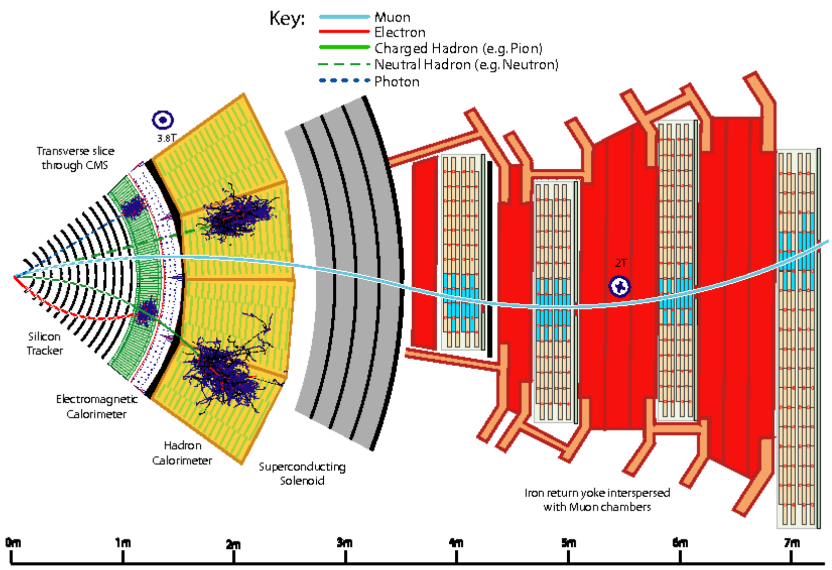

Figure 2.4: A sketch of the specific particle interactions in a transverse slice of the CMS detector, from the beam interaction region to the muon detector. The muon and the charged pion are positively charged, and the electron is negatively charged. The beam direction is perpendicular to the picture plane. (Image: CMS-PRF-14-001.)

2.2 The Superconducting magnet

The CMS magnet (Fig. 2.5) can be grouped into three main systems: a) the yoke, consisting of a barrel, a vacuum tank and two endcaps, b) the coil, consisting of the general engineering, a superconductor, and coil winding, and c) the ancillaries, consisting of the external cryogenics, the power systems and circuit, and the control system. Its task is to bend the paths of particles emerging from high-energy collisions in the LHC. CMS's aim from the beginning was to have the strongest magnet possible because a stronger magnetic field bends trajectories more and, combined with high-precision position measurements in the Tracker and Muon chambers, this allows accurate measurement of the momenta even of highly energetic particles. The CMS solenoid magnet is a superconducting one, allowing electricity to flow without resistance and creating a powerful magnetic field. It is designed in such a way that the Tracker, the ECAL and the HCAL fit conveniently inside the magnet coil whilst the Muon chambers are interleaved with the return yoke. The return yoke is a 12-sided iron structure made up of three layers which surrounds the magnet coils, and contains and guides the field. It reaches out 14 metres in diameter and in addition acts as a filter, allowing through only muons and weakly interacting particles (e.g. neutrinos). The enormous magnet also provides most of the experiment's structural support, and must be strong enough to withstand the forces of its own magnetic field. It weighs 12000 tonnes and is the largest superconducting magnet ever built, while when cooled to its operational temperature (-268.5 °C) it is only a degree warmer than outer space [1], [5], [6].

Since a larger number of coils gives a stronger field, a stronger field brings more precise results, and with more precise results more physics can be obtained, the initial idea was to make the solenoid magnet as big as possible during the detector design. However, for the sake of efficiency the magnet had to be built offsite and transported to Cessy by road. So its size had to be limited since in order to fit through the streets, physically it could not be more than

Figure 2.5: The CMS magnet during CMS construction.

7 meters in diameter [1].

2.3 The Tracker

The CMS Tracker has been designed to record the paths of charged particles through the magnetic field by finding their positions at a number of key points. This system can reconstruct the paths of high-energy muons, electrons and hadrons. It can also view tracks coming from the decay of very short-lived particles such as the b quarks which are used to study the differences between matter and antimatter. The tracker needs to perform accurate track measurements yet be lightweight so as to disturb the particles as little as possible. Its position measurements are so accurate that tracks can be reliably reconstructed using merely a few measurement points. The accuracy of each measurement is of the order of a few μm, which is less than the width of a human hair. Moreover, the Tracker is the innermost layer of CMS and that's why it receives the highest volume of particles and it is crucial that it will resist the respective radiation [7].

The CMS Tracker is entirely made of silicon, having the front-end modules with silicon pixels at the very core of the detector (Inner Tracker, IT) that are dealing with the highest intensity of particles, and the silicon microstrip front-end modules (Outer Tracker, OT) that surround the Pixel detector (Fig. 2.6). As particles traverse the tracker the pixels and microstrips produce tiny electric signals which are subsequently amplified and detected. Particle tracks are reconstructed when combining information from all the Tracker layers. The Tracker employs sensors covering an area the size of a tennis court, with tens of millions of separate electronic readout channels: in the Pixel detector there are several thousands connections per square centimeter. However, the total thickness has to be kept at minimum in order to avoid multiple scattering which could worsen the resolution [7].

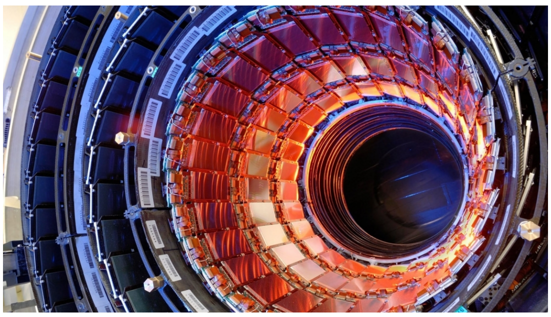

Figure 2.6: CMS Tracker showing silicon strips detectors in the barrel module. (Image: CERN.)

The IT which is comprised of pixel modules experiences the highest density of particle tracks, hence it needs to have the largest granularity. The first Pixel detector was comprised of three 53 cm long concentric barrel layers at radii of 4.4 cm, 7.3 cm and 10.2 cm. Two endcap disks were located on each side of the barrel covering radii from 6 cm to 15 cm. The first pixel size in the Pixel detectors was designed to be 150 μm by 150 μm. The CMS Pixel sensors were n-on-n devices so that, in the barrel, their response was strongly affected by the large Lorentz angle of the electrons. The barrel Pixel geometry was deliberately arranged such that this large Lorentz angle induced significant charge sharing across neighboring pixels and this resulted in hit resolutions of the order of 10 μm. Similar resolutions, of the order of 20 μm, were obtained in the endcap pixels, by rotating the sensors 20° around their central radial axis [7], [8].

Due to the accumulated radiation damage through the years of operation and the increase in the delivered instantaneous luminosity of the LHC, the efficiency of the Inner Tracker was reduced, and thus the rate of falsely reconstructed tracks started to increase. In the beginning of 2017, the Pixel detector was replaced with a new one according to the Phase-1 Upgrade of the CMS Tracker. The upgraded Pixel detector consists of four concentric barrel layers located at radii of 2.9 cm, 6.8 cm, 10.9 cm and 16.0 cm. The endcap is comprised of 3 disks on each circular side of the barrel, which are positioned at distances of z = ±29.1 cm, ±39.6 cm and ±51.6 cm, where z is the axis along the beam direction. Furthermore, there is a greater number of detecting layers (four instead of the three in Phase-0) which leads to a larger amount of readout channels. A new digital readout chip with higher rate capability has been added and the power of the b-tagging algorithms for events with a large number of collisions per bunch crossing (pileup) has been significantly improved. Novel and even more lightweight support structures have been added and a new CO_2 evaporative cooling system is now used, replacing the previous C_6F_{14} mono-phase cooling system, with the heat removal of the new two-phase cooling system being far more effective. The service electronics is displaced from inside the tracking volume covered by the silicon strip tracker ($|\eta| < 2.5$) to larger pseudorapidities, where the pseudorapidity is defined as $\eta = -\ln(\tan(\theta/2))$. (It should be mentioned that CMS uses a right-handed coordinate system, where the x-axis points to the center of the LHC ring, the y-axis points up vertically, the z-axis points along the beam direction, as mentioned before, the azimuthal angle ϕ is measured in the xy-plane, the radial coordinate is denoted by r and the polar angle θ is defined in the rz-plane.) Replacing the aluminum disk supports with ones with carbon based compounds effectively reduces further the material budget [9], [10]. A schematic layout of the Phase-1 upgraded Pixel detector compared to the original one can be seen in Fig. 2.7 [9].

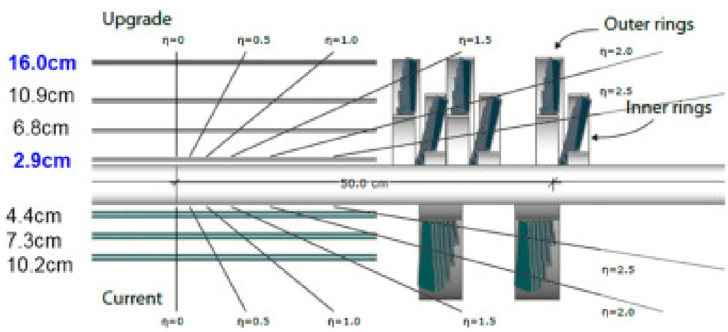

Figure 2.7: Comparison of the geometrical layouts of the Phase-0 (bottom) and upgraded Phase-1 (top) CMS Pixel detectors.

Given the fact that the track multiplicity per unit area is much lower for higher radii, there is a lesser demand for high granularity there. Therefore, the CMS OT consists of strip sensors instead of pixel sensors. In addition, the presence of pixels in the OT would tremendously increase the total number of readout channels, since the total area of the OT is larger, obstructing thus the effective data transferring. The OT is composed of thousands of strip sensor modules distributed among the four different subsystems indicated in Fig. 2.8: Tracker Inner Barrel (TIB), Tracker Inner Disks (TID), Tracker Outer Barrel (TOB) and Tracker End-Cap (TEC). Each module carries either one thin (320 μm) or two thick (500 μm) silicon sensors [1], [7].

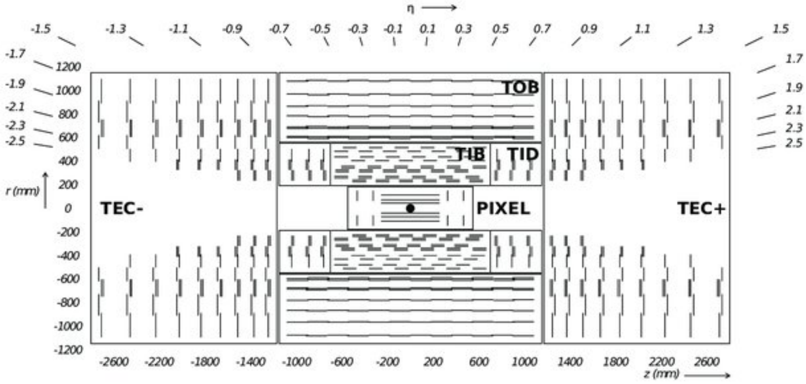

Figure 2.8: Schematic cross section of the CMS tracker. Each line represents a detector module. Double lines indicate double-sided modules.

2.4 The Electromagnetic Calorimeter (ECAL)

The ECAL (Fig. 2.9) forms a layer between the Tracker and the HCAL. It is made up of a barrel section (consisting of tens of thousands of crystals formed into supermodules, with every supermodule weighing around three tonnes) and two flat endcaps (made up of approximately 15000 further crystals) that seal off the barrel at each end. The ECAL also contains Preshower detectors that sit in front of the endcaps which allow CMS to distinguish between single high-energy photons (that could be signatures of new physics) and the trivial close pairs of low-energy photons [11].

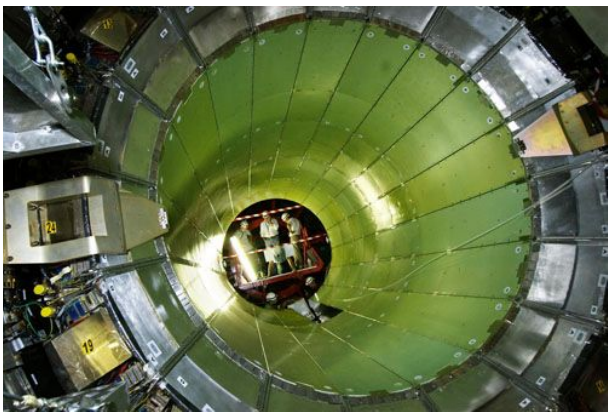

Figure 2.9: CMS ECAL during construction. (Image: CMS/CERN.)

To draw a picture of events taking place in the LHC, CMS has to know the energies of emerging particles. In the beginning of the CMS operation, electrons and photons were of particular interest because they are possible final products of the decay of a Higgs boson. These particles are measured in the ECAL, but in order to find them with the specified precision due to the high magnetic field, large levels of radiation and 25 ns between collisions, very particular detector materials are required. Lead tungstate (PbWO4) crystal with a density of 8.3 g/cm^3 was considered the most suitable material for the ECAL. It is made mainly of metal and is heavier than stainless steel, but with the presence of oxygen in this crystalline form it is a highly transparent material. In addition, it scintillates, i.e. produces light in fast, short and unambiguously defined photon bursts when electrons and photons pass through it, in proportion to their energy. (This tells us the energy of the incoming electron or photon.) Each crystal has a mass of 1.5 kg and a volume roughly equal to that of a small coffee cup. The ECAL contains around 80000 crystals produced in Russia and China for a total period of 10 years (as it takes two days to artificially grow a single one of them). During the "production" crystals were cut, machined, polished with diamond and tested. (For replacing the crystals' cloudy surfaces with a transparent finish they had to pass over a fine suspension of diamond, to obtain a smoother surface, since the very fine transparent surface is essential for light collection in the crystals.) Especially designed to work within the high magnetic field photodetectors were glued onto the back of each crystal to detect the scintillation light and convert it to an electrical signal which will be subsequently amplified and analyzed. Groups of crystals were assembled side-by-side in glass-fibre or carbon-fibre pockets to form larger structures, the supermodules. Each supermodule contains several modules, each module contains several supercrystals and each supercrystal consists of several crystals. For the endcaps, the supercrystals are five-by-five blocks which are inserted into one of four "Dees", structures named for their resemblance to the letter D, that fit around the beam, thus allowing easy installation. Inside CMS the supermodules are supported on a strong but lightweight system, designed to add only a minimum amount of material in front of the detector. The 2.5-tonne weight of each supermodule is cantilevered from one end so that two-thirds of it is taken at the back and the remaining third on a slender arm of aluminium and glass fibre composite [11].

It's not a secret that the PbWO4 material also has its drawbacks that the designers of CMS had to overcome. Since the yield of light depends strongly on temperature, a cooling system has to maintain the temperature of 100 tonnes of crystal to within 0.1 °C in order to counterpoise the heat released by the close by electronics. Furthermore, the photodetectors required for the signal amplification need to be radiation hard and operate within a strong magnetic field, and that's why avalanche photodiodes (APDs) were chosen for the crystal barrel, and vacuum phototriodes (VPTs) for the endcaps. Finally, researchers found that lead tungstate would still suffer limited radiation damage inside CMS. For that reason, a light monitoring system is used during operation that sends pulses of light through each crystal to measure its optical transmission. The crystals can anneal (reverse radiation damage) when the accelerator stops and they are again at room temperature, since the warmer temperature shakes atoms back into their ordered structure [11].

The above-mentioned photodetectors are sensors of light or other electromagnetic radiation. Each photo detector has a p-n junction that converts light photons into electric current. APDs are photodetectors made of semiconducting silicon. A strong electric field is applied to them and when a scintillation photon enters the depletion region and creates an electron-hole pair, these charge carriers will be pulled by the very high electric field away from one another. As their velocity increases they will collide with the lattice and will create further e-h pairs. The process will repeat itself producing an avalanche of electrons with their numbers increasing exponentially. This avalanche action enables the gain of the diode to be increased many times, ensuring a great level of sensitivity. Through this method APDs are able to produce a very high current in a short amount of time, which is necessary as the lead tungstate crystals give a relatively low yield of light per incident particle. The signal is afterwards amplified, digitized and immediately transported away by fibre optic cables, so that the analysis can be done away from the radiation area. On the other hand, VPTs are used for crystals in the endcaps where the radiation is too high to use a silicon photodiode. A VPT contains three electrodes within a vacuum. Initially, electrons are released when photons strike atoms in the first electrode in the normal way. Then the voltage difference between electrodes accelerates the electrons into the second electrode, the anode), where several more electrons are produced. These new electrons are then accelerated to the third electrode, the dynode, releasing a second batch of electrons. Thus this also creates a large current from the initial minuscule amount of scintillation light, which is turned into a digital signal and sent along the optic fibres to the upper level readout [11].

One of the Higgs boson possible decays is into high-energy photons whose detection was one of the ECAL's primary jobs before the discovery of the Higgs boson. However, neutral pions which are also produced in collisions can inadvertently mimic high-energy photons during their decay into two closely-spaced photons with a lower energy that the ECAL picks up together. The angle between the two emerging photons from the decay of a neutral pion is specifically close in the endcap region. That's why the Preshower sits in front of the ECAL to prevent such false signals. The Preshower has a much finer granularity than the ECAL with strips 2 mm wide, compared to the 3 cm wide ECAL crystals, and is capable of seeing each of the pion-produced particles as a separate photon. It is made of two planes of lead followed by silicon sensors, similar to those used in the Tracker. When a photon passes through the lead layer it causes an electromagnetic shower, containing electron-positron pairs, which will be detected and measured by the silicon sensors, thus giving a measurement of the photon's energy. Having two detector layers to give two measurements allows finding the exact location of the particle. When seemingly high-energy photons are then found in the ECAL their paths can be extrapolated back to the center of the collision. Physicists can look for their hits in the preshower along the way, adding the energy deposited there to the total energy from the ECAL, and thus deducing if they were individual high-energy photons or photon pairs [11].

The complete preshower system forms a disc, about 2.5 m in circumference with a 50 cm diameter hole in the middle where the beam pipe passes through. Each endcap Preshower uses 8 square meters of silicon with each silicon sensor measuring about 6.3 cm $\times$ 6.3 cm $\times$ 0.3 mm and divided into 32 strips. The sensors are arranged in a grid in the endcaps to form an approximately circular shape covering most of the area of the crystal endcap. For optimum performance during the lifetime of the experiment the silicon detectors must be kept at a temperature of between -10 °C and -15 °C, and since the nearby ECAL is very sensitive and must be kept within precisely 0.1 °C of its (higher) optimum temperature, the preshower must be cold on the inside but warm on the outside. This is achieved by using both heating and cooling systems [11].

2.5 The Hadron Calorimeter (HCAL)

The Hadron Calorimeter (HCAL) is famous for making use of over a million World War II brass shell casements from the Russian Navy in making some of its detector components! It is the system that measures the energy of the particles consisting of quarks and gluons called hadrons. Furthermore, it provides indirect measurement of the presence of non-interacting, uncharged particles such as neutrinos. Measuring these particles is important as they can tell if new particles such as the Higgs boson or supersymmetric particles have been formed. As these particles decay they may produce new particles that do not leave traces of their existence in any sub-detector of CMS. To spot them the HCAL must be hermetic, i.e. to ensure that it will capture as many emerging from the collisions particles as possible. This way if particles shooting out only one side of the detector are observed, with an imbalance in the momentum and energy, it can be deduced that "invisible" particles were produced [12].

The HCAL finds a particle's position, energy and arrival time using repeating layers of dense absorber (brass or steel) and tiles of fluorescent plastic scintillator that produce a rapid light pulse when a hadronic particle passes through, thus acting as a sampling calorimeter. When the hadron hits a plate of absorber an interaction can occur producing a shower or cascade of secondary particles. As this shower develops, the particles pass through the alternating layers of the scintillator causing them to emit blue-violet light. Within each tile tiny optical wavelength-shifting fibres absorb this blue-violet light and shift it into the green region of the spectrum. Clear optic cables then carry the green light away to readout boxes located at specific locations within the HCAL. In the readout boxes photodetectors called Hybrid Photodiodes (HPDs) amplify the signal about 2000 times. (420 of these HPDs are used in CMS, and each HPD's light-sensitive surface serves as a photocathode which converts light into electrons by the photoelectric effect, while inside the HPD, these low-energy electrons are quickly accelerated across a narrow gap onto a silicon diode target divided up into 19 pixels, each of which can generate its own amplified electronic signal when the accelerated electrons strike it.) The related electronics which contain the so-called QIE (Charge Integration and Encode) chips then integrates and encodes the signal and sends it to the DAQ system for event triggering and event reconstruction. The particle's energy is measured as the amount of light in a given region, which is summed up over many layers of tiles in depth collectively known as tower [12].

As the HCAL is thick and bulky it was a challenge to fit it into CMS, since the produced showers are large, and the minimum amount of material needed to measure them is approximately one meter. The HCAL is organized into HCAL Barrel (HB), Outer HCAL (HO), HCAL Endcap (HE) and HCAL Forward (HF) sections. There are 36 barrel wedges, each weighing 26 tonnes, which form the last layer of detector inside the magnet coil whilst the few additional layers of the HO are placed outside the coil, ensuring no energy leaks out the back of the HB undetected. Likewise, 36 endcap wedges measure particle energies as they emerge through the ends of the solenoid magnet. The two radiation-hard HF are positioned at each end of CMS, to pick up the countless particles coming out of the collision region at shallow angles relative to the beam line [12].

2.6 The Muon chambers

Detecting muons is one of CMS's most important tasks, as its name implies, since muons were expected to be a signature of the Higgs boson (before it was discovered it was known that it would decay into four muons if it existed) and they are produced in the decay of a number of potential new particles. Muons can penetrate several meters of iron without interacting (since they are not stopped by the calorimeters like most other particles). Therefore, the Muon chambers (Fig. 2.10) are positioned at the very edge of the experiment where muons are the only particles likely to register a signal. Four muon stations sit outside the magnet coil and are interleaved with iron return yoke plates. When a curve is fitted to the hits among the multiple layers of these stations, the particle's path is traced (in combination with measurements in the Tracker, as the Muon system is aligned with the central Tracker to within one sixth of a millimeter), and thanks to its bending caused by the CMS magnet the particle's momentum can be calculated [13].

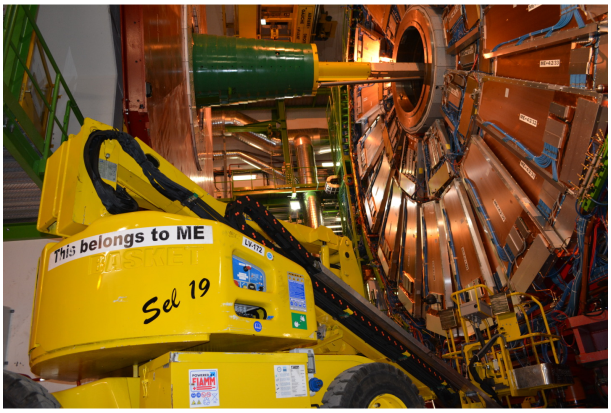

Figure 2.10: Work on CMS Muon Detector (RPC) during Long Shutdown 1 (LS1) - Point 5, Cessy, CMS cavern. (Image: CMS/CERN.)

There are 1400 muon chambers in total: 250 drift tubes (DTs) and 540 cathode strip chambers (CSCs) track the particles' positions and provide a trigger, while 610 resistive plate chambers (RPCs) form a redundant trigger system, which quickly decides if the acquired muon data should be kept or not. Because of the many and diverse layers of detector, the system is naturally robust and able to filter out background noise. DTs and RPCs are arranged in concentric cylinders around the beam line (barrel), whilst CSCs and RPCs, make up the endcap disks that cover the ends of the barrel [13].

The DT system measures muon positions in the barrel. Each tube is 4 cm wide and contains a stretched wire within a gas volume. When charged particles such as muons pass through the volume they knock electrons off the atoms of the gas, and the electrons afterwards follow the electric field ending up at the positively-charged wire. By registering where along the wire electrons hit and by calculating the muon's original distance away from the wire, two coordinates of the muon's position are obtained. Each DT chamber is on average $2\,\mathrm{m} \times 2.5\,\mathrm{m}$ in size and consists of 12 aluminum layers, arranged in three groups of four, each up with up to 60 tubes, where the middle group measures the coordinate along the direction parallel to the beam and the two outside groups measure the perpendicular coordinate [13].

CSCs are used in the endcap disks where the magnetic field is uneven and particle rates are high. They consist of arrays of positively-charged wires (serving as anodes) crossed with negatively-charged copper strips (serving as cathodes) within a gas volume. When muons pass through, they knock electrons off the gas atoms, which cluster to the anode wires producing an avalanche of electrons. Positive ions move away from the wire and towards the cathode, at the same time inducing a charge pulse in the strips, at right angles to the wire direction. Because the strips and the wires are perpendicular, two position coordinates are obtained for each passing particle. The closely spaced wires also make the CSCs fast detectors suitable for triggering [13].

RPCs are fast gaseous detectors that provide a muon trigger system parallel with those of the DTs and CSCs. Each of them consists of two parallel plates, a positively-charged anode and a negatively-charged cathode, both made of a very high resistivity plastic material and separated by a gas volume. When muons pass through the chamber, electrons are knocked out of the atoms in this gas volume. These electrons in turn hit other atoms causing an electron avalanche. The electrodes are transparent to the signal, and the electrons are instead picked up by external metallic strips after a small but precise time delay. The pattern of hit strips gives a quick measure of the muon momentum, which is subsequently used by the trigger to make decisions about whether the data is useful and should be kept or not. RPCs combine a satisfactory spatial resolution with a good time resolution of 1 ns [13].

2.7 Triggering and data acquisition (DAQ)

At the peak performance of CMS about one billion proton-proton interactions will take place every second inside the detector. Not all these interactions reveal new phenomena and it is impossible that all the related events could be read out. Then the Trigger and DAQ System (TriDAS) takes action. The Trigger's job is to select the potentially interesting events and reduce the rate to just a few hundred events per second, which can be read out, stored and finally analyzed. Trigger data is collected from the front-end electronics, decisions are developed about retaining the small portion coming from interactions of interest and these decisions are propagated to the readout electronics front-end buffers. A decision to retain an event for further consideration is made every 25 ns during CMS operation (as groups of protons collide 40 million times per second in the LHC). This decision is based on the event's suitability for inclusion in one of the various data sets to be used for analysis, which may include di-lepton and multi-lepton data sets for top and Higgs searches, lepton plus jet data sets for top physics, and inclusive electron data sets for calorimeter calibrations. Furthermore, other samples are necessary for measuring efficiencies in event selection and studying backgrounds. The Trigger has to select these samples in real time together with the main data samples. As new waves of particles are being generated before those from the last event have even left the detector, the data is stored in pipelines that can retain and process information from many interactions at the same time. To avoid confusing particles from two different events, the detectors have very good time resolution and the signals from the millions of electronic channels are synchronized so that they can all be identified as being from the same event [14].

Before CMS, other experiments (the ZEUS experiment, the Tevatron experiments) had incorporated a three-level trigger system which consisted of: pure hardware (L1), mostly custom hardware (L2) and the computer farm (L3). At CMS, the TriDAS group decided not to have a second level trigger. They would take the output of L1 straight to the computer farm for software processing. The main reason behind this desicion was that the L2 hardware was too restrictive, not fully programmable, and was only used at the time because there was no telecom switch that could convey the full L1 output of 100 kHz of 1 MB events to the farm. This way, L1 had to be more efficient than in previous systems in order to perform certain tasks traditionally performed by L2 [14].

Level 1 (L1) of the trigger is an extremely fast and wholly automatic process that looks for signs of interesting physics, like particles with an unexpectedly large amount of energy or in unusual combinations. The best 100000 events are selected each second from the billion available. For the next test, the higher level trigger (HLT), information is assimilated and synchronized from different parts of the detector to recreate the entire event, and then sent to a farm of more than 1000 standard computers [15]. The computers review with more details the information for longer, but still less than a tenth of a second. They run complex physics tests to look for specific signatures, such as matching tracks to hits in the Muon chambers. Overall they select 100 events per second with potential for new physics and throw out the remaining 99900. However, despite the Trigger system, CMS still records and analyzes several petabytes of data [14].

Prior to the CMS Trigger, triggers were designed to count objects: e.g. the number of electrons/muons over a certain threshold, providing a histogram. In CMS, the characteristics of objects (their energy, coordinates etc.) would be retained, which required sorting of the objects so that only the prime candidates would be selected. The latency (trigger processing time) is longer than it would have been for the L1 trigger in a three-level trigger system, since sorting consumes time. The solution was to build custom chips for the Calorimeter trigger to implement the sorting fast enough [14].

Apart from performing the readout of the front-end electronics after a L1 Trigger accept, another crucial function of the DAQ system is the operation of a Detector Control System (DCS) for the operation and supervision of all detector components and the general infrastructure of the experiment. The DCS is a key feature of CMS, and guarantees its safe operation to obtain high-quality data [16].

A distinguishing characteristic of the CMS DAQ system is that its required performance depends on the performance of the accelerator and of the detector. At the LHC start-up, once the commissioning of the accelerator was completed and stable machine running was achieved, the instantaneous luminosity was significantly below the design luminosity and started to grow with time. Thus, the DAQ design had to be be sufficiently modular to accommodate both planned and unplanned increases in machine performance. Since it was impossible to know the precise experimental conditions in advance, the DAQ structure had to be such that its performance could be increased in a straightforward manner with the installation of additional components, without any additional design or development time [16].

Since the period of the initial TriDAS design it was expected that the DAQ system would undergo major changes in the system over the lifetime of the experiment due to the opportunity to employ newer technologies that can increase the system performance, simplify its operation and increase its reliability. Another reasons for the upgrades include the inability to maintain out-of-date hardware, the desire to introduce unforeseen capabilities into the system and changes in the accelerator and experiment parameters [16].

2.8 The Computing Grid

Even after the Trigger selection, CMS still possesses a huge amount of data that must be analyzed - more than five petabytes per year when running at peak performance. To face this challenge, the LHC employs a novel computing system, a distributed computing and data storage infrastructure called the Worldwide LHC Computing Grid (WLCG) where tens of thousands of standard PCs collaborate worldwide to have far more processing capacity than could be achieved by a single supercomputer. The WLCG provides access to data to thousands of scientists all over the world. The "Tier-0" center at CERN reconstructs the full collision events before data analysts start to look for patterns. It is directly connected to the experiment for initial processing and data archiving. Once CERN has made a primary backup of the data it is then sent to large "Tier-1" computer centers in various locations around the world (in France, Germany, Italy, Spain, Taiwan, the UK and the US). At these centers events are reconstructed again, using information provided by the experiment to improve calculations using refined calibration constants. Tier-1 begins to interpret the particle events and collate the results to discover patterns emerging. Meanwhile each center sends the most complex events to a number of "Tier-2" facilities (there are totally around 40), for further specific analysis tasks. In this way information flows out from each tier across the world so that, physicists can study CMS data from their own computer, updated on a regular basis by the LHC Computing Grid [17].

Event data has been carefully evaluated and organized into streams that may be reconstructed, archived, replicated, split or skimmed, as required. Requirements for auditing the data provenance and propagating it as the data travels from center to center and is possibly re-processed multiple times, have been examined and finally fulfilled. A similar analysis for non-event data, such as calibrations and job parameter lists has been performed. It has been decided that management services will be responsible for locating, storing and transferring the data in a safe, efficient and auditable manner. Workload management services employ the data management services and additional (Grid and CMS) services to manage large computational tasks, such as re-processing a large data set, in a distributed environment [17].

During the CMS operation, successive degrees of processing (event reconstruction) refine the initially raw data produced from the online system, apply calibrations and create higher-level physics objects. CMS uses a number of data formats with varying degrees of detail, size, and refinement to write this data in its various stages. In turn, the data formats get grouped within an Event file into multiple Event formats, according to the data's origin or content. An Event consists of the signals from all particles of an interaction, or possibly even several interactions, joined together. After sorting out which bits of information are related to the same particle (pattern recognition) the kinematic properties of each particle have to be reconstructed to reveal the physical nature of the whole event (reconstruction). Each bit of data in an event must be written in a supported data format. A data format is essentially a C++ class, where a class defines a data structure [17].

The format of data after reconstruction is called RECO. RECO is derived from RAW data and provides access to reconstructed physics objects for physics analysis in a convenient format. Event reconstruction is structured in several hierarchical steps (detector-specific processing, tracking, vertexing, particle identification). On the other hand, Analysis Object Data (AOD) are derived from the RECO information. They are intended to contain, in a convenient, compact format, enough information about the event to support all the typical usage patterns of a physics analysis. They are usable directly by physics analyses and are produced by the same, or subsequent, processing steps as those that produce the RECO data. AOD are available at Tier-2 sites (unlike the full RECO data) [17].

2.9 Civil engineering

As mentioned above, the CMS cavern, at Point 5 of the LHC near Cessy, was excavated from scratch in an old LEP access point. The work took six and a half years and finished in February 2005. Two caverns, 100 m underground had to be created, including the 53 m long, 27 m wide and 24 m high experiment cavern, as well as two new shafts. As assembling and testing each of the slices of detector took place on the surface and they were lowered underground afterwards, this meant that huge but delicate pieces of detector, weighing as much as 2000 tonnes had to be transported and lowered, down a 100 m shaft. (In fact it took that heaviest piece weighing 2000 tonnes 12 hours to travel the 100 meters underground.) Since civil engineering work on the cavern was going on in parallel with detector construction, CMS was in a unique position where its builders were able to excavate where geology was difficult, without any delays hindering the development of the detector itself [1]. It was an enormous challenge to excavate through the loose earth and soft rock - 75 m of moraine (a glacially formed accumulation of unconsolidated glacial debris like regolith and rock) [18], followed by molasse (a form of soft sandstone) [19]. It is worth noting that whilst excavating trial pits around the site in 1998, engineers found an ancient Roman villa from the 4th century AD with pots, tiles and coins [20].

2.10 The CMS Phase-2 Upgrade

The Phase-2 Upgrade of CMS is required in order to replace or improve the existing detector systems to provide the necessary physics performance under the challenging high-luminosity conditions and the pileup of up to 200 vertices per bunch crossing. One of the requirements for the Upgrade will be to distinguish among these hundreds of soft collisions the hard proton collisions. Thus arises the demand for high resolution, to separate the trajectories and energy deposits of particles produced in the different collisions and then to associate them to their correct origin. The installation of the upgraded detector systems is expected to be completed in Long Shutdown 3 (LS3), presently scheduled for 2024 to mid-2026 [21].

The Tracker will suffer significant radiation damage by LS3 and must be completely replaced for Phase-2. The new CMS Tracker (made entirely of silicon) will have an essential increase in the number of channels and an improved spatial resolution. The outer part of the detector, exploiting the high magnetic field of CMS, will also enable the usage of track elements in the event selection at the 40 MHz beam crossing frequency. More sophisticated trigger algorithms will be explicated and the current physics acceptance will be maintained at the highest luminosity, thanks to the improvements in the field-programmable gate array (FPGA) processing power and bandwidth. The Pixel detector will extend into the forward regions, which will greatly enhance the performance for major signals of the HL-LHC physics program, such as Vector Boson Fusion processes and the searches for new physics with missing energy [22].

The electromagnetic and hadronic endcap calorimeters will also suffer significant radiation damage by LS3, and so will be fully replaced by a new system called the High Granularity Calorimeter (HGCAL). The replacement has electromagnetic and hadronic sections with excellent transverse and longitudinal segmentation which will provide detailed three dimensional images of showers induced by incident electrons, photons and hadrons. The interleaved detector layers within the absorber structure will involve a high granularity electromagnetic section based on 28 layers of silicon sensors (as the active material) with pad segmentation (of variable sizes, less than $1.0\,\mathrm{cm}^2$), and a hadronic section of 24 layers using the same technology in its innermost layers, with a less segmented plastic scintillator tile section at higher radius. The hadronic part will have a front section of 12 brass and copper plates with silicon sensors. The high granularity will allow precise time-stamping of neutral particles down to low transverse momentum [23].

An electronics upgrade is scheduled for the barrel section of the calorimeter, while the existing crystals and APDs will be kept intact. The dynamic range will be between a few tens of MeV to the equivalent of 2 TeV signals from electrons or photons. The lower bound is defined by the intrinsic noise from the APDs, currently around 60 MeV, and this will increase further with radiation. The upgrade will reduce the noise to around 200 MeV through a re-optimization of the preamplifier architecture and characteristics and a lowering of the supermodule operating temperature from $18\,^{\circ}\mathrm{C}$ to $9\,^{\circ}\mathrm{C}$. The upgraded electronics will also feature reduced shaping times of the signals for better timing precision [24].

To disentangle collisions that occur close together in space during the bunch crossings, but at different times, it is necessary to know the time of flight (ToF) of minimum ionizing particles (MIPs) from their identified spatial vertex. To exploit this technique, CMS has proposed an additional hermetic detector - the MIP Timing Detector (MTD) with a timing precision of $\approx 30\,\mathrm{ps}$. The conceptual design makes use of small LYSO crystals (Cerium doped Lutetium based scintillation crystals that offer high density and short decay time) with Silicon Photomultiplier (SiPM) readout in the barrel region (the SiPMs are pixelated avalanche photodiodes operating in Geiger breakdown mode) and a new generation of specialized silicon detectors with internal gain of

10-30, the Low Gain Avalanche Diodes (LGADs), in the endcap region (where radiation tolerance is more demanding). Studies, which also take into account the new timing abilities of the upgraded Barrel and Endcap Calorimeters for neutral particle showers, show that the MTD can significantly enhance the performance for reconstructing physics objects associated with hard collisions. This could improve significantly the reach for all physics channels. Furthermore, the MTD will provide a new means to execute and extend the searches for long lived particles (LLP), which are predicted in a range of extensions of the Standard Model and some SUSY models [25].

The Muon chamber upgrades will provide new trigger capabilities for the LLPs and an enhanced acceptance in the forward regions that will benefit several physics channels. The muon system in the region $1.5 \leq |\eta| \leq 2.4$ currently consists of four stations of Cathode Strip Chambers (CSC) and it lacks redundant coverage despite the fact that the region is challenging for muons in terms of backgrounds and momentum resolution. It has been proposed to enhance these four stations with additional chambers which make use of new detector technologies with higher rate capability, in order to maintain good L1 muon trigger acceptance in the aforementioned region. The two first stations are located in a space where the magnetic field of CMS is relatively high and so will use Gas Electron Multiplier (GEM) chambers for good position resolution, thus improving momentum resolution for the standalone muon trigger and the matching with tracks in the global muon trigger. The two next stations will use low-resistivity Resistive Plate Chambers (RPC) with lower granularity but good timing resolution for the reduction of background effects. The implementation of a GEM station in the space that becomes free behind the new endcap calorimeters has been proposed in order to increase the coverage for muon detection to $|\eta| \approx 3$. In addition, the electronics of the Muon chambers will be upgraded to handle the future data rate, using the latest technology such as high bandwidth optical data transfer. The new requirements on the L1 trigger and the data acquisition in terms of latency can only be met with deeper buffering and faster processing of the upgraded electronics [26].

The systems that provide protection against beam background and measurement of the luminosity will require upgrade work in several areas to manage the high radiation levels of the HL-LHC. The protection systems will be upgraded with new poly-crystalline diamond sensors that will be read out using the standard LHC Beam Loss Monitor hardware and software and fully integrated into the LHC control system. On the other hand, since the latency of the present L1 trigger is limited to 3.4 μs by the tracker readout, for Phase-2 operation, it will be increased to 12.5 μs to provide sufficient time for the hardware track reconstruction and matching of tracks to muons and calorimeter information. Finally, the DAQ system will also be upgraded to implement the increase of bandwidth and computing power that will be required to accommodate the larger event size and L1-trigger rate, and the greater complexity of the reconstruction at high pileup [21].

2.11 The Tracker Upgrade for the HL-LHC

The upgraded CMS Tracker will consist of about 220 m^2 of silicon detector. The design of the detector will preserve the ease of access of the current detector that enables the possibility to replace degraded parts over an Extended Technical Stop, as some of the detector components might not survive the full radiation dose provided by the HL-LHC. The Outer Tracker will consist of a combination of silicon double-sided (strip-strip and pixel-strip) modules, while the Inner Tracker will be made by silicon pixel modules. In order to maintain a reasonable track reconstruction performance at the much higher PU levels of the HL-LHC, the granularity of both the Outer Tracker and Inner Tracker will be increased by roughly a factor 4 for the upcoming Phase-2 Upgrade. In the OT, this will be achieved by shortening the lengths of silicon sensor strips relative to those in the current detector, without making significant changes to the pitch. A series of design improvements will lead to a much lighter Outer Tracker providing an optimized p_T resolution and a lower rate of γ-conversions compared to the present detector. The module design will provide track-stub information to the L1 trigger at 40 MHz for tracks with $p_T \geq 2$ GeV, thus securing better background rejection at the earliest stage of the event selection. The Inner Tracker will incorporate smaller pixels and thinner sensors with thicknesses of the order of a few hundreds micrometers (which offer advantages in terms of lower bias voltage and lower leakage current) for improved impact parameter resolution and better two-track separation for improved b-tagging along with better τ-hadronic decay and track reconstruction efficiencies within boosted jets. With up to 10 additional pixel disks in each of the forward regions (Fig. 2.11) the system coverage will be extended to close to $|\eta| = 4$, to better match the range of coverage of the calorimeter system. The target integrated luminosity of 3000 fb^{-1} corresponds to a hadron fluence of 2×10^{16} n_{eq} cm^{-2} and 10 MGy at 3 cm from the interaction region, roughly where the first layer of the Pixel detector will be located, and the fluence decreases rapidly with distance and is about 3×10^{15} n_{eq} cm^{-2} at a radius of 11 cm [22], [27], [28].

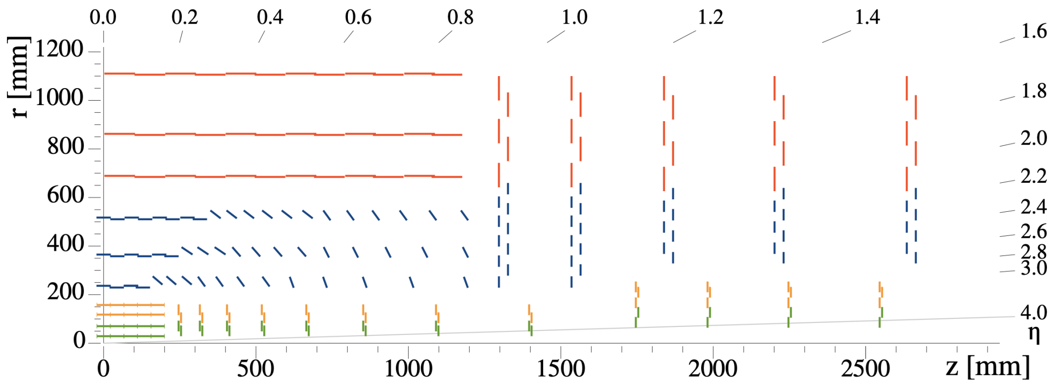

Figure 2.11: Sketch of one quarter of the tracker layout in *r-z* view. In the Inner Tracker the green lines correspond to pixel modules made of two readout chips and the yellow lines to pixel modules with four readout chips. In the Outer Tracker the blue and red lines represent the two types of modules, respectively equipped with pixel-strip and strip-strip sensors.

The Outer Tracker for the HL-LHC will consist of six barrel layers and five endcap disks per side. It can be subdivided in four main large structures: the Tracker Barrel with 2S modules (TB2S), the Tracker Barrel with PS modules (TBPS) and two Tracker Endcap Double Disks (TEDDs), where the Phase-1 geometry with four Barrel layers and 3 forward disks is taken as a starting point. The basic unit of the detector is a p_T module. Two type of p_T modules will be inserted into both the Endcap Disks as well as in the Barrel region: the 2S module and the PS module. 2S modules populate the outer regions, above R ≈ 60 cm, while the PS modules are deployed in the radial range between R ≈ 20 cm and R ≈ 60 cm. Both module types have two closely spaced silicon sensors, but while the 2S modules have two sensors with micro-strips, the PS modules consist of one sensor with micro-strips and one sensor with macro-pixels. The two sensors are read out by common front-end ASICs capable of correlating the hits from the two sensors. Tracking information is provided by the modules to the L1 trigger level by measuring the transverse momentum of tracks. The p_T module's functionality relies upon local data reduction in the front-end electronics, which is achieved by the capability of the p_T modules to reject signals from particles with transverse momentum smaller than a given p_T threshold. The front-end ASIC receives the locations of hits caused by charged particles bent in the transverse plane by a p_T-dependent angle (thanks to the strong magnetic field), measures the local distance, and compares it to a predefined acceptance window to select candidates with high p_T. A track stub (a type of a local track segment and matching pair of hits in the two sensors of a module within a given acceptance window) is formed and subsequently pushed out to the L1 trigger system at every bunch crossing. All other signals are stored in the front-end pipelines to be read out when a trigger is received. The back-end Track Finding system receives the stub data from the individual modules and afterwards performs track finding (Fig. 2.12). The design of modules should provide for efficient removal of the heat generated by the electronics and sensors, accurate geometrical positioning, minimal mass, and finally a simple and reproducible assembly procedure. For the thermal performance, the design requirement is to achieve a sensor temperature of -20 °C or lower with a coolant temperature of -30 °C for modules irradiated with the full HL-LHC integrated luminosity [22], [27], [28].

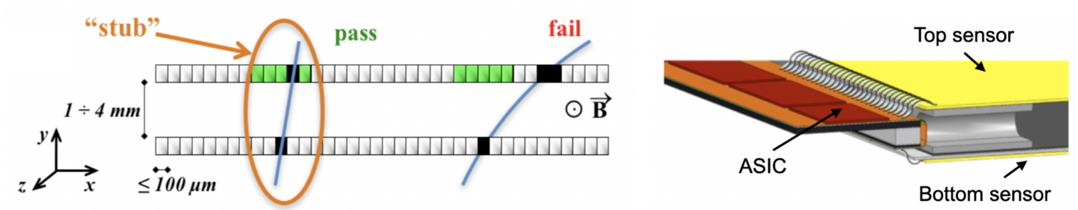

Figure 2.12: Sketch of the track stub finding principle (left) and the p_T module concept (right). A track passes both sensors of a module. A low momentum track falls outside the acceptance window and produces no stub.

To ensure that a track will cross both the bottom and top sensors of a module for a given η, and to enable a good hermetic coverage and a better trigger performance, a tilted geometry is employed in the tracker barrel equipped with PS modules (Fig. 2.11). Despite the higher number of readout channels in the upgraded Tracker, the estimated material budget of the OT is reduced thanks to a limited number of layers, an optimized routing of the services, a use of lightweight material for support structures, a low-mass CO_2 cooling and a use of DC-DC converters. It is expected that the new Tracker will achieve better performances with respect to the p_T resolution and the impact parameter resolution, compared to the Phase-1 CMS Tracker (Fig. 2.13) [22], [27].

The 2S and PS modules are equipped with on-module electronics and service hybrids (Fig. 2.14). They are standalone units that are directly connected to the back-end electronics without any intermediary aggregator system. The sensor technology chosen for the sensors of both module types is the Float Zone (FZ) silicon n-in-p with an active sensor thickness of 290 μm (referred as FZ290), produced by Hamamatsu Photonics K.K. An extensive irradiation and characterization program showed that FZ290 provides sufficient signal-to-noise ratio at the standard operation voltage of 600 V (absolute value) and the expected maximum fluence after 3000 fb^{-1} (which corresponds to a hadron fluence of $1.5 \times 10^{15}\, n_{eq}\, cm^{-2}$ at 20 cm from the interaction region), while for scenarios up to and beyond 4000 fb^{-1}, an increase to the absolute value of the operation voltage of 800 V would allow FZ290 to maintain adequate performance [22], [27]. Before that, Float-Zone, Magnetic Czochralski and Epitaxial substrate, both p-in-n and n-in-p sensors, and with different active thicknesses had been examined in order to find the most suitable material for the CMS OT sensors. The results collected had shown that sensors with electron readout are more robust in terms of high field effects after irradiation, and also provide higher Charge Collection (CC) than p-in-n sensors [28].

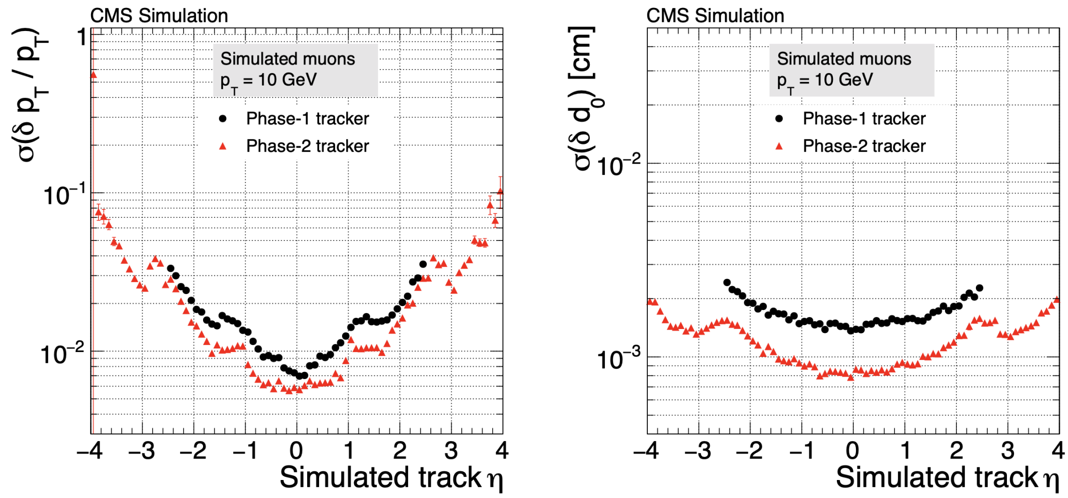

Figure 2.13: Relative resolution of the transverse momentum (left) and resolution of the transverse impact parameter (right) as a function of the pseudorapidity for the Phase-1 (black dots) and the new Phase-2 Tracker (red triangles), using single isolated muons with a transverse momentum of 10 GeV.

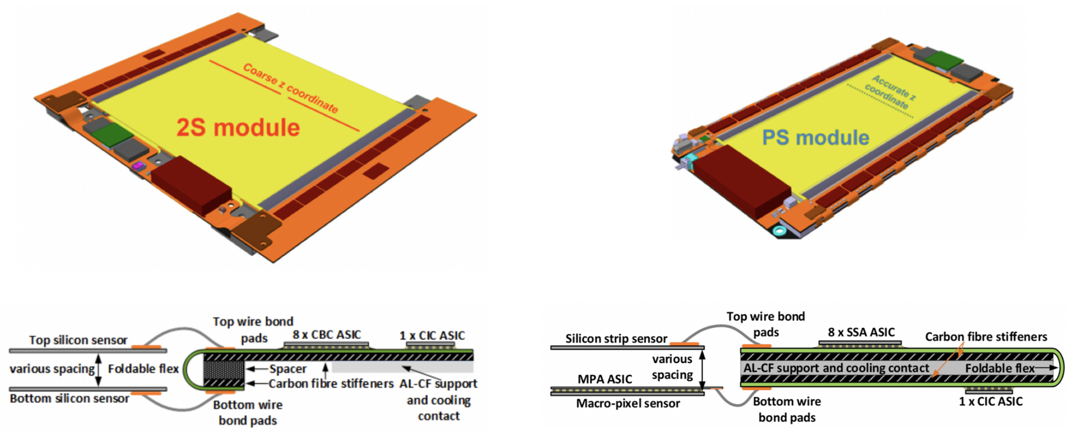

Figure 2.14: The 2S module (left) and PS module (right) of the Outer Tracker. Shown are views of the assembled modules (top), and sketches of the front-end hybrid folded assembly and connectivity (bottom).

The 2S module consists of two superimposed silicon micro-strip sensors, mounted with the strips parallel to each other. Each sensor contains two rows of 1016 AC-coupled strips. The sensor area is approximately $10{\times}10\,\mathrm{cm}^2$, and the strips are of size $90\,\mu\mathrm{m} \times 5\,\mathrm{cm}$ The micro-strip sensors are read out by the CMS Binary Chip (CBC) implemented in 130 nm CMOS technology. Each chip reads 254 strips (127 from bottom and 127 from top sensor strips) and performs correlation of hits between two sensors forming track stubs and sending the stub data out at each bunch crossing. Eight CBCs are hosted on each front-end hybrid per side and each CBC exchanges data with its neighboring chip to enable stub finding across boundaries (Fig. 2.14, left). The CBCs send data to the Concentrator Integrated Circuit (CIC), designed in 65 nm CMOS technology, that performs data sparsification, formats the output data, and sends them to the service hybrid. The CIC processes the track stub data at 40 MHz and the detector payload which is sent out after a L1 accept signal with a maximum rate of 750 kHz. Each 2S module hosts the service hybrid, with the Low Power GigaBit Transceiver (LpGBT, a radiation tolerant serializer/deserializer ASIC for Data, Timing, Trigger and Control Applications in HL-LHC), Versatile Link chips, DC-DC converters and HV distribution circuitry (Fig. 2.14, left). Wire bonds at opposite ends of the sensor provide the connectivity of both sensors to the readout hybrid. The use of one optical link per module provides the bandwidth required for the trigger functionality, and offers significant advantages in the overall system design by avoiding additional electrical interconnectivity in the tracking volume. Each module has two DC-DC converters to convert to the voltages used by the various module components (optical electronics, ASICs) (Fig. 2.15). To enable a homogeneous p_{T} ($> 2\,\mathrm{GeV/c}$) filtering in different detector regions different sensor spacings are selected for the 2S module: 1.8 mm and 4.0 mm [22], [27].

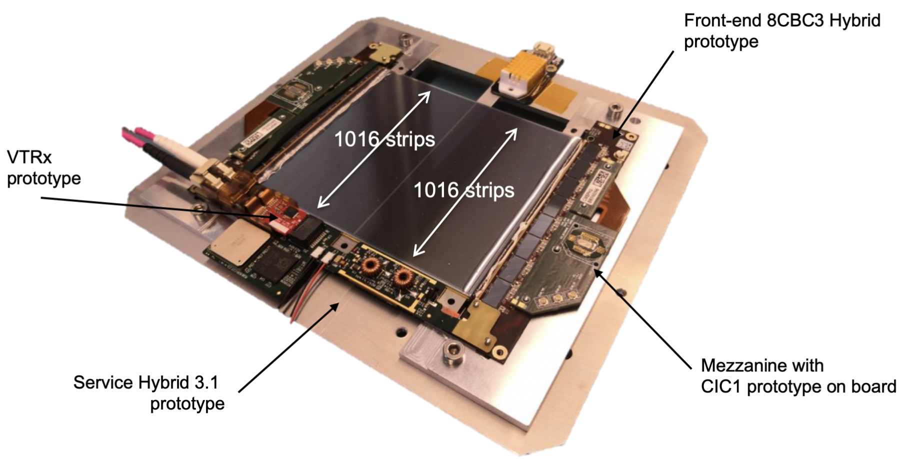

Figure 2.15: Photo of the most recent 2S module prototype.

The PS module is made of one silicon micro-strip sensor arranged in two rows of 960 AC-coupled strips each with single cell size of $2.35\,\mathrm{cm} \times 100\,\mu\mathrm{m}$, and a macro-pixel sensor with a matrix of 32×960 pixels with a pixel size of $1.5\,\mathrm{mm} \times 100\,\mu\mathrm{m}$. The chosen pixel size permits the use of the "C4" bump-bonding technology, an industrial process that is expected to be affordable for a large-scale production. The strip sensor is read out by a Strip Sensor ASIC (SSA) which sits on the front-end hybrid and contains 254 channels, while the macro-pixel sensor is read out by a Macro-Pixel ASIC (MPA), with both having been implemented in 65 nm CMOS technology. A total of 16 MPAs are bump-bonded to the pixel sensor forming a macro-pixel sub-assembly

(MaPSA). To build the stubs, the hit correlations of micro-strip and macro-pixel take place in the MPA chip. The SSA chip processes the sensor signals and sends sparsified cluster data to the corresponding MPA chip at each bunch crossing. Then the MPA processes and sparsifies the hits from each macro-pixel, correlates the bottom macro-pixel sensor hits with the data received from the SSA strips and builds stubs. The CIC on the front-end hybrid buffers and aggregates the stub and cluster data received from the MPAs, and sends them to the service hybrid, which is divided into a readout hybrid and a power hybrid (Fig. 2.14, right). The macro-pixel sensors provide sufficiently precise measurements of the z-coordinate for tracking to enable primary vertex discrimination at L1. To enable a homogeneous p_T filtering in different detector regions various sensor spacings are chosen (1.6 mm, 2.6 mm and 4.0 mm) [22], [27], [28].

To guarantee the correct functioning of the stub finding procedure, the maximum rotation allowed between the top and the bottom sensor is 400 μrad in the 2S modules and 800 μrad in the shorter PS modules [22].

At each bunch crossing the "stub data" obtained by the T modules will be processed to form "L1 tracks", which are tracking primitives that are combined with information from the other sub-detectors to form L1 triggers. The performance of the stub finding capability of p_T modules is characterized in terms of the efficiency achieved for particles above the chosen threshold, and the rate reduction obtained. The reduction rate drops below ten at the largest radii because the rate of hits from low-p_T tracks decreases faster than the total rate (due to the CMS magnetic field), which doesn't cause any problems in terms of bandwidth. The reduction rate also drops for the inner layers because secondary particles produce a larger fraction of fake stubs. Simulations of the resulting stub finding efficiency for muons have indicated that the efficiency plateau is reached at 2 GeV in all the layers of the Tracker, with the appropriate tuning of the front-end parameters. Several approaches with respect to pattern recognition and track fitting were taken into consideration to process stub data in the back-end electronics and construct tracks for the L1 Trigger, such as conventional track finding methods (using commercially available FPGAs) and Associative Memories. The performance of these methods on single particles has been evaluated from samples of single muons, pions and electrons, uniformly distributed in ϕ, η and p_T, overlaid with an average of 140 PU events. Both have proved to be fully functional delivering tracks to the L1 Trigger system within the allotted time-budget of 4 μs. Currently, a hybrid approach combining the best of both algorithms is under study [22], [28], [29].

The Inner Tracker is the main detector used in the offline track reconstruction for the pattern recognition. It will be made of hybrid pixel modules comprising a pixel sensor and two (1×2) or four (2×2) readout chips (ROCs). The IT is structured into a Tracker Barrel Pixel (TBPX) consisting of four layers with 9 modules/ladder and no projective gap at $|\eta| = 0$, a Tracker Forward Pixel (TFPX) made of 8(×2) small discs with 4 rings/disc, and a luminosity Tracker Extension Pixel (TEPX) made of 4(×2) large discs with 5 rings/disc. The innermost ring of the last TEPX disc will be entirely devoted to the measurement of the bunch-by-bunch luminosity. Overall, the IT will cover a surface of about 4.9 m^2 [22], [30].

High granularity in the IT sensors will be achieved using small pitch pixel cells with either a rectangular (25×100 μm^2) or a square (50×50 μm^2) aspect ratio, both compatible with the same bond pattern. In any case, n-in-p silicon sensors with 100-150 μm active thickness will be adopted. Results from TCAD simulations indicate that charge above three times the foreseen threshold of the front-end chip can be collected up to a fluence of 0.8×10^{16} 1 MeV n_{eq}/cm^2, which is about the fluence expected in the most exposed regions of the IT after half the HL-LHC timespan, if the detector is constantly operating at 800 V (absolute value). Since the sensors will be produced from single-side processing, no guard rings on the backplane will limit the electric potential on the cut edge. For the innermost modules, usage of 3D silicon sensors is under consideration, since they would allow efficient charge collection after irradiation operating at 150-200 V (absolute value) [22], [30].

In the IT, compared to the Phase-1 implementation, the Phase-2 pixel ROC will contain six times smaller pixels and will have to deal with about five times higher hit rates, five or ten times higher trigger rates, as well as longer trigger latency. The ROC is required to operate with low noise at low thresholds (1000 e) for efficient detection of signal on irradiated sensors. A common pixel chip architecture for the CMS and ATLAS detectors has been defined by the RD53 Collaboration to be fully digital after the basic threshold detection and charge digitization in the analogue pixel cell. The ROC is currently being developed in CMOS 65 nm technology and a first prototype (RD53A) with dimensions $1{\times}2\,\mathrm{cm}^2$, half-size of the final chip, has already been delivered for standalone qualification and for use in single-chip assemblies with IT prototype sensors. Single chip assemblies with 3D sensors irradiated up to $1{\times}10^{16}\,1\,\mathrm{MeV}\,\mathrm{n_{eq}/cm^2}$ and exposed to 120 GeV/c proton beam at CERN SPS indicate that after irradiation the decrease in the hit efficiency can be as low as 1% when operating the sensor at a moderate bias voltage of 150 V (absolute value) [22], [28], [30].

A buffer depth of 16 pixel clusters for a 4×4 pixel region is sufficient to guarantee a hit loss probability below 10^{-3} for the highest hit rate of $2\,\mathrm{GHz/cm^2}$. With an appropriate bump-bonding pattern the same ROC can be used for the two different pixel aspect ratios, and also for larger pixels with compatible dimensions by disabling the unused channels. A LpGBT chip will transfer the signal to high speed optical links at 10 Gb/s. The LpGBT chip and associated laser and driver will not be used in the central part of the Pixel detector, as they are not expected to have sufficient radiation tolerance. They will be located on the support cylinders at the outer boundary of the detector volume instead and electrical links with lengths up to 2 m will connect the modules to the LpGBTs [22], [28].

There are two types of IT modules, with 1×2 and 2×2 ROCs (Fig. 2.16). Each module consists of the silicon sensor, a High-Density Interconnect (HDI) circuit and the ROC. To reduce the power loss in the cable with an acceptable cable mass, IT modules will be powered serially in groups of 8-12 modules each with the ROCs on the same module being powered in parallel. Since the ROC is the only ASIC present on the module, the 1.2 V required by the front-end is provided by a Low-Dropout (LDO) voltage regulator integrated in the ROC together with a shunt designed to absorb the extra current flowing in case of a failure of one of the chips. (A LDO regulator is a DC linear voltage regulator that can regulate the output voltage even when the supply voltage is very close to the output voltage.) Attention is paid to locate the cooling circuit under the region where the Shunt-LDOs, one for the analog and one for the digital domain, are placed in the ROC [22], [30].

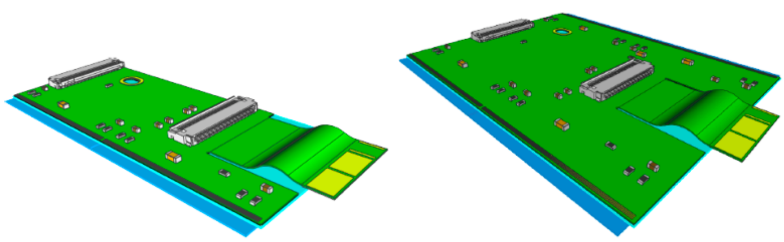

Figure 2.16: IT modules: rendering of the 1×2 (left) and 2×2 (right) readout chips modules.

In the next years the project will move to the large-scale production of the components (4000 IT modules and 14000 OT modules). Quality assurance (QA) during production and care to system aspects in the integration of the different subsystems will be crucial to guarantee the expected performance of the upgraded Tracker [22], [30].

Bibliography

[1] CMS Collaboration, *The CMS experiment at the CERN LHC. The Compact Muon Solenoid experiment*, JINST 3 S08004 (2008).

[2] CMS Collaboration, *Observation of a new boson at a mass of 125 GeV with the CMS experiment at the LHC*, Phys. Rev. Lett. B 716 (2012), pp. 30-61.

[3] CMS Collaboration, *Indications of suppression of excited* Υ *states in PbPb collisions at* $\sqrt{S_{NN}}$ *= 2.76 TeV*, Phys.Rev.Lett. 107 (2011) 052302.

[4] V. Khachatryan et al, *Observation of the rare* $B_s^0 \to \mu^+\mu^-$ *decay from the combined analysis of CMS and LHCb data*, Nature 522 (2014).

[5] A. Hervé, *The CMS Detector Magnet*, IEEE Transactions on Applied Superconductivity, vol. 10, no. 1, March 2000.

[6] V. I. Klyukhin et al, *The CMS Magnetic Field Map Performance*, IEEE Transactions on Applied Superconductivity, vol. 20, no. 3, June 2010.

[7] CMS Collaboration, *The CMS tracker system project: Technical Design Report*, CERN-LHCC-98-006 (1997).

[8] CMS Collaboration, *The CMS tracker: addendum to the Technical Design Report*, CERN-LHCC-2000-016 (2000).

[9] CMS Collaboration, *CMS Technical Design Report for the Pixel Detector Upgrade*, CERN-LHCC-2012-016 (2012).

[10] Anirban Saha, *Phase 1 upgrade of the CMS pixel detector*, 2017 JINST 12 C02033.

[11] CMS Collaboration, *The CMS electromagnetic calorimeter project: Technical Design Report*, CERN-LHCC-97-033 (1997).

[12] CMS Collaboration, *The CMS hadron calorimeter project: Technical Design Report*, CERN-LHCC-97-031 (1997).

[13] CMS Collaboration, *The CMS muon project: Technical Design Report*, CERN-LHCC-97-032 (1997).

[14] CMS Collaboration, *CMS TriDAS project: Technical Design Report, Volume 1: The Trigger Systems*, CERN-LHCC-2000-038 (2000).

[15] V. Gori, *The CMS high level trigger*, International Journal of Modern Physics: Conference Series 31 (2014), p. 1460297.

[16] CMS Collaboration, *CMS TriDAS project: Technical Design Report, Volume 2: Data Acquisition and High-Level Trigger*, CERN-LHCC-2002-026 (2002).

[17] CMS Collaboration, *CMS The Computing project: Technical Design Report*, CERN-LHCC-2005-023 (2005).

[18] Benn, D. I. and Evans, D. J. A., *Glaciers & Glaciation*, New York: Oxford University Press (1998).

[19] Robert Bakewell, *An Introduction to Geology: Comprising the Elements of the Science in Its Present Advanced State, and All the Recent Discoveries; with an Outline of the Geology of England and Wales*, H. Howe, 1829, The New York Public Library.

[20] Michael Richard Krause, *CERN: How We Found The Higgs Boson*, 2014 by World Scientific Publishing Company.

[21] CMS Collaboration, *Technical Proposal for the Phase-II Upgrade of the CMS Detector*, CERN-LHCC-2015-010 (2015).

[22] CMS Collaboration, *The Phase-2 Upgrade of the CMS Tracker*, CERN-LHCC-2017-009 (2017).

[23] CMS Collaboration, *The Phase-2 Upgrade of the CMS Endcap Calorimeter*, CERN-LHCC-2017-023 (2017).

[24] CMS Collaboration, *The Phase-2 Upgrade of the CMS Barrel Calorimeters*, CERN-LHCC-2017-011 (2017).

[25] CMS Collaboration, *A MIP Timing Detector for the CMS Phase-2 Upgrade*, CERN-LHCC-2019-003 (2019).

[26] CMS Collaboration, *The Phase-2 Upgrade of the CMS Muon Detectors*, CERN-LHCC-2017-012 (2017).

[27] A. La Rosa, *The CMS Outer Tracker for the High Luminosity LHC upgrade*, JINST 15 (2020) C02029.

[28] S. Mersi, *Phase-2 Upgrade of the CMS Tracker*, Nucl.Part.Phys.Proc. 273-275 (2016) 1034-1041.

[29] A. Dierlamm, *The CMS Outer Tracker Upgrade for the HL-LHC*, Nucl.Instrum.Meth.A 924 (2019) 256-261.

[30] E. Migliore, *The CMS Tracker Upgrade for the High-Luminosity LHC*, Proceedings of the CTD/WIT 2019, PROC-CTD19-088.

Chapter 3

Silicon sensors

This chapter's scope is to make a brief summary of the operation principles of silicon detectors, and specifically of silicon strip sensors like the ones used in the upgraded CMS Outer Tracker.

3.1 Properties of silicon

Silicon (Si) is the chemical element with atomic number 14. It can be described as a hard, dark-grey solid with a bluish tinge, which is impervious to air at ordinary temperatures. It is a hard, brittle crystalline solid, and is a tetravalent metalloid and semiconductor. It is relatively unreactive and has high chemical affinity for oxygen. Its oxides form a family of anions known as silicates. Its melting and boiling points of 1414 °C and 3265 °C respectively are the second-highest among all the metalloids and nonmetals (with the exception of boron). Silicon is widely distributed in dusts and sands, and more than 90% of the Earth's crust is composed of silicate minerals, making silicon the second most abundant element in the Earth's crust (about 28% by mass) after oxygen.

It is used among others for industrial construction (with clays, silica sand, and stone), concrete (for walkways, foundations, and roads), whiteware ceramics (porcelain), specialty glasses, abrasives and components of high-strength ceramics (in the form of silicon compounds such as silicon carbide), basis of synthetic polymers called silicones, steel refining, aluminum-casting and fine chemical industries. In the late 20th century it caused a revolution in the so-called Information Age, as its semiconducting properties made it an essential ingredient in the metal-oxide-semiconductor (MOS) transistors and integrated circuit chips used in modern computers and cell phones [1].

Silicon has a face-centered diamond-cubic (FCC) crystal structure with a lattice constant of 5.431020511 Å (Fig. 3.1), and a diamagnetic magnetic ordering. Its thermal expansion at 25 °C is 2.6 µm/(m·K), its thermal conductivity is 149 W/(m·K), its electrical resistivity at 20 °C is $2.3\times10^3\ \Omega\cdot$m, and its density is 2.3290 g/cm^3 [1].

Silicon can be found in nature as a solid. All solids have their own characteristic energy band structures. The valence band is the highest band filled with electrons at absolute zero temperature (T = 0 K), where E_V is its upper energy edge. Electrons from the valence band are bound to the nucleus and cannot move through the crystal. At absolute zero temperature the valence band should be fully occupied. The lowest non-occupied energy band that should be completely empty at absolute zero temperature is the conduction band, where E_C is its lower

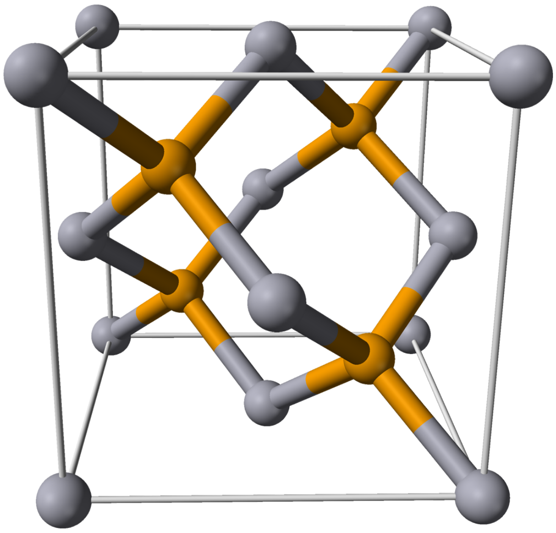

Figure 3.1: Diamond cubic crystal structure for silicon.

energy edge. Electrons in the conduction band can move unobstructed through the crystal. The forbidden area between the valence band and the conduction band $E_G = E_C - E_V$ is called band gap. If $E_G \gg 0$ in a given solid, then the conduction band is almost entirely empty and there is no charge that could produce electric current, so the solid is classified as an insulator (Fig. 3.2, a). If $E_G > 0$ in a given solid (and E_G is of the order of only a few eV), then the band gap is small and thermally excited electrons at room temperature can jump from the valence band to the conduction band easily, so the solid is classified as a semiconductor (Fig. 3.2, b). If $E_G < 0$ in a given solid, then the valence band and the conduction band are overlapping and electrons can always move freely, so the solid is classified as a conductor (Fig. 3.2, c) [2].

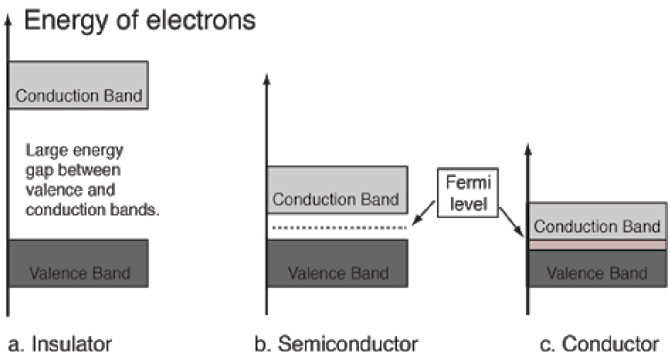

Figure 3.2: Energy bands for solids. (Image: HyperPhysics.)

Electrons will move to the conduction band at high temperatures. In the valence band, a vacancy is created at the place where an electron was present before jumping to the conduction band. This vacancy is called a hole. An intrinsic semiconductor is one for which at thermal equilibrium, the free electron density and the free hole density are equal.

In the band theory of solids, electrons are considered to occupy a series of bands composed of single-particle energy eigenstates each labeled by E. The Fermi-Dirac distribution, f(E), gives the probability that (at thermodynamic equilibrium) a state having energy E is occupied by an electron:

$$f(E) = \frac{1}{e^{\frac{E-E_F}{k_B T}} + 1} \tag{3.1}$$

where T is the absolute temperature, k_B is Boltzmann's constant and E_F is the Fermi level which is defined as the level at which if there is a state, then this state will have a 50% chance of being occupied. The location of E_F within a material's band structure is important in determining the electrical behavior of the material [2].

The free electron density n and the free hole density p can be calculated by convoluting the density of states N(E) near the bottom of the conduction band or near the top of the valence band, respectively, with the corresponding occupation probability F(E):

$$n = N_C e^{-\frac{E_C - E_F}{k_B T}} \tag{3.2}$$

$$p = N_V e^{-\frac{E_F - E_V}{k_B T}} \tag{3.3}$$

where N_C is the effective state density in the conduction band and N_V is the effective state density in the valence band:

$$N_C = 2\left(\frac{2\pi m_e^* k_B T}{h^2}\right)^{\frac{3}{2}} \tag{3.4}$$

$$N_V = 2\left(\frac{2\pi m_h^* k_B T}{h^2}\right)^{\frac{3}{2}} \tag{3.5}$$

where m_e^* and m_h^* stand for the effective masses of electrons and holes, respectively, h is the Planck's constant and the factor 2 is derived from the two possible spin states of the electrons [2].

For an intrinsic semiconductor at thermal equilibrium, the free electron density and the free hole density are equal, and the carrier density is:

$$n_i = \sqrt{np} = n = p = \sqrt{N_C N_V} e^{-\frac{E_G}{2k_B T}} \tag{3.6}$$

For intrinsic silicon this results in $n_i \approx 1.45 \times 10^{10}\,\mathrm{cm}^{-3}$ [2].

Silicon has a band gap of approximately 1.09 eV at room temperature, hence is a semiconductor, and thus its resistivity drops as temperature rises. The Fermi level is about halfway between the valence and conduction bands and pure silicon is effectively an insulator at room temperature. However its behavior can change with doping (Fig. 3.3) [2].

3.2 The effects of doping

An intrinsic semiconductor can be changed to an extrinsic one through the process of semiconductor doping. During this process, impurity atoms are introduced to the intrinsic semiconductor. They are atoms of a different element than the atoms of the intrinsic semiconductor and can act as either donors or acceptors to the intrinsic semiconductor, altering

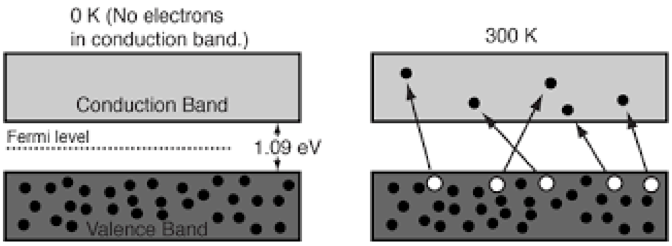

Figure 3.3: Silicon energy bands. (Image: HyperPhysics.)

its electron and hole concentrations (Fig. 3.4). The donors are elements from Group V of the periodic table which have additional electrons compared to silicon (or the respective semiconducting material), and thus they can donate electrons to the semiconductor's conduction band. This provides excess electrons to the intrinsic semiconductor, which increase the electron carrier concentration n, creating am n-type semiconductor. On the other hand, the acceptors are elements from Group III of the periodic table which have one electron less than silicon (or the respective semiconductor material), and thus they can accept electrons from the semiconductor's valence band. This provides excess holes to the intrinsic semiconductor, which increase the hole carrier concentration p, creating a p-type semiconductor. When silicon, having four valence electrons, needs to be doped as an n-type semiconductor elements like phosphorus (P), arsenic (As), antimony (Sb) and bismuth (Bi) having five valence electrons can be used, while when silicon needs to be doped as a p-type semiconductor, elements like boron (B), aluminium (Al), indium (In) and gallium (Ga) having three valence electrons, can be used (Fig. 3.4) [2], [3].

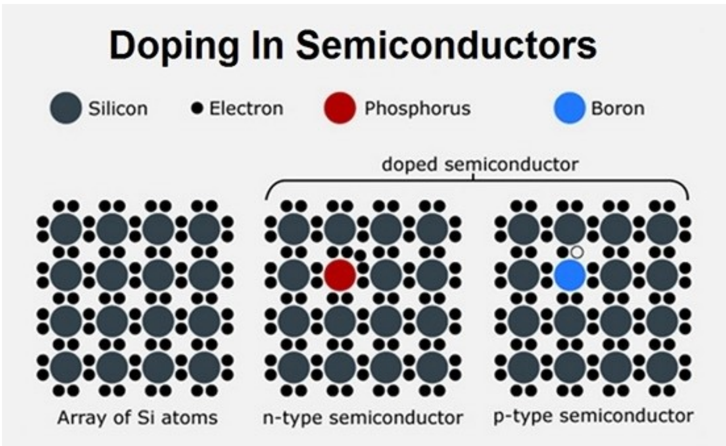

Figure 3.4: Doping in n-type and p-type semiconductors. (Image: FPGA Marketplace.)

Phosphorus diffuses fast, so is usually used for bulk doping, or for well formation. The slower diffusion of arsenic and antimony allows using them for diffused junctions, and they are also used for buried layers. Bismuth is a promising dopant for long-wavelength infrared photoconduction silicon detectors. Boron is common in Complementary MOS (CMOS) technology, since its diffusion rate allows easy control of junction depths. Aluminum is popular for deep p-diffusions. Indium and gallium are dopants used for long-wavelength infrared photoconduction silicon detectors.

Various techniques of doping are well known. For example, the synthesis of n-type semiconductors may involve the use of vapor-phase epitaxy where a gas containing the negative dopant is passed over the substrate wafer. Neutron transmutation doping (NTD) is an unusual doping method used for doping of silicon n-type in high-power electronics, and it is based on the conversion of the Si-30 isotope into phosphorus atom by neutron absorption [4].

The doping of silicon with donors increases the amount of negatively charged carriers and introduces energy states slightly below the lower conduction band edge (Fig. 3.5). The doping of silicon with acceptors increases the amount of positively charged carriers (as the missing electrons act as positive carriers) and introduces energy states slightly above the upper valence band edge (Fig. 3.5). The Fermi level E_F of a doped semiconductor is shifted towards the conduction band in an n-type material and towards the valence band in a p-type material (Fig. 3.5) [2], [3].

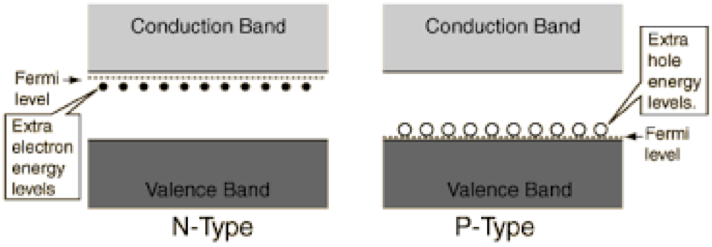

Figure 3.5: Band structures of doped n-type and p-type semiconductors. The donor state energy level slightly below the conduction band in the n-type semiconductor and the acceptor state energy level slightly above the valence band in the p-type semiconductor are indicated, respectively. (Image: HyperPhysics.)

3.3 The p-n diode

A p-n junction consists of two semiconductor regions of opposite type and shows a rectifying behavior. It is also called a p-n diode. Apart from a rectifier, it can be used as a voltage-dependent capacitor. The opposite doping types are denoted in Fig. 3.6. The region on the left is p-type with an acceptor density N_A, while the region on the right is n-type with a donor density N_D. If the dopants are considered shallow, then the electron (hole) density in the n-type (p-type) region is approximately equal to the donor (acceptor) density. During operation the diode is biased with a voltage V_a, and is considered forward-biased if a positive voltage is applied to the p-doped region or reversed-biased if a negative voltage is applied to the p-doped region. The contact to the p-type region is called an anode, while the contact to the n-type region is called a cathode. One can imagine that both semiconductor regions are brought together by aligning both the conduction and valence band energies of each region [2], [3].

At the junction, the free electrons in the n-type region are attracted to the positive holes in the p-type region. Thus, the free electrons diffuse into the p-type region, combine with the holes, and cancel each other out. In a similar manner the positive holes in the p-type region are attracted to the free electrons in the n-type region. Thus, the holes diffuse into the n-type region, combine with the free electrons, and cancel each other out. This diffusion process leaves the ionized donors/acceptors behind, creating a region around the junction, which is depleted of mobile carriers. This region is called the depletion region, extending from $x = -x_p$ to $x = x_n$. The charge due to the ionized donors and acceptors causes an electric field, which is responsible for the drift of carriers in the opposite direction. The diffusion of carriers continues until the

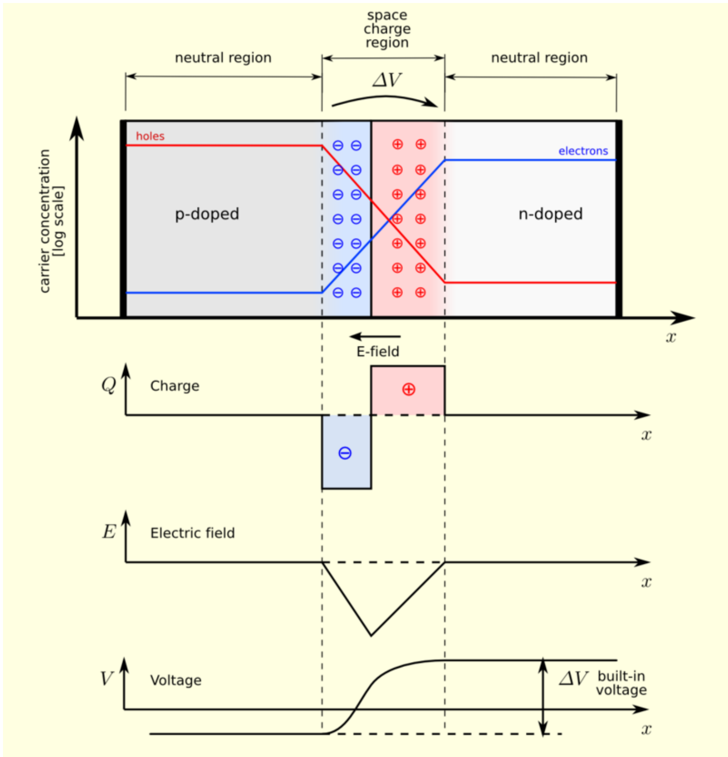

Figure 3.6: A p-n junction in thermal equilibrium with zero-bias voltage applied. Under the junction, plots for the charge density, the electric field, and the voltage are reported.

drift current balances the diffusion current. Thermal equilibrium is reached when there is a constant Fermi energy [2], [3].

The current density for holes is [2], [3]:

$$J_p = J_{p,Drift} + J_{p,Diffusion} = q\mu_p pE - qD_p \nabla p \tag{3.7}$$

where q is the elementary charge, μ_p the mobility of holes, p the number of holes per volume, E the applied electric field intensity and D_p the diffusion coefficient for holes in the considered medium. The current density for electrons is [2], [3]:

$$J_n = J_{n,Drift} + J_{n,Diffusion} = q\mu_n nE + qD_n \nabla n \tag{3.8}$$

where q is the elementary charge, μ_n the mobility of electrons, n the number of electrons per volume, E the applied electric field intensity and D_n the diffusion coefficient for electrons in the considered medium. The total current density in the p-n diode is then [2], [3]:

$$J = J_p + J_n \tag{3.9}$$

The electric field created by the diffusion process creates a built-in potential difference across the junction with an open-circuit (zero bias) potential V_{bi} of:

$$V_{bi} = V_T \ln\left(\frac{N_D N_A}{n_i}\right) \tag{3.10}$$

where V_T is the thermal voltage (26 meV) at room temperature [2], [3]. The total potential across the semiconductor equals the built-in potential minus the applied voltage [2], [3]:

$$V = V_a - V_{bi} \tag{3.11}$$

If one obtains the capacitance-voltage characteristic of the diode, one can perform the electrostatic analysis of a p-n diode (starting from Poisson's equation) and gain knowledge about its charge density and electric field in the depletion region. This analysis makes use of a full-depletion approximation which assumes that the depletion region around the metallurgical junction has well-defined edges. The sum of the two depletion layer widths in each region is the total depletion layer width x_d [2], [3]:

$$x_d = x_n + x_p \tag{3.12}$$

The charge density is constant in each region, and the charge per unit area in each region is [2], [3]:

$$Q_n = qN_D x_n \tag{3.13}$$

$$Q_p = -qN_A x_p \tag{3.14}$$

The expression for the depletion layer width is the following:

$$x_d = \sqrt{\frac{2\epsilon_s}{q}\left(\frac{1}{N_A} + \frac{1}{N_D}\right)(V_{bi} - V_a)} \tag{3.15}$$

where ϵ_s is the dielectric constant of the semiconductor. Thus, the solutions for the individual depletion layer widths, x_p and x_n can be obtained:

$$x_n = \sqrt{\frac{2\epsilon_s}{q}\frac{N_A}{N_D}\frac{1}{N_A + N_D}(V_{bi} - V_a)} \tag{3.16}$$

$$x_p = \sqrt{\frac{2\epsilon_s}{q}\frac{N_D}{N_A}\frac{1}{N_A + N_D}(V_{bi} - V_a)} \tag{3.17}$$

Any variation of the charge within a p-n diode with an applied voltage yields a capacitance, which is related to the depletion layer charge and is called a junction capacitance (C_j). A combination of the expressions used in the analysis of the full-depletion approximation yields [2], [3]:

$$C_j = \sqrt{\frac{q\epsilon_s}{2(V_{bi} - V_a)}\frac{N_A N_D}{N_A + N_D}} \tag{3.18}$$

A comparison with equation (3.15) reveals that the expression for the junction capacitance, C_j, seems to be identical to that of a parallel plate capacitor [2], [3]:

$$C_j = \frac{\epsilon_s}{x_d} \tag{3.19}$$

The resistivity ρ (the inverse of the conductivity σ) is another important parameter of a semiconductor, since it significantly affects its electrical properties. It can be expressed as [2], [3]:

$$\rho = \frac{1}{q(n\mu_n + p\mu_p)} \tag{3.20}$$

3.4 The Metal-Oxide-Semiconductor (MOS) capacitor

The metal-oxide-semiconductor (MOS) is a commonly used structure in several applications of microelectronics. The structure is obtained by growing a layer of silicon dioxide (SiO_2) on top of a silicon substrate commonly by thermal oxidation and depositing a layer of metal or polycrystalline silicon (referred to as the gate). Since the silicon dioxide is a dielectric material, its structure is equivalent to a planar capacitor, with the semiconductor playing the role of one of the electrodes. A second metal layer forms an Ohmic contact to the back of the semiconductor and is called the bulk contact. When a voltage is applied across a MOS structure, it modifies the distribution of charges in the semiconductor [2], [5].

Two techniques are commonly used for the fabrication of silicon dioxide which is usually the oxide of a MOS structure: the oxidation of the silicon yielding a thermal oxide and the deposition of SiO_2 using a chemical vapor-deposition (CVD) process. The thermal oxidation of silicon is obtained by heating silicon in an oxygen or water vapor ambient (with temperatures ranging from 800 to 1200 °C). At high temperatures, oxygen or water molecules can easily diffuse through the oxide and that way further oxidation can take place. Thermal oxidation provides a high quality interface and oxide, however it is used less these days because of the high process temperature. On the other hand, during the deposition of SiO_2 using a CVD process two gases (like silane and oxygen) react to form silicon dioxide, which then sublimes onto any solid surface. The wafers are heated to 200-400 °C yielding high quality oxides. The CVD method is preferred nowadays for the fabrication of MOS oxides due to the lower process temperature and the higher quality of the deposited layers [5].

Let's consider three regimes in a MOS structure which correspond to different regions of operation regarding the applied gate voltage: the accumulation mode below the flatband voltage V_{FB}, the depletion mode between the flatband voltage and the threshold voltage V_T, and finally the inversion mode above the threshold voltage. These modes and the charge distributions associated with each of them are shown in Fig. 3.7 [5].

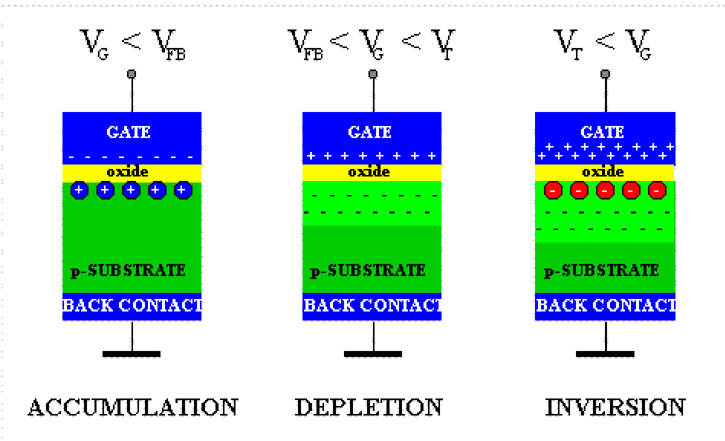

Figure 3.7: Charges in a p-type substrate Metal-Oxide-Semiconductor structure under accumulation, depletion and inversion conditions.

Accumulation occurs typically for negative voltages where the negative charge on the gate attracts holes from the substrate to the oxide-semiconductor interface, while depletion occurs for positive voltages when the positive charge on the gate pushes the mobile holes into the substrate. Therefore, the semiconductor is depleted of mobile carriers at the interface and a negative charge is left in the space charge region due to the ionized acceptor ions. Inversion takes place at voltages beyond the threshold voltage (beyond twice the bulk potential ϕ_F), where a negatively charged inversion layer exists (in addition to the depletion-layer) at the oxide-semiconductor interface due to the minority carriers that are attracted to the interface by the positive gate voltage. If one further increases the gate voltage, the depletion layer width barely will increase further since the charge in the inversion layer increases exponentially with the surface potential [5].

In the general case, the flatband voltage is given by:

$$V_{FB} = \Phi_{MS} - \frac{Q_i}{C_{ox}} - \frac{1}{\epsilon_{ox}} \int_0^{t_{ox}} \rho_{ox}(z) z dz \tag{3.21}$$

where Φ_{MS} is the difference between the gate metal work function and the semiconductor work function, Q_i is any charge that might be located at the interface between the oxide and the semiconductor, C_{ox} the oxide capacitance, ϵ_{ox} the dielectric constant of the oxide, t_{ox} the oxide thickness and $rho_{ox}(z)$ a charge density distributed within the oxide [5].

For the p-type substrate MOS capacitor the MOS parameters at threshold are usually calculated with the assumptions that a full depletion approximation is valid, that the inversion layer charge is zero below the threshold voltage and that beyond the threshold voltage the inversion layer charge changes linearly with the applied gate voltage. Then, the charge per unit area in the depletion layer Q_d is given by [5]:

$$Q_d = -qN_A x_d \tag{3.22}$$

where q is the elementary charge, N_A the acceptor density in the substrate and x_d the depletion layer width. The electric field in the semiconductor at the interface will then be [5]:

$$E_s = \frac{qN_A x_d}{\epsilon_s} \tag{3.23}$$

where ϵ_s is the dielectric constant of the semiconductor.

From the full depletion analysis it can be proven that the threshold voltage is [5]:

$$V_T = V_{FB} + 2\phi_F + \frac{\sqrt{4\epsilon_s q N_A \phi_F}}{C_{ox}} \tag{3.24}$$

Capacitance-voltage (CV) measurements of MOS capacitors can provide plenty of information about the MOS structure. There is a frequency dependence of the measurement which occurs primarily in inversion since a certain time is needed to generate the minority carriers in the inversion layer and thermal equilibrium is therefore not immediately obtained. The low frequency (LF, or quasi-static) measurement maintains thermal equilibrium at all times. The LF capacitance is the ratio of the change in charge to the change in gate voltage, measured (while the capacitor is in equilibrium) with an electrometer, which measures the charge added per unit of time as one slowly varies the applied gate voltage. The high frequency (HF) capacitance is obtained from a small-signal capacitance measurement at high frequency where the bias voltage on the gate is varied again slowly. Under such conditions, it is found that the charge in the inversion layer does not change from the equilibrium value at the applied DC voltage, and so the HF capacitance therefore describes only the charge variation in the depletion layer and the movement of the inversion layer charge. If during the measurement of the HF capacitance the gate voltage is swept quickly enough so that the structure is not in thermal equilibrium, deep depletion will occur in the MOS capacitor. It can be observed then that when ramping the voltage from flatband to threshold and beyond, the inversion layer is only partially formed or not formed at all. This happens because the generation of minority carriers cannot keep up with the amount needed to form the full inversion layer. The depletion layer therefore doesn't stop to increase, resulting in a capacitance which further decreases with voltage. Deep depletion measurements are done in the dark, as the carrier generation due to light will increase the generation rate beyond the thermal generation rate and therefore will reduce the time needed to reach equilibrium. All the above measurements are summarized in Fig. 3.8 [5].

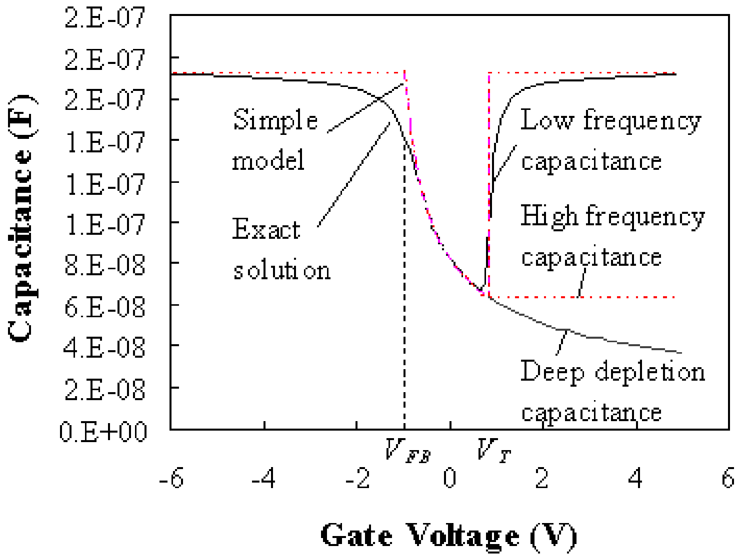

Figure 3.8: Low frequency capacitance of a p-type body MOS capacitor. Shown are the exact solution for the low frequency capacitance (solid line) and the low and high frequency capacitance obtained with the simple model (dotted lines). $N_A = 10^{17}\,\mathrm{cm}^{-3}$ and $t_{ox} = 20\,\mathrm{nm}$.

The simple model predicts that the flatband capacitance equals the oxide capacitance, but the comparison with the exact solution of the low frequency capacitance reveals that the error can be substantial. This occurs because charge variation in the semiconductor should be included in the model. The exact flatband capacitance when calculated by using the linearized Poisson's equation is the following [5]:

$$C_{FB} = \frac{1}{\frac{1}{C_{ox}} + \frac{L_D}{\epsilon_s}} \tag{3.25}$$

where L_D is the Debye length:

$$L_D = \sqrt{\frac{\epsilon_s V_T}{q N_A}} \tag{3.26}$$

By performing a capacitance-voltage measurement one can identify several types of non-ideal effects in MOS capacitors: fixed charge, mobile charge and charge in surface states. Fixed charge in the oxide shifts the measured curve, and more specifically positive fixed charge at the oxide-semiconductor interface will shift the flatband voltage by an amount, which equals the charge divided by the oxide capacitance. A fixed charge is caused by ions incorporated in the oxide during growth or deposition. In the case of mobile charge, the flatband voltage shift is similar to the fixed charge case. However, the measured curves differ since a positive gate voltage causes any negative mobile charge to move away from the gate electrode, while a negative voltage attracts the charge towards the gate, and this phenomenon causes the curve to shift towards the applied voltage. Mobile charge can be recognized by the hysteresis in the high frequency capacitance curve when sweeping the gate voltage back and forth [5].

Charge due to electrons occupying surface states also causes a shift in flatband voltage, with the difference that as the applied voltage is varied, the Fermi energy at the oxide-semiconductor interface also changes, thus affecting the occupancy of the surface states. The transition in the capacitance measurement is less abrupt thanks to the interface states. The surface state density over a limited range of energies within the band gap can be calculated from the combination of the low frequency and high frequency capacitance. Measurements on n-type and p-type capacitors at various temperatures provide the surface state density throughout the band gap [5].

3.5 Particle-matter interaction, radiation damage and the NIEL hypothesis

The beam particles and secondary particles which are products of interaction or decay will interact with the detector material. According to the particle type and energy, penetrating particles will be subject to different atomic and nuclear processes. When particles like protons with high energies of the order of GeV impact on a material, they are subject to inelastic nuclear collisions, producing a number of fast secondary hadrons like protons, neutrons and charged pions. Some of them can have further nuclear collisions, resulting in a hadronic cascade, while others such as neutral pions will decay almost instantly and their decay products can initiate electromagnetic showers, which are sustained by electron-positron pair production by photons and Bremsstrahlung losses of electrons and positrons. As the particle energy decreases, other processes like the Compton scattering of photons, the photoelectric effect and the ionization losses of charged particles become dominant. Some of the charged pions (and other hadrons) will also decay and produce muons. Nuclear collisions also give rise to neutrons, protons, light ions (alpha particles) and gamma rays, which are emitted during the de-excitation of target nuclei, with lower energies of the order of MeV. While the protons and light ions will mainly range out because of ionizing losses, the neutrons can be very penetrating. Neutrons will mainly undergo elastic nuclear collisions until they thermalize and are finally captured. Eventually, the residual nuclei of elastic and inelastic collisions can also recoil and impart their energy on neighbouring nuclei through Coulomb interactions [6].

The mean rate of energy loss by moderately relativistic charged heavy particles in the region $0.1 \lesssim \beta\gamma \lesssim 1000$ for intermediate-Z materials with an accuracy of a few percent is well-described by the Bethe formula [7]:

$$\left\langle -\frac{dE}{dx} \right\rangle = Kz^2 \frac{Z}{A} \frac{1}{\beta^2} \left[\frac{1}{2} \ln \left(\frac{2m_e c^2 \beta^2 \gamma^2 W_{max}}{I^2} \right) - \beta^2 - \frac{\delta(\beta\gamma)}{2} \right] \tag{3.27}$$

where $K = 0.307075$ MeV mol^{-1} cm^2, z is the charge number of incident particle, Z is the atomic number of the absorber, A is the atomic mass of absorbe in g mol^{-1}, β and γ are the relativistic kinematic variables, m_e is the electron mass, c is the speed of light, I is the mean excitation energy in eV, $\delta(\beta\gamma)$ is the density effect correction to ionization energy loss and W is the energy transfer to an electron in a single collision in MeV. This is the mass stopping power and its units are MeV g^{-1} cm^2. (For heavy projectiles, such as ions, additional terms are required to account for higher-order photon coupling to the target, and to account for the finite target radius.) As can be seen from Fig. 3.9, $\left\langle -\frac{dE}{dx} \right\rangle$ defined in this way is about the same for most materials, decreasing slowly with Z. W_{max} is defined as follows [7]:

$$W_{max} = \frac{2m_e c^2 \beta^2 \gamma^2}{1 + 2\gamma \frac{m_e}{M} + \left(\frac{m_e}{M}\right)^2} \tag{3.28}$$

where M is the mass of the particle. At the lower limit the projectile velocity becomes comparable to atomic electron velocities and at the upper limit radiative effects begin to be important, but in any case both limits are Z dependent. A minor dependence on M at the highest energies is introduced through W_{max}, but for all practical purposes $\left\langle -\frac{dE}{dx} \right\rangle$ in a given material is a function of β alone [7].

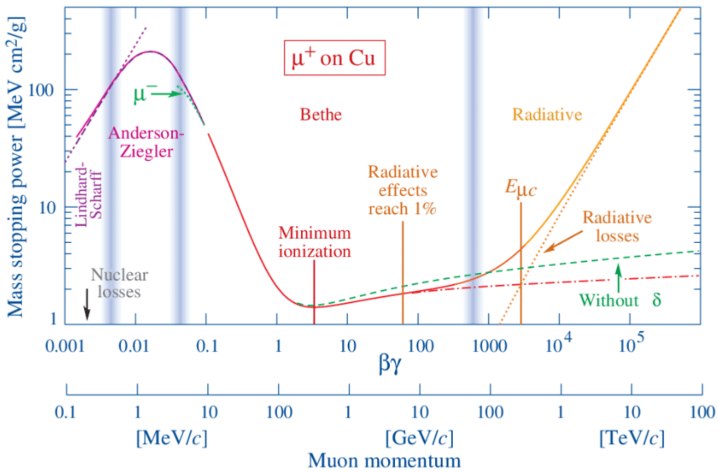

Figure 3.9: Mass stopping power (= $\langle -dE/dx \rangle$) for positive muons in copper as a function of $\beta\gamma = p/Mc$ over nine orders of magnitude in momentum (12 orders of magnitude in kinetic energy). Solid curves indicate the total stopping power. Vertical bands indicate boundaries between different approximations. The short dotted lines labeled "μ^-" illustrate the "Barkas effect", the dependence of stopping power on projectile charge at very low energies. dE/dx in the radiative region is not simply a function of β.

The stopping power function as computed for muons on copper is shown as the Bethe region of Fig. 3.9. Only in the Bethe region is it a function of β alone and the mass dependence is more complicated elsewhere. In other materials, except in hydrogen, particles with the same velocity have similar rates of energy loss in different materials, although there is a slow decrease in the rate of energy loss with increasing Z. The qualitative behavior difference at high energies between a gas and other materials is due to the density-effect correction $\delta(\beta\gamma)$. The stopping power functions are characterized by broad minima whose position drops from $\beta\gamma = 3.5$ to 3.0 as Z goes from 7 to 100. In practical cases, most relativistic particles (like cosmic-ray muons) have mean energy loss rates close to the minimum. For that reason they are known as minimum-ionizing particles (MIPs) [7].

By integrating Eq. 3.27 the total continuous slowing-down approximation (CSDA) range R for a particle which loses energy only through ionization and atomic excitation, can be found. Since dE/dx depends only on β, R/M is a function of E/M or pc/M. Range is a useful concept solely for low-energy hadrons ($R \lesssim \lambda_I$, where λ_I is the nuclear interaction length), and for muons below a few hundred GeV above which radiative effects dominate. The mass scaling of dE/dx and range is valid for the electronic losses described by the Bethe formula, but not for radiative losses, which are relevant only for muons and pions [7].

Electrons and positrons of low energies primarily lose energy by ionization, although Møller scattering, Bhabha scattering, e^+ annihilation and other processes contribute too (Fig. 3.10). Ionization loss rates rise logarithmically with energy, contrary to bremsstrahlung losses which rise nearly linearly (fractional loss is nearly independent of energy). For electrons, large energy transfers to free atomic electrons are described by the Møller cross section. For photons, at low energies the photoelectric effect dominates, although Compton scattering, Rayleigh scattering, and photonuclear absorption also contribute. The photoelectric cross section is characterized by discontinuities (absorption edges) as thresholds for photoionization of various atomic levels are reached [7].

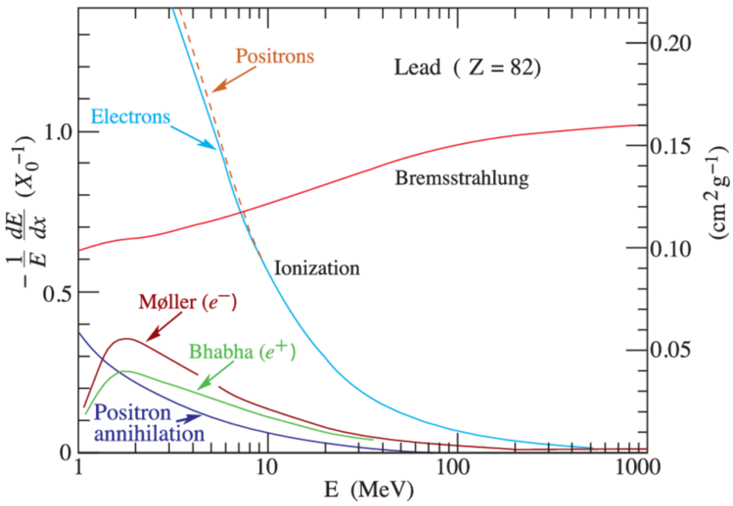

Figure 3.10: Fractional energy loss per radiation length in lead as a function of electron or positron energy. Electron (positron) scattering is considered as ionization when the energy loss per collision is below 0.255 MeV, and as Møller (Bhabha) scattering when it is above.

Both charged and uncharged high-energy particles can interact with the nuclei of the material that they are traversing. For silicon, even an interaction energy of a few tens of eV is enough to displace a lattice atom, while if the initial particle energy and the energy of the recoiled atom are high enough, several displacements can take place. In general, a displacement of a lattice atom occurs when the energy transferred to it is larger than the energy binding the atom in its lattice site. Low recoil energies generate single point defects, while energies of the order of a few keV can produce clusters of defects. The most commonly met lattice defects are vacancies, interstitials, Frenkel pairs and impurity atoms (Fig. 3.11). A vacancy is a vacant lattice site. An interstitial atom is an additional atom in a crystal structure that is closely packed into a void between normal lattice sites. A Frenkel pair is a neighboring pair of defects composed of a vacancy and an interstitial. An impurity is an atom other than the host atom and is not related to radiation damage [8], [9].

Forms of radiation damage in silicon can be classified as bulk-related or surface-related. A big amount of observations has led to the conclusion that damage effects by energetic particles in the bulk of any material can be described as being proportional to the displacement damage cross section D, which is quantified in MeV mb. D is equivalent to the non-ionizing energy loss (NIEL), quantified in keV cm^2/g. The proportionality between the NIEL-value and the resulting

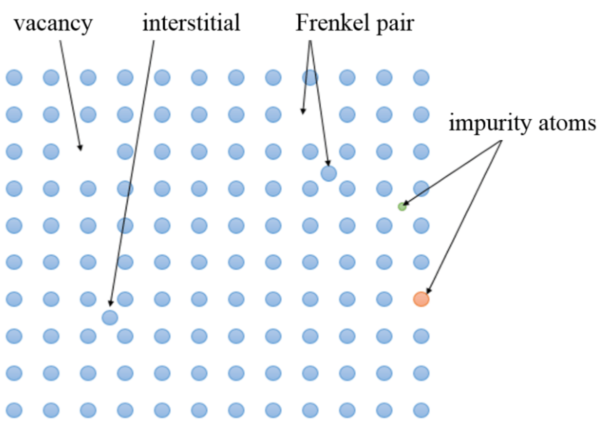

Figure 3.11: Point defects in a crystal lattice; schematic representation of a vacancy, an interstitial, a Frenkel pair and impurity atoms.

damage effects is referred to as the NIEL-scaling hypothesis. For silicon with A = 28.086 g/mol the relation between D and NIEL is the following: 100 MeV mb = 2.144 keV cm^2/g. The D or NIEL value is depending on the particle type and energy, and usually the displacement damage cross section for 1 MeV neutrons is set as a normalizing value: $D_{1\,\mathrm{MeV\,n}}$ = 95 MeV mb. Thus, if one follows the NIEL hypothesis, the damage efficiency of any particle with a given kinetic energy E can be described by a hardness factor k, defined as $k_{particle}(E) = D_{particle}/D_{1\,\mathrm{MeV\,n}}$. The normalized displacement damage function $D(E)$ for different particles is shown in Fig. 3.12. The NIEL-value can also be referred to as the displacement-Kinetic Energy Released to MAtter (KERMA). KERMA is responsible for displacements of atoms in the crystal lattice, which are causing the bulk-related damage effects. In contrast to the displacement KERMA, the pure ionization losses are monitored by the radiation dose and are considered responsible for the surface-related damage effects. The two quantities are not proportional to each other and clearly distinct from one another [10].

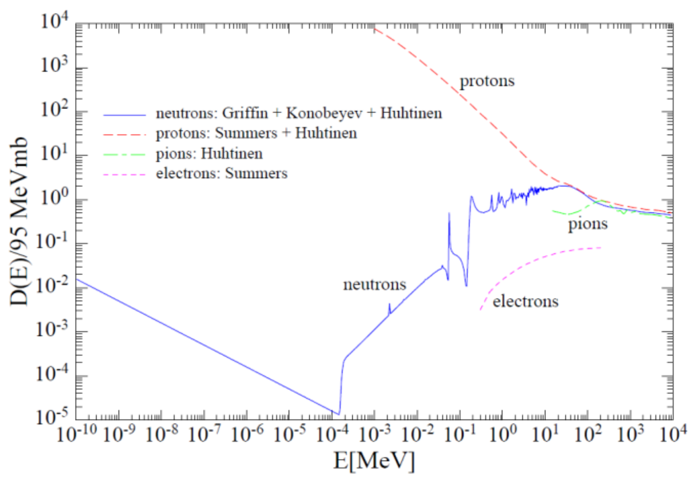

Figure 3.12: Displacement damage function $D(E)$ normalized to 95 MeV mb for various particles.

It has been found out by the ROSE Collaboration that the NIEL scaling does not hold ideally for charged hadrons. Radiation hardened silicon by the Diffusion Oxygenated Float Zone (DOFZ) process shows appreciably less damage caused by high energy protons or pions than that due to neutrons if normalized to the NIEL equivalent fluence. The NIEL hypothesis breaks down even worse in the damage produced by electrons. For hadron irradiation mostly displacement clusters are formed via nuclear interaction leading to a high generation current, whereas this is not valid for electron irradiation. Furthermore, the Coulomb interaction, responsible solely for the energy transfer by electrons, leads to much lower Si recoil energies which has as consequence the formation of more close pairs being formed among the primary Frenkel defects, which will recombine to a large extent and will not produce any permanent damage [10], [11].

It can be proven that the point defects can capture and emit electrons or holes and can increase the volume-generated leakage current. There is a linear parameterization between current I_{vol} in a volume V and fluence Φ:

$$\frac{\Delta I_{vol}}{V} = \alpha\Phi \tag{3.29}$$

where α is a leakage current damage parameter [11].

The so-called Perugia model was one of the first attempts to build an overall radiation damage model for silicon. It combines an extended surface damage model for silicon by introducing parameters extracted from experimental measurements carried out on p-type substrate test structures after gamma irradiations at doses in the range a few hundreds Mrad, combined with an extended bulk model, by considering impact ionization and deep-level cross-sections variation. The model has been validated through the comparison of the simulation results with experimental measurements carried out at very high fluences. The behavior of silicon is described by parameterizing the impact of bulk damage which causes donor-type deep-levels acting as generation/recombination centers and/or trap states, and the impact of surface damage which introduces oxide charges and interface traps. The Perugia model is a three-level model and is able to reproduce the radiation damage macroscopic effects up to fluences of the order of 10^{15} n/cm^2 1 MeV equivalent neutrons [12].

An interesting feature of silicon (and similar materials) is the annealing - the diminishing of the effects of radiation over time. This can be partly explained by the recombination of vacancies and interstitials. After a period of several weeks or months at room temperature, reverse annealing might take place, due to the conversion of radiation induced electrically inactive defects into electrically active ones. Both annealing and reverse annealing are strongly dependent on temperature [13].

3.6 Silicon sensors as particle detectors

Semiconductor detectors are devices that use a semiconductor, usually silicon or germanium, to measure the effect of incident charged particles or photons. Silicon is a suitable material due to its existence in abundance in nature, optimal energy band gap, possibility to alter the gap properties by adding certain dopants and the existence of a natural oxide.

Semiconductor detectors find broad application in the fields of radiation protection, gamma and X-ray spectrometry, and as particle detectors (in the case of experiments like CMS and ATLAS). In this type of detectors, ionizing radiation is measured by the number of electrons and holes set free by the radiation in the detector material which is located between two electrodes. The number of electron-hole pairs is proportional to the energy of the radiation stored in the volume of the semiconductor. During the electron-hole pair production, a number of electrons are transferred from the valence band to the conduction band, and an equal number of holes are created in the valence band. Under the influence of an electric field, electrons and holes travel to the electrodes of the device. There they generate a pulse that can be measured in an outer circuit, as described by the Shockley-Ramo theorem which allows one to easily calculate the instantaneous electric current induced by a charge moving in the vicinity of an electrode. The Shockley-Ramo theorem is based on the concept that current induced in the electrode is due to the instantaneous change of electrostatic flux lines which end on the electrode. It states that the instantaneous current i induced on a given electrode due to the motion of a charge is given by [14]:

$$i = qvE_v \tag{3.30}$$

where q is the charge of the particle, v is its instantaneous velocity, and E_v is the component of the electric field in the direction of v at the charge's instantaneous position, under the conditions that charge is removed, the given electrode is raised to unit potential, and all other conductors are grounded. The intensity of the incident particles can be determined by measuring the number of electron-hole pairs, since the amount of energy required to create a single electron-hole pair is known and does not depend on the energy of the incident particles [15].

The energy required to generate electron-hole pairs in a semiconductor detector is significantly lower than the energy required to produce paired ions in a gas detector. Thus, semiconductor detectors have a smaller statistical variation of the pulse height, higher energy resolution and better time resolution, since electrons travel fast. Semiconductor detectors have also considerably high density compared to gaseous ionization detectors. That's why charged particles of high energy can emit their energy in a semiconductor of relatively small dimensions. Especially silicon detectors have a much higher resolution in tracking charged particles compared to cloud chambers or wire chambers. However, silicon detectors are much more expensive than these older technologies and in order to reduce leakage currents which produce noise, a more sophisticated cooling is required for them [14].

Despite the fact that silicon detectors suffer degradation over time due to radiation, this can be greatly reduced due to the Lazarus effect, described as follows: In harsh radiation environments, defects begin to appear in the crystal lattice of the semiconductor detectors as atoms become displaced because of the interaction with the highly energetic particles that traverse its volume. These defects are lattice vacancies and atoms at interstitial sites, and may temporarily trap the electrons and holes which are created when ionizing particles pass through the detector. When large amounts of defects are produced, the detector signal can be importantly reduced leading to an unusable detector. At room temperature, electrons or holes will be emitted back to the conduction band or valence band in a time that is typically longer than the readout time of the connected electronics. At cryogenic temperatures, however, the trapped electron or hole remains in this state for a long time due to the very low thermal energy of the lattice. Thus, a significant fraction of traps will become filled and therefore inactive. Further trapping of electrons and holes generated by particles traversing the detector is then obstructed and little signal is lost [16].

Even for a fully depleted sensor bulk volume, sources of statistical electron and hole fluctuations, called noise, are always present. The noise completes with the signal arising from traversing ionizing particles, with a strong dependence on the peaking time t_p and operating temperature T. As signal-to-noise ratio (SNR) is considered a figure of merit of a detector, noise must be minimized while signal can only be increased by increasing the sensor thickness. Noise is generally expressed as Equivalent Noise Charge (ENC), representing the number of electrons contributing to the noise, while the various noise contributing elements (due to load capacitance

C_d, leakage current I_L, parallel and series resistances R_P and R_S, respectively (). The different contributions sum up quadratically (Fig. 3.13) [14]:

$$ENC = \sqrt{ENC_{C_d}^2 + ENC_{I_L}^2 + ENC_{R_P}^2 + ENC_{R_S}^2} \tag{3.31}$$

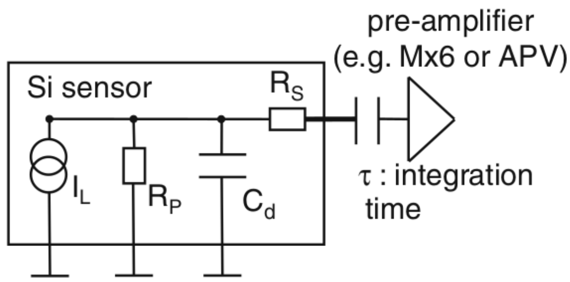

Figure 3.13: A simplified equivalent network of a sensor together with its preamplifier. The main noise sources leakage current I_L, parallel and series resistance R_P, R_S and load capacitance C_d are shown.

For detectors of moderate thickness x the energy loss (Δ) probability distribution $f(\Delta, \beta\gamma, x)$ for traversing ionizing particles is adequately described by the highly-skewed Landau (or Landau-Vavilov) distribution. The most probable energy loss is then [7]:

$$\Delta_p = \xi \left[\ln\left(\frac{2mc^2\beta^2\gamma^2}{I} \right) + \ln\left(\frac{\xi}{I} \right) + j - \beta^2 - \delta(\beta\gamma) \right] \tag{3.32}$$

where $\xi = (K/2)\langle Z/A\rangle z^2(x/\beta^2)$ and $j = 0.2$. While dE/dx is independent of thickness, Δ_p/x scales as $a\ln(x) + b$. The density correction $\delta(\beta\gamma)$ was not included in Landau's or Vavilov's work, but it was later included by Hans Bichsel [7].

The distribution function for the energy deposit by a 10 GeV muon going through a detector of about this thickness is shown in Fig. 3.14, where M_0 is the mean number of collisions in δx and M_1 is the mean energy loss in δx. In this case the most probable energy loss is 62% of the mean ($M_1(\langle\Delta\rangle)/M_1(\infty)$). 90% of the collisions ($M_1(\langle\Delta\rangle)/M_1(\infty)$) contribute to energy deposits below the mean value, and the very rare high-energy-transfer collisions, extending to several GeV, are those that drive the mean into the tail of the distribution. The large weight of these rare events makes the mean of an experimental distribution consisting of a few hundred events subject to large fluctuations and sensitive to cuts. Thus, the mean of the energy loss given by the Bethe equation is ill-defined experimentally and is practically useless for describing energy loss by single particles. That's why the most probable energy loss should be used instead [7].

3.7 Silicon strip and pixel sensors

The simplest way to make a silicon sensor capable of measuring the position of charged particles that traverse its volume is by dividing its large-area diode into many small strip or pixel-like regions. Then, the position of passage of the ionizing particle is given by the location of the strip or pixel showing the signal. The measurement precision depends mainly on the strip (pixel) spacing and the method of readout. In the strip sensors, strips usually extend along the

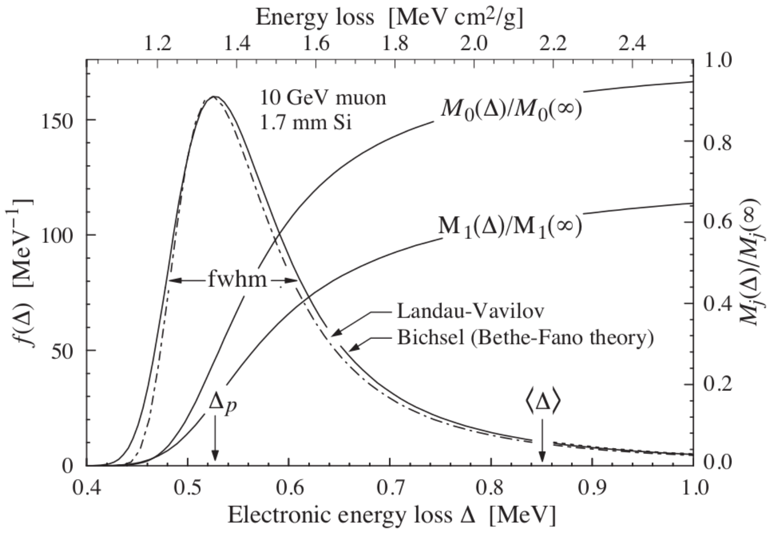

Figure 3.14: Electronic energy deposit distribution for a 10 GeV muon traversing 1.7 mm of silicon, the stopping power equivalent of about 0.3 cm of PVT-based scintillator. The Landau-Vavilov function (dot-dashed) uses a Rutherford cross section without atomic binding corrections but with a kinetic energy transfer limit of W_{max}. The solid curve was calculated using Bethe-Fano theory. $M_0(\Delta)$ and $M_1(\Delta)$ are the cumulative 0th moment (mean number of collisions) and 1st moment (mean energy loss) in crossing the silicon. Δ_p is the most probable energy loss, and $\langle\Delta\rangle$ divided by the thickness is the Bethe $\langle dE/dx\rangle$.

full length of the sensor, or have a length equal to half the sensor length, therefore providing one-dimensional information on the location of a hit on the sensor. The width of a strip is of the order of tens of microns, while the pitch between strips can be from tens of microns up to several hundreds of microns. Pixel sensors, on the other hand, provide two-dimensional spatial resolution, due to the fact that the pixel size in each direction is of the order of tens of microns or hundreds of microns, and thus the sizes in the two directions are comparable with each other. Every single pixel is read out by a separate amplifier, and the number of readout channels becomes significantly higher compared to the strip sensors [14], [17]

In a strip sensor, whenever only digital information is used, the center position of a strip is taken as the measured coordinate, and the effects arising from track inclination and charge diffusion during collection can be neglected. The spatial resolution x is given by the strip pitch p (where typical strip pitches are twenty to few hundred micrometers) as [17]:

$$x = \frac{p}{\sqrt{12}} \tag{3.33}$$

These conditions apply to the sensors of the CMS OT as well.

Digital readout may be used if no energy information is required and if the position accuracy given by the strip pitch is sufficient. Position resolution is not lost compared to analog readout if the strip pitch is large with respect to the width of the diffusion cloud. The measurement precision is substantially improved with analog readout if the strip pitch is chosen small enough so that the signal charge caused by diffusion is collected on more than one strip and the coordinate is found by interpolation. Furthermore, the simultaneous measurement of energy loss becomes possible. Finally, a third method called charge division readout reduces the number of readout channels as only a fraction of the strips is connected to a readout amplifier. Charge collected at the other (interpolation) strips is divided between the two neighboring readout channels according to the relative position, and this can be accomplished by resistive or capacitive division [17].

Fig. 3.15 shows the baseline of a CMS microstrip sensor at the LHC in 2008, developed at KIT. In general, the term n-in-p refers to a p-doped bulk with n+ doped strip implants, while the term p-in-n refers to an n-doped bulk with p+ doped strip implants, where the + symbol indicates a higher doping concentration. Passivation is a step to protect the sensor from the environment, consisting most of the times of a crude form of SiO_2 sputtered on the sensor or a film of polyimide. Passivation openings are created during the sensor production at given positions to be potentially used for probing or to wire-bond the sensor. The strips are surrounded by a bias ring and connected to it by small polysilicon resistors shaped as meanders. Resistors are used to electrically isolate the strips from each other and to protect each strip from high currents. The bias ring runs around the whole active area of the sensor to ensure a homogeneous potential for all strips. The surrounding guard ring shapes the field inside the sensitive area to minimize edge effects and to guarantee a defined homogeneous potential for all strips, including the edge ones. Both guard and bias rings are Al structures located on top of the implants they are directly contacting. The backside of the sensor connects the bulk to a terminal thanks to a conducting aluminum coating. In general, the bias ring and backplane are the main contacts to apply the bias voltage. The active volume where traversing charged particles can produce signal is formed between the strips, the bias ring and the backside. Usually, ion implantation is utilized between the bulk and the aluminum on the backplane to obstruct the formation of a Schottky contact, which is a potential energy barrier for electrons formed at a metal-semiconductor junction. A highly doped implant can minimize that barrier [14].

It is known that a small current still flows through a reverse biased pn diode, and in a full sensor, in each strip such a small DC current of the order of nA can be measured. When the sensor is severely irradiated this reverse bias current can reach the order of μA per strip. For bias voltages V_b less than or equal to the full depletion voltage V_{FD} (absolute value), it is known for the leakage current I_{leak} that $I_{leak} \propto \sqrt{V_b}$. For higher absolute values of the bias voltage, above the full depletion voltage, the current saturates when there is no breakdown. The amplifiers in the readout chips are usually protected from this current through the incorporation of current compensation circuits which remove the DC fraction of the current and allow only the AC signals to reach the amplifier. When the strips are covered with an aluminum electrode above the thin layer of oxide which covers the strip implant (with the full structure operating as capacitor), the DC currents can be filtered out during operation while the AC fraction of the signal is coupled to the electrode connected to the readout chip amplifiers. In such AC-coupled sensors DC pads and AC pads are used as contact pads for qualification purposes (Fig. 3.15). DC pads are used to contact the implant of the strip for electrical tests. AC pads are used to contact the readout metallization of the strip in order to connect each strip to the the readout chip. When an ionizing particle passes through the AC-coupled microstrip detector, the collected charge by the strips is read out capacitively (Fig. 3.16). After intense irradiation, a degeneration of the interstrip resistance is observed, which is caused by the positively charged defects in the oxide which start to attract electrons that will accumulate at the silicon-oxide interface [14], [17].

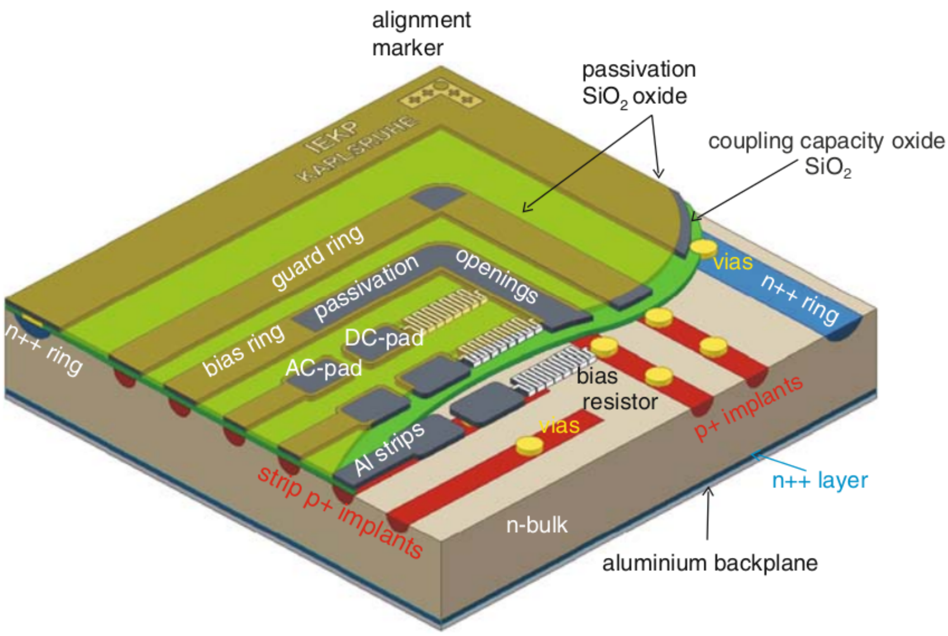

Figure 3.15: A 3D schematic which shows the baseline of the CMS sensor at the LHC in 2008, but could represent basically any single-sided AC-coupled, R_{poly} biased sensor. In operation, the bias ring is connected to GND potential, which is then distributed to the p+ implant strips, while the Al backplane is set to positive high voltage depleting the full n-bulk volume by forming a pn-junction p+ strip to n-bulk. The coupling capacitor is defined between aluminum strip and p+ implant, the interstrip capacity between neighboring strips (both p+ and Al part). The guard ring shapes the field at the borders. The n++ ring defines the volume and prevents high field in the real cut edge regions.

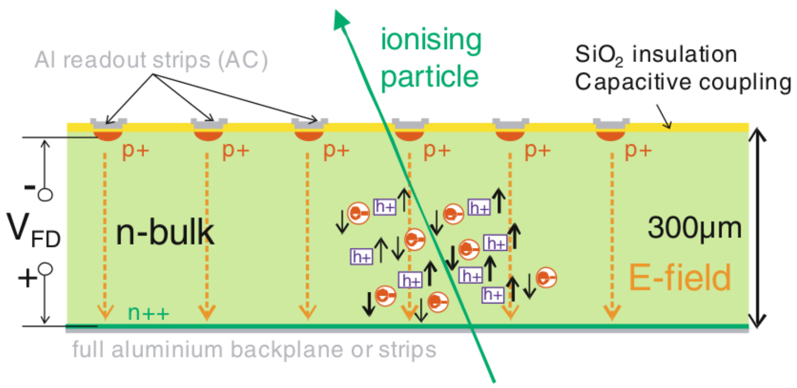

Figure 3.16: Working principle of an AC-coupled silicon microstrip detector under voltage bias equal to the full depletion voltage V_{FD}. Electron-hole pairs resulting from the ionization of the crossing charged particle, according to the Bethe equation, travel to the electrodes on the sensor planes. The segmentation in the pn-junctions allows to collect the charges on a small number of strips, where they capacitively couple to the Al readout strips. These are then connected to the readout electronics, where the intrinsic signal is shaped and amplified. In the case of segmented p-strip implants in an n-bulk silicon material, holes are collected at the p+ strips.

Bibliography

[1] *Silicon*, Encyclopædia Britannica. Retrieved 22 June 2020.

[2] Safa O. Kasap, *Principles of Electronic Materials and Devices*, McGraw-Hill Higher Education, 2017.

[3] S.M. Sze, Kwok K. Ng, *Physics of Semiconductor Devices*, Third Edition, John Wiley & Sons, 2007.

[4] Schmidt, P. E. and Vedde, J., *High Resistivity NTD Production and Applications*, Electrochemical Society Proceedings (1998), 98-13. p. 3.

[5] Bart V. Van Zeghbroeck, *Principles Of Semiconductor Devices And Heterojunctions*, Prentice Hall, December 1st 2009.

[6] A. Lechner, *Particle Interactions with Matter*, Proceedings of the CAS-CERN Accelerator School: Beam Injection, Extraction and Transfer, Erice, Italy, 10-19 March 2017, edited by B. Holzer, CERN Yellow Reports: School Proceedings, Vol. 5/2018, CERN-2018-008-SP (CERN, Geneva, 2018).

[7] M. Tanabashi et al. (Particle Data Group), *Review of Particle Physics*, Phys. Rev. D 98, 030001 - Published 17 August 2018.

[8] Slavica Grdanovska, *CHARACTERIZATION OF RADIATION DAMAGE TO A NOVEL PHOTONIC CRYSTAL SENSOR*, Dissertation submitted to the Faculty of the Graduate School of the University of Maryland, College Park, 2015.

[9] M. Moll, *Displacement Damage in Silicon Detectors for High Energy Physics*, in IEEE Transactions on Nuclear Science, vol. 65, no. 8, pp. 1561-1582, Aug. 2018, doi: 10.1109/TNS.2018.2819506.

[10] A. Vasilescu and G. Lindström, *Displacement Damage in Silicon*, [online]: https://rd50.web.cern.ch/ .

[11] ROSE Collaboration, *3rd RD48 status report: the ROSE collaboration (R & D on silicon for future experiments)*, CERN-LHCC-2000-009.

[12] F. Moscatelli et al., *Combined Bulk and Surface Radiation Damage Effects at Very High Fluences in Silicon Detectors: Measurements and TCAD Simulations*, IEEE Trans.Nucl.Sci. 63 (2016) 2716-2723.

[13] T. Schulz et al., *Long term reverse annealing in silicon detectors*, IEEE Trans.Nucl.Sci. 41 (1994) 4, 791-795.

[14] Frank Hartmann, *Evolution of Silicon Sensor Technology in Particle Physics*, Springer Tracts Mod.Phys. 275 (2017).

[15] Zhong He, *Review of the Shockley-Ramo theorem and its application in semiconductor gamma-ray detectors*, Nuclear Instruments and Methods in Physics Research A 463 (2001) 250-267.

[16] Vittorio Giulio Palmieri et al., *Evidence for charge collection efficiency recovery in heavily irradiated silicon detectors operated at cryogenic temperatures*, Nuclear Instruments and Methods in Physics Research Section A: Accelerators, Spectrometers, Detectors and Associated Equipment, 413 (2-3), pp. 475-478.

[17] G. Lutz, *Semiconductor Radiation Detectors: Device Physics*, ed. Springer, 1999.

Chapter 4

Characterization of silicon test structures

This chapter gives an insight of the characterization (electrical characterization and climate tests) and irradiation (with a cobalt-60 source) activities of the CMS NCSR "Demokritos" group.

4.1 Research and development of silicon sensors for the upgraded OT

The members of the Detector Instrumentation Laboratory (DIL) at the Institute of Nuclear and Particle Physics (INPP), NCSR "Demokritos" have been actively working in the last years on the CMS Outer Tracker (OT) Sensor Working Group (WG) activities. The OT Sensor Working Group consists of members from various institutes in Europe, North America and Asia. Its tasks are related to the R&D through characterization methods for the optimization of the sensor devices which will be integrated in the upgraded CMS OT. For a period longer than 10 years, the WG had to take important decision on the sensor material, design and manufacturer(s).

The AC coupled strip sensors and related test structures used in the studies of the OT Sensor WG are processed by a single vendor, Hamamatsu Photonics Kabushiki-kaisha (HPK) [1], on several wafer types. Each wafer contains a 2S sensor in its center, which is surrounded by test structures, organized in the halfmoons of the wafer, that provide quick and easy access to critical process parameters. Despite the fact that other vendors were considered too in the beginning of the R&D phase, the characterization process showed that their sensors didn't fulfill the specifications set by CMS. During the past years, the sensor researchers had to figure out which are the best strip length, strip width, strip pitch, strip metal width, number of strips per sensor, number of guard rings, overall dimensions, coupling dielectric thickness and peak value of the strip doping concentration. The sensor types which were examined were n-in-p (highly n-doped strips in p-doped bulk), sensors with p-stop or p-spray strip isolation, as well as p-in-n sensors. (Sensors of n-in-n type were not considered as the associated costs were expected to be much higher and the required double-sided process is more prone to damage of the sensitive backside.) Different thicknesses and wafer types were studied, like the thinned wafers made from float-zone silicon (FZ) with a physical and active thickness of 200 μm and deep-diffused FZ wafers (ddFZ) with a physical thickness of 320 μm and a nominal active thickness of 300 μm or 200 μm. The active thickness (low doping concentration) for these ddFZ wafers was reduced from the physical thickness of 320 μm by a long-term thermal treatment allowing the high backside doping to diffuse deep into the bulk. Thin sensors were taken into consideration due to the demand to reduce the material of the tracker (less conversions and multiple-scattering), and since they have a higher average electric field at the maximum operation voltage of 600 V compared to thicker sensors and therefore reduce the drift time (and trapping probability after irradiation). Complementary irradiation studies with neutrons, protons and charged pions were performed, supplemented by electrical characterization (total leakage current, total capacitance, strip leakage currents, coupling capacitance, current through the dielectric, bias resistance, interstrip capacitance and interstrip resistance measurements), charge collection and noise occupancy measurements, before and after irradiation, as well as by simulations of the electric field [2].

After an extensive irradiation and characterization campaign, during which the performance of the various sensors was compared, it was concluded in 2017 that n-in-p type sensors are the most appropriate choice for operation in the CMS outer tracker region at HL-LHC. This was supported by the fact that strip isolation of n-in-p sensors can be well controlled. In addition, sensors with n-type readout strips mainly collecting electrons provide equivalent or higher signals after irradiations beyond $5 \times 10^{14}\,n_{eq}/cm^2$ than achieved for p-in-n sensors for equal thickness and bias voltage. Furthermore, the investigated p-in-n type sensors show non-Gaussian noise effects after irradiation related to high electric fields, while n-in-p type sensors do not [2].

The decision for the Phase-2 CMS OT sensor thickness was another milestone of the OT Sensor WG activities, that took place in 2019. Thin ($<300\,\mu m$ active thickness) sensors are in general expected to provide better performance (wrt. the SNR) at high fluences, as the higher fields at same voltage reduce trapping. The deep diffused float zone (ddFZ) sensor was the most promising candidate introduced by HPK due to its fixed physical thickness but selectable active thickness at reasonable costs. A further low-cost option was the thinned sensor (thFZ), again available for production by HPK. Thus, the two final options left were the the HPK Standard FZ (FZ290, with an active thickness of 290 µm) and the thinned FZ (thFZ240, with an active thickness of 240 µm). The FZ290 sensor is produced in the same way as the currently used OT sensors (but in n-in-p version) and has a fixed physical thickness of 320 µm. The 30 µm deep backside implant provides robustness against mechanical damage and works as a field stop (which improves the IV characteristics). On the other hand, the thinned thFZ240 sensor is based on the same wafer material, but is thinned after front side processing. The backside implant can only be 1 µm thick and the more complicated production would come along with a slightly increased cost.

The irradiation and characterization campaign of HPK sensors (the so-called HPK Campaign) showed that the FZ290 sensors provides sufficient SNR at the standard operation voltage of 600 V and the expected maximum fluence after $3000\,fb^{-1}$. If operation of the detector is required beyond $4000\,fb^{-1}$, an increase to an operation voltage of 800 V would allow FZ290 to survive even at the most exposed locations. The thFZ240 sensors exhibit lower performance for low fluences and have an advantage only at high fluences and very long annealing times. However, with the thFZ240 sensors there is no clear gain in terms of electrical currents and power dissipation after irradiation, while they are more prone to mechanical damage. For all the above reasons, the FZ290 sensors were selected for usage throughout the full volume of the CMS Tracker.

The OT Sensor WG has developed a quality assurance plan to ensure that all sensors that will be integrated in the detector meet a set of predefined quality standards. Initially, all sensors will be pretested by the vendor during the vendor quality control (VQC), and only the sensors and corresponding test structures that meet the specifications and all corresponding test structures will be distributed to the test centers of the OT Sensor WG. Subsequently, the test centers will perform three main quality control procedures: the sensor quality control (SQC), during which about 10% of the sensors of each delivered batch will be characterized to ensure that they fully satisfy the specifications; the process quality control (PQC) during which the quality and stability of the production process will be tracked by measuring process parameters on test structures and around 20% of the delivered wafers will be characterized; and the irradiation tests (IT), during which up to 5% of the dedicated test sensors and test structures will be characterized after irradiation to ensure that the radiation effects on the delivered material do not change over production time. The results of all the quality control measurements are combined and a decision is made if the quality of the delivered sensor batches is sufficient to send their sensors for module assembly and finally integrate them into the CMS Tracker. The steps described above are summarizes in Fig. 4.1 [3].

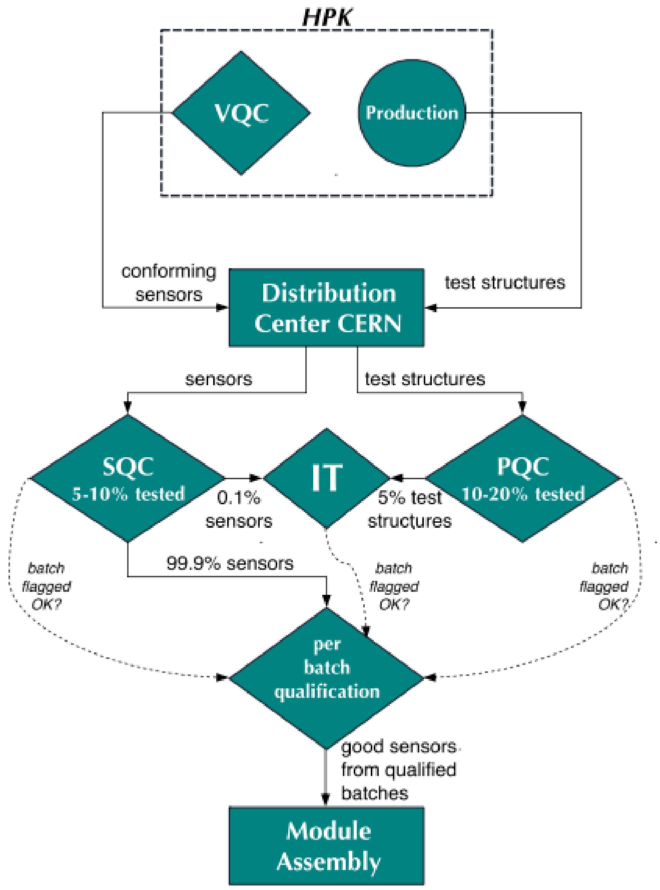

Figure 4.1: The Tracker quality control process flow.

During the sensor production phase, DIL at INPP, NCSR "Demokritos" will operate as a PQC center, along with test centers managed by Brown University, the Institute of High Energy Physics (HEPHY) of the Austrian Academy of Sciences, and the Perugia group consisting of Istituto Officina dei Materiali (IOM) of the Italian National Research Council (CNR), INFN Sezione di Perugia and the University of Perugia. The same set of test structures (from an individual halfmoon) will be sequentially measured at three institutions, starting at different centers (e.g. firstly at "Demokritos", then in Perugia, and finally at Brown University).

The structures set for automated process quality control and their location on wafers containing sensors for 2S modules are shown in Fig. 4.2, left. These test structures are connected to arrays of 20 contact pads (which comprise a flute) that facilitate measurements with the use of a 20-needle probe card. The four main flutes, named PQC1, PQC2, PQC3 andPQC4, respectively, provide a comprehensive overview of all relevant process parameters (Fig. 4.2, right) [3].

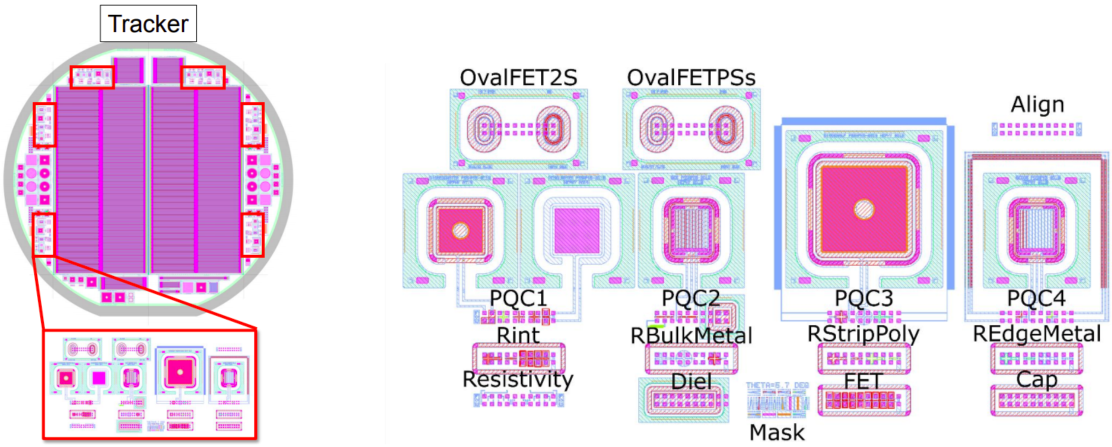

Figure 4.2: Left: The 2S sensor wafer where the halfmoons containing the various test structures are indicated. Right: Set of PQC Flutes with naming conventions superimposed on each unit.

PQC1 contains a diode for the determination of the full depletion voltage, dark current, bulk resistivity and bulk doping concentration; a MOS capacitor for the determination of the flatband voltage, fixed oxide charge concentration, interface trap density, mobile oxide charges and oxide thickness;, Van-der-Pauw crosses for the determination of the n+, p-stop and polysilicon sheet resistance; capacitors for the determination of the coupling capacitance and dielectric thickness; and a field-effect transistor (FET) for the determination of the threshold voltage and interstrip properties [3].

PQC2 contains a gate-controlled diode (GCD) with width ratio n+/gate = 1 for the determination of the surface current, interface recombination velocity and interface trap density; a polysilicon resistor for the determination of the bias resistance; linewidth structures for the determination of the n+ and p-stop implant linewidth; and a dielectric breakdown test structure for the determination of the the dielectric strength of the coupling dielectric [3].

PQC3 contains a diode for the determination of the full depletion voltage, dark current, bulk resistivity, bulk doping concentration and the correction for edge effects; a bulk resistivity test structure for the determination of the bulk resistivity and bulk doping concentration; Van-der-Pauw crosses for the determination of the metal and p++ sheet resistance, and the p++ implant linewidth; and a metal meander for the determination of the metal sheet resistance [3].

PQC4 contains a GCD with width ratio n+/gate = 1/3 for the determination of the surface current, interface recombination velocity, interface state density and generation lifetime; Cross-Bridge-Kelvin-Resistance (CBKR) test structures for the determination of the metal to n+ implant and metal to polysilicon contact resistance; and contact chains for the determination of the metal to n+ implant, metal to p++ implant and metal to polysilicon contact quality [3].

The four central flutes of the set that provide a comprehensive overview on all relevant process parameters are labeled "main PQC flutes" and are separated in "quick flutes" for quick evaluation of process quality and "extended flutes" for providing additional parameters not accessible via the quick flutes [3].

4.2 The Detector Instrumentation Laboratory (DIL)

The Detector Instrumentation Laboratory (DIL) at NCSR "Demokritos" has an area of 120 m^2 (Fig. 4.3) which is under temperature and humidity control, constantly kept at RH$\approx$ 40% and θ = 23 °C±1 °C. A Meaco 20L Low Energy Dehumidifier is responsible for the humidity control required for preserving moisture-sensitive items. High dry air quality is achieved through an Atlas Copco oil-free air compressor, with a 1.02 L/sec flow and a 24 L reservoir. Electrical characterization is performed using a Carl Suss PA 150 automatic probe station and supplementary equipment (a 5Hz - 13 MHz HP4192A LF impedance analyzer for CV measurements, a Keithley 6517A electrometer/high resistance meter and a Keithley 2410 1100V SourceMeter for IV measurements, a Keithley 707B switching matrix with a Keithley 7072 Semiconductor Matrix Card and a Keithley 7072-HV Semiconductor Matrix Card for switching between IV and CV measurements), as shown in Fig. 4.4. A 20-needle probe card (based on one developed at HEPHY) designed to allow testing each pad of a PQC flute while other pads are biased is used for the automatization of measurements (Fig. 4.5). The whole setup is operated through LabVIEW virtual instruments (VIs). A Delvotec 5430 wire bonder is placed in the lab for making interconnections between integrated circuits and their packaging (Fig. 4.6, left). Environmental simulations with regard to extreme temperature and humidity are performed with a climate test chamber Weiss WKS 3-180/40/5 (Fig. 4.6, right).

Figure 4.3: The Detector Instrumentation Laboratory (DIL) at the Institute of Nuclear and Particle Physics (INPP), NCSR "Demokritos".

4.3 Some indicative measurements

During the R&D phase for the HPK silicon sensor selection several measurements were performed by members of the CMS INPP group on batches containing different samples. The ones presented below are from the VPX28442 batch of thinned samples at 240 μm. During the current-voltage (IV) measurements up to 1000 V (absolute value) on 5 mm sized diodes (called full diodes), conducted at room temperature, in almost all cases no breakdown was observed and the current didn't exceed 10 nA (Fig. 4.7, left). The IV plots were compared to the respective ones obtained from the measurements on the 2S sensors from the same wafers, which were performed at the University of Rochester (Fig. 4.7, right). The ratio of the active area of a 2S sensor to the active area of a full diode is roughly equal to 400. It can be noted that the ratio

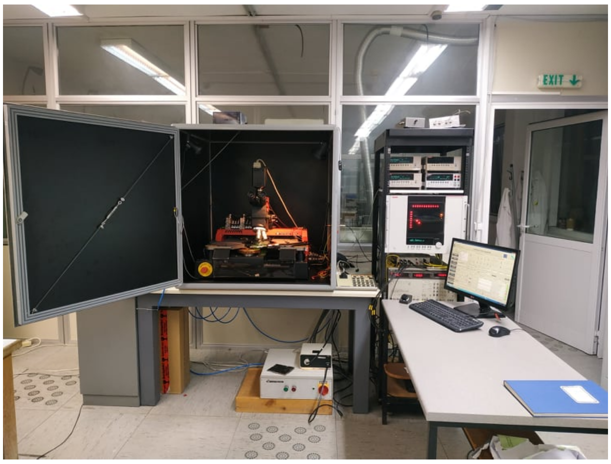

Figure 4.4: The Karl Suss PA 200 probe station at DIL, along with a HP4192A for CV measurements and a Keithley 6517A for IV measurements.

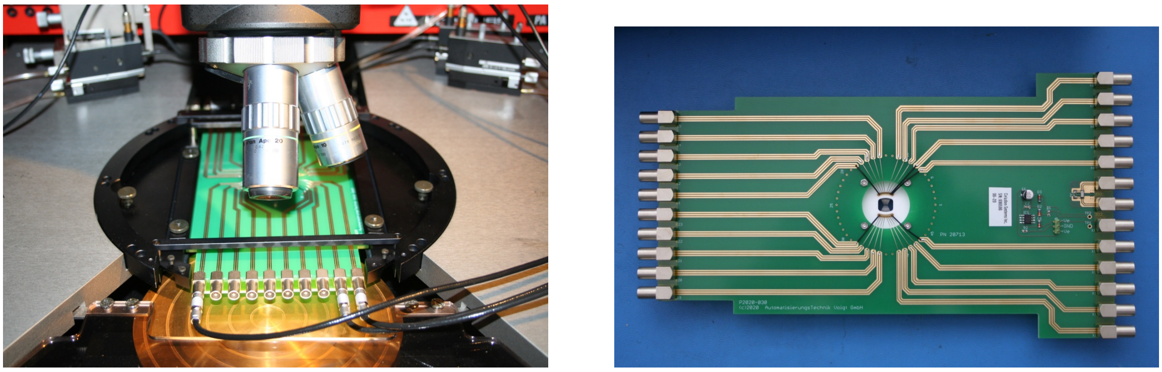

Figure 4.5: The HEPHY probe card for automatic PQC measurements viewed as placed on the chuck of the probe station at DIL (left), and viewed from top (right).

Figure 4.6: Left: The Delvotec 5430 wire bonder at DIL. Right: The Weiss WKS climate test chamber at DIL.

of the leakage current at 400 V (absolute value) for the 2S sensor over the ratio of the leakage current at 400 V (absolute value) for the full diode is approximately equal to 300 [4].

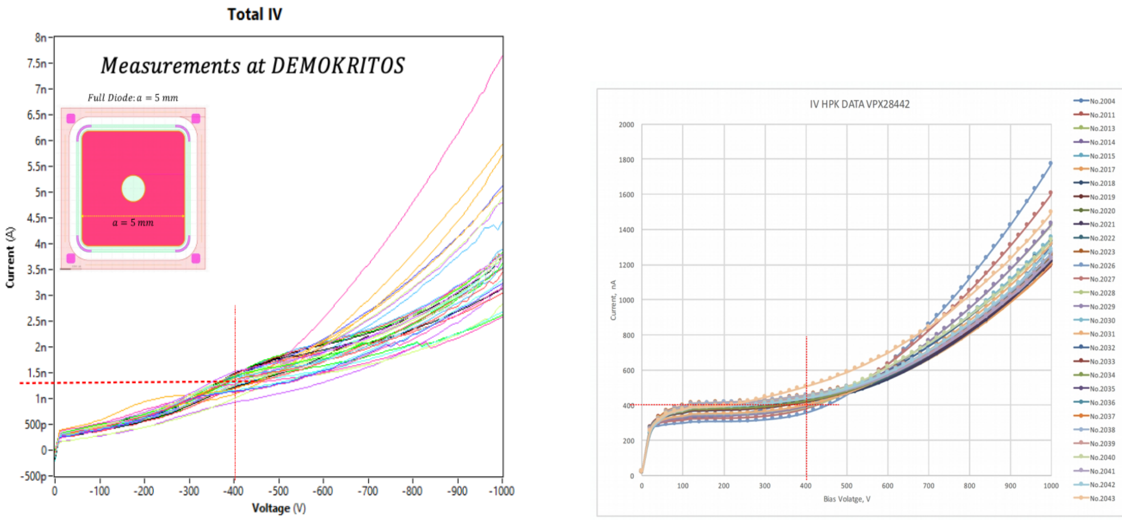

Figure 4.7: Left: Indicative IV curves of 5 mm sized diodes (full diodes) from a VPX28442 batch of 240 μm thinned samples, as shown on the LabVIEW interface. Right: IV curves of the sensors cut from the same wafers as the full diodes, as measured at the University of Rochester.

The leakage current measured on the round diodes with a radius of 0.75 mm from the same batch remained below 1 nA in most cases. It never exceeded 1.3 nA (Fig. 4.8) [4].

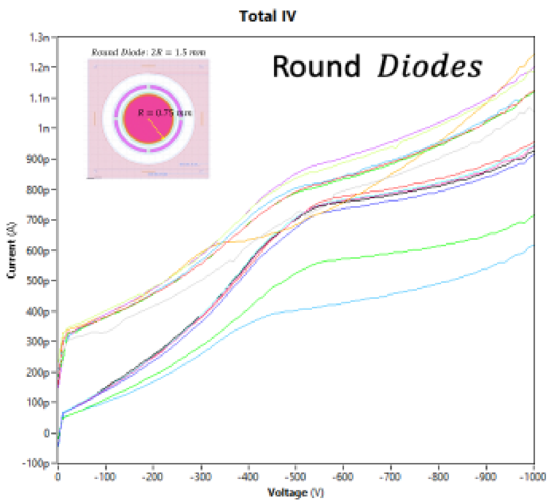

Figure 4.8: Indicative measured IV curves of round diodes with a 0.75 mm radius, from a VPX28442 batch of 240 μm thinned samples, as shown on the LabVIEW interface.

Capacitance-voltage (CV) measurements were performed on all diodes and MOS capacitors of the same batch. The full depletion voltage is determined from the $1/C^2$-V curves of the diodes with voltages up to 1000 V (absolute value), at the point where there is a change in the slope. In every sample, for a given type of diode, the depletion voltage was always found to be in the same order of magnitude. For example, in all the measured 2.5 mm sized diodes (half diodes) of the batch, the depletion voltage was around 200 V (absolute value, Fig. 4.9). A homogeneity of the CV measurements per frequency is also observed in the 4 mm sized MOS capacitors for all frequencies ranging from 100 Hz to 1 MHz (as seen in Fig. 4.10 for a frequency of 10 kHz and an oscillation level of 250 mV), from where valuable information regarding the flatband voltage and other parameters can be extracted [4].

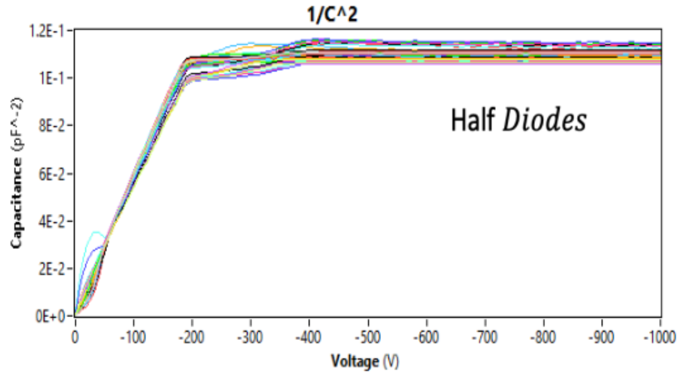

Figure 4.9: Indicative measured $1/C^2$-V curves of 2.5 mm sized diodes (half diodes) from a VPX28442 batch of 240 µm thinned samples, as shown on the LabVIEW interface.

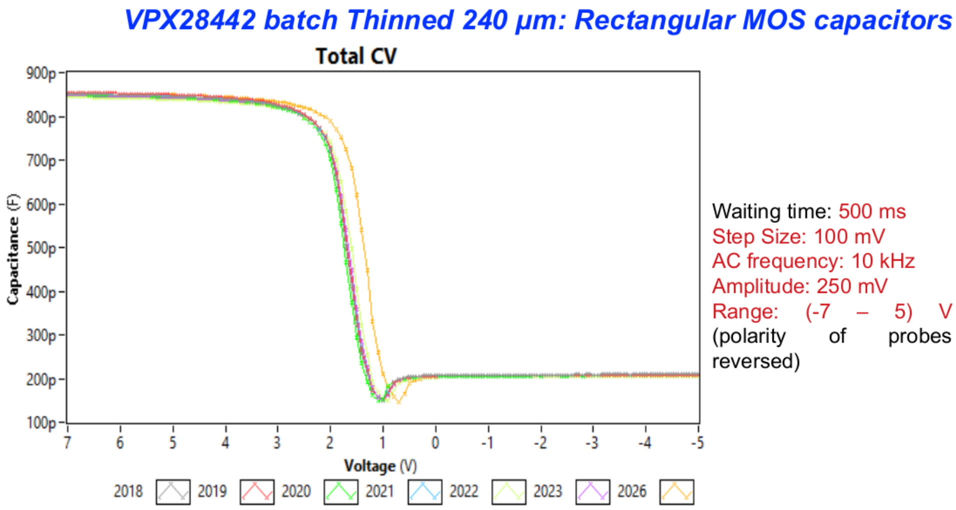

Figure 4.10: Indicative measured CV curves of 4 mm sized MOS capacitors from a VPX28442 batch of 240 µm thinned samples, as shown on the LabVIEW interface.

Three day-long tests for different values of the relative humidity (10%, 20%, 30%, 40%, 50%) at room temperature and at a steady bias voltage of −350 V were performed on some of the diodes, while they were placed inside the climate test chamber, in order to investigate the stability of their electrical behavior. For all RH values the measured electric current was stabilizing after the end of the first day. After that only slight variations of maximum 20-30 pA were noticed. Up to RH = 40% there doesn't seem to be any clear dependence of the current on humidity, but at RH = 50%, the measured leakage current has visibly increased. The results for a 1.25 mm sized diode (quarter diode) are summarized in Fig. 4.11. From plots like this, conclusions can be drawn on the extent to which humidity affects the operation of the silicon sensors [4].

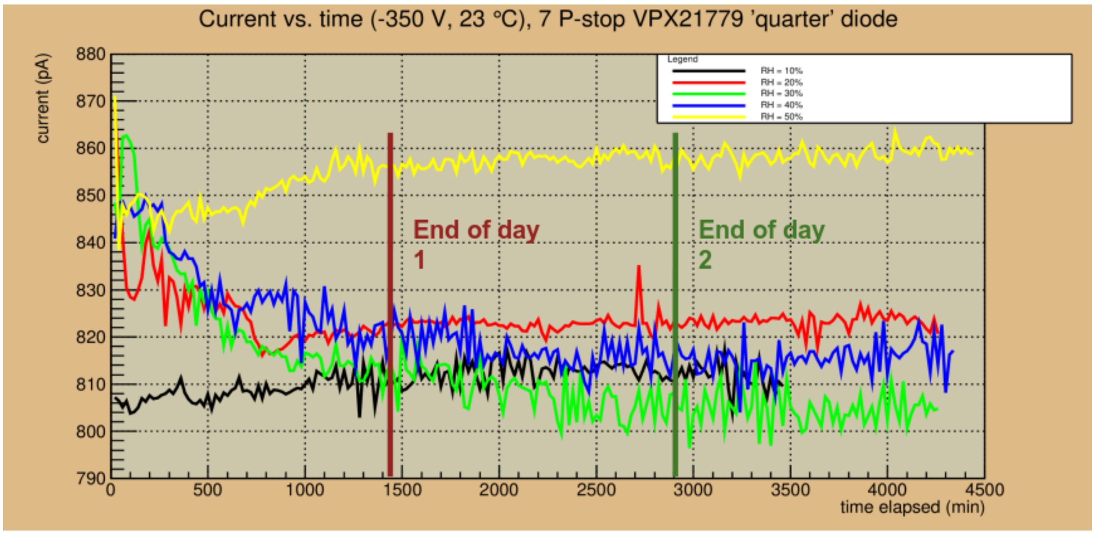

Figure 4.11: Evolution of a 1.25 mm sized diode (quarter diode from the VPX28442 batch) current over time, at $V = -350\,V$, and room temperature, for different values of the relative humidity.

Different CMS quality assurance centers might perform different measurements on diodes and sensors. For example, fluorescence image capture scientific cameras can obtain images in low light environment where areas of biased diodes/sensors through which higher current are flowing are visible (Fig. 4.12).

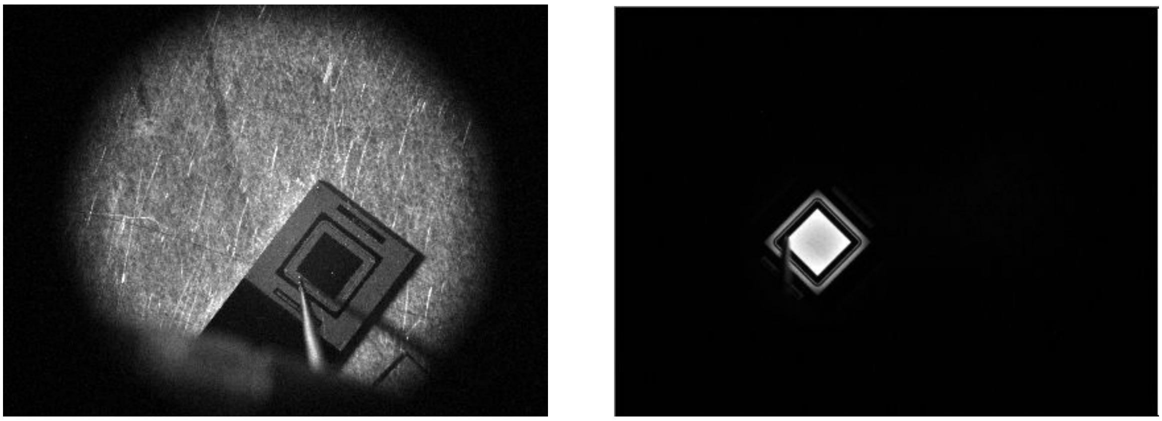

Figure 4.12: IR imaging of an Epi 50P diode with a scientific camera (EHD SciCam SC8300). Left: With lights on. Right: With the diode placed inside the lightproof probe station, bias voltage V = 350 V (absolute value), CCD temperature: -5 °C, exposure time: 300 s and measured current of the order of 1.2 mA (absolute value). (Images taken by the author at KIT.)

Through the years of R&D a plethora of sample types have been tested by the OT Sensor WG. One of them is the multigeometry silicon strip detector (MSSD), a strip sensor containing multiple regions which vary in strip-to-pitch ratio and number of intermediate strips (Fig. 4.13, left). MSSDs are useful when a multitude of strip geometries need to be tested at once (e.g.

under beam). Members of the CMS group at NCSR "Demokritos" have used measurements on MSSDs (Fig. 4.13, right) for comparison with the outputs of simulation programs which aim to predict the backplane and interstrip capacitances in silicon microstrip sensors for distinctive geometries [5].

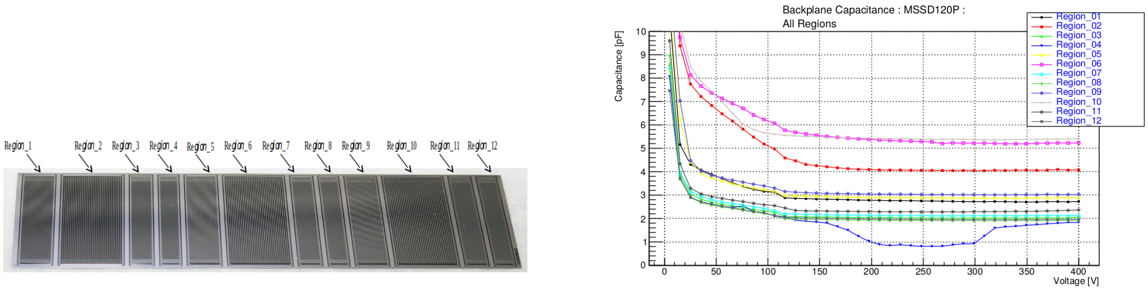

Figure 4.13: Left: The twelve regions (each with a different combination of width and pitch) of an MSSD. Right: CV curves for each region of the MSSD. It is observed that in one region probably either the electrode hasn't been in good contact with the sample during the measurement or the region is damaged.

4.4 Irradiation campaign with a ^{60}Co source

In the High Luminosity era [6] the total absorbed doses in the outer layers of the tracking systems of the major LHC experiments (CMS included) are estimated to be in the order of 10-100 kGy, depending on the distance from the beam line. A systematic campaign of irradiation tests with neutrons and charged hadrons initiated by the LHC collaborations is ongoing in order to estimate how will the candidate devices for the tracking systems cope with the demands for higher luminosity and radiation fluxes. Complementary radiation studies with ^{60}Co-γ photons are performed with the doses equivalent to those that the outer layers of the silicon tracker systems of the two large LHC experiments will be subjected to. The CMS group at NCSR "Demokritos" has performed one such study which will be subsequently presented here [7].

The samples used for this irradiation are float-zone oxygenated silicon n-in-p test structures from thinned 240 μm thick wafers produced by Hamamatsu Photonics K.K. Each test structure contains one square MOS (area = 4 mm × 4 mm) and two square diodes (area = 2.5 mm × 2.5 mm and area = 1.25 mm × 1.25 mm, respectively).

Cobalt-60 has two gamma-ray decay modes with decay energies 1.1732 MeV and 1.3325 MeV, respectively (Fig. 4.14). The ^{60}Co source is a Picker teletherapy unit [8] with a radioactivity of 30 TBq as of March 2012, estimated at approximately 11 TBq by the time the measurements were performed, with a horizontal orientation (Fig. 4.15, left). It was calculated by using FC65-P Ionization Chambers from IBA Dosimetry [9] that the dose rate at irradiation point (4 m from the source) is 0.96 kGy/h. The irradiation was performed in the secondary standard ionizing radiation laboratory of the Greek Atomic Energy Commission (GAEC), accredited according to ISO 17025 in the field of radiotherapy, and the relevant CMCs (calibration and measurement capabilities) are published in the BIPM database [10]. The cooling system consisted of a thermoelectric cooler (Peltier element, type TEC1 12704) operating at temperature lower than room temperature (20 °C ± 1 °C during the first phase of the experiment and 8 °C ± 1 °C during the second phase of the experiment), an aluminum plate and a fan for heat dissipation (Fig. 4.15, right). The selected Peltier is sealed with 704 silicon rubbers and proved to be robust against

γ-irradiation from the Cobalt-60 source. A microcontroller for the stabilization of temperature and the respective power supplies were used in addition (Fig. 4.16, left). Charged particle equilibrium (CPE) was achieved due to a box of 2 mm thick Pb and 0.8 mm of inner lining Al sheet, i.e. a lead-aluminum container for the absorption of low energy photons and secondary electrons [11] where the samples were kept during irradiation (Fig. 4.16, right). The energy spectrum inside the CPE container and 40 cm away from the source was measured (Fig. 4.17) with a Micro-sized CZT Gamma Spectrometer with a volume of 0.5 cm^3, a spectral response in the range 30 keV - 3 MeV and an energy resolution < 2.5% at 662 keV (^{137}Cs) [12]. Subsequent comparisons with the corresponding spectrum of the source outside the container gave satisfactory results. As for the calculation of absorbed doses in silicon, it should be noted that this is quite straightforward since for γ-rays of energies ranging from 200 keV to 2 MeV conversion from Gray in Air to Gray in Silicon is simply a multiplication by 1 [13].

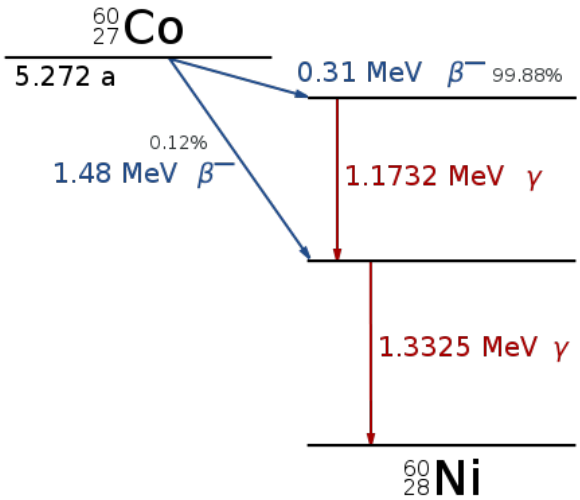

Figure 4.14: Decay scheme of ^{60}Co.

Figure 4.15: Left: The Cobalt-60 source: Picker therapy unit. Right: The container with the samples in front of the source. The fan and the thermoelectric cooler are visible.

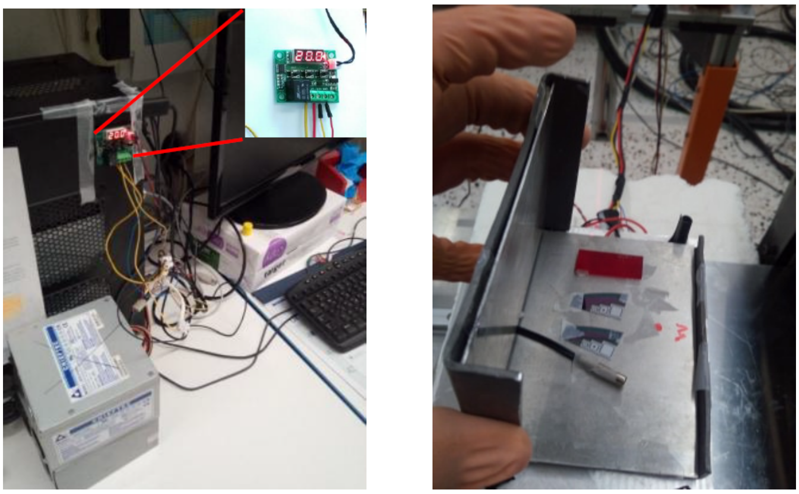

Figure 4.16: Left: The microcontroller and power supplies of the experimental setup. Right: The lead-aluminum container for charged particle equilibrium.

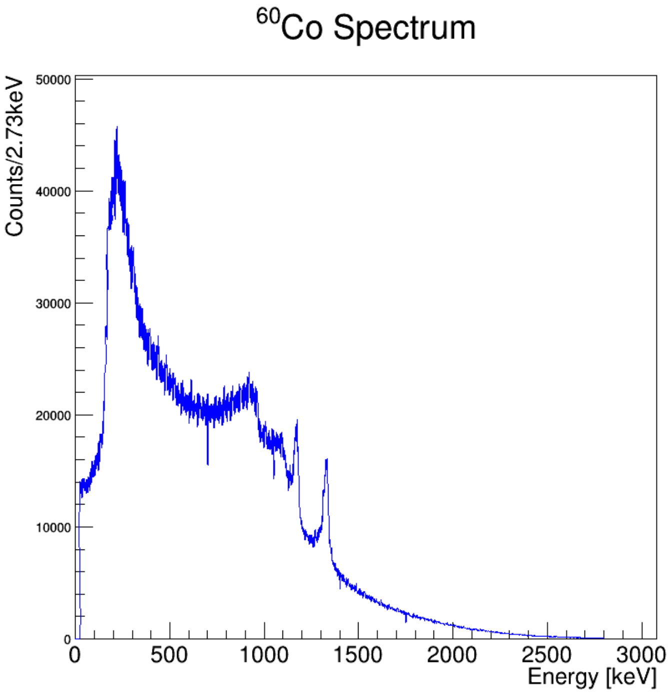

Figure 4.17: Energy spectrum taken 4 m away from the cobalt-60 source and after 5.2 cm of Pb (a 5 cm thick Pb block was placed between the source and the CPE box and the Pb thickness of the CPE box was 0.2 cm), as measured inside the charged particle equilibrium (CPE) box. The left peak is a backscatter peak at approximately 200 keV which emerges when γ-rays enter the material around the detector and are scattered back into the detector. The right peaks are the peaks corresponding to the 1.1732 MeV and 1.3325 MeV gamma-ray decay modes of cobalt-60. The β-peak is not measurable inside the CPE container due to the successful Al shielding.

Electrical measurements were performed at 20 °C (and below) using the automatic probe station and its supplementary equipment (HP4192A, Keithley 6517A) for electrical characterization of microelectronic devices. The samples were annealed in the Weiss climate test chamber. Data analysis was subsequently performed using ROOT [14].

4.5 Experimental procedure and protocol followed during the irradiation campaign

During each phase of the experiment, the CPE container with the samples was held 40 cm away from the source while being irradiated.

For the first phase of the experiment, the irradiation was split in slots of 6-16 hours of irradiation. After each slot, annealing of the samples was performed in the climate test chamber at 60 °C for 10 min (corresponding to four days of annealing at room temperature). The electrical tests at the probe station after the annealing were performed at 22-24 °C using LabVIEW as data taking and control software. However, humidity was not controlled and relative humidity (RH) was varying between 30-45%. The oscillation amplitude for the CV measurements was set at 250 mV. CV measurements were carried out for various frequencies (100 Hz, 1 kHz, 10 kHz, 100 kHz, 1 MHz for MOS capacitors; 10 kHz, 100 kHz, 1 MHz for diodes). Between each set of electrical measurements and the next irradiation slot, the samples were stored in a freezer at -28 °C.

For the second phase of the experiment, the irradiation was split in slots of approximately 14-16 hours of irradiation. After each slot, annealing of the samples was performed in the climate test chamber at 60 °C for 10 min (corresponding to four days of annealing at room temperature). The electrical tests at the probe station after the annealing were performed at 15-23 °C using LabVIEW as data taking and control software. Humidity in the lab was controlled with a desiccator and during all measurements RH was below 30%. The oscillation amplitude for the CV measurements was set at 250 mV. CV measurements were carried out for various frequencies (100 Hz, 1 kHz, 10 kHz, 100 kHz, 1 MHz for MOS capacitors).

4.6 Results from MOS capacitors (CV analysis)

From the first phase of the experiment, after the exposure to gamma photons there is a clear evidence of positive charge induced in the oxide of the p-type MOS capacitors as seen in Fig. 4.18, where a shift of the flatband voltage (V_{FB}, the voltage where the MOS behavior changes from accumulation to depletion) to higher absolute values is observed at higher doses initially. The above trend is reversed after an irradiation dose of about 50 kGy. A possible explanation could be that the positive charge in the oxide created by irradiation is strong enough to start to attract negative charges from the surrounding material, but the observed effect could also be attributed to sample defects. The numerical value of the flatband voltage, along with the numerical values of the capacitance in the different MOS regions are validated by TCAD simulations (Fig. 4.19).

The behavior of some other features of MOS capacitors (capacitance in the accumulation region C_{acc}, capacitance in the inversion region C_{inv}, oxide thickness t_{ox}) before and after irradiation is summarized in Fig. 4.20, where the reverse of the initial flatband voltage increase is also indicated. The derivation for these features has been done by known rules (Chapter 6 of [15]), while V_{FB} can be evaluated from the CV curve of the MOS capacitor using the inflection

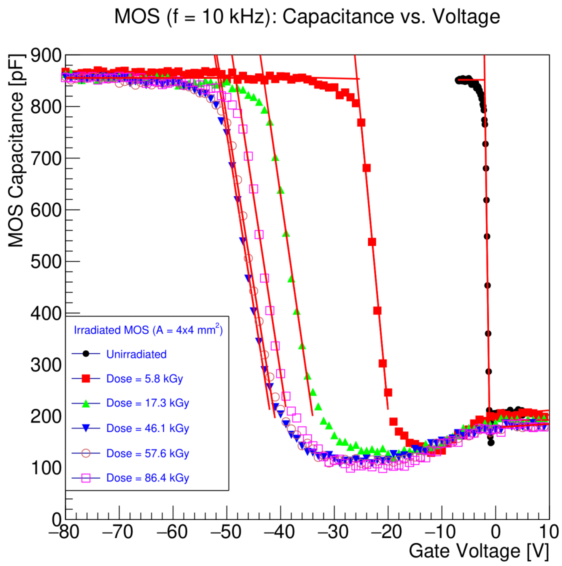

Figure 4.18: Capacitance-voltage curves for a MOS capacitor for various doses; measurement frequency = 10 kHz. First phase of the experiment: irradiation time slots of 6-16 hours, storage in freezer between irradiation time slots, no control over humidity during electrical measurements. The points of each curve have been fitted to three lines corresponding to each of the three regions of the MOS capacitor: accumulation, depletion and inversion. The slope of a curve in the depletion region is related to the acceptor concentration (Chapter 6 of [15]).

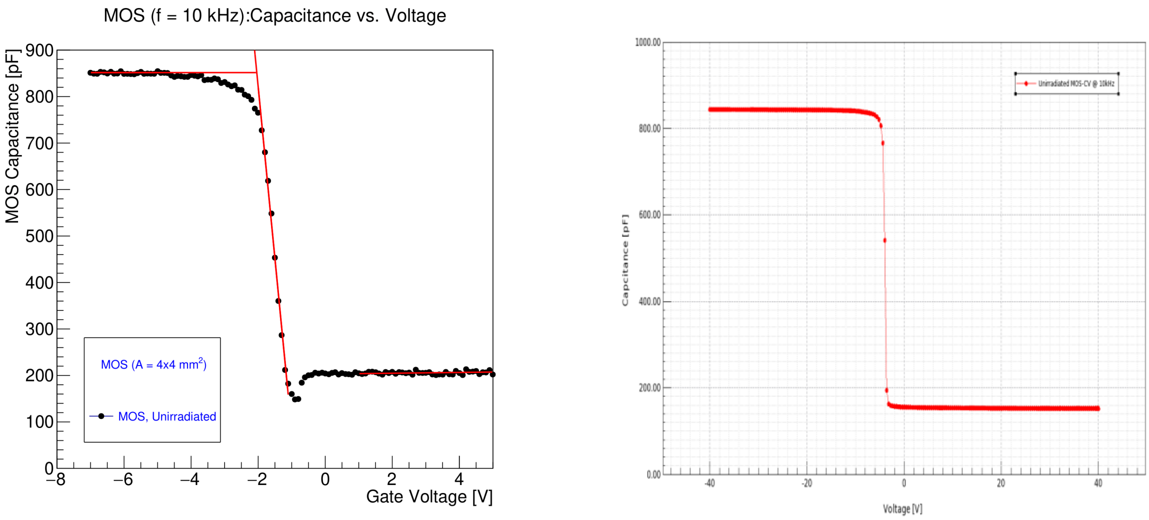

Figure 4.19: Left: Experimental capacitance-voltage curve for an unirradiated MOS capacitor; measurement frequency = 10 kHz. First phase of the experiment: irradiation time slots of 6-16 hours, storage in freezer between irradiation time slots, no control over humidity during electrical measurements. Right: Capacitance-voltage curve for an unirradiated MOS capacitor obtained from a TCAD simulation; frequency = 10 kHz.

point [16] (a point on a continuous plane curve at which the curve changes from being concave to convex, or vice versa) of the curve. After the analysis, it can be noticed that the percentage variation for the MOS capacitance in the accumulation region is 4% and for the MOS capacitance in the inversion region is 10%, respectively. On the other hand, the oxide thickness t_{oxide} was calculated to be 0.65 μm. (It remains stable as expected, since it is a geometric characteristic of the device.) The oxide thickness can be calculated when the low frequency capacitance of the MOS structure per unit area C_{oxide} and the dielectric constant of the oxide ϵ_{oxide} are known, as shown in Chapter 6 of [15]:

$$t_{oxide} = \frac{\epsilon_{oxide}}{C_{oxide}} \tag{4.1}$$

where the oxide capacitance C_{oxide} can be calculated considering the capacitance measured in accumulation C_{acc}.

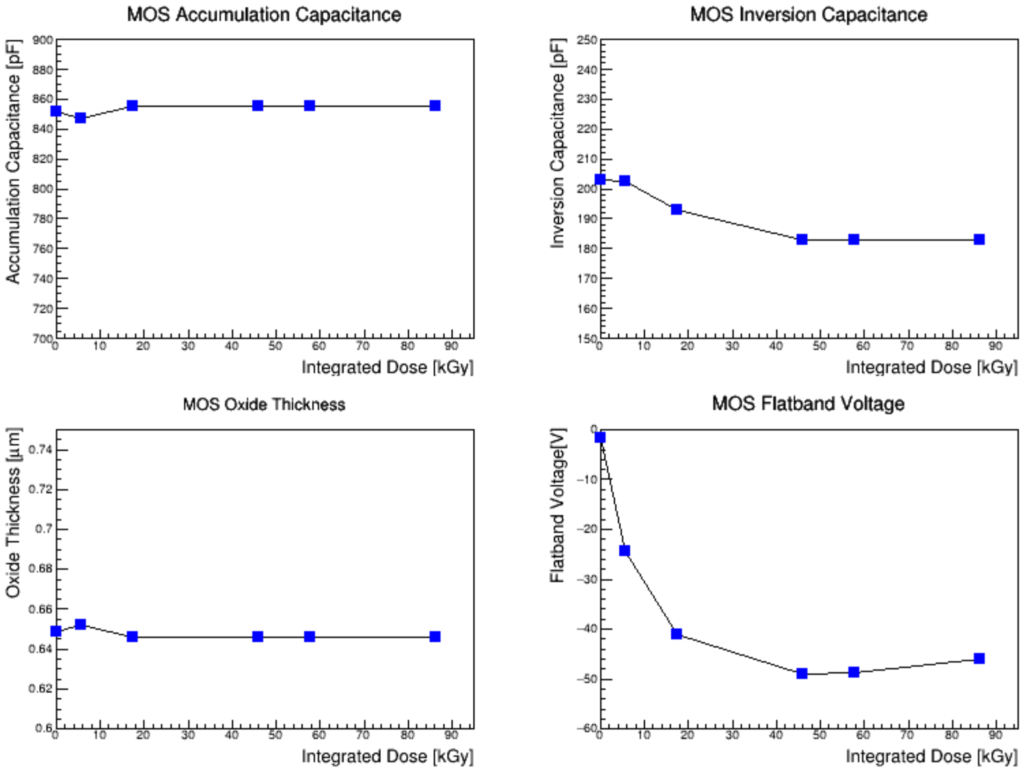

Figure 4.20: Various features of a MOS capacitor before and after irradiation; measurement frequency = 10 kHz. (Derived from Chapter 6 of [15].) Top left: Accumulation capacitance. Top right: Inversion capacitance. Bottom left: Oxide thickness. Bottom right: Flatband voltage. First phase of the experiment: irradiation time slots of 6-16 hours, storage in freezer between irradiation time slots, no control over humidity during electrical measurements.

Furthermore, the behavior of the flatband capacitance C_{FB} and the effective density of charges present in the oxide layer N_{oxide} is summarized in Fig. 4.21. The flatband capacitance of the MOS structure at flatband is obtained by calculating the series connection of the oxide capacitance and the capacitance of the semiconductor, yielding:

$$C_{FB} = \frac{1}{\frac{1}{C_{oxide}} + \frac{L_D}{\epsilon_s}} \tag{4.2}$$

where L_D is the extrinsic Debye length in the semiconductor [15], ϵ_s is the dielectric constant of the semiconductor and all capacitances are per unit area. It is observed that the flatband capacitance of a MOS capacitor increases after the initial irradiation but remains almost stable afterwards. On the other hand, the flatband voltage can be expressed as a sum of three terms: the difference between work functions of metal and semiconductor (which remains stable), the voltage across the oxide due to the charge at the oxide-semiconductor interface and a third term which is due to the charge density in the oxide N_{oxide} [15]. So, the behavior of the flatband voltage described above implies an initial increase of the effective oxide concentration N_{oxide} and a decrease after 50 kGy, which is indeed observed in Fig. 4.21, bottom. N_{oxide} is calculated as follows:

$$N_{oxide} = \frac{C_{oxide}}{qA_{gate}}(\Phi_{ms} - V_{FB}) \tag{4.3}$$

where Φ_{ms}V is the work function difference between the aluminum gate layer and p-type silicon changing varying slightly as function of the doping concentration as a consequence of the irradiation of our sample.

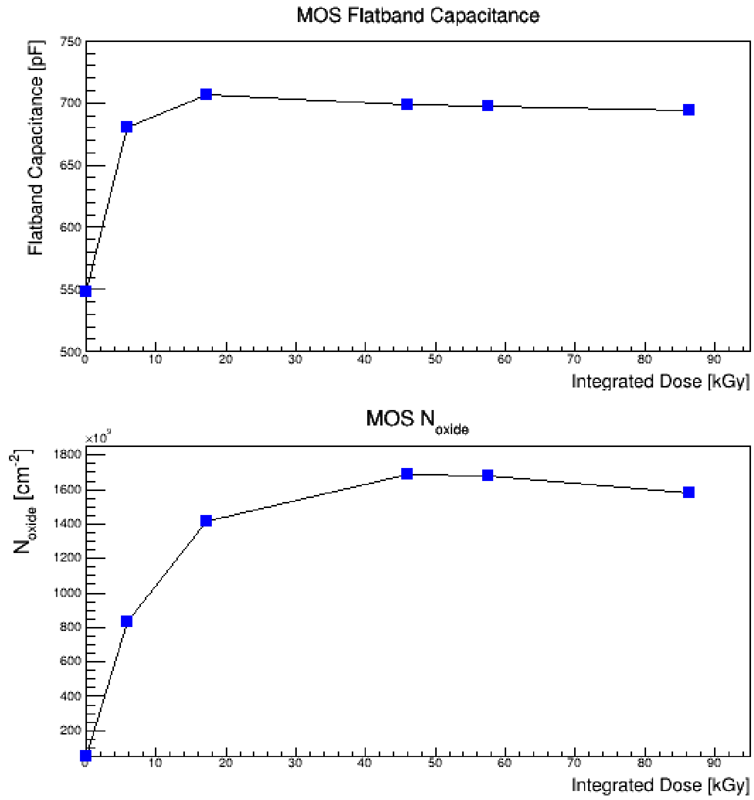

Figure 4.21: Various features of a MOS capacitor before and after irradiation; measurement frequency = 10 kHz. (Derived from Chapter 6 of [15].) Top: Flatband capacitance. Bottom: Effective density of charges present in the oxide layer N_{oxide}. First phase of the experiment: irradiation time slots of 6-16 hours, storage in freezer between irradiation time slots, no control over humidity during electrical measurements.

Similar results as the ones described above were observed during the second phase of the experiment with slight variations (Fig. 4.22, Fig. 4.23, Fig. 4.24). When a MOS capacitor is irradiated incessantly (with small breaks between the irradiation slots and with each break lasting around 6 hours) the flatband voltage increase to higher absolute values again stops around 50 kGy. However, in this case the reverse shift is not visible, but there is rather a saturation of the numerical value of the flatband voltage instead, as seen in Fig. 4.22 and Fig. 4.23 bottom right. This leads to stabilization of N_{oxide} after the initial increase even at high doses, compared to the reverse observed during the first phase of the experiment (Fig. 4.24, bottom). The flatband voltage V_{FB} continues to increase until the dose of 50 kGy in both cases, therefore indicating a growing accumulation of charges.

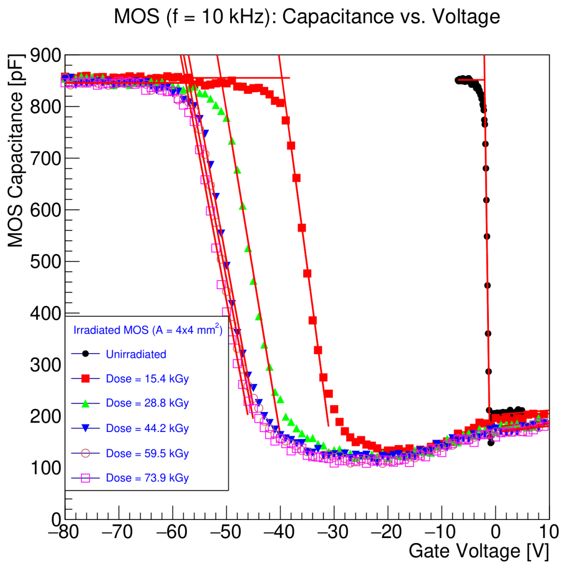

Figure 4.22: Capacitance-voltage curves for a MOS capacitor for various doses; measurement frequency = 10 kHz. Second phase of the experiment: irradiation time slots of 14-16 hours, no removal of the samples from the cobalt-60 source between the irradiation time slots, control over humidity during electrical measurements. The points of each curve have been fitted to three lines corresponding to each of the three regions of the MOS capacitor: accumulation, depletion and inversion. The slope of a curve in the depletion region is related to the acceptor concentration (Chapter 6 of [15]).

4.7 Results from 2.5 mm sized diodes (CV and IV analyses)

The CV curves of a 2.5 mm sized diode before and after irradiation during the first phase of the experiment prove to be almost identical. From $1/C^2$ calculated after the CV measurement, useful information about the depletion voltage (V_d, the bias voltage required so that the region depleted of free carriers reaches through the whole of the semiconductor bulk), capacitance in the depletion region (C_d) and acceptor concentration (N_a) can be obtained. From our measurements V_d is defined as the voltage where a saturation of the capacitance (the capacitance in the depletion region C_d) is observed. N_a is calculated using a known relation from [17]:

$$N_a = \frac{2\epsilon_{Si}|V_d|}{ed^2} \tag{4.4}$$

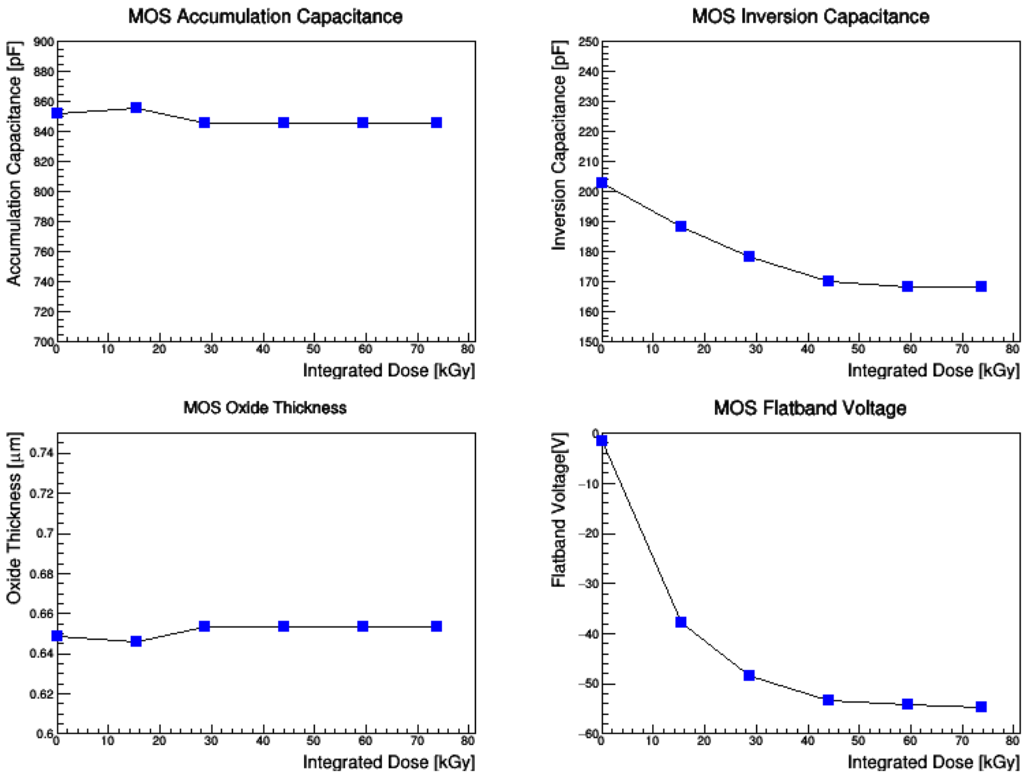

Figure 4.23: Various features of a MOS capacitor before and after irradiation; measurement frequency = 10 kHz. (Derived from Chapter 6 of [15].) Top left: Accumulation capacitance. Top right: Inversion capacitance. Bottom left: Oxide thickness. Bottom right: Flatband voltage. Second phase of the experiment: irradiation time slots of 14-16 hours, no removal of the samples from the cobalt-60 source between the irradiation time slots, control over humidity during electrical measurements.

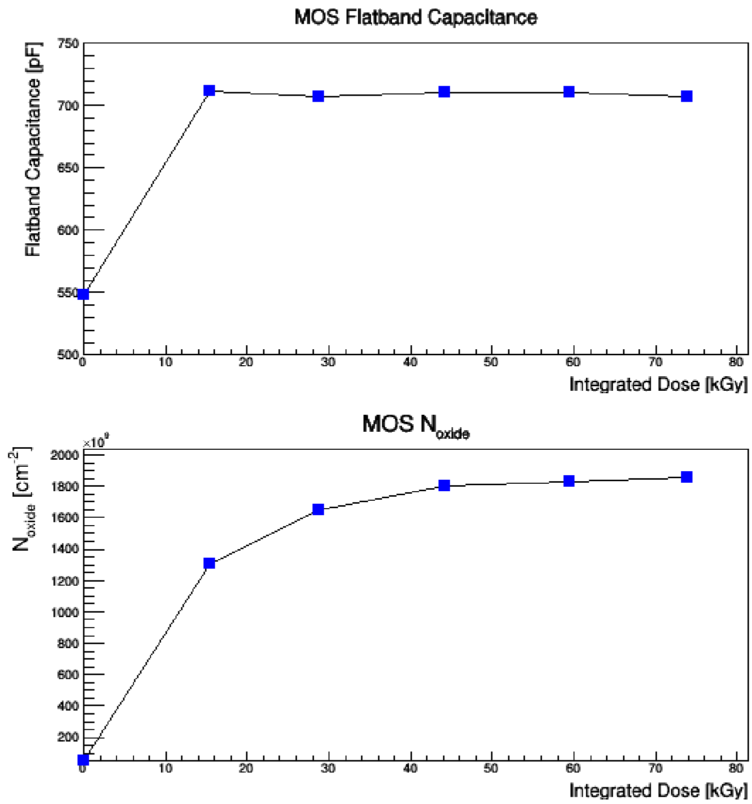

Figure 4.24: Various features of a MOS capacitor before and after irradiation; measurement frequency = 10 kHz. (Derived from Chapter 6 of [15].) Top: Flatband capacitance. Bottom: Effective density of charges present in the oxide layer N_{oxide}. Second phase of the experiment: irradiation time slots of 14-16 hours, no removal of the samples from the cobalt-60 source between the irradiation time slots, control over humidity during electrical measurements.)

where ϵ_{Si} is the dielectric permittivity of silicon, e is the elementary charge and d = 240 µm is the active thickness of the diode. The results are summarized in the insets of Fig. 4.25. After the CV analysis, it is observed that the depletion voltage remains almost unchanged after irradiation (Fig. 4.26, left). This occurs as a result of the oxygen enrichment of silicon which is known to improve the radiation hardness properties of silicon detectors [18] and is in agreement with independent studies of other groups (Fig. 4.26, right).

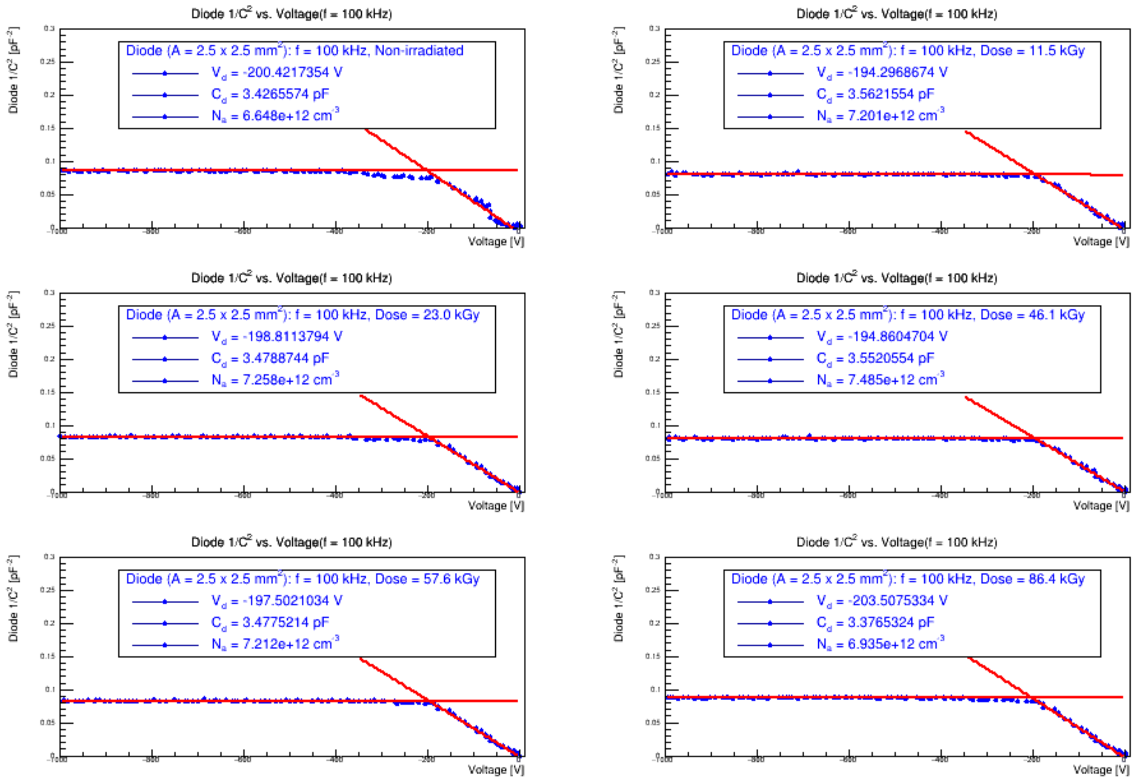

Figure 4.25: $1/C^2$-V curve for a 2.5 mm sized diode for various doses; measurement frequency = 100 kHz. First phase of the experiment: irradiation time slots of 6-16 hours, storage in freezer between irradiation time slots.

The IV results are scaled to 20 °C as follows:

$$I(20\,^{\circ}C) = I(T)\left(\frac{293\ K}{T}\right)^2 e^{-\frac{E_g}{2k_B}\left(\frac{1}{293\,K}-\frac{1}{T}\right)} \tag{4.5}$$

where T is the temperature of the measurement in K, k_B is the Boltzmann constant and E_g = 1.21 eV is the temperature-dependent effective band gap [19]. The increase of the diode leakage current (absolute value) with the total irradiation dose (for a selected number of measurements) is presented in Fig. 4.27.

Since the members of the CMS "Demokritos" group aren't the only users of the cobalt-60 source, we were forced to stop the irradiation for a few hours every day. During the time lapses between any two consecutive irradiation slots, the samples were stored in a freezer at -28 °C. When performing the IV measurement after each period of storage in the freezer, an annealing effect was observed every time (Fig. 4.28, top). The annealing effect was also observed after

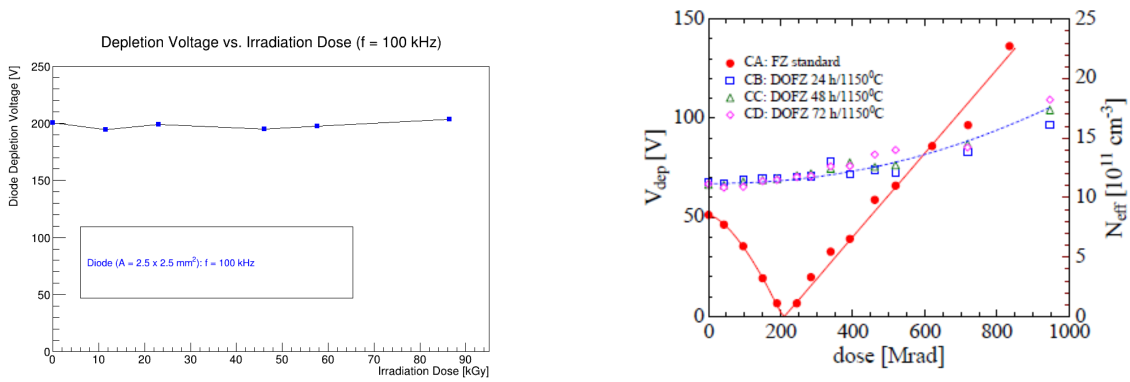

Figure 4.26: Left: Depletion voltage (absolute value) of a 2.5 mm sized diode as function of the integrated absorbed dose; measurement frequency = 100 kHz. First phase of the experiment: irradiation time slots of 6-16 hours, storage in freezer between irradiation time slots. Right: Depletion voltage (and effective doping concentration) as function of gamma dose for standard (closed) and DOFZ silicon (open symbols). (Taken from [17].)

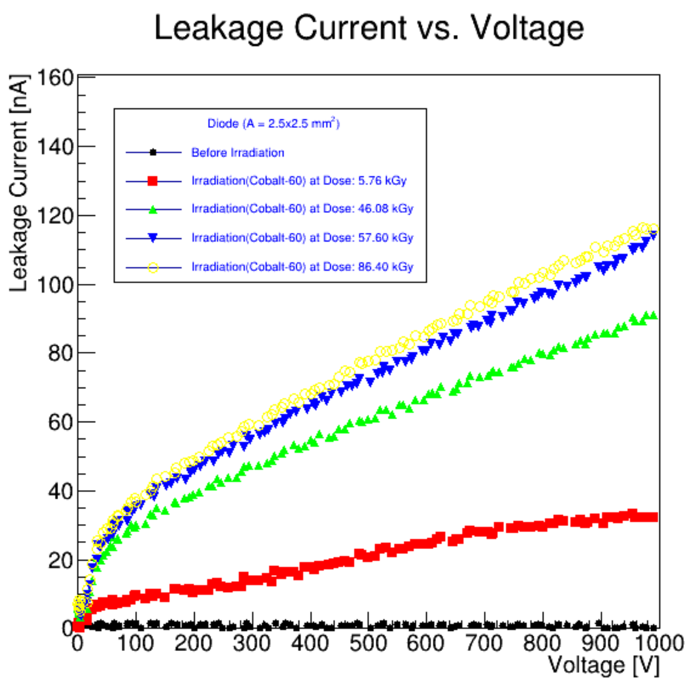

Figure 4.27: IV curves for a 2.5 mm sized diode for various doses. Voltages and currents are in absolute values. First phase of the experiment: irradiation time slots of 6-16 hours, storage in freezer between irradiation time slots.

storage of the samples in a bottle of liquid N_2 (Fig. 4.28, bottom). It is believed that the higher current before the cold storage is due to surface effects. It is notable that even after severe radiation and even before the annealing, the leakage current in the diodes is of the orders of a few hundreds nA and breakdown is never observed.

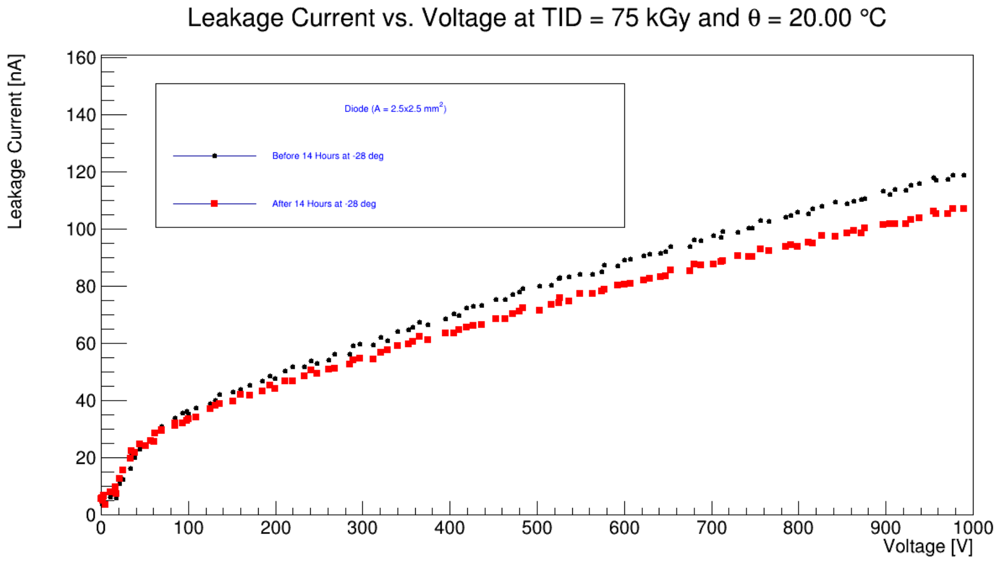

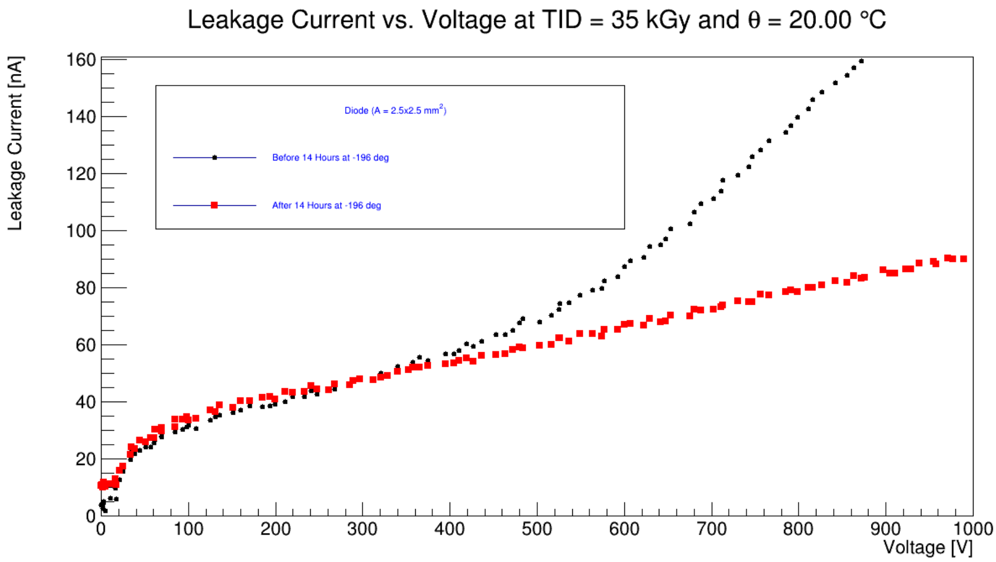

Figure 4.28: IV curves for an irradiated 2.5 mm sized diode before (black) and after (red) 14 hours of storage in a freezer at -28 °C (top) and 14 hours of storage in a bottle of liquid nitrogen at -196 °C (bottom) for different total irradiation doses. Voltages and currents are in absolute values. First phase of the experiment: irradiation time slots of 6-16 hours.

4.8 Suitability of the devices for high-luminosity applications

To summarize, the silicon MOS capacitors and n-in-p diodes which were irradiated with ^{60}Co-γ photons from a ~11 TBq source, absorbed a total dose (obtained in several steps) of ~86 kGy for the first phase and ~74 kGy for the second phase of the experiment. The level of the radiation-induced charge in the test structures was determined from the shift of the flatband voltage in the MOS capacitors after irradiation and a saturation effect was observed during the second phase of the experiment when humidity was controlled and lower. Apart from the flatband voltage, the irradiation of the MOS capacitors showed significant change in the threshold voltage and depletion region slope, which is related to the charge concentration. For the diodes it was noticed that the depletion voltage remained stable with the increasing dose, as expected for oxygenated test structures. Furthermore, even for high doses the leakage current of each diode was in the order of 10-100 nA (absolute value), which is still considered very low. Finally, it should be noted that not a single diode IV measurement showed any sign of breakdown behavior.

The increase in the leakage current to the order of tens/hundreds of nA at high voltages (absolute values) after irradiation (Fig. 4.27) is believed to be due to surface effects. The role of these effects is slightly diminished after annealing for some hours/days (Fig. 4.28). This gives an indication that during the operation of the CMS experiment even if after a total absorbed dose of a few dozens of kGy the leakage current is raised at a higher order of magnitude, a shutdown for a few days might improve the operation of the sensors. It is thus deduced that the material and devices under examination are suitable for high-luminosity applications.

Bibliography

[1] H. Simon, *"Chapter 1: The Mystique of the Hidden Champions". Hidden Champions of the Twenty-First Century: The Success Strategies of Unknown World Market Leaders*, London: Springer Science+Business Media, p.4 ISBN 978-0-387-98147-5.

[2] W. Adam et al., *P-Type Silicon Strip Sensors for the new CMS Tracker at HL-LHC*, 2017 JINST 12 P06018.

[3] V. Hinger, *Process Quality Control Strategy for the Phase-2 Upgrade of the CMS Outer Tracker and High Granularity Calorimeter*, 12th International 'Hiroshima' Symposium on the Development and Application of Semiconductor Tracking Detectors (HSTD12), 14-18 December 2019. Hiroshima, Japan (C19-12-14).

[4] Patrick Asenov, *Contribution of INPP to the CMS Phase-2 Upgrade*, HEP 2019 - Conference on Recent Developments in High Energy Physics and Cosmology 17-20 April 2019, NCSR "DEMOKRITOS", Athens, Greece.

[5] P. Assiouras, P. Asenov, I. Kazas, A. Kyriakis and D. Loukas, *Calculation of capacitances of silicon micro-strip sensors with a two dimensional numerical solution of the Laplace's equation*, Proceedings of Science, The 28th International Workshop on Vertex Detectors - Vertex2019, 13-18 October, 2019, Lopud, Croatia.

[6] G. Apollinari et al., *High-Luminosity Large Hadron Collider (HL-LHC): Technical Design Report V. 0.1*, CERN Yellow Rep. Monogr. 4, (2017) 1-516, [CERN-2017-007-M].

[7] P. Asenov, P. Assiouras, A. Boziari, K. Filippou, I. Kazas, A. Kyriakis and D. Loukas, *Cobalt-60 gamma irradiation of silicon test structures for high-luminosity collider experiments*, Proceedings of Science, The 28th International Workshop on Vertex Detectors - Vertex2019, 13-18 October, 2019, Lopud, Croatia.

[8] K. Tsien, R. Robbins, *A comparison of a cobalt-60 teletherapy unit and a 2-MEV Van de Graff x-ray generator on the basis of physical measurements*, Radiology 1958 Apr; 70(4): 486-500; discussion 501-2.

[9] L. Burigo, S. Greilich, *Impact of new ICRU 90 key data on stopping-power ratios and beam quality correction factors for carbon ion beams*, Phys Med Biol., 2019 Sep 23; 64(19):195005.

[10] C.H. Page, P. Vigoureux, eds., *The International Bureau of Weights and Measures 1875-1975: NBS Special Publication*, 420, Washington, D.C.: National Bureau of Standards, pp. 26-27.

[11] *Total dose steady-state irradiation test method*, ESCC Basic Specification No. 22900.

[12] IMS - Innovation & Measurement Systems, *Micro-Sized gamma Spectrometer, MGS Series* datasheet.

[13] J. H. Hubbell and S. M. Seltzer, *X-Ray Mass Attenuation Coefficients*, NIST Standard Reference Database 126, NISTIR 5632, DOI: https://dx.doi.org/10.18434/T4D01F .

[14] R. Brun and F. Rademakers, *ROOT - An Object Oriented Data Analysis Framework*, Proceedings AIHENP'96 Workshop, Lausanne, Sep. 1996, Nucl. Instr. & Meth. in Phys. Res. A 389 (1997) 81-86.

[15] Bart V. Van Zeghbroeck, *Principles Of Semiconductor Devices And Heterojunctions*, Prentice Hall, December 1st 2009.

[16] G. S. Baranenkov, *Problems in mathematical analysis*, Moscow: Mir Publishers, 1976.

[17] Gunnar Lindström, *Radiation Damage in Silicon Detectors*, invited talk presented at the 9th European Symposium on Semiconductor Detectors, Schloss Elmau, Germany, June 23-27, 2002; accepted for publication in Nucl. Instr. and Meth. A.

[18] E. Fretwurst et al., *Bulk damage effects in standard and oxygen-enriched silicon detectors induced by ^{60}Co-gamma radiation*, Nuclear Instruments and Methods in Physics Research Section A: Accelerators, Spectrometers, Detectors and Associated Equipment Volume 514, Issues 1-3, 21 November 2003, Pages 1-8.

[19] A. Chilingarov, *Generation current temperature scaling*, RD50 and EP Technical Note [RD50 TN 2011-01].

Chapter 5

CHROMIE: Simulation and test beam data analysis

This chapter presents the standalone simulation of CHROMIE, a high-rate particle telescope, and highlights the comparison of its output with test beam data, as well as the development of the telescope's tracking algorithm.

5.1 The need for novel high-rate telescopes

As mentioned previously, demands for the probing of new physics have led to the planned upgrade of the LHC to the HL-LHC (High-Luminosity LHC). An increase of the total integrated luminosity in proton-proton collisions at the LHC by an order of magnitude is foreseen to 3000 fb^{-1} over the period 2026-2037. It is worth emphasizing that the instantaneous luminosity is expected to reach a peak of $7.5\times10^{34}\ \mathrm{cm}^{-2}\mathrm{s}^{-1}$, yielding about 200 collisions per bunch crossing with a 25 ns bunch spacing [1]. This increase in luminosity will require for the silicon trackers in the major LHC experiments a considerably higher granularity and improved radiation hardness. An important milestone of the CMS Phase-2 Tracker upgrade is the replacement of the entire silicon strip Tracker. That is why the future CMS tracker will be built with so-called p_{T} modules consisting of two closely spaced silicon sensors read out by common front-end ASICs, which allow on-detector transverse momentum (p_{T}) discrimination of tracks. They will identify the high-p_{T} tracks by coincidence of signals in both sensors, contributing thus to the reduction of data [2]. More details were shown in previous chapters.

The ongoing second long shutdown of the LHC (LS2) concurs with the prototyping period of the new Phase-2 Tracker modules. Extensive beam tests of the silicon sensors and their readout electronics are necessary in order to examine the behavior of the sensors in realistic conditions. Thus, new detectors under development, usually referred to as Devices Under Test (DUT), can be tested for channel efficiency, cluster size and cross-talk between adjacent channels. During these beam tests a DUT is placed inside a complex system consisting of well known tracking modules called telescope. The tracking modules are highly segmented in order to reconstruct with high accuracy particle tracks and measure the tracking efficiency of the DUT. Existing telescopes commonly used by the CMS Collaboration use a Monolithic Active Pixel Sensor chip with an integration time of 115.2 μs, which is equivalent to a 8.68 kHz readout frequency. However, the integration time of the Phase-2 Tracker modules (and other HL-LHC sensors) is 25 ns, which corresponds to a 40 MHz rate [1], i.e. 4600 times the today's CMS telescope readout frequency. It is obvious that under these conditions the Phase-2 modules can't be tested at nominal rates with the old telescopes used by the CMS Collaboration. This is the main reason why new telescopes are being developed right now, like CHROMIE (CMS High Rate telescOpe MachInE) at CERN [3], [4] and CHROMini at CYRCé, IPHC-Strasbourg [5], [6], the telescopes with the highest rate compatible with up-to-date CMS-standard hardware and software.

Subsequently, the design of CHROMIE and its commissioning procedure will be outlined. A brief description of the applied tracking and preliminary alignment method will be described, and finally, a comparison will be made between the data from a small beam test that took place in 2018 at CERN and the related output of a standalone Geant4 simulation program.

5.2 The design of CHROMIE

As mentioned before, the detector modules for the Phase-2 Tracker need to be tested under beam to ensure good production quality before the next replacement of the Tracker detector. The highest rate that a Phase-2 Outer Tracker module might reach is expected to be $50\,\mathrm{MHz/cm^2}$ [2]. CHROMIE was designed to withstand particle rates up to $200\,\mathrm{MHz/cm^2}$ with an expected resolution of the order of $10-20\,\mu\mathrm{m}$ [4].

CHROMIE is equipped with the same custom-made triggering, control and readout boards and DAQ (data acquisition) software as the CMS pixel detector. CHROMIE is set up in the beam line H6 of the test beam North Area at CERN, where the Super Proton Synchrotron (SPS) [7] supplies the different experiments with high-energy particles.

CHROMIE consists of two "arms" (Fig. 5.1), each one of four layers (planes) with some dead areas (i.e. areas where the beam never strikes), each layer containing two CMS Phase-1 BPIX (barrel pixel) modules (Grade C, with an active area of $2 \times 16.2 \times 64.8\,\mathrm{mm^2}$) in a metal frame (Fig. 5.2). One arm is in front of the DUT, and the other one behind it, on the way of the beam. The pixel size is $100 \times 150\ \mu\mathrm{m}^2$ (except from the boundaries between two readout chips of the same module where the size in the respective direction is doubled). In order to improve the resolution and allow charge sharing between adjacent pixels, each layer is rotated by a 20° tilt angle about the x-axis and a 30° skew angle about the y-axis. Each layer is held by a block mounted on a carriage that can slide over rails. Auxiliary electronics is mounted close to the modules, on the rails. In between the arms of the telescope a large DUT can be placed into a box with a size of $550 \times 350 \times 40\,\mathrm{mm^3}$, with actuators for the DUT provided for translation in the x- and y-directions, while a rotation of the DUT about the x-axis is also allowed. Cooling is currently based on computer fans but in the near future it will be updated to support irradiated DUTs. Two overlapping scintillators for triggering are mounted on the rails on each end of CHROMIE and attached to photomultipliers. The trigger signal is then sent to a NIM (Nuclear Instrumentation Module) logic for shaping, discriminating and coinciding the signal with itself and a clock signal. After that, the trigger is sent to the CMS-standard AMC13 (Advanced Mezzanine Card for Slot 13) [8] board which distributes the trigger signal from the NIM logic and the 25 ns LHC clock to the units for the control of the modules and the readout of its values: the FEC (Front End Controller) [9] and FED (Front End Driver) [10], respectively. The AMC13, FEC and FED cards and their communication interface are all housed in a μTCA crate. The FEC and FED are connected via optical fibers to the FEROL (Front-End Readout Optical Link), while the auxiliary electronics (motherboard, voltage and temperature probes) is connected via $\mathrm{I^2C}$ to the computers [4]. The readout and DAQ of CHROMIE are displayed in Fig. 5.3, while the complete mechanical design of CHROMIE is shown in Fig. 5.4. A photo of CHROMIE on the commissioning site is shown in Fig. 5.5.

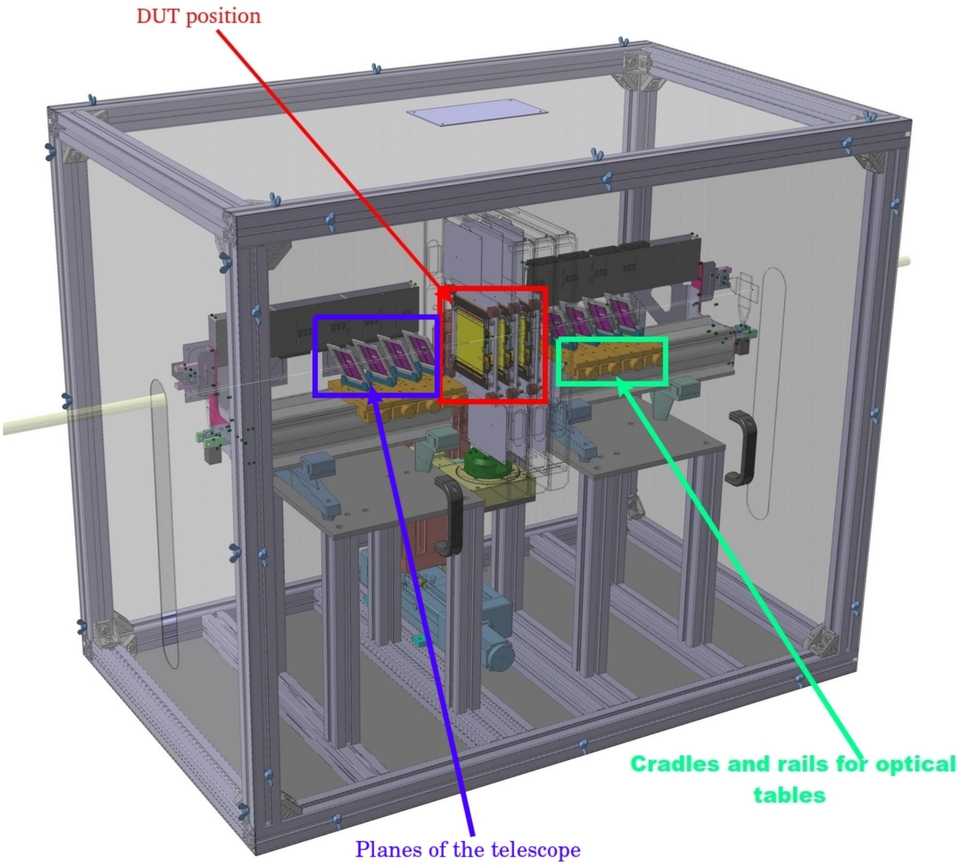

Figure 5.1: Left: Conceptual design of CHROMIE with the positions of the DUT, the telescope planes and the cradles and rails for optical tables. (Image: CMS.)

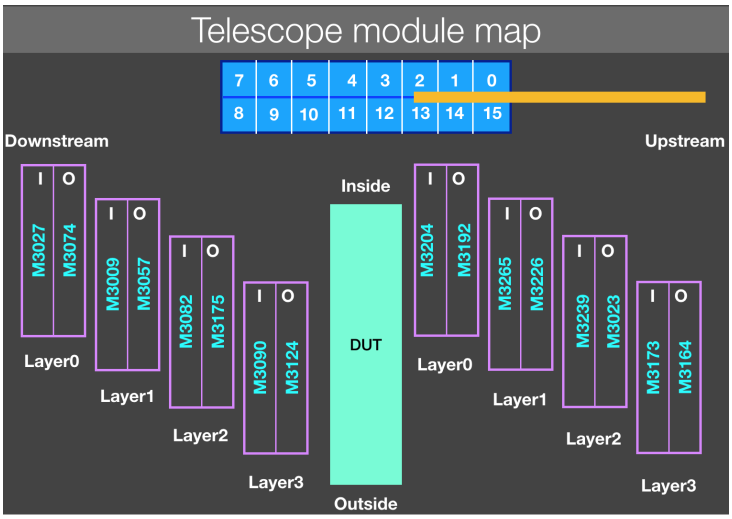

Figure 5.2: The module map of CHROMIE, where the production ID of each Phase-1 pixel module can be seen. (Modified from a CMS image.)

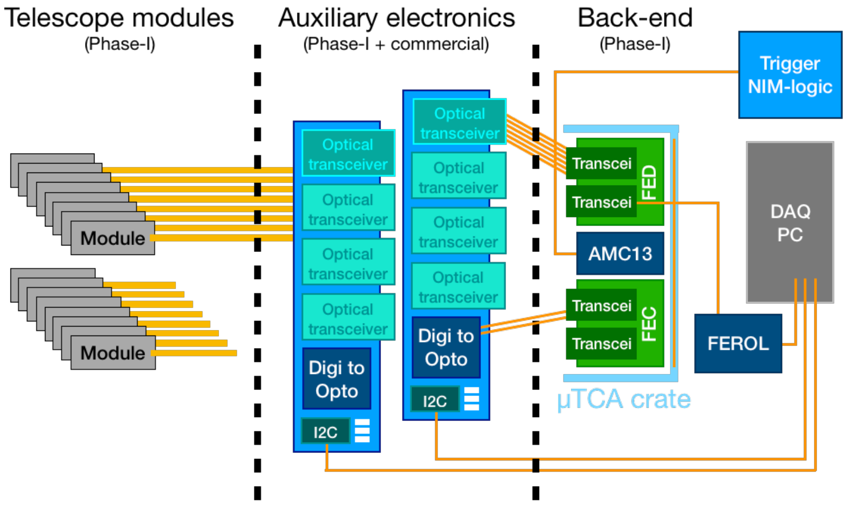

Figure 5.3: Left: The mostly CMS standard readout and DAQ of the CHROMIE telescope. It is analogous to the readout of the CMS Phase-1 Inner Tracker readout. The yellow ribbons represent electrical links. The orange arrows represent optical links. (Image: CMS.)

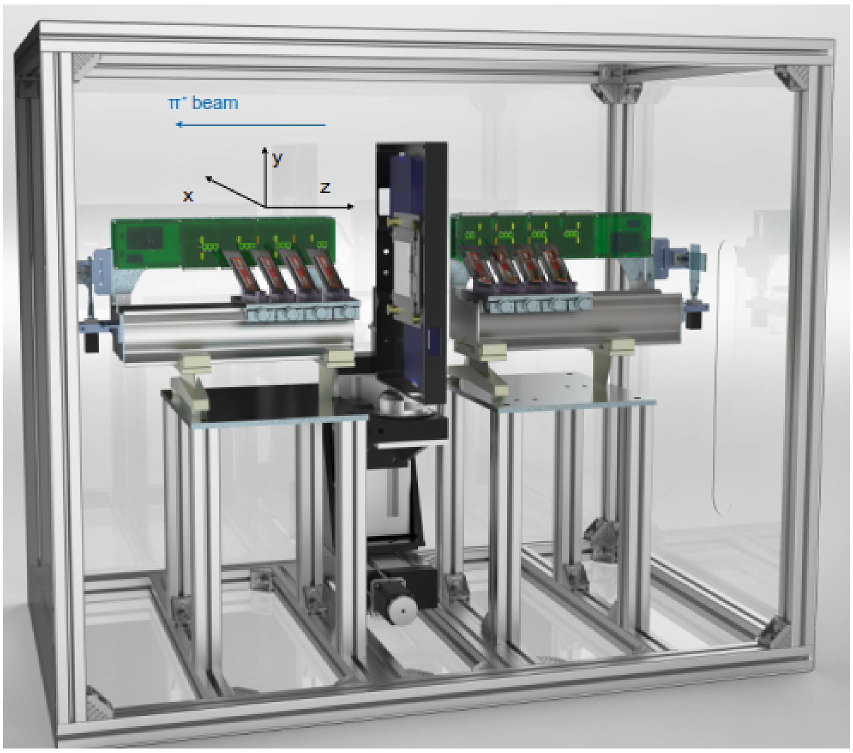

Figure 5.4: The mechanical design of the CHROMIE telescope, with a full-size 2S module in the center as the device under test (DUT). The length of the whole box is 1.30 m. (The beam direction is right-to-left. Drawing by Nicolas Siegrist, rendering with KeyShot.)

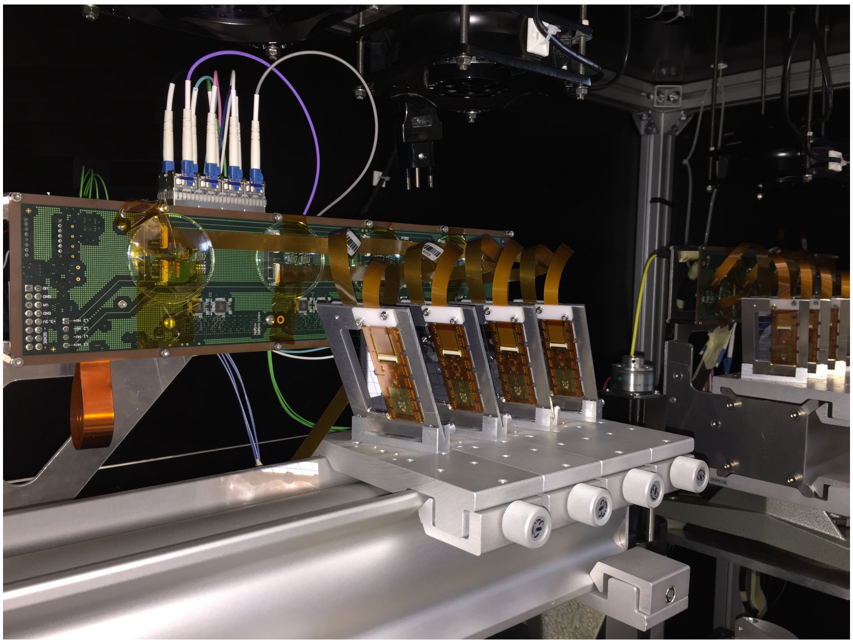

Figure 5.5: CHROMIE during its commissioning phase.

The readout software used by CHROMIE are the CMS-standard POS (Pixel Online Software) [11] and XDAQ [12]. XDAQ allows the usage of distributed, hardware controlling applications called Supervisors, which can be run distributed and independently on different machines, thus controlling various components of the telescope readout, while ensuring remote data-taking and monitoring of the machine during operation. For the data unpacking and analysis CMSSW (CMS Software) [13] is used (which is also CMS-standard). Moreover, a standalone tracking program based on CMSSW was developed by the CHROMIE Team, along with a standalone simulation program based on Geant4 [14] for the prediction of residuals, cluster charge, cluster size and other magnitudes before the beam tests.

5.3 Calibration tests

Before being mounted on the telescope each BPIX module had to undergo a set of tests called pre-calibration, which included an IV test (for leakage current measurement), a pixel functionality test, a soldering (bump bond) test, a pulse height optimization test and a module response to radioactive sources test. After the installation of the modules in the telescope the calibration tests "timing calibration", "trigger latency of the calibration pulse calibration", "threshold calibration with calibration pulse" and "gain calibration of individual pixels" were performed before the commissioning in the beam, when the modules were made to run synchronously. The functionality and integrity of CHROMIE were confirmed as all telescope modules could run synchronously and there was a strong correlation between the hits in different telescope layers which serves as an indication for particle tracks [15].

The ROC used in the original CMS pixel detector, psi46, showed expected inefficiencies when operated at higher data rates as soon as the LHC started operating at instantaneous luminosities above the design value. Therefore, new pixel ROCs had to be designed: an update of the original psi46, the psi46dig used in FPIX and BPIX layers 2, 3, and 4, and a dedicated ROC for BPIX layer 1, the PROC600, to cope with the tremendously high rates of up to 600 $\mathrm{MHz/cm^2}$.

psi46dig kept most of its predecessor's characteristics: pulse height readout, and 52×80 pixels organized in 26 double-columns of 2×80 pixels with common data transfer to latency buffers in the periphery outside the active pixel region. It is manufactured in the same 250 nm CMOS technology as the psi46, and its two main improvements are the larger data buffers and higher readout speed [16]. The layout of the readout chip can be divided into three functional blocks: pixel unit cells, double column periphery, and a controller - interface block [17].

A block diagram of a pixel unit cell (PUC) is shown in Fig. 5.6. Each pixel of the silicon sensor is connected to the bump pad of a PUC. Test pulses can either be injected into the amplifier directly or into a metal pad, which is capacitively coupled to the sensor. An important digital-to-analog converter (DAC) is the 8-bit Vcal which adjusts the height of test pulses. An additional control register (named CtrlReg) is used to increase the test range. The CalDel DAC delays the calibration pulse, which is a tool to test the functionality of the pixel cell and the bump bond connection, by a programmable amount of time. Signals are amplified and subsequently shaped in the PUC before they are passed to a comparator, which rejects pulses below a programmable threshold. Several DACs adjust the threshold, while a global threshold, which is common to all pixels, is set with the VthrComp DAC. Each pixel unit cell also has four individual trim bits, which reduce the global threshold by a programmable amount. If a signal passes the threshold, the pulse height is sampled after a programmable time delay and then the signal height is stored in the sample and hold circuit, and the PUC requests a readout from the double column periphery by sending a signal on the ColOr line. The PUC becomes insensitive while the readout is ongoing [17].

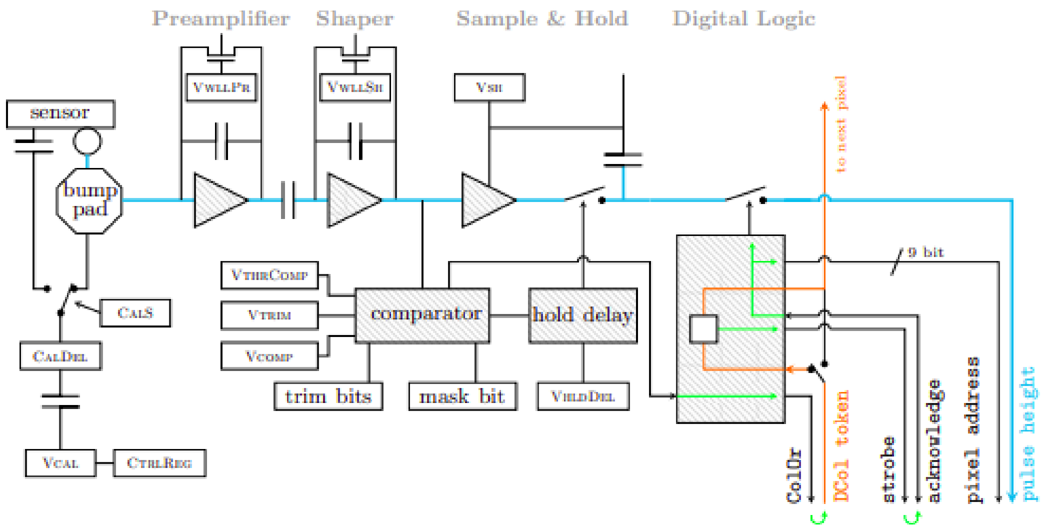

Figure 5.6: A simplified schematic of the pixel unit cell where some of the DACs and registered can be programmed (e.g. the pulse height).

The program used for hardware testing of the Phase-1 BPIX module is the Pixel eXpert Analysis Readout (pXar). pXar can be used to program and read out devices featuring psi46-type ROCs via the PSI digital test board (DTB). Most of the DTB firmware complexity is abstracted to allow users to address the attached devices via a simple interface [17].

Members of the CMS group at NCSR "Demokritos" performed all the required pre-calibration tests on a single Phase-1 BPIX module. More details about the test steps on a single BPIX module are described below.

Before the set of tests, during the pre-test, a VthrComp-CalDel scan is performed. For a fixed Vcal DAC value, which relates to the strength of internal calibrate signal, the ROC works in a certain region of VthrComp-CalDel DAC values. To perform further ROC tests, one has to find a stable working point (Fig. 5.7). The working point found for one pixel is also valid for all other pixels in the same ROC because the variation between pixels in a ROC are relatively small, and then the series of tests can begin. The first test, the IV test, is necessary in order to ensure the electric quality of the silicon sensor in a pixel module. The IV measurement is performed by varying reverse biased voltage from 0 V to 300 V in steps of 5 V (absolute values) to verify the absence of sensor breakdown. The purpose of the second test, the pixel functionality test (PixelAlive), is to check if pixels can respond as expected. This is done by inducing signal from internal calibration capacitance. A tested pixel is considered alive if all the calibration signals are registered, but is considered completely dead if no signal is recorded. At the end of the test the number of dead pixels for each ROC is returned as output. The aim of the third test, the soldering or bump-bonding (BB) test is to identify missing or damaged bumps. Damage of the bonds between ROCs and the silicon sensor might have occurred during the module assembly, and thus it is necessary to check the quality of bumps. Calibration signal is injected from the ROC directly to the sensor for each pixel, and if there is a missing or damaged bump, no signal will be received from the corresponding pixel. A map of good bumps is returned as output. The fourth test, the pulse height optimization (GainPedestal), is required, since the pulse height contains the information of how many electron-hole pairs are created. The pulse height is measured (in ADC units) as function of the calibration voltage (in DAC units). It has been found that the correlation between the pulse height and the amplitude of the calibration signal can be described by a linear function over a large range. Calibration signals with various amplitudes are injected into every pixel, and the corresponding pulse heights are measured in order to determine the correlation for each pixel. The gain is the slope of the linear fit, while the pedestal is the offset. Finally, during the fifth test, the radioactive source test (XRay test), measures the efficiency of ROCs under X-ray hit rates through the hit rate for each pixel under various X-ray fluxes. The efficiency of a pixel is measured by sending a number of calibration signals to a specific pixel and checking how many Vcal hits are received. It is then defined as the number of received Vcal hits over the number of sent triggers. Every time, during an X-ray test, the tested module was sealed inside a protective light-tight box for cutting the background noise, and tests were performed with both americium-241 and caesium-137.

5.4 Tracking and alignment

The preliminary tracking algorithm used in the data analysis was developed in Python and C by members of the NCSR "Demokritos" and IPHC-Strasbourg CMS groups, and added as a separate module to CMSSW (CMS Software) [13]. It is called during the analysis of every test beam run data and consists of a set of steps which are followed every time: Firstly, the clusters from noise hits are removed, secondly, an alignment is applied, thirdly, the seeding is performed and finally, the pattern recognition is conducted.

Knowing the accurate position of the telescope modules is crucial for optimizing the resolution. By reconstructing particle tracks from different data runs and minimizing the residuals over all the valid tracks, by translating the detectors parallel to the three axes and rotating them around the axes, the alignment procedure can be performed. The translations and rotations are usually performed following a series of iterations. However, at this point it should be mentioned that a detailed iterative alignment hasn't been implemented in CMSSW yet, but this work is still in progress. Instead of the iterative alignment, only a coarse alignment is applied in our tracking algorithm, consisting of a translation of the telescope modules +50 cm parallel to the

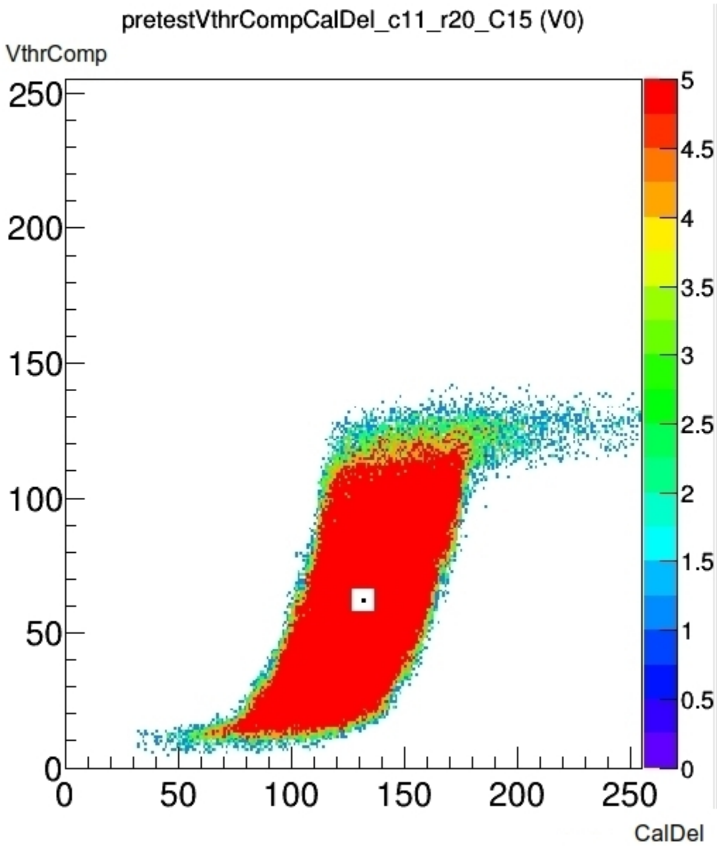

Figure 5.7: Optimization of the calibration pulse time delay where a two-dimensional scan of CalDel (delay of the pulse) versus VThrComp (global ROC threshold) is performed. The number of registered hits is color-coded. It is worth noting that VThrComp is an inverted DAC so that a low value corresponds to a large threshold. The optimized value is indicated as the black dot in the white square. This plot is also nicknamed as "tornado plot", due to its shape, and is a direct output of pXar.

x-axis in global coordinates. It is demanded that all tracks should be parallel to the beam axis (the z-axis).

The seeding in our method is basically a search over clusters (conducted using global coordinates) for 2 points, one in the first Seeding Layer SL1 and one in the second Seeding Layer SL2 (where SL1 and SL2 run through various combinations of CHROMIE layers, e.g. the first and second Layers: L1-L2), with $\Delta x < 0.1$ cm and $\Delta y < 0.1$ cm. During the seeding procedure initially two detid (detector ID) iterators are defined and it is checked that the first detid corresponds to one of the two modules of SL1, and that the second detid corresponds to one of the two modules of SL2. Loops are executed over the clusters of these modules, and then a subsequent check for clusters from noise hits follows. Afterwards, the (non-iterative) alignment is applied. Finally, the conditions for Δx, Δy are checked.

The seeding is initially applied on the combination of Layers L1-L2, then on L2-L3, and finally on L3-L4, until a seed is found. Further combinations are not examined, since on the layers of the arm of CHROMIE behind the DUT on the way of the beam (the second arm) two dead and one noisy modules are located.

For the pattern recognition the program looks for the cluster with the smallest distance (in two dimensions) from the track within the telescope layer, then the track is fitted including the new cluster in the list minimizing the 2D distance in the telescope layer. Short tracks which don't correspond to hits in at least 4 modules are not considered valid tracks in our algorithm.

Driven by the main goal of minimizing the tracking inefficiency, our groups performed an extended analysis on a reference run (run 100368) with a total number of 32536 events, from a beam test with 120 GeV π^+ which had taken place at CERN, for the selection of the optimal maximum limits for Δx, Δy, and the best combination of seed layers. The results, which show why the final version of the tracking algorithm is as described above, are summarized in Tables 5.1, 5.2 and 5.3. Additionally, for $\Delta x < 0.1$ cm and $\Delta y < 0.1$ cm it is observed that for the L1-L8 seed layers there are 15286 events with no seeds, which corresponds to a 15286/32536 = 47% inefficiency limit. This is how it is deduced that L8 is not a good layer for seeding, since it is also far from the first functional layers. Furthermore, it is observed that for the L3-L8 seed layers there are 14178 events with no seeds, which corresponds to a 14178/32536 = 43.58% inefficiency limit. For L1-L4 there are 16208 events with no seeds, which corresponds to a 16208/32536 = 49.82% inefficiency limit. For L1-L5 there are 15146 events with no seeds, which corresponds to a 15146/32536 = 46.55% inefficiency limit. An even further optimization is achieved when multiple combinations of layers are taken into account, e.g. if a seed isn't found in L1-L2, it is searched in L2-L3, and then if a seed isn't found even there, it is searched in L3-L4, as described above. For $\Delta x < 1$ cm and $\Delta y < 1$ cm the L1-L2 & L2-L3 & L3-L4 combination of seed layers returns 3417 events with no seeds, corresponding to a 10.5% inefficiency.

After performing the tracking algorithm on a run of 32536 events (run 100368), it is found that:

$$\begin{aligned}&\frac{\text{Number of events with at least 4 layers with at least 1 cluster and 0 seeds}}{\text{Number of events with at least 4 layers with at least 1 cluster}}\\&\qquad = \frac{6082}{28551} = 21.3\%\end{aligned} \tag{5.1}$$

From (5.1) it is found that the seeding efficiency is 78.7%. Furthermore, since the number of events with 0 layers with at least 1 cluster is 1015 in that run and 1015/32536 = 3.1%, the performed analysis on run 100368 gives us a good estimation at 96.9% for the upper limit of the efficiency.

Table 5.1: Inefficiency for various combinations of $(\Delta x)_{max}$ and $(\Delta y)_{max}$ with L1-L2 seeds.

$(\Delta x)_{max}$ (cm)	$(\Delta y)_{max}$ (cm)	Events with 0 seeds	Total events	Inefficiency (%)
0.1	0.1	9761	32536	32.0
0.1	0.2	9534	32536	29.3
0.1	0.5	9436	32536	29.0
0.1	1.0	9414	32536	28.9
2.0	0.1	6812	32536	20.9
0.2	0.2	8398	32536	25.8
0.3	0.3	7642	32536	23.5
0.5	0.5	6866	32536	21.1
1.0	1.0	6601	32536	20.3
2.0	2.0	6565	32536	20.2

Table 5.2: Inefficiency for various combinations of $(\Delta x)_{max}$ and $(\Delta y)_{max}$ with L2-L3 seeds.

$(\Delta x)_{max}$ (cm)	$(\Delta y)_{max}$ (cm)	Events with 0 seeds	Total events	Inefficiency (%)
1.0	1.0	5896	32536	18.1
0.1	0.1	9267	32536	28.5

Table 5.3: Inefficiency for various combinations of seeding layers; $(\Delta x)_{max} = (\Delta y)_{max} = 0.1$ cm.

Layers for seeding	Events with 0 seeds	Total events	Inefficiency (%)
L1-L2	9761	32536	30.0
L2-L3	9267	32536	28.5
L1-L2 & L2-L3	6254	32536	19.2
L1-L2, L2-L3 & L3-L4	4798	32536	14.8

5.5 Test beam data and simulation comparison

Subsequently, a comparison between the test beam data and the Geant4 simulation results is presented. The Geant4 simulation program developed for CHROMIE is very similar to the Geant4 simulation program developed for the CHROMini telescope. The latter will be described in detail in Chapter 6, and that's why here we will focus exclusively on the simulation results and will not dive into technical details related to the implementation of the program.

All the plots from the beam test are derived from the analysis of the aforementioned run 100368 with 32536 events, where the beam diameter is estimated from the simulation to be 15 mm, while only the left modules of each telescope layer (as seen on the way of the beam) are hit. As there are 2 inactive modules on the left side of CHROMIE (in L6 and L7) only 6 out of 8 modules are used in the experimental data analysis, contrary to the 8 out of 8 modules used in the simulation. Of those six modules one is significantly noisier than the rest in the analyzed run.

Different ionizations, Bremsstrahlung, pair production, annihilation, the photoelectric effect, gamma production, Compton scattering, Rayleigh scattering and the Klein-Nishina model for differential cross section calculations are among the processes included in the physics list [14] of the standalone Geant4 program for CHROMIE. The chosen statistical parameters of the general particle source (GPS) for the 120 GeV π^+ are: σ = 100 keV; position =

$(-0.3, -0.65, 200)$ cm; the shape of the beam is selected ellipsoidal with $x_{half} = y_{half} = 7.5$ mm. For each event the program calculates the stored energy in each pixel on each of the telescope modules and when dividing this energy by the one required for a single electron-hole pair production in silicon (= 3.67 eV) one can find the charge (in number of electrons) collected in each pixel. If this charge exceeds the threshold of the Phase-1 pixels (set at 1700 electrons) it is considered that there is a hit in the examined pixel in the current event. Charge sharing between adjacent pixels has also been included in the simulation, taking into account weight factors resulting from the pulse heights corresponding to the different collected charge in each pixel. The impact point of the beam in each module is defined as the mean point of the centroids of the front surfaces of the hit pixels multiplied by their corresponding weight factors. A line of best fit is then calculated for the impact points in all the layers, which is afterwards used in the estimation of the residuals.

The visualized geometry of the Geant4 simulation with a primary π^+ track, a secondary δ-electron track and a 2S module used as a DUT is shown in Fig. 5.8. From the simulation, the angular straggling is estimated at about 50-60 μrad on average.

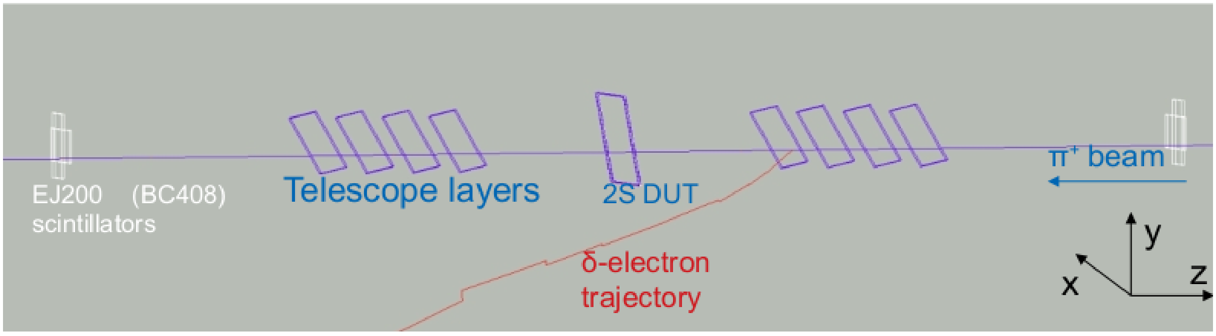

Figure 5.8: Visualization of the Geant4-simulated geometry of CHROMIE under beam. The DUT is a 2S module: 2 Si sensors (102700 μm × 94108 μm × 320 μm), with spacing between the sensors: 2 mm (for the given type of 2S module it was later decided that the spacing would be 1.7 mm for the production phase modules); strip pitch: 90 μm; active depth: 240 μm.

The total energy lost by the primary pions of the beam inside the silicon volume of CHROMIE Layer 1 is given in Fig. 5.9 as the sum of the energy deposited in the material and the kinetic energy of newly produced secondary particles (mostly δ-electrons), with a most probable value (MPV) equal to 1.086 MeV and $\sigma = 0.098$ MeV after a Landau fit (Fig. 5.10). These values are indicative for all the other CHROMIE layers (Table 5.4).

As seen in Fig. 5.11 and 5.12, the residuals in the x and y-directions, respectively, of Layer 3, are slightly larger in the test beam data than the predicted ones. The same behavior is observed in the rest of the modules where sometimes the experimental standard deviation might even exceed 30 μm. This is mostly due to the oversimplified one-step alignment method and the noise in specific pixels of the sensors, which is not present in the simulation.

Fig. 5.13 depicts the hit positions for the left module of Layer 2. By counting the size of the beam spot on the module in pixels (from the test beam plot) and multiplying it by the pixel size in each direction, the value of the beam diameter is estimated, and thus it is introduced as parameter in the simulation run. The shape of the beam spot can be explained by the rotations of the modules initially about the x-axis and subsequently about the y-axis. The noisy pixels are clearly visible. The related test beam and simulation plots are similar for all the other layers of CHROMIE.

In addition, a cluster size investigation is made for all the modules in the x- and y-directions.

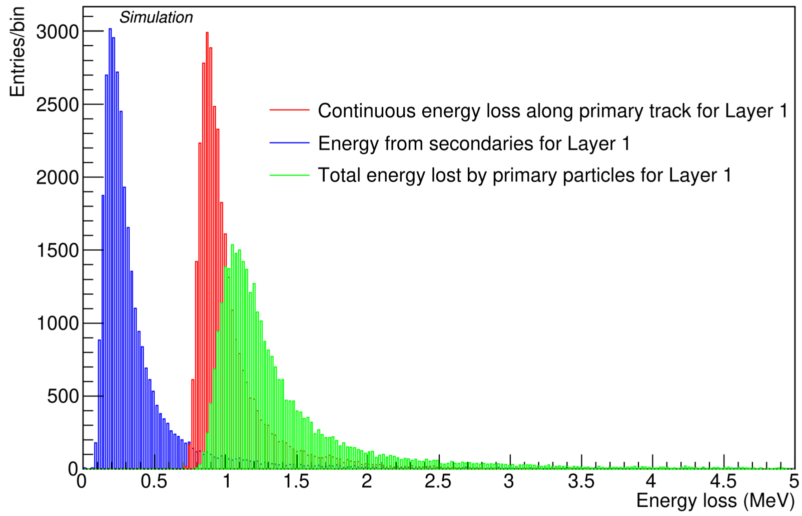

Figure 5.9: Energy lost by primary particles (120 GeV π^+) in CHROMIE Layer 1 (simulation).

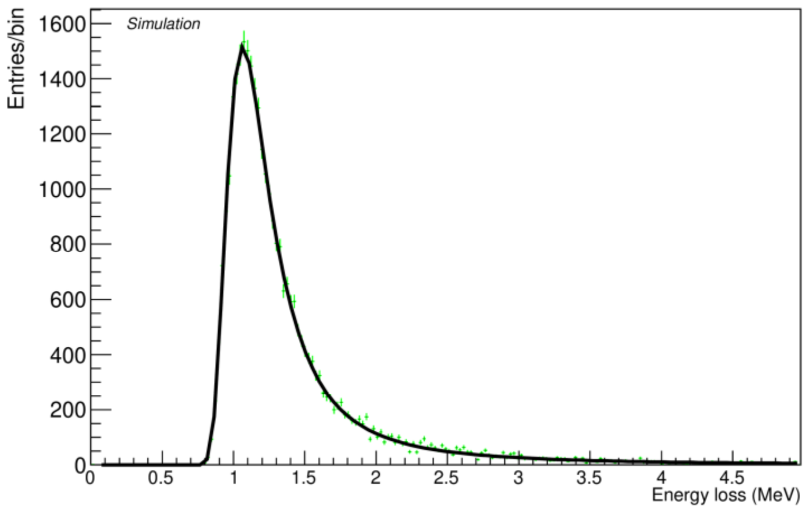

Figure 5.10: Total energy lost by primary particles (120 GeV π^+) in CHROMIE Layer 1 after a Landau fit (simulation).
Most probable value (MPV): 1.086 MeV. Sigma: 0.098 MeV.

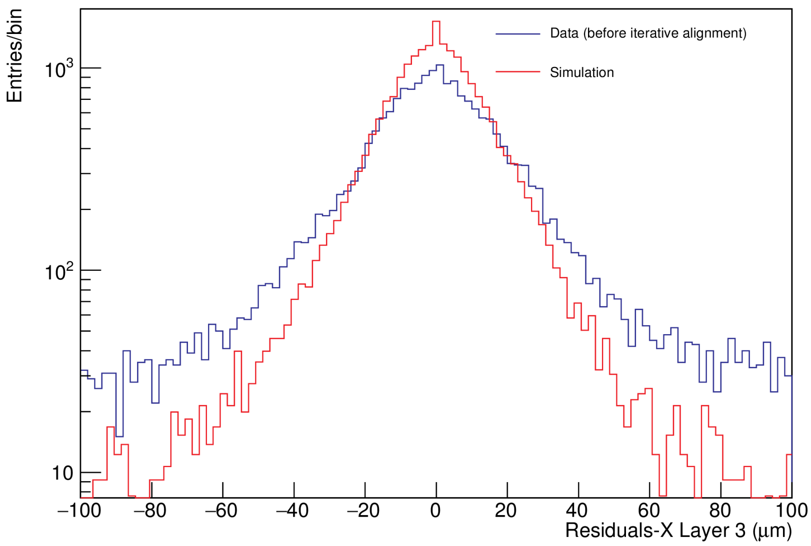

Figure 5.11: X-residuals for the left module of Layer 3 for a 120 GeV π^+ beam (comparison between beam test data before iterative alignment and simulation). Simulation residuals scaled for 26814 valid tracks from the beam test run out of 32536 total events.
Standard deviation (beam test): 29.1 μm; standard deviation (simulation): 19.8 μm.

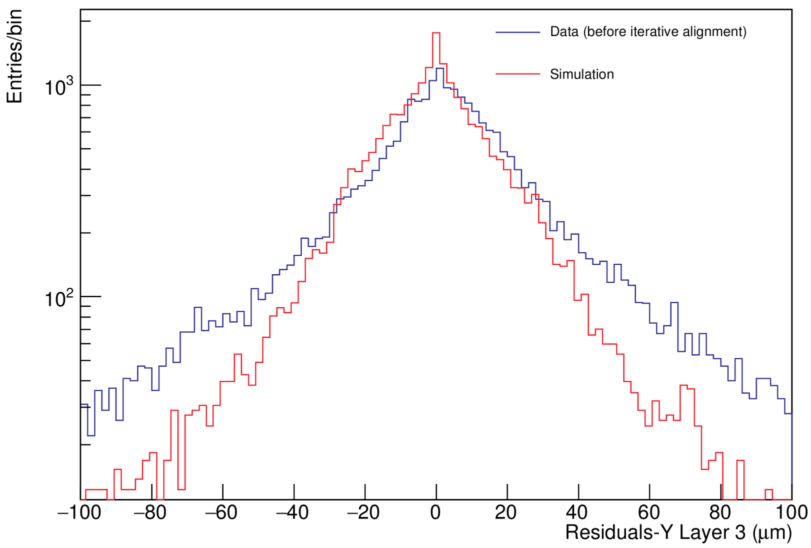

Figure 5.12: Y-residuals for the left module of Layer 3 for a 120 GeV π^+ beam (comparison between beam test data before iterative alignment and simulation). Simulation residuals scaled for 26814 valid tracks from the beam test run out of 32536 total events.
Standard deviation (beam test): 31.4 μm; standard deviation (simulation): 23.3 μm.

Table 5.4: Total energy lost by primary particles (120 GeV π^+, simulation) for the CHROMIE layers. A Landau fit has been performed.

CHROMIE layer ID	Most probable value (MeV)	Mean value (MeV)
1	1.086	1.398
2	1.089	1.412
3	1.090	1.421
4	1.091	1.428
5	1.084	1.394
6	1.093	1.413
7	1.090	1.424
8	1.095	1.429

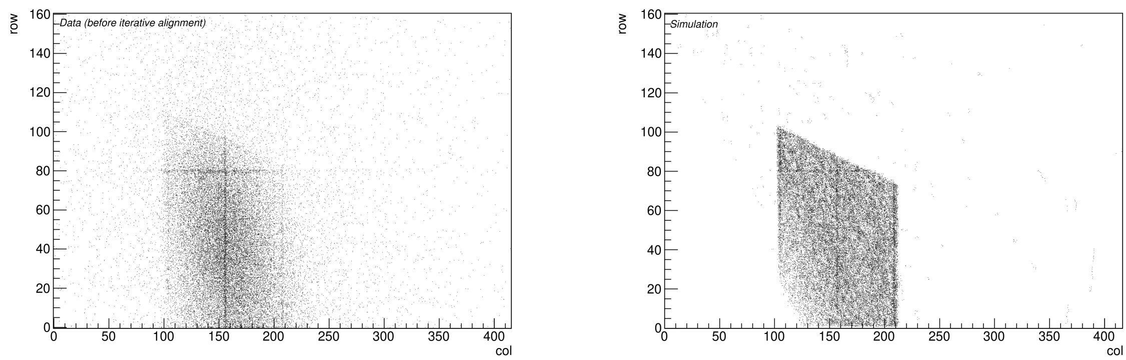

Figure 5.13: Hit positions per column per row for the left module of Layer 2 for a 120 GeV π^+ beam (left: beam test, right: simulation with beam diameter = 15 mm and σ_E = 100 keV); the beam size is measured from the beam spot on the hit position map for the same module, obtained from the analysis of the real run, and thus the above parameters are selected for the simulation run.

The mean cluster size in x in number of pixels derived from the beam test data lies in the range [1.469, 1.991] for the different modules, where the average value for all modules is 1.875, compared to the range [1.639, 1.669] extracted from the simulation, where the average value for all modules is 1.654. On the other hand, the mean cluster size in y in number of pixels derived from the beam test data lies in the range [1.355, 1.754] for the different modules, where the average value for all modules is 1.665, compared to the range [1.577, 1.608] extracted from the simulation, where the average value for all modules is 1.596. The slightly larger values from the test beam data could be due to the presence of broken and noisy pixels. Detailed results are summarized in Tables 5.5 and 5.6.

5.6 Future prospects

As CHROMIE, the new high-rate telescope, is mostly based on technology developed for the CMS experiment, it is thus being compatible with previously existing CMS hardware and software. It can be used for tests of front-end (FE) electronics under high particle rate and high occupancy, to study the performance and saturation effects vs. track rate, and to monitor

Table 5.5: Mean value of cluster size in the x-direction for CHROMIE; comparison between beam test data and simulation.

CHROMIE layer (only left modules are hit)	1	2	3	4	5	6	7	8
Mean value of cluster size-X (in pixels; beam test)	1.983	1.937	1.973	1.469	1.899	-	-	1.991
Mean value of cluster size-X (in pixels; simulation)	1.639	1.642	1.649	1.653	1.658	1.661	1.664	1.669

Table 5.6: Mean value of cluster size in the y-direction for CHROMIE; comparison between beam test data and simulation.

CHROMIE layer (only left modules are hit)	1	2	3	4	5	6	7	8
Mean value of cluster size-Y (in pixels; beam test)	1.695	1.736	1.730	1.355	1.718	-	-	1.754
Mean value of cluster size-Y (in pixels; simulation)	1.577	1.583	1.594	1.599	1.598	1.603	1.603	1.608

effects of radiation damage e.g. on silicon sensors. That's why its commissioning constituted a milestone in the R&D phase for the upgrade of the CMS detector. A standalone simulation program based on the Geant4 toolkit has been developed to predict the response of the telescope under various types of particle beams, which could be used as a potential base for future simulations of any particle telescope with a 2S module as DUT (e.g. CHROMini and DATURA, which will be described in the next chapters) or any experiment containing a 2S module (such as MUonE [18]). This program could be used for estimating unknown beam parameters through comparison of its output with plots from real data where some magnitudes are unknown. There is currently a good comparison in the resolution and cluster occupancy between the test beam data and the simulation results [15].

In 2020 a test of the Phase-2 CMS Tracker readout in the lab with CHROMIE was scheduled. In 2021-2022 beams will be back at CERN and CHROMIE will be again available for beam tests. In the near future the amount of layers of CHROMIE might be reduced to 6 and some modules might be replaced for better coverage. In order to accommodate more users, CHROMIE will also become less CMS-standard and more compatible with non-CMS DAQ and trigger logic units (TLU) [19].

Bibliography

[1] G. Apollinari et al., *High-Luminosity Large Hadron Collider (HL-LHC): Technical Design Report V. 0.1*, CERN Yellow Rep.Monogr. 4 (2017) 1-516 CERN-2017-007-M.

[2] CMS Collaboration, *The Phase-2 Upgrade of the CMS Tracker, CERN-LHCC-2017-009, [CMS-TDR-17-001]* (2017).

[3] Nikkie Deelen, *Characterizing detector modules for the Upgrade of the Silicon Tracker of the Compact Muon Solenoid experiment*, CERN-THESIS-2019-275; 1000100329.

[4] N. Deelen, S. Mersi, *CHROMIE - The CMS High Rate Telescope*, 7th Beam Telescopes and Test Beams Workshop, 14-18 January 2019, CERN.

[5] P. Marchand, A. Ouadi, M. Pellicioli, D. Brasse, *Cyrcé, un cyclotron pour la recherche et l'enseignement en Alsace*, L'Actualité Chimique 386 (2014) 9-14.

[6] P. Asenov, *Test beam facility at CYRCé for high particle rate studies with a CMS upgrade module: design and simulation*, 7th Beam Telescopes and Test Beams Workshop, 14-18 January 2019, CERN.

[7] J.B. Adams, *A design of the European 300 GeV research facilities*, MC-70-60; CERN-SPC-299, CERN, Geneva Switzerland, 1970.

[8] E. Hazen, A. Heister, C. Hill, J. Rohlf, S.X. Wu, D. Zou, *The AMC13XG: a new generation clock/timing/DAQ module for CMS MicroTCA*, JINST 8 (2013) C12036.

[9] K. Kloukinas, W. Bialas, C. Ljuslin, A. Marchioro, E. Murer, C. Paillard, F. Drouhin, E. Vlasov, *FEC-CCS: A common front-end controller card for the CMS detector electronics*, C06-09-25.12, Sep 2006, p.179-184.

[10] S. A. Baird et al., *The CMS Tracker Readout Front End Driver*, 8th Workshop on Electronics for LHC Experiments, Colmar, France, 9 - 13 Sep 2002, pp.296-300 (CERN-2002-003).

[11] *CMS Pixel Online Software for the CMS Pixel Telescope*, https://gitlab.cern.ch/telescopePOS.

[12] *XDAQ CMS Online Software project page*, https://twiki.cern.ch/twiki/bin/view/CMSPublic/CMSOS.

[13] *CMS Offline Software*, https://cms-sw.github.io/.

[14] S. Agostinelli et al., *Geant4: A simulation toolkit*, Nucl. Instrum. Meth. A vol. 506 (2003) pp. 250-303.

[15] Patrick Asenov, *Commissioning and simulation of CHROMIE, a high-rate test beam telescope*, JINST 15 (2020) 02, C02003.

[16] W. Adam et al., *The DAQ and control system for the CMS Phase-1 pixel detector upgrade*, JINST 14 (2019) 10, P10017.

[17] Simon Spannagel, Beat Meier, Hanno Perrey, *The pxarCore Library - Technical Documentation, Reference Manual, and Sample Applications*, CMS NOTE -2016/001.

[18] Umberto Marconi, *The MUonE experiment*, EPJ Web Conf. 212 (2019) 01003.

[19] N. Deelen, *First results and future plans of the CHROMIE telescope*, 8th Beam Telescopes and Test Beams Workshop, 27-31 January 2020, Tbilisi State University.

Chapter 6

CHROMini: Simulation and comparison with test beam data

This chapter presents the standalone simulation of CHROMini, which is another high-rate particle telescope that has been assembled at the 25 MeV proton test beam facility at IPHC-Strasbourg. The standalone simulation was used to verify the design of the telescope and to estimate its expected performance, with respect to energy deposition in the detector components, multiple scattering of the protons, spatial resolution, beam profile, hit occupancy and hit multiplicity.

6.1 The cyclotron CYRCé and the CHROMini telescope

It has been previously mentioned that the upgrade of the LHC to the High-Luminosity LHC (HL-LHC) is expected to increase the current instantaneous luminosity by a factor of 5 to 7 [1]. The new silicon tracking devices that CMS [2] will build should be tested under beam during the R&D period. In order to test the CMS tracker modules under the nominal LHC rate, a novel pixel telescope named CHROMini (a mini-version of CHROMIE, the CMS High-Rate telescOpe MachInE, see https://chromie-telescope.web.cern.ch/chromie-telescope/ and the previous chapter) was built and commissioned at the Institut Pluridisciplinaire Hubert Curien (IPHC) in Strasbourg for beam tests. The aim of these tests will be the measurement of the response of prototype modules for the upcoming CMS Phase-2 Tracker upgrade [3].

IPHC has already installed a specific CMS beam line for the irradiation tests of detectors with the 25 MeV proton beam of the cyclotron CYRCé. CYRCé is a particle accelerator managed by the Centre national de la recherche scientifique (CNRS), which produces radioactive elements by transmutation for the study of living organisms, diagnostics and the evaluation of new medical drugs. The cyclotron is confined in a concrete bunker to contain the radiation emitted when the accelerator is in operation, and is surrounded by aseptic clean rooms (of a total area of 130 m^2) that house chemistry laboratories with shielded enclosures for the preparation of the radioactive molecules intended for medical research applications [4], [5], [6].

The Plateforme de Radiobiologie Expérimentale auprès de Cyrcé (PRECy, Experimental Radiobiology Platform at Cyrcé) is an experimental radiobiology platform. Its objective is to allow a better understanding of the effect of proton radiation on living organisms. A first prototype of the PRECY transport beam line has been installed in the cyclotron casemate. The first in vivo and in vitro irradiations in the new experiment room have begun in the beginning of 2020. With

PRECY, a homogeneous dose deposit (at ±2%) is achieved on a surface of 24 mm in diameter and a path in water of 6 mm. The dose rates are planned to range from 0.01 Gy/minute to 10 Gy/ms (under development).

The PRECY transfer beam line is connected to the dedicated CMS beam line. The CMS beam line is composed of quadrupoles and steerers, and contains several beam diagnostic instruments, while the beam leaves the vacuum chamber through a thin aluminum foil (window). Beam intensities range from 1 fA to 100 nA. The Cyclotron delivers a pulsed beam with a frequency of 85 MHz, which can be brought down to 42.5 MHz with a kicker, thus allowing detector and electronics operation at frequencies close to the nominal LHC rate. Schematics and photographs of the CYRCé cyclotron and the PRECY transfer line are shown in Fig. 6.1, and additional schematics of the CMS beam line are shown in Fig. 6.1 and Fig. 6.2 [5], [6].

The CHROMini telescope (sort of a mini version of the CHROMIE telescope which was described in the previous chapter) is the experimental setup for the aforementioned irradiation tests. It consists of two thin beam scintillators, a mechanical *x-y* positioner for the device under test (DUT) and two reference planes (one in front and one behind the DUT), each containing two CMS Barrel Pixel (BPIX) Phase-1 modules (of the same type as the ones used in the current CMS pixel detector) positioned side by side. The pixel modules are read out by an intermediate board. CHROMini allows to determine individual trajectories of protons and the impact point in the DUT with a spatial resolution of the order of 100 microns (the granularity of the DUT is 90 μm), while it is mainly limited by multiple scattering. The electronic readout and Data Acquisition (DAQ) chain of CHROMini are mostly CMS-standard [5], [6].

It is worth emphasizing that in its final edition CHROMini should consist of two reference planes placed in front and behind the full 2S module device under test (DUT), respectively, with each plane consisting of two CMS Pixel Phase-1 silicon modules. Nevertheless, during the first beam tests in July and December 2019 only a single pixel module was placed behind a 2S mini-module (on the way of the beam). The 2S mini-module was assembled at KIT. The differences in the setups are sketched in Fig. 6.3 and a photo of the 2019 test beam setup is shown in Fig. 6.4. More than two telescope planes cannot be added, since the range in Si for 25 MeV protons is about 3 mm, which is only slightly larger than the total thickness of the planned components along the way of the beam [5], [6].

6.2 Structure of the simulation program

Subsequently, the development and various outputs of a standalone Geant4 [7] simulation program which was used for the design of CHROMini and the optimization of its geometry and materials will be analyzed. The physics processes used in the simulation, as well as the algorithms for all the related calculations with respect to resolution and charge sharing, will be discussed. (Apart from the beam characteristics and the number/orientation of Phase-1 pixel modules and scintillators, all technical details described here apply for CHROMIE and the simulation outlined in the previous chapter as well.)

The repositories containing the various versions of the code used for this application can be found here: https://github.com/pasenov. They are named *PhaseIIBeam_vN*, where N is the version number. The latest versions of the code contain all the features described in this document.

The program for the simulation of CHROMini (and of CHROMIE as well) is structured more or less like a standard Geant4 program. It consists of the main *PhaseII.cc*, a *CMakeLists.txt* file which contains a set of directives and instructions describing the project's source files and targets (executable), a *GNUmakefile* tool which is designed to build libraries and programs

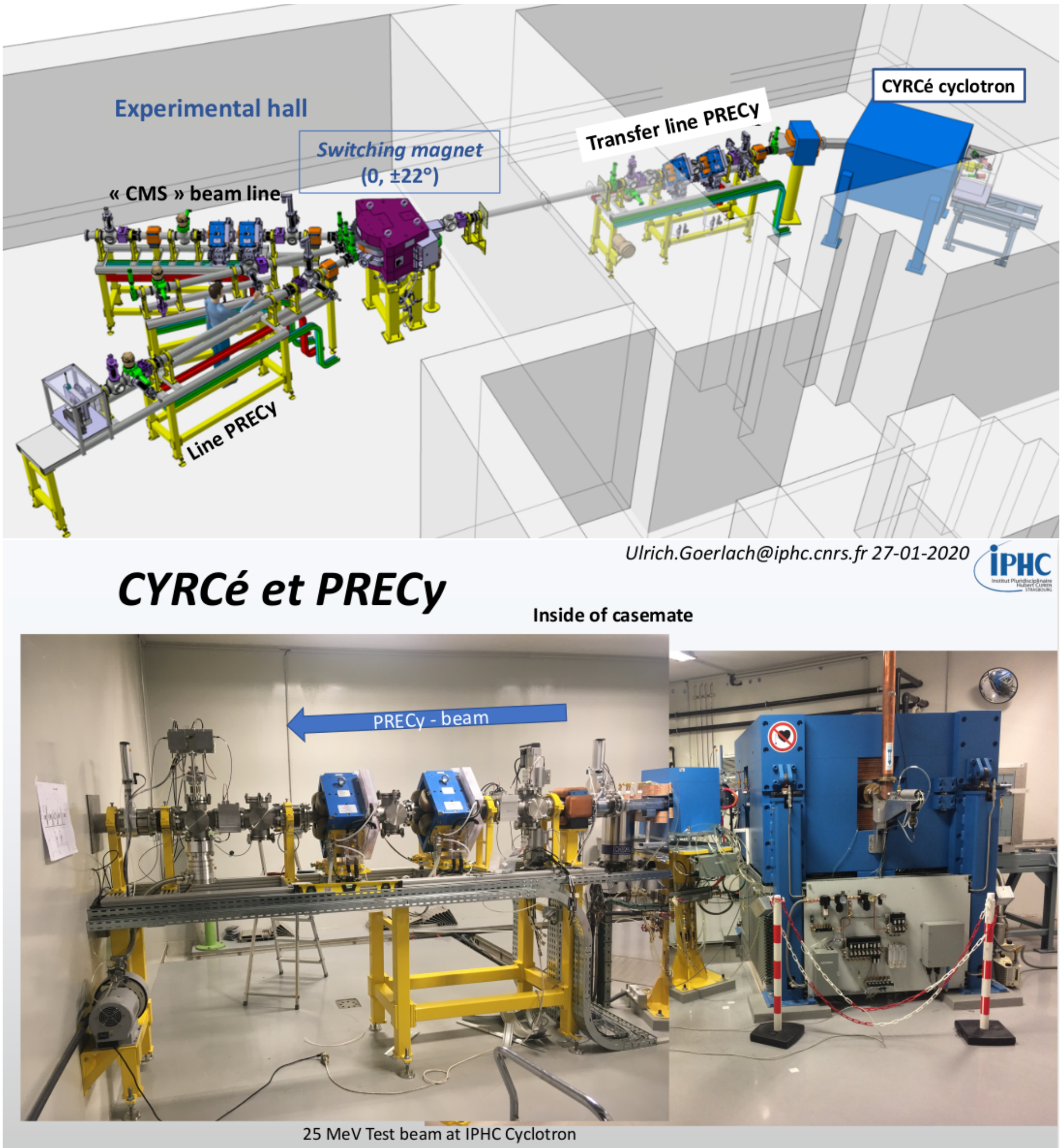

Figure 6.1: Schematics (top) and photographs (bottom) of the CYRCé cyclotron, the PRECY transfer line and the new CMS line. (Images: IPHC.)

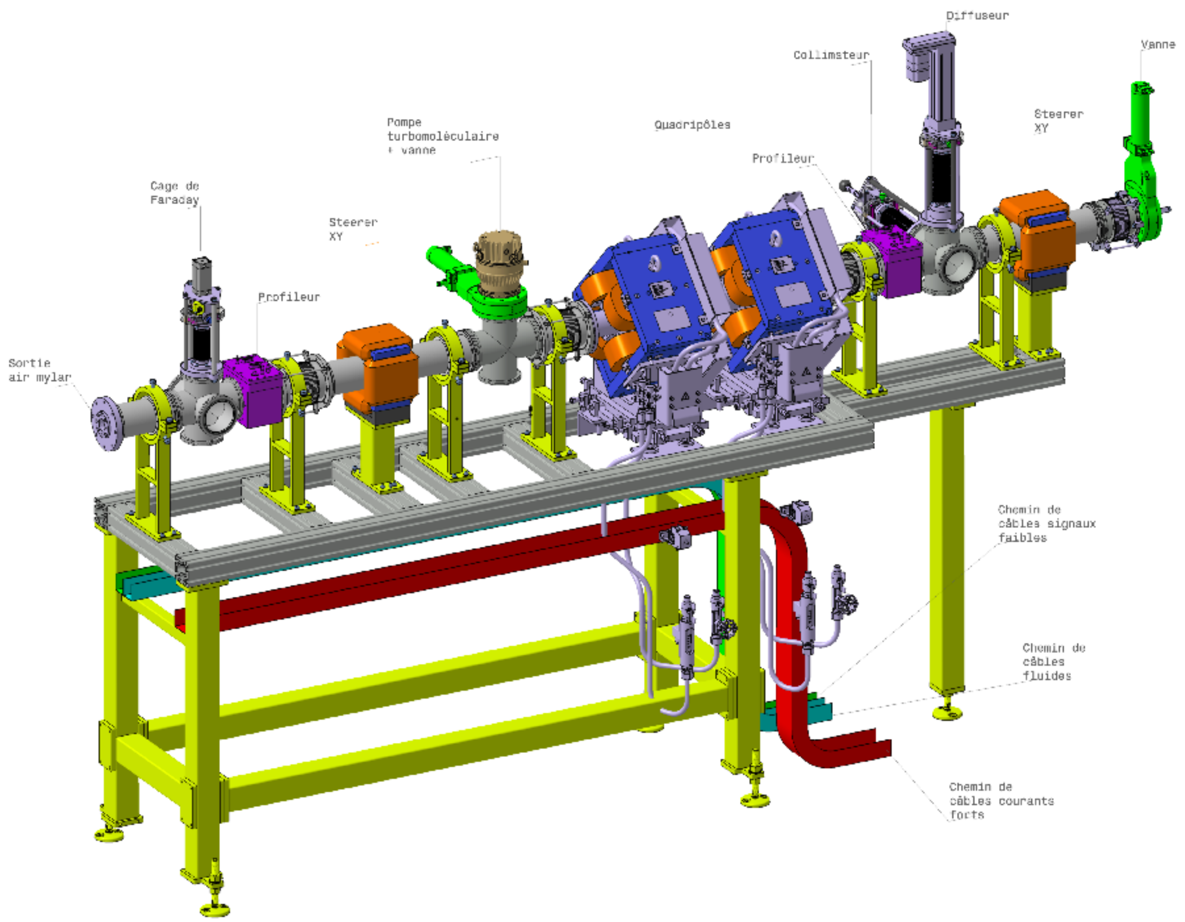

Figure 6.2: Schematic of the new CMS beam line with all its elements pointed out. (Image: IPHC.)

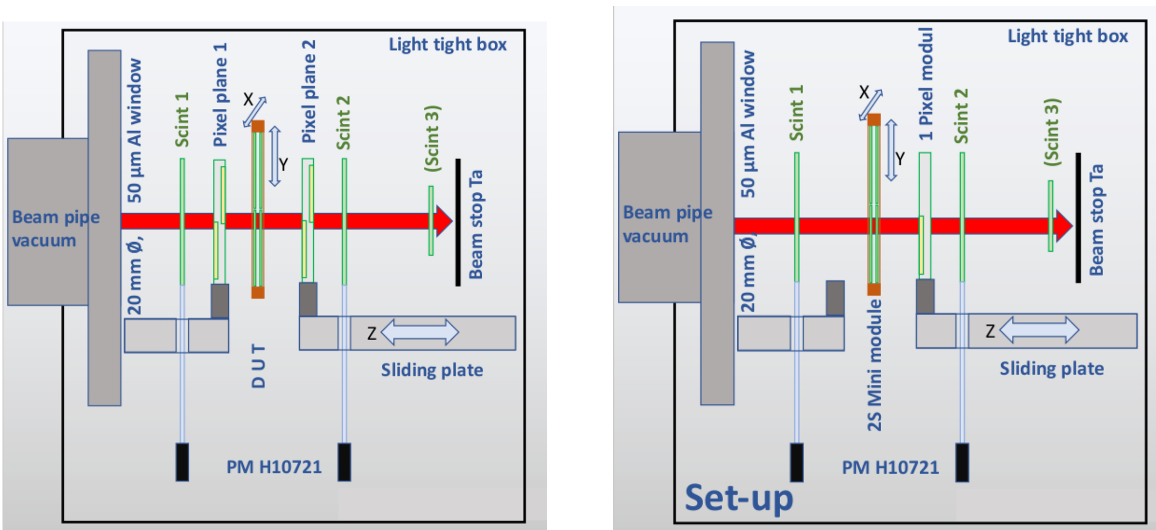

Figure 6.3: Left: Planned nominal setup of CHROMini with two reference planes, each containing two pixel modules, and a 2S module as DUT. Right: Preliminary setup during the beam tests in July and December 2019, with only a single pixel module and a 2S mini-module assembled at KIT. (Images: IPHC.)

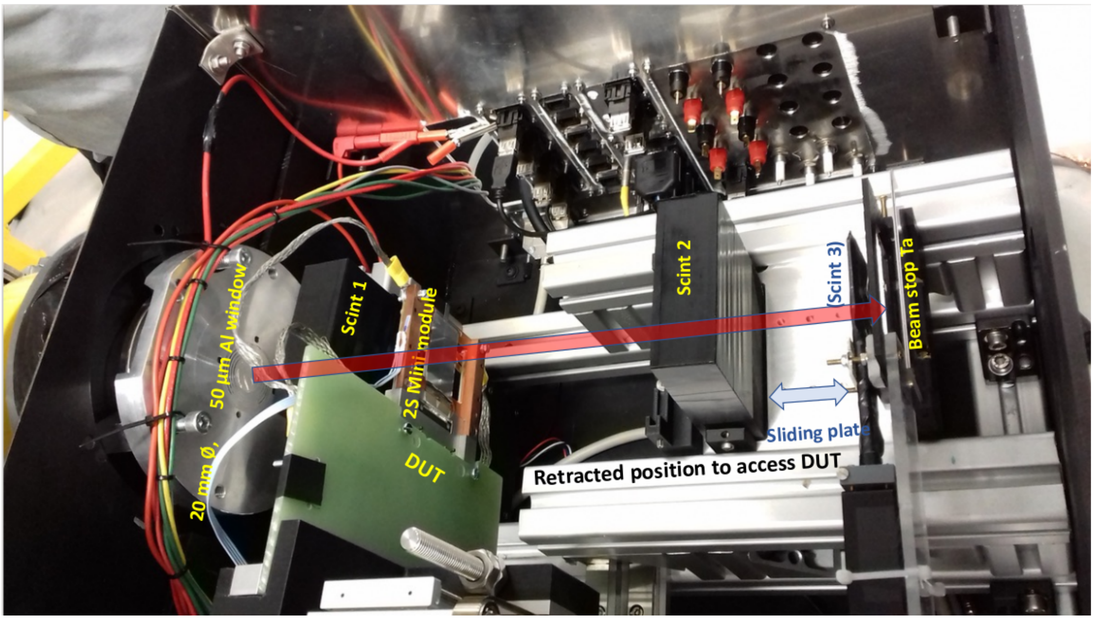

Figure 6.4: Photo of the test beam setup of the CHROMini telescope where the positions of the two scintillators (and a potential third scintillator), the DUT and the Al window at the exit of the beam line can be seen. Nominally, the telescope will consist of two layers of CMS Phase-1 pixel modules. (Image: IPHC.)

by executing source code or makefiles, a *History* file where all changes performed between the current and previous versions of the program are documented, and some macro files (*proton.mac* for the execution of one run of the program for selected number of events and creation of output ROOT files; and *vis.mac* for the visualization of the simulated geometry and particle interactions). Furthermore, the *include* directory contains header files (*.hh*) and the *src* directory contains the related implementation files (*.cc*). For example, the *DetectorConstruction.hh* header file in the *include* directory is related to the *DetectorConstruction.cc* implementation file in the *src* directory and the *DetectorConstruction* class etc. The classes corresponding to these header files and implementation files are summarized below.

The *HistoManager* class is responsible for the analysis manipulations such as defining, filling and saving histograms, n-tuples and trees in an output ROOT file [8].

The *PhysicsList* class summarizes all the settings and selection of physics processes used in the simulation. Particles and processes are constructed here along with particle transportation and decays. The *PhysicsListMessenger* class is responsible for printing out guidance messages for the user and information on the setting of parameter names related to *PhysicsList* while the program is running. In addition, the following conventional physics list electromagnetic (EM) constructors can be selected through *PhysicsList* or by using macros: *PhysListEmStandard* is the default EM constructor which is used in a significant part of reference physics lists like FTFP_BERT, QGSP_FTFP_BERT etc; *PhysListEmStandardSSM* is a new physics constructor for validation of single scattering models and includes modifications on top of the EM standard physics constructor; *PhysListEmLivermore* and *PhysListEmPenelope* are constructors for any application requiring higher accuracy of electron, hadron and ion tracking without magnetic field. More details on physics lists can be found in the Geant4 manual for application developers [8].

The *ElectricFieldSetup* class sets up and manages the electric field (which will be responsible for the biasing of the silicon sensors in the simulation later called by another class, the *DetectorConstruction*) and for its numeric stepper. In the CHROMini simulation program a uniform electric field is applied across the volumes of the sensors and along the z-direction (which is parallel to the thin dimension of each sensor) by integrating the equations of the motion of a particle in an electric field using the classical Runge-Kutta 4th order method. The *FieldMessenger* class is responsible for printing out guidance messages for the user and information on the setting of parameter names, steppers, definitions of values and unit categories related to *ElectricFieldSetup* while the program is running [8].

The *DetectorConstruction* class handles the usage of constants and units, the definition of elements, materials and mixtures, the placement of the various logical and physical volumes (by defining sizes, distances, translations, rotations), the construction of the simulated geometry, the application of electric fields locally (on specific volumes) and the visualization attributes (which can later be changed by the user from *vis.mac*). The *DetectorMessenger* class is responsible for printing out guidance messages for the user and information on the setting of parameter names, distances, materials and unit categories related to *DetectorConstruction* while the program is running [8].

The *PrimaryGeneratorAction* provides the primary particle generator, which can later be utilized by the user in the macro files. The primary particles in our case are the 25 MeV protons, while the generator itself could be a particle gun or a general particle source. The primary particle generator should be positioned at a given point of the geometry before the beginning of a simulation run [8].

In Geant4, the run is the largest unit of simulation. Conceptually, a run is a collection of events which share the same detector and physics conditions. Every run of the simulation is processed by the *RunAction* class. A run consists of a sequence of events and each of them is handled by the *EventAction* class. In the end of each event, the particle hits in the various volumes are collected, information is processed and the outputs are stored in the histograms, trees and n-tuples previously defined in *HistoManager*. In each event a loop is performed over the primary particles (25 MeV protons in our case) and each primary particle is tracked through the detector undergoing the registered physics processes which may create secondary particles (daughters, mostly δ-electrons in our case). The secondaries are also tracked. The tracking actions are processed by the *StackingAction*. When the stack becomes empty, processing of one event is over. Each track is processed via steps by the *SteppingAction* class. While a track is a snapshot of a particle and it has physical quantities of current instance only, a step is a *delta* information for a track. A track is not a collection of steps, but rather a track is being updated by steps. A step has two points, the pre-step and the post-step, and also *delta* information of a particle (energy loss on the step, time-of-flight spent by the step, the current volume and material at the step etc.) [8].

The maximum step size is defined by the *StepMax* class. The *StepMax Messenger* class is responsible for printing out guidance messages for the user, information on the setting of parameter names, ranges and unit categories related to *StepMax* while the program is running. The *SteppingVerbose* class activates the printing of different stepping information depending on the verbose level set by the user. This information could regard e.g. the step ID, the global coordinates of the step, the energy lost during the step, the step length, the track length up to this step etc [8].

The simulation is run from a separate *build* directory after executing the *cmake* and *make* commands. All histograms are stored in an output ROOT file called *proton.root*.

6.3 The simulated geometry

The geometry of the Geant4 [7] simulation consists of a 47 cm sized cubic World which contains a full 2S module [3] as a device under test (DUT) placed between the two arms of the CHROMini telescope. Each arm of the CHROMini telescope is made up of one layer with two side-by-side Phase-1 BPIX (barrel pixel) modules [9]. Two scintillators, one before the first pixel layer (along the way of the beam) and one behind the second pixel layer, are used for triggering. A general particle source (GPS) placed at $z = -23.5$ cm is used as primary particle generator. This z-position corresponds to the exit of the beam from the beam line (and furthermore is the boundary of the simulated World). The (x, y) coordinates of the GPS are chosen in such a way as to ensure that most beam particles will hit only one BPIX module per layer (as this was the case in the test beam reference run which was used for comparison with the simulation). The proton beam has a circular Gaussian shape with $\sigma_r = 2.123$ mm (corresponding to a measured experimental value), a (0, 0, 1) direction (along the z-axis) and 25 MeV energy (which follows a Gaussian distribution). A 50 μm thick Al foil is positioned exactly at the exit of the beam line. In this document the first and second scintillators, pixel modules and 2S sensors along the way of the beam will be simply referred to as first scintillator, second scintillator, first pixel module, second pixel module, first 2S sensor and second 2S sensor, respectively.

The World is full of dry air (78.08% N, 20.95% O, 0.93% argon gas, 0.04% CO_2). The scintillators' material is C_9H_{10} polyvinyltoluene (PVT) with a density of 1.032 g/cm^3 and a 0.126 mm/MeV Birks' constant in the Birks' Law:

$$\frac{dL}{dr} = \frac{S\,\frac{dE}{dr}}{1 + k_B \frac{dE}{dr}} \tag{6.1}$$

where dL is the scintillation yield, dE is the released energy, S is the absolute scintillation factor and k_B is the Birks' constant [10]. Both the sensor and the readout chip (ROC) of each pixel module, as well as each strip sensor of the 2S DUT, are considered to be entirely made of Si (with a density of 2.33 g/cm^3). In reality, in the 2S module the connection of individual readout chips to both sensors is realized by flex Kapton hybrids bent around a stiffener providing bond pads on both sides and traces to connect to the bump bonded readout chips [3]. The box in which the 2S module is tested contains Kapton as an insulation and protection layer on the electrostatic sensitive and fragile components of the module, as Kapton is a material with high mechanical and thermal stability, electrical isolation ability and high transmittance to different rays, while it is also relatively insensitive to radiation damage. However, the Kapton volumes have been entirely omitted from the simulation of CHROMini as studies on thin Kapton foils have shown that the stopping power and energy loss of protons are significant when the energy of protons is below 1-3.5 MeV [11], [12]. In the current simulation, the kinetic energy of protons was measured at the entrance and exit of each pixel layer and each 2S sensor without the presence of Kapton. The results show that the energy of the primary protons is 17.20 MeV on average at the exit of the first pixel layer (before the 2S module), 17.15 MeV on average at the entrance of the first 2S sensor, 13.46 MeV on average at the exit of the second 2S sensor and 13.39 MeV on average at the entrance of the second pixel layer (after the 2S module). All these energies are well above the 1-3.5 MeV range and there are no indications that there would be significant differences in energy loss if the intermediate air volumes were replaced with Kapton volumes.

The layout of a CMS Phase-1 BPIX module is shown in Fig. 6.5. Each of the pixel modules of the telescope has dimensions of 66 mm × 25 mm × 460 μm. The y-size of each pixel layer is approximately twice that value as there are two pixel modules side-by-side per layer. (In reality, the two modules might be a bit overlapping.) The active y-size of each pixel sensor is 16.2 mm. Each BPIX module comprises $8 \times 2 = 16$ ROCs, and there are 52×80 pixels corresponding to each ROC (in the x- and y-directions, respectively). Most pixels have the area of 150 µm × 100 µm (columns in the x- and rows in the y-directions, respectively). However, the first and the last columns of pixels for each ROC have twice this length (300 µm each) in order to cover the gap between a ROC and its neighboring one. The same is valid for the pixels in the last row for each ROC, as they have twice this length too (200 µm each). (This does not apply for those in the first row of each ROC though.) The active depth of each pixel is 285 µm. The bias voltage applied on each pixel sensor is 150 V.

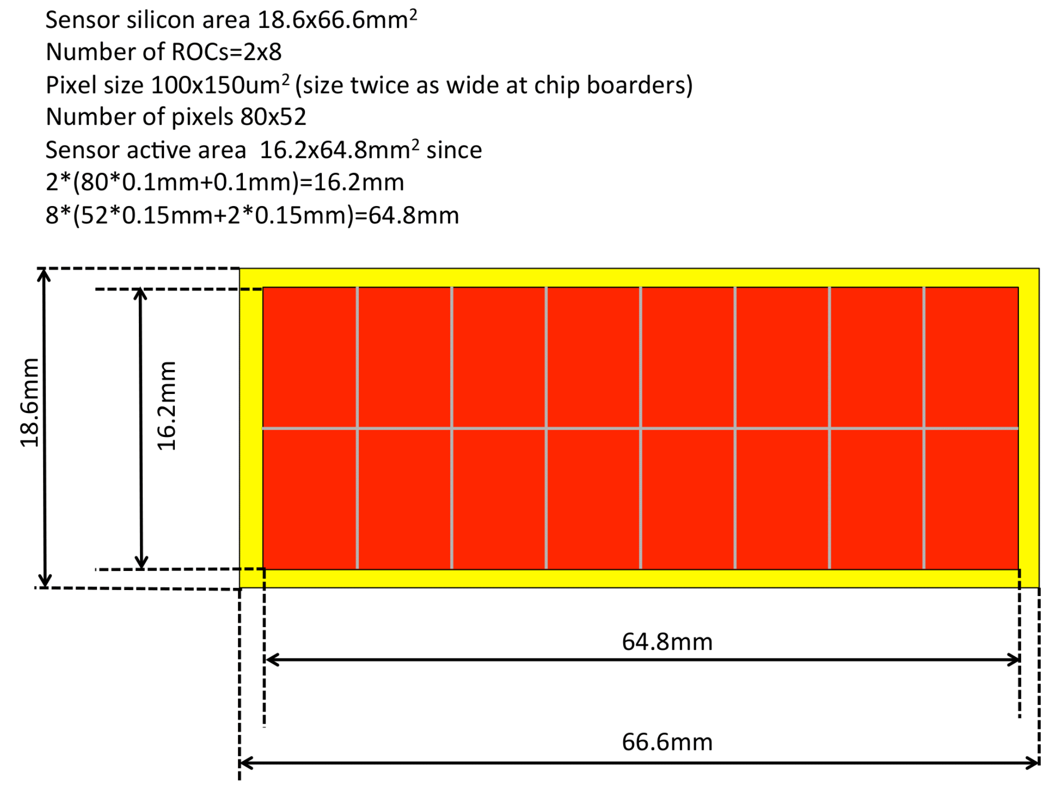

Figure 6.5: The layout and pixel map of a CMS Phase-1 BPIX module. (Image: PSI.)

The 2S module consists of two Si strip sensors set apart by a gap of ~2 mm (between the sensor surfaces) along the thinnest dimension of the 2S module (z-axis). Each of the strip sensor has dimensions of 102700 µm × 94108 µm × 320 µm. There are two rows of 1016 strips on each of the two sensors. The long side of the strip (with a length of ~5 cm) is along the x-axis and there is a spacing of 1368 µm between the edge of each strip and the edge of the module. The distance (along the y-axis) between any two adjacent strips in the same row is 68 µm, the width of each strip is 22 µm, and thus the strip pitch is 90 µm. The active depth of each strip is 290 µm and starting from the front plane of the respective sensor. The direction of the thinnest dimension of the 2S module is along the z-axis. The high voltage applied on the backplane of each strip sensor is −400 V, while the respective front plane (the strip plane) is grounded. (More details and schematic representations can be found in the Technical Design Report for the Phase-2 Upgrade of the CMS tracker [7].)

Let us consider $z_0 = -23.5$ cm (the World boundary). Then the z-positions of the centroids of each physical volume are: z_0 + 7.6 cm for the first scintillator, z_0 + 11.7 cm for the first pixel layer, z_0 + 13.5 cm for the 2S DUT, z_0 + 15.3 cm for the second pixel layer and z_0 + 16.7 cm for the second scintillator. None of the simulated physical volumes is rotated (but the user may rotate the telescope planes and/or DUT about the x- and/or y-axes). The entire Geant4-simulated geometry is presented in Fig. 6.6.

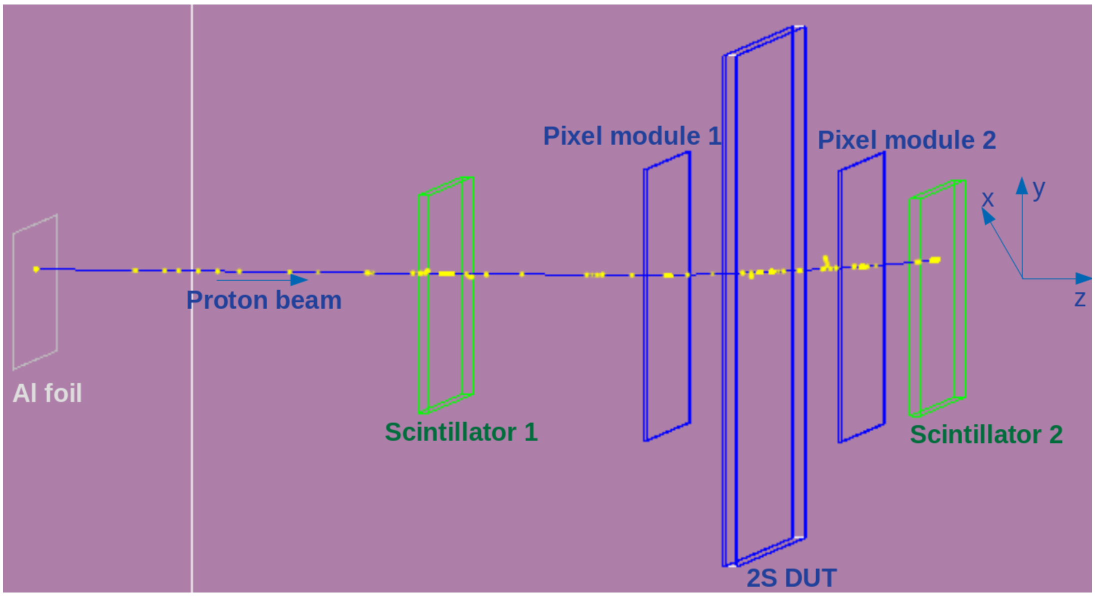

Figure 6.6: Visualization of the simulated geometry.

6.4 Physics processes in the simulation

In the physics list of the standalone Geant4 program [7] for the simulation of CHROMini the boson, lepton, meson, baryon, ion and short-lived particle (SLP) constructors are defined initially. Subsequently, the decay and transportation are added to the hadronic physics list, as well as $StepMax$ which limits the step size. In addition, several other standard processes are included in the physics list for hadrons, electrons, muons and ions (although no muons or ions are detected after running the simulation): single Coulomb scattering, multiple scattering, Bremsstrahlung, pair productions, annihilation, ionization, atomic de-excitation, universal fluctuation, the photoelectric effect, γ production, Compton scattering, Rayleigh scattering and the Klein-Nishina model for differential cross section calculations are among them. (It is worth noting that light production in the scintillators is a rare event in the current telescope and DUT configuration.)

Furthermore, minimum and maximum energy limits are set and the continuous slowing down approximation (CSDA) range is built. (The CSDA range is a very close approximation to the average path length traveled by a charged particle as it slows down to rest, calculated in the approximation where the rate of energy loss at every point along the track is assumed to be equal to the total stopping power and energy-loss fluctuations are neglected. The CSDA range is obtained by integrating the reciprocal of the total stopping power with respect to energy [13].)

6.5 Results of the simulation

All simulation results presented below are for a run of 20000 events (with each event corresponding to a single primary proton) unless stated otherwise. Similar results can be obtained from the program for the simulation of CHROMIE described in the previous chapter.

In Geant4 when a particle passes through a volume, it loses energy in two distinct ways:

a) By depositing energy continuously in the traversed physical volume at each step. Each pixel/strip sensor of the simulated geometry is divided into smaller sub-volumes, with each of them corresponding to a single pixel/strip and the program calculates the continuously deposited energy in every pixel/strip as shown in Fig. 6.7.

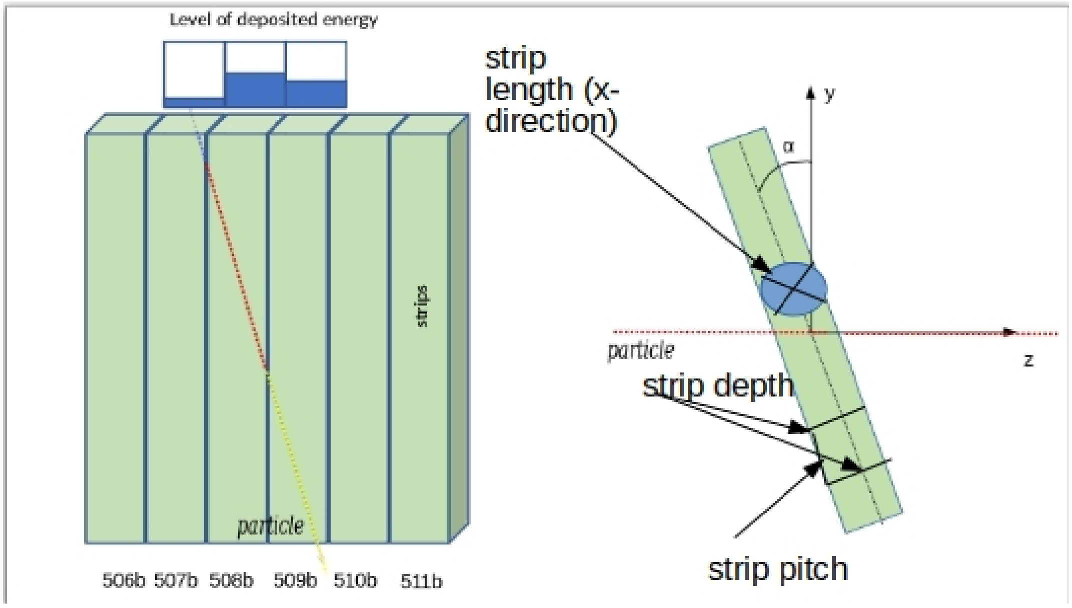

Figure 6.7: Left: Schematics of the energy deposition in the strip (or pixel) volumes of the 2S sensors (pixel modules). As the particles traverse the silicon material they store different amounts of energy in neighboring strips (pixels). Right: The angle α will be 0 in the nominal operational setup of CHROMini, i.e. the 2S module nominally won't be rotated about the x-axis. The x-direction is perpendicular to the plane of the paper and pointing inside, as indicated by the X in a circle. In addition, the directions of the strip pitch and strip depths are denoted (black line segments). [The sketch is for illustrative purposes and doesn't reflect the relative dimensions of the real setup.]

b) By producing new secondary particles. In Geant4 the user implements a production cut so that all particles below it are not generated, but their energy is accounted as deposited energy in the traversed material. Thus, secondary particles unable to travel at least the range cut value are not produced. Geant4 uses production cuts in range, instead of in energy as used by other Monte Carlo codes. In the program for the simulation of CHROMini a global cut of 1 μm is used for secondaries. This means that no secondary particle (e.g. δ-electron) will be produced if the expected range in the current material is less than 1 μm.

Let's consider the impact points of the primary protons in each volume as the entrance points at the front (along the way of the beam) boundary of each volume: A for the hit pixel module of the telescope plane in front of the DUT (first layer), B for the first 2S sensor (along the way of the beam), C for the second 2S sensor (along the way of the beam) and D for the hit pixel module of the telescope plane behind the DUT (second layer), as shown in 6.8.

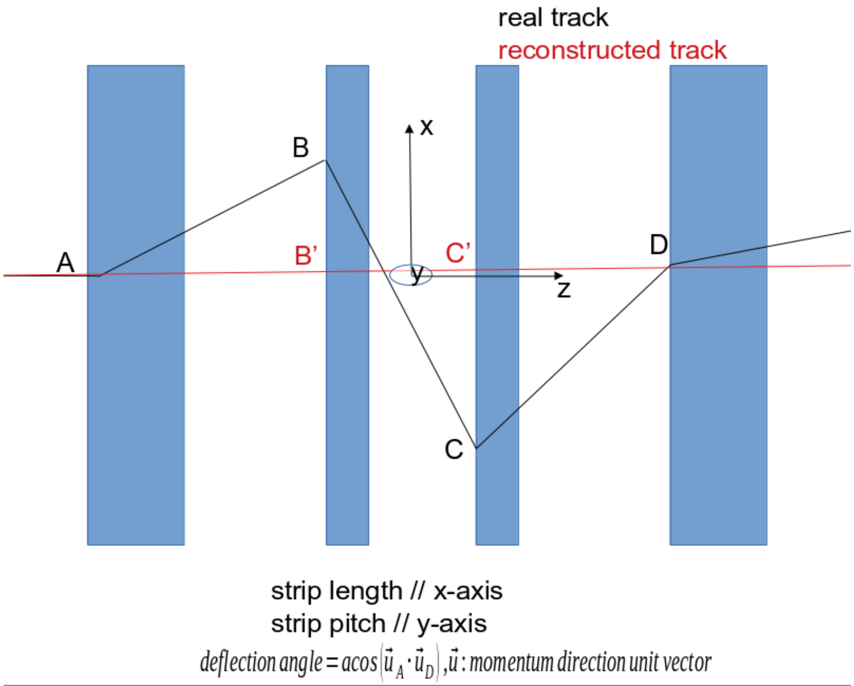

Figure 6.8: Schematics of the entrance points of the primary protons in each volume: A (first pixel layer along the way of the beam), B (first 2S sensor along the way of the beam), C (second 2S sensor along the way of the beam), D (second pixel layer along the way of the beam). (The sketch is for illustrative purposes and doesn't reflect the relative dimensions of the real setup.)

For each pixel in the BPIX modules the 5σ noise threshold is set to 10000 electrons, while the 5σ noise threshold for each strip of the 2S module is set to 5000 electrons. For every event, Geant4 calculates the stored energy in each pixel/strip, respectively, and when dividing this energy by the energy required for a single electron-hole pair production in silicon (= 3.67 eV) the charge collected in each pixel/strip in number of electrons is obtained. If this charge exceeds the threshold of 10000/5000 electrons, respectively, the program decides that a hit is counted in the examined pixel/strip in the current event.

Let's consider the points $R_{\text{pixel}} = A,\ D$ (see Fig. 6.8) as described above. Each of them is defined as follows:

$$R_{\text{pixel}} = \frac{1}{N_{\text{pixels}}} \sum_{i=1}^{N_{\text{pixels}}} w_{pi} P_{pi} \tag{6.2}$$

where N_{pixels} is the total number of pixels that have counted a hit in the current module, the weight $w_{pi} = \frac{\text{charge collected in the } i\text{−th pixel with a hit}}{\text{total charge collected in all hit pixels in the current module}}$ and P_{pi} the geometrical center of the front surface (along the way of the beam) of the i-th pixel that has counted a hit in the current event.

Let's consider the points $R_{\text{strip}} = B,\ C$ (see Fig. 6.8) as described above. Each of them is defined as follows:

$$R_{\text{strip}} = \frac{1}{N_{\text{strips}}} \sum_{i=1}^{N_{\text{strips}}} w_s P_{si} \tag{6.3}$$

where N_{strips} is the total number of strips that have counted a hit in the current sensor, the weight $w_s = \frac{1}{\textit{number of hit strips in the current sensor}}$ and P_{si} the geometrical center of the front surface (along the way of the beam) of the i-th strip that has counted a hit. Here it should be noted that the ASIC CMS Binary Chip (CBC) designed for the readout of the silicon strip sensors of CMS does not provide any information about the charge collected per strip contrary to the CMS pixel readout chip which has an on-chip 8-bit ADC and provides information on the pulse height [3].

Let's define the following vector:

$$\vec{r}_{AD} = \vec{r}_D - \vec{r}_A = (x_{AD}, y_{AD}, z_{AD}) \tag{6.4}$$

We know that the equation of line AD will then be:

$$\frac{x - x_A}{x_{AD}} = \frac{y - y_A}{y_{AD}} = \frac{z - z_A}{z_{AD}} \tag{6.5}$$

Let $B^{'}, C^{'}$ be the points on line AD with the same z as B, C, respectively (see Fig. 6.8). Therefore, their coordinates will be calculated as follows:

$$z_{B'} = z_B, \; z_{C'} = z_C \tag{6.6}$$

$$x_{B'} = x_{AD} \frac{z_B - z_A}{z_{AD}} + x_A, \; x_{C'} = x_{AD} \frac{z_C - z_A}{z_{AD}} + x_A \tag{6.7}$$

$$y_{B'} = y_{AD} \frac{z_B - z_A}{z_{AD}} + y_A, \; y_{C'} = y_{AD} \frac{z_C - z_A}{z_{AD}} + y_A \tag{6.8}$$

From the points described above we can define the residuals for the first and the second strip sensors of the 2S DUT, respectively, as follows:

$$s_{1x} = x_B - x_{B'}, \; s_{1y} = y_B - y_{B'} \tag{6.9}$$

$$s_{2x} = x_C - x_{C'}, \; s_{2y} = y_C - y_{C'} \tag{6.10}$$

The histograms of the above y-residuals for runs with different beam diameters and for vertical incidence of the beam are presented in Fig. 6.9 for the first 2S sensor and 6.10 for the second 2S sensor, respectively. (The strip size is much larger in the x-direction and that's why the x-residuals are not examined here.) The standard deviation in all cases is of the order of 100 μm which is the same order of magnitude as the pixel y-size of the telescope sensors and the strip pitch of the DUT sensors. These results proved that the resolution of the CHROMini telescope would be reasonable and that the project was feasible. (Note: In the case of CHROMIE (described in the previous chapter) which consists of 8 layers of pixel modules, the 8 impact points were used to fit a straight line ϵ to them using the singular value decomposition (SVD) factorization. In that case, the residuals are calculated using ϵ instead of AD.)

The deflection angle (angular straggling) θ_d is the parameter that gives us a perception of the impact of the multiple scattering occurring in the array of telescope planes and silicon

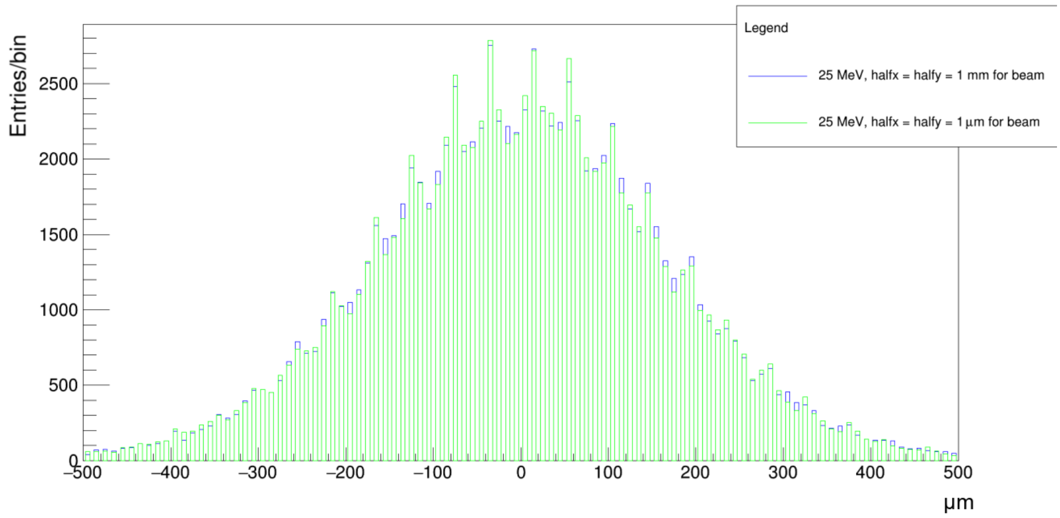

Figure 6.9: Y-residuals ($B^{'}B_y$) for the first 2S sensor along the way of the beam: comparison between a 1 µm wide circular beam and a 1 mm wide circular beam (simulation).

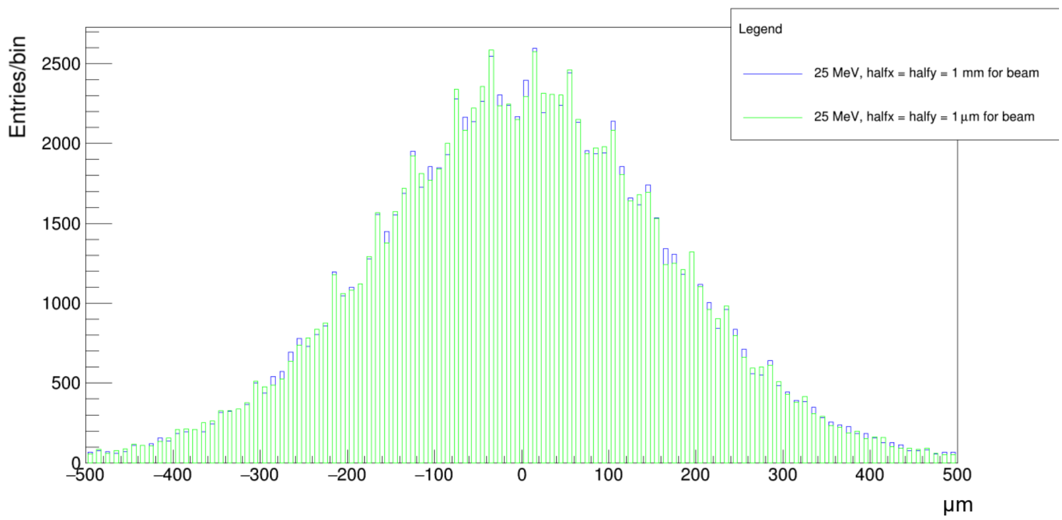

Figure 6.10: Y-residuals ($C^{'}C_y$) for the second 2S sensor along the way of the beam: comparison between a 1 µm wide circular beam and a 1 mm wide circular beam (simulation).

sensors. If $\vec{u}_A$ and $\vec{u}_D$ are the momentum directions of the primary particle at points A and D, respectively, then θ_d is defined as follows:

$$\theta_d = \arccos\left(\vec{u}_A \cdot \vec{u}_D\right) \tag{6.11}$$

The histogram of the deflection angle for a run of 20000 events and for vertical incidence of the primary particles on the surfaces of the sensors is presented in Fig. 6.11. On average it is less than 70 mrad. It gives a good estimation of the significance of the scattering of protons in the air and silicon volumes.

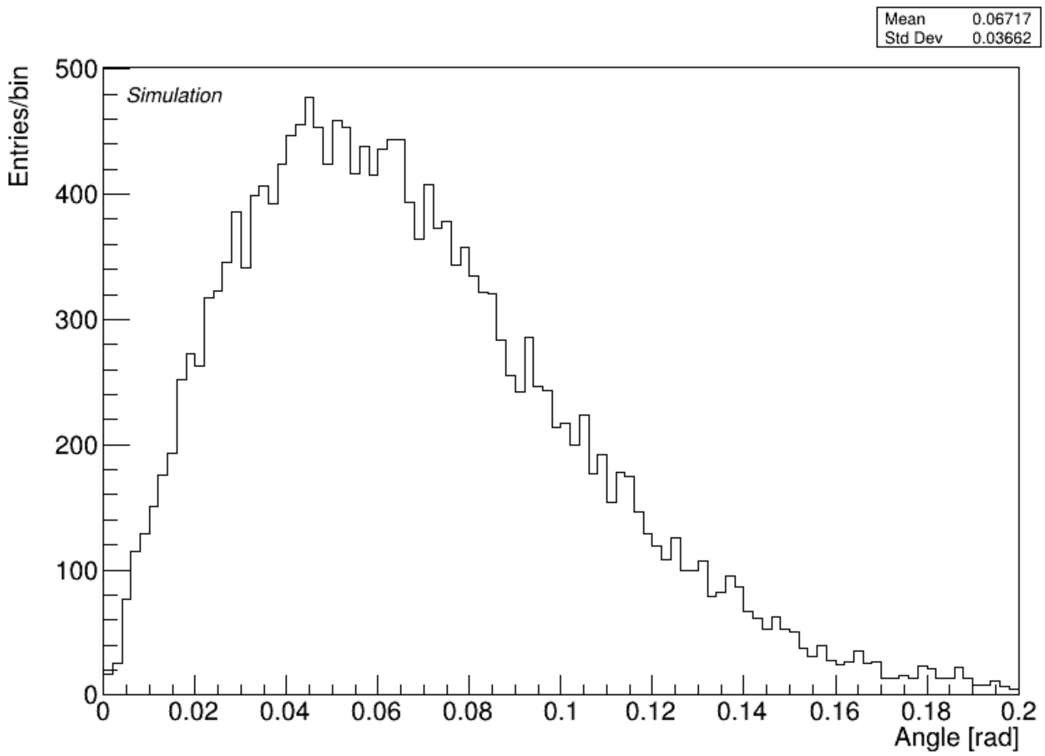

Figure 6.11: Angular straggling (deflection angle) of the primary protons between the two pixel layers (simulation).

As mentioned before, the program is capable of calculating the energy deposition per volume. Furthermore, it can calculate the kinetic energy of the primary protons at every step in each event and perform a check if the current step is at the boundary between two physical volumes. The energy depositions in each component of the simulated geometry are summarized in Fig. 6.12. A separate logarithmic plot for the energy deposited in each volume can be found in the Appendix (Fig. 6.36-6.44). Fig. 6.13 shows the kinetic energy of a proton vs. the z-coordinate (here measured from the exit of the beam line) of its position for a single event, indicating thus how much energy is approximately lost by a primary particle in each pixel module, 2S sensor or scintillator. A more detailed complementary plot for 20000 events is presented in Fig. 6.14 from where it becomes obvious that the most common scenario is that of a primary proton losing all its remaining energy before exiting the second scintillator. (This implies that a third scintillator cannot be added to the setup.) Fig. 6.15 is a correlation plot between the stored energy in the second scintillator and the kinetic energy of the primary proton at its entrance. A separate logarithmic plot for the kinetic energy of primaries at the entrance and exit of each volume can be found in the Appendix (Fig. 6.45-6.57).

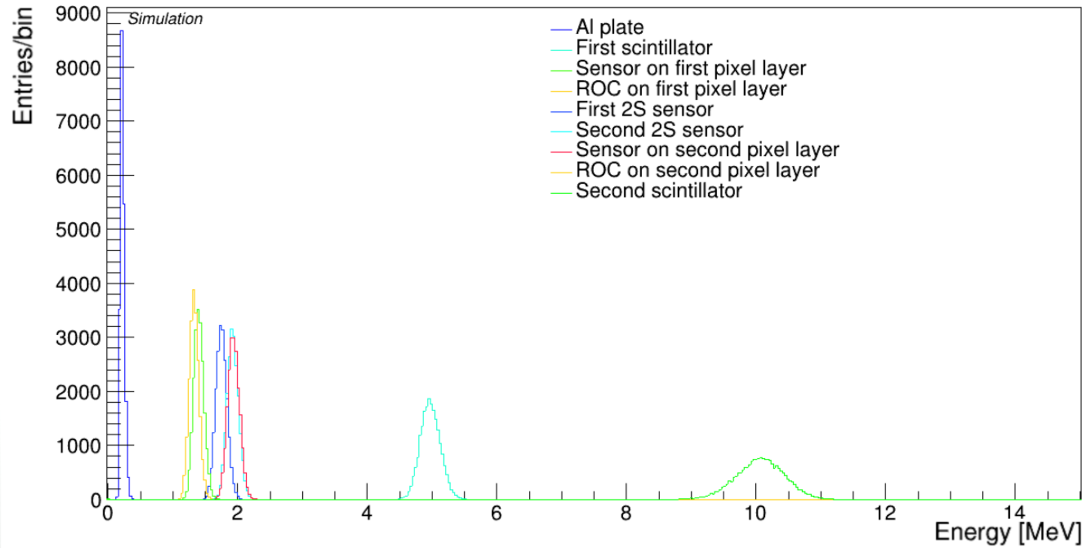

Figure 6.12: Energy deposited in the various volumes of the geometry (simulation).

The simulation program in addition can calculate the kinetic energy of the secondary particles. In Fig. 6.16 the kinetic energy of secondary particles produced in each sensor of the 2S module is shown. The total track length of the secondary particles produced in the entire simulated geometry is shown in Fig. 6.17. Fig. 6.18 shows the number of electrons produced in the sensors of the 2S module which can travel a distance at least as large as the defined production cut range. The total energies lost by the primary proton in each 2S sensor, either continuously (as energy deposited in the material) or as kinetic energy of newly produced secondaries, are summed up in Fig. 6.19. Separate logarithmic plots for the kinetic energies of secondaries in the 2S sensors and the total energy losses of primary protons in the 2S sensors can be found in the Appendix (Fig. 6.58-6.61).

The global time of proton arrival at each scintillator, as well as the time of flight (ToF) of the beam particles between the two scintillators, is shown in Fig. 6.20. The ToF is smaller than the scintillator coincidence width of 7 ns, which is a characteristic of the experimental setup.

The column and row hit maps of the hit module of the second pixel layer of CHROMini are shown in Fig. 6.21 and 6.22, respectively. The central peaks correspond to the double sized pixels at the ROC boundaries mentioned above which count more hits compared to their neighbors. There is a good agreement between the simulated column and row plots and the corresponding ones obtained from a beam test at CYRCé [5].

The degradation of the *xy* beam profile after crossing the various volumes of the simulated geometry can be observed gradually in Fig. 6.23-6.29. As mentioned before, the primary particles usually deposit all their remaining energy in the second scintillator. The Gaussian nature of the beam is clearly visible in the lego plot of the *xy* beam profile at the exit of the 2S sensor shown in Fig. 6.30. The hit occupancy map (column vs. row of hit pixels) of the hit module of the second pixel layer, as shown in Fig. 6.31, top, is in agreement with the corresponding *xy* beam profile (Fig. 6.28). In the simulation, the beam spot *xy*-coordinates were chosen to be in agreement with the hit occupancy map obtained from a beam test at IPHC, as shown in Fig. 6.31, bottom [5].

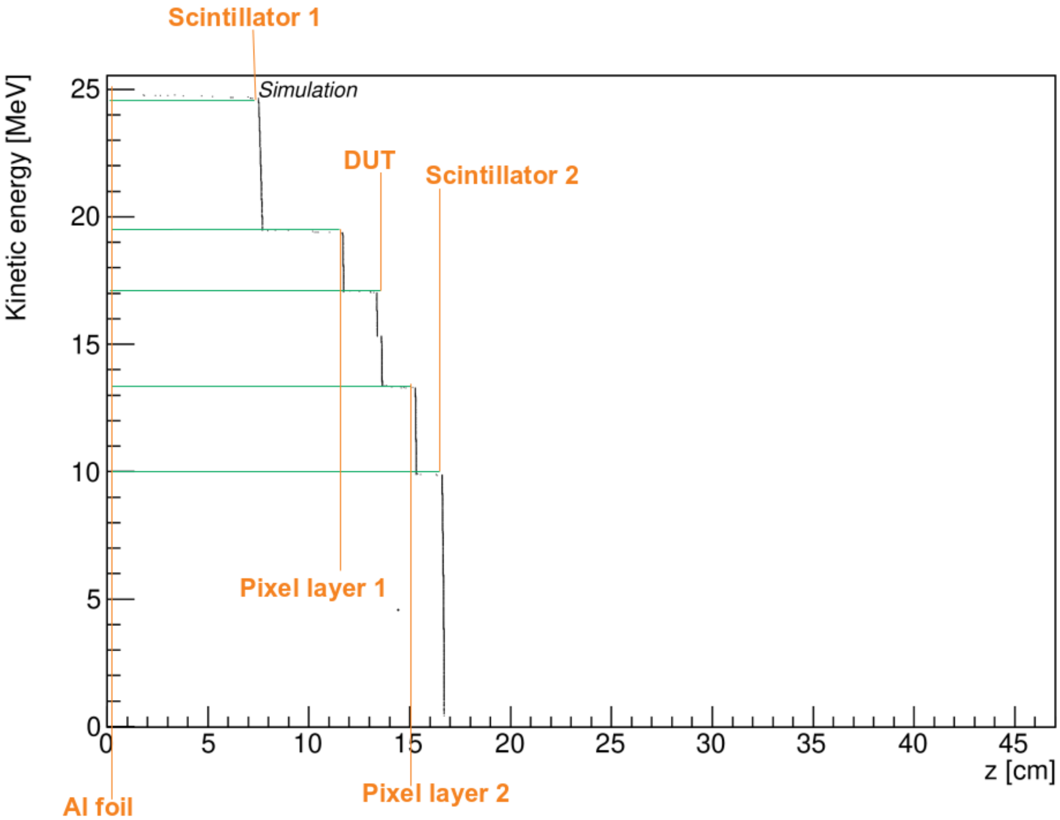

Figure 6.13: Kinetic energy of a primary proton vs. z for a single event (simulation).

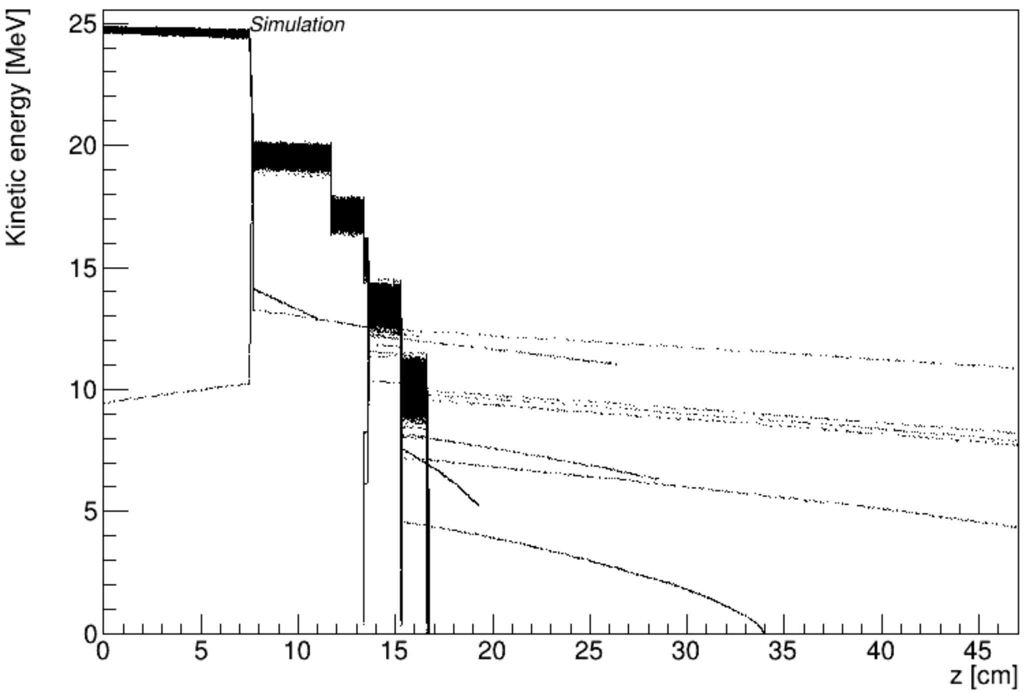

Figure 6.14: Kinetic energy of a primary proton vs. z for 20000 events (simulation).

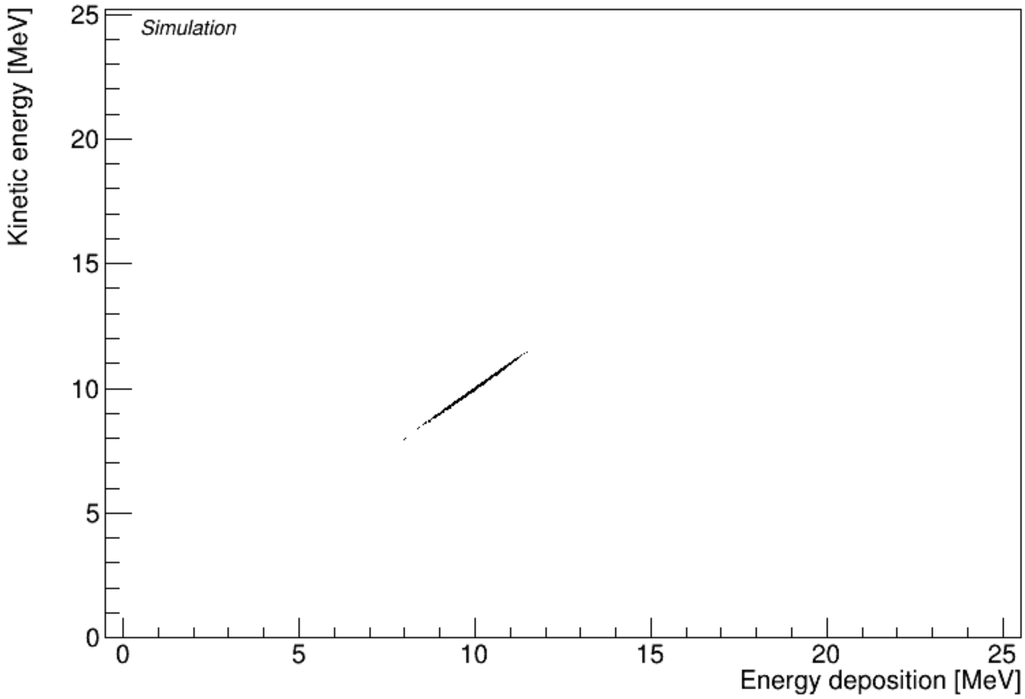

Figure 6.15: Energy deposited in the second scintillator (along the way of the beam) vs. kinetic energy of primary protons at the entrance of the second scintillator (simulation).

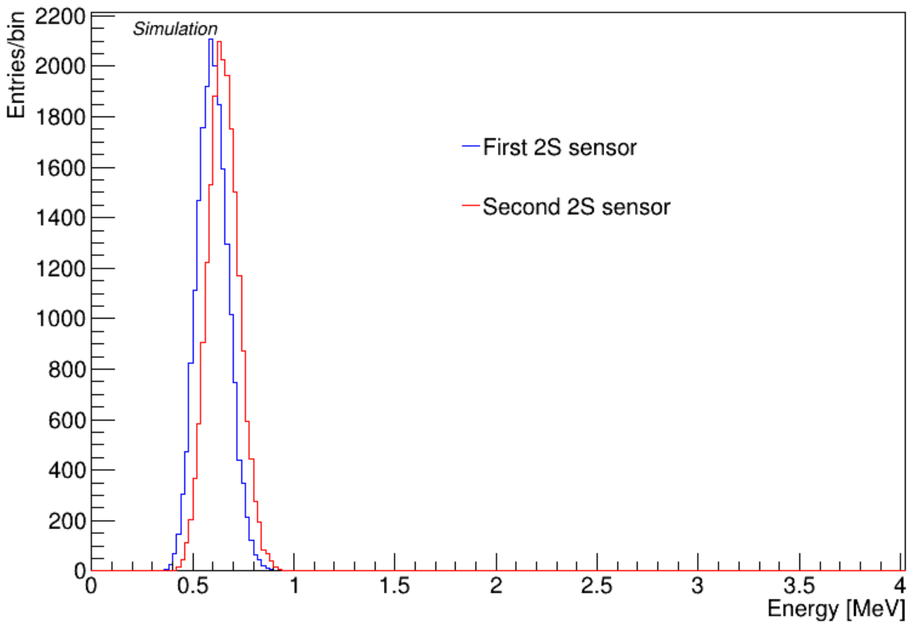

Figure 6.16: Kinetic energy of secondary particles produced in the 2S sensors (simulation).

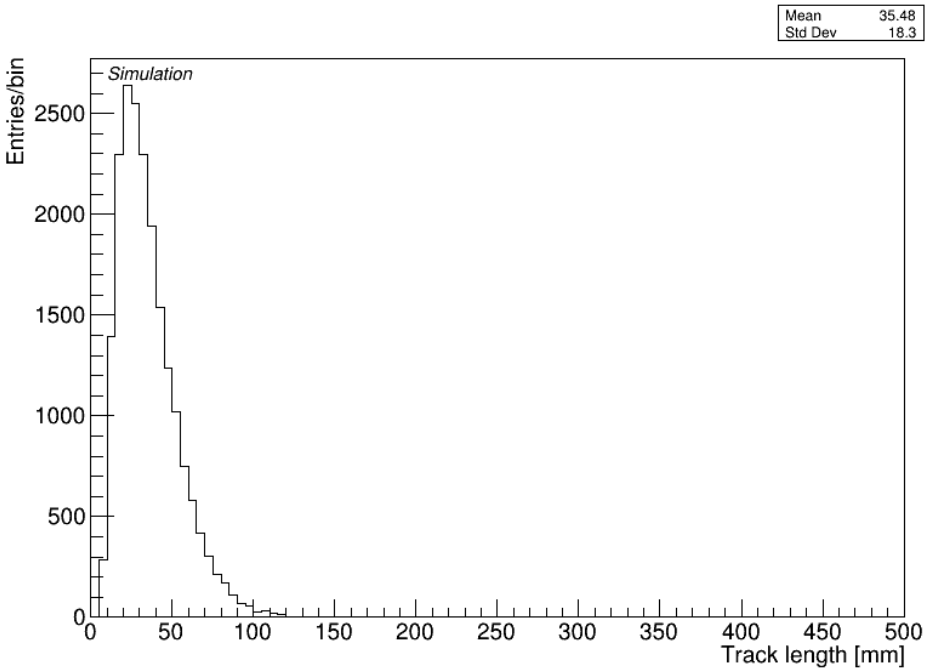

Figure 6.17: Total track length of secondary particles (simulation).

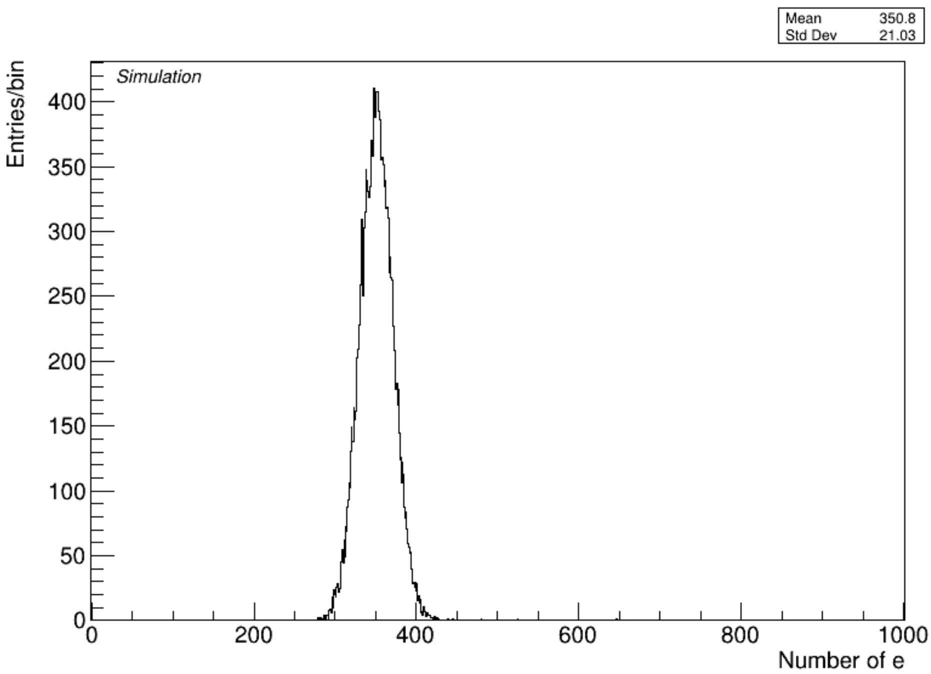

Figure 6.18: Number of electrons per event produced in the sensors of the 2S DUT and which have sufficient energy to travel at least 1 μm from their production point (simulation).

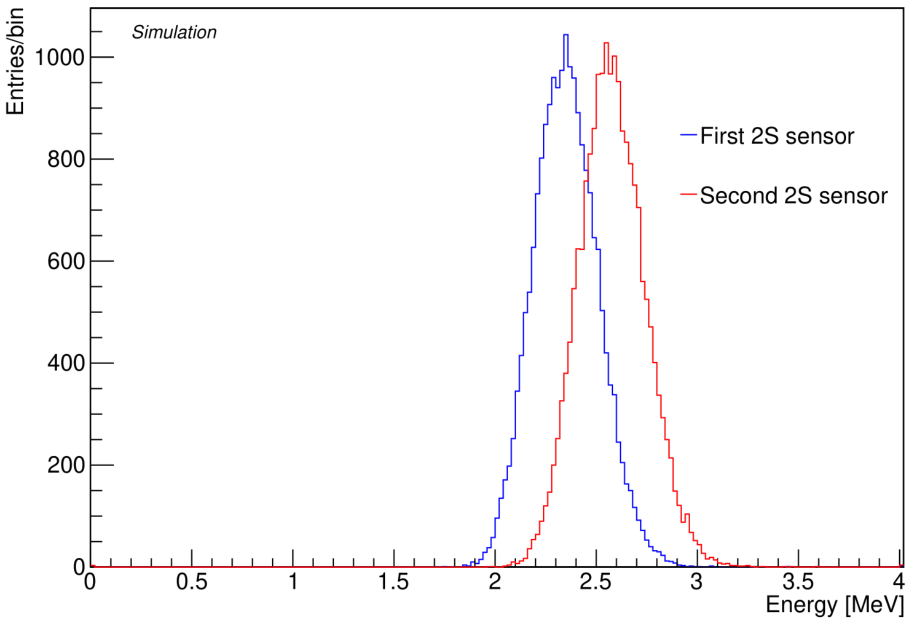

Figure 6.19: Total energy lost by the primary protons in the 2S sensors (simulation).

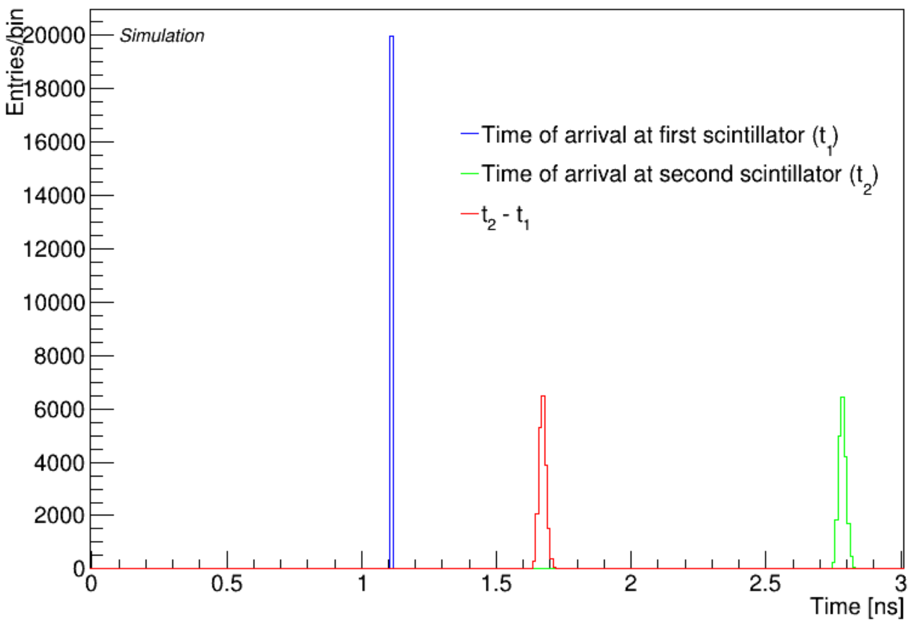

Figure 6.20: Time of flight (ToF) and times of arrival at each scintillator for the beam particles (25 MeV protons) along the z-direction in a simulated run of 20000 events. The ToF is smaller than the scintillator coincidence width of 7 ns.

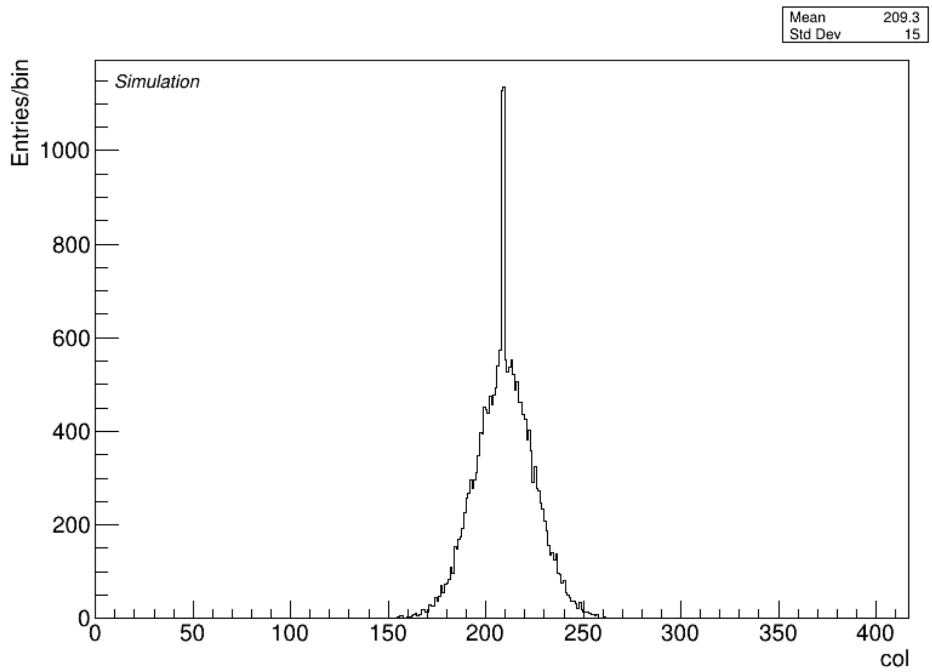

Figure 6.21: Projected hit map along columns for the hit module of the second pixel layer along the way of the beam (simulation).

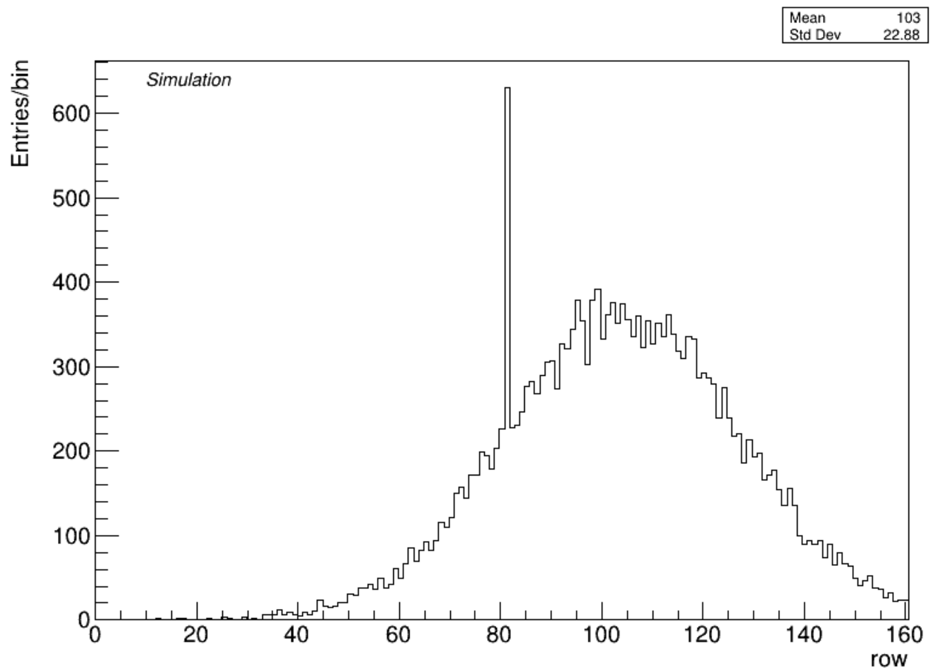

Figure 6.22: Projected hit map along rows for the hit module of the second pixel layer along the way of the beam (simulation).

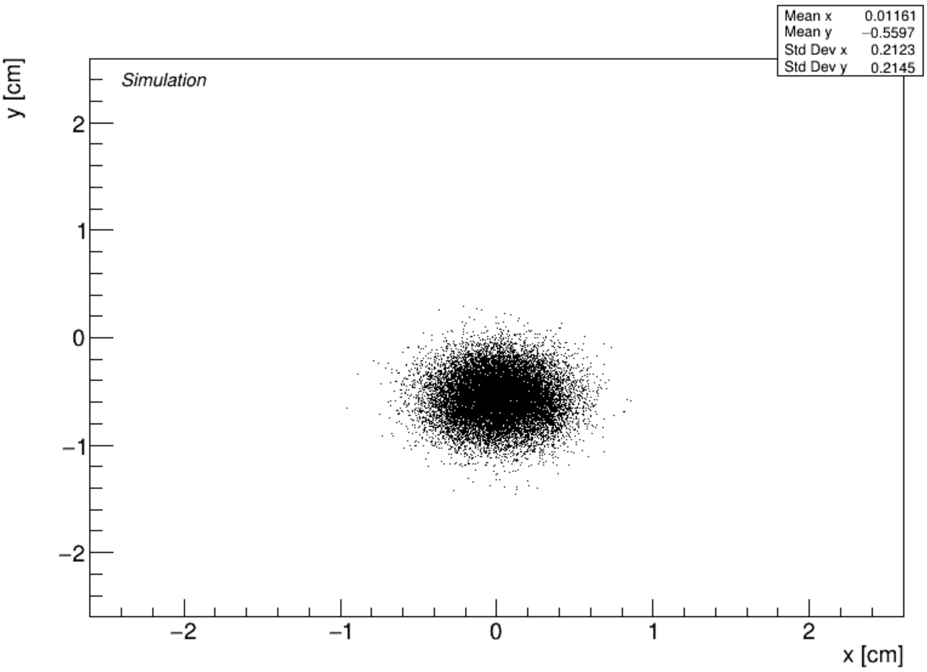

Figure 6.23: Beam profile at the exit of the Al foil at the exit of the beam line from a simulated run of 20000 events.

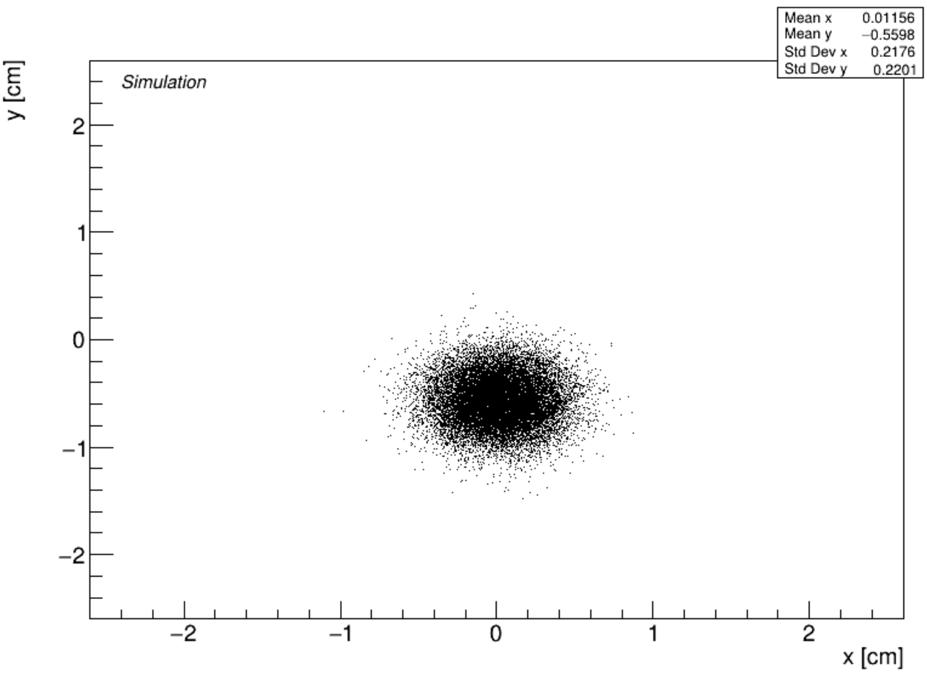

Figure 6.24: Beam profile at the exit of the first scintillator (along the way of the beam) from a simulated run of 20000 events.

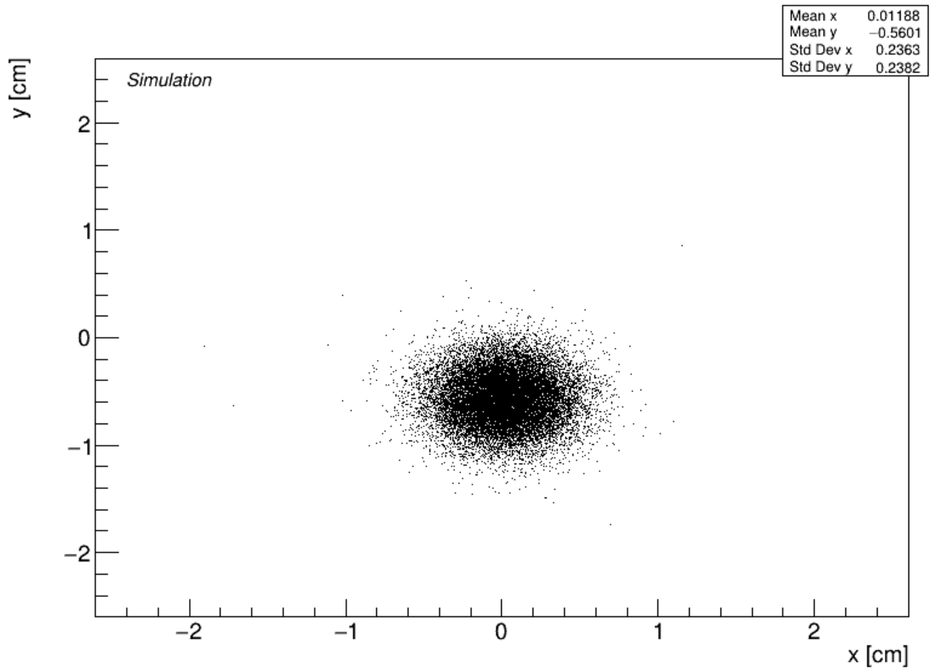

Figure 6.25: Beam profile at the exit of the first pixel layer (along the way of the beam) from a simulated run of 20000 events.

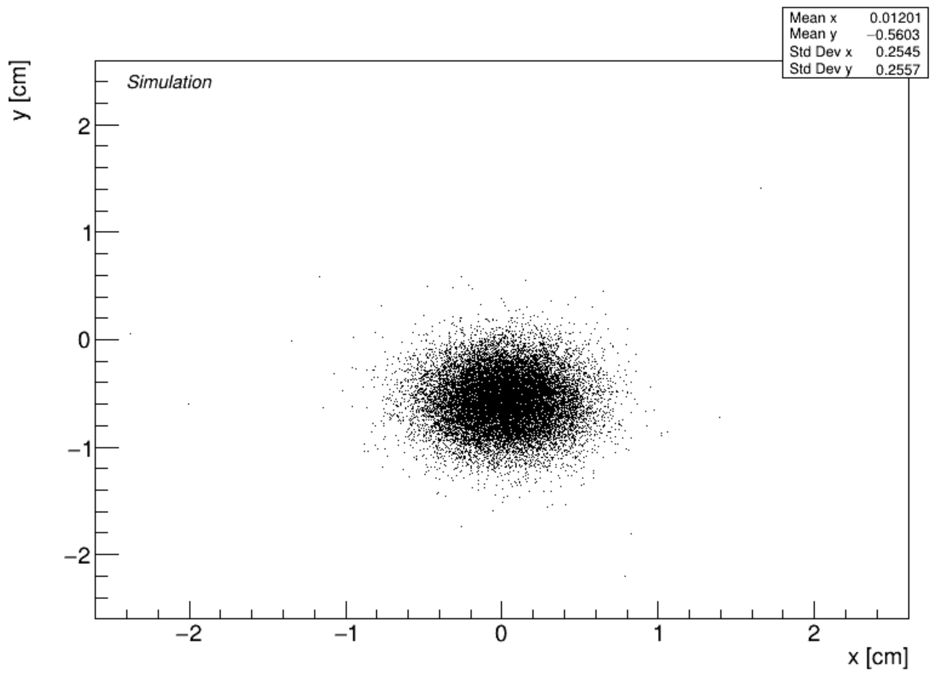

Figure 6.26: Beam profile at the exit of the first 2S sensor (along the way of the beam) from a simulated run of 20000 events.

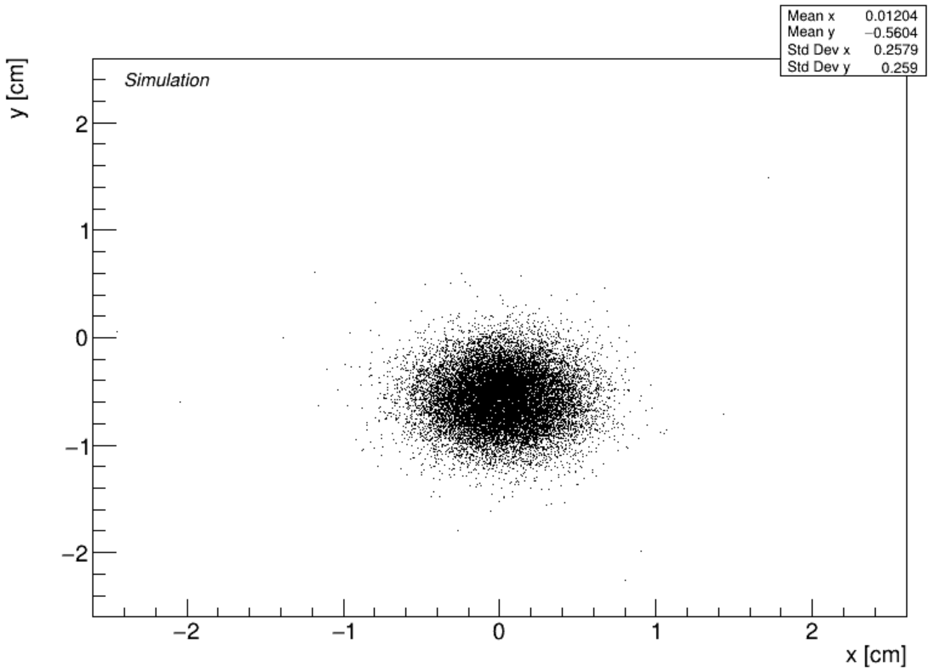

Figure 6.27: Beam profile at the exit of the second 2S sensor (along the way of the beam) from a simulated run of 20000 events.

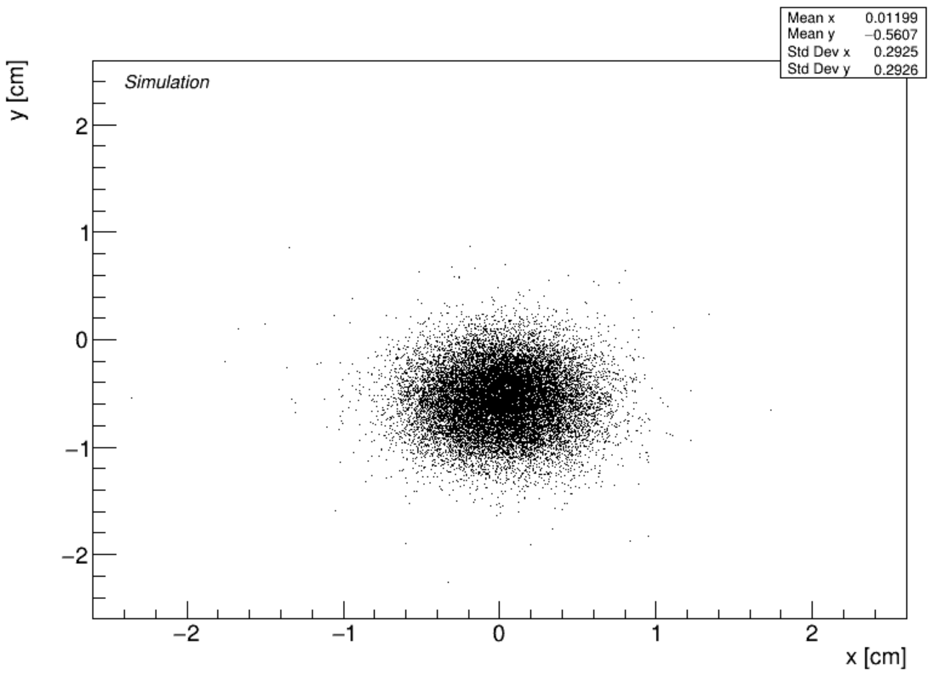

Figure 6.28: Beam profile at the exit of the second pixel layer (along the way of the beam) from a simulated run of 20000 events.

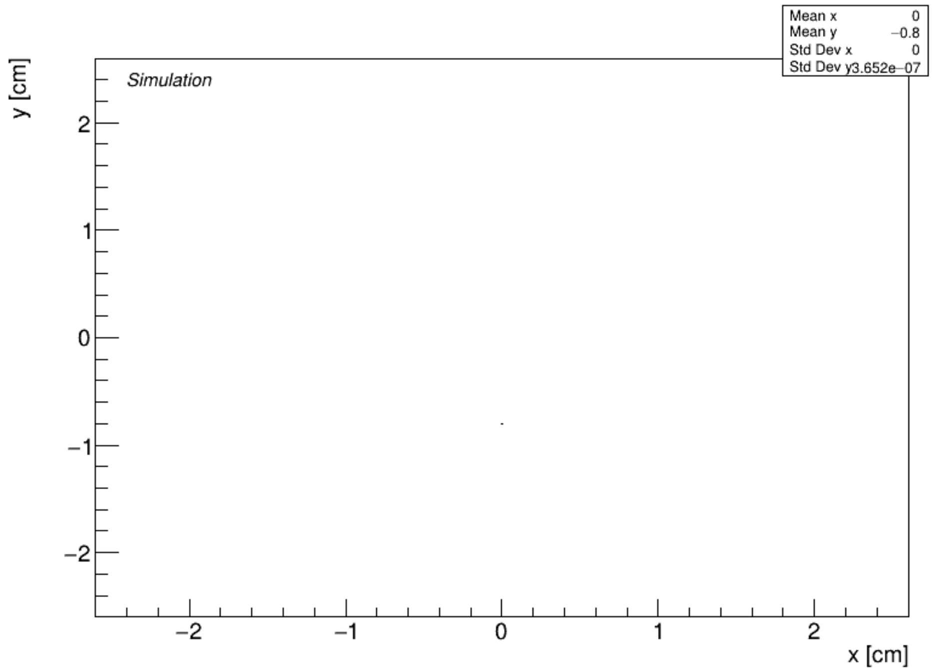

Figure 6.29: Beam profile at the exit of the second scintillator (along the way of the beam) from a simulated run of 20000 events. In most cases the beam doesn't pass through this volume.

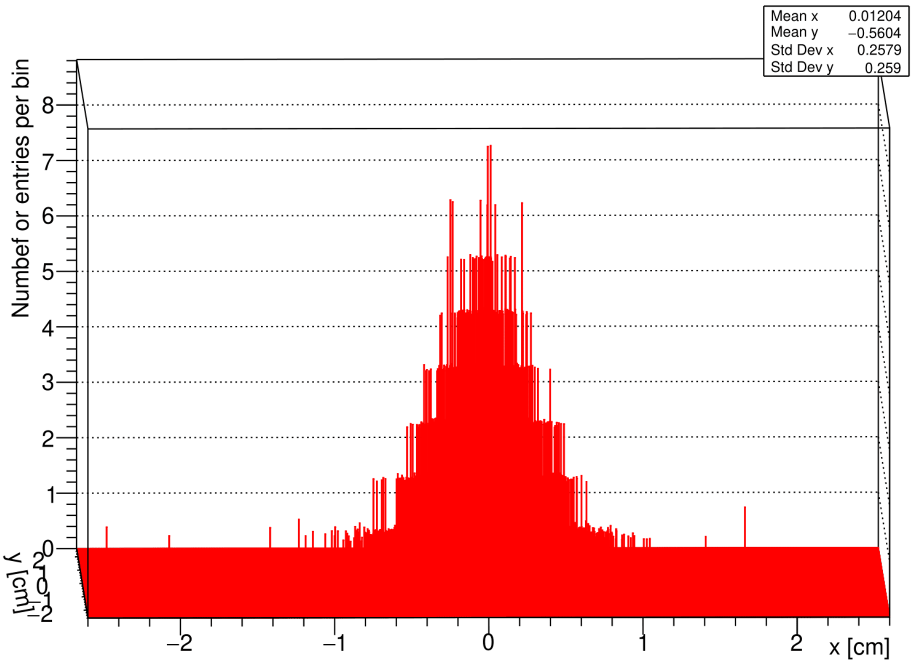

Figure 6.30: Lego beam profile at the exit of the second 2S sensor (along the way of the beam) from a simulated run of 20000 events where the Gaussian distributions of the beam xy-coordinates are visible.

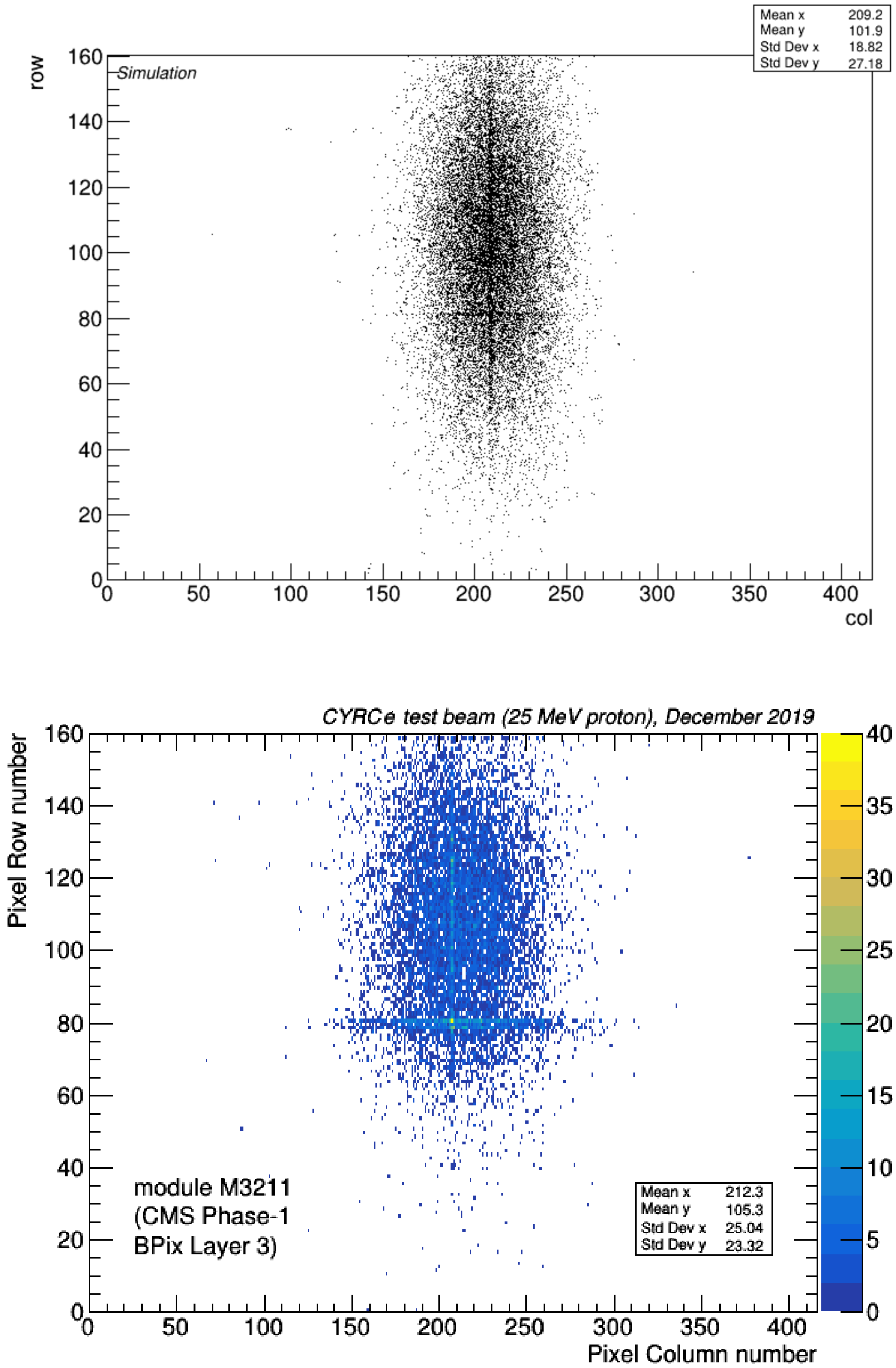

Figure 6.31: Top: Hit occupancy per column per row for the hit module of the second pixel layer (along the way of the beam) from a simulated run of 20000 events. Bottom: 2D (column, row) hit occupancy map for a CMS Phase-1 Pixel module. The module has been previously calibrated using pXar software and is operated at a depletion voltage of $-100\,\mathrm{V}$. Data are taken under a 25 MeV proton beam with random triggers (with the help of a Digital Test Board). There is no magnetic field, and the module is rotated by 90 degrees around the axis of the beam. The pixels with higher occupancy correspond to pixels of larger sizes, located at the edges of ROCs. This run was used as reference for the definition of the beam xy-position in the simulation run (and the experimental cluster occupancy map is noisier than the simulated one). (Image: IPHC.)

The hit multiplicity in a current event is defined as the number of pixels/strips which have counted a hit during the event. However, the transportation physics process in the physics list is not sufficient to describe completely the firing of several neighboring pixels/strips such as those observed during the 2019 beam tests at IPHC. For this reason, an artificial charge sharing and digitization algorithm is applied for both the pixel and strip sensors. It is based on the approach presented by Esposito et al. [14] (with some modifications) and takes into account the charge transfer from one pixel/strip to the neighboring ones after the energy deposition in their volumes has been calculated.

For each pixel which has counted a hit (i.e. the collected charge is above its defined threshold) its charge is divided by 4, and each quarter corresponds to one of the four directions. For each quarter of the initial pixel charge it will be checked if it will be transferred to its related direction (top, bottom, left, right). The values produced by four different random number generators (corresponding actually to pixels in the upper, lower, left and right directions, respectively) determine if charge will be shared between the current and some of the neighboring pixels. (In the case of the edge pixels, the random number generators will be less than four.) Thus, for the common case of non-edge pixels, in 50% of the cases charge will be shared with a pixel in the top direction, in 50% of the cases charge will be shared with a pixel in the bottom direction, in 50% of the cases charge will be shared with a pixel in the left direction and in 50% of the cases charge will be shared with a pixel in the right direction. (For simplicity purposes diagonal movements, e.g. in the top-left direction are not examined.) The occurrence of transferring charge in one direction does not affect the occurrence of transferring charge in any other direction (stochastically independent cases). In case that it has been determined that charge will be shared with a neighboring pixel, the outcome of a Gaussian random number generator dictates how much charge will be shared with this specific neighboring pixel. The mean value of the random number generator is equal to 1/4 of the charge of the initial pixel which has counted the hit, while its standard deviation is set to 1400 electrons (this value was chosen to best fit the simulation output to the experimental data). Subsequently, it is checked if the final charge of the neighboring pixel of the hit pixel is above the threshold of 10000 electrons, in order to evaluate if it should be considered a part of the pixel cluster or not.

For the strips the method is similar, but since only one row of strips is hit in each sensor of the 2S module, the charge of each hit strip is divided by 2 and charge sharing takes place only with the left and right strips of the strip which has counted a hit. Again, in 50% of the cases charge will be shared with the left strip and in 50% of the cases charge will be shared with the right strip. The occurrence of transferring charge in one direction does not affect the occurrence of transferring charge in any other direction (stochastically independent cases). In case that it has been determined that charge will be shared with a neighboring strip, the outcome of a Gaussian random number generator determines how much charge will be shared with this specific neighboring strip. The mean value of the random number generator is equal to 1/2 of the charge of the initial strip which has counted the hit and its standard deviation is set to 1500 electrons (value chosen to best fit the output to the experimental data). Subsequently, it is checked if the final charge of the neighboring strip of the hit strip is above the strip threshold of 5000 electrons, in order to evaluate if it should be considered a part of the strip cluster or not.

The hit multiplicities of the hit pixel sensors of the telescope and the 2S sensors of the DUT are shown in Fig. 6.32-6.35. The mean values of the hit multiplicities of the pixel sensors in the simulation are within the range of 4.2-4.4 pixels, which is of the same order of magnitude as the corresponding experimental mean values of approximately 4.2 pixels. The mean values of the hit multiplicities of the 2S sensors in the simulation are within the range of 3.7-3.8 pixels, which is of the same order of magnitude as the corresponding experimental mean values of 3.2-3.5 pixels. The product of the hit multiplicity of a 2S sensor multiplied by the strip threshold is equal to the cluster charge, which is usually of the order of 10000-60000 electrons.

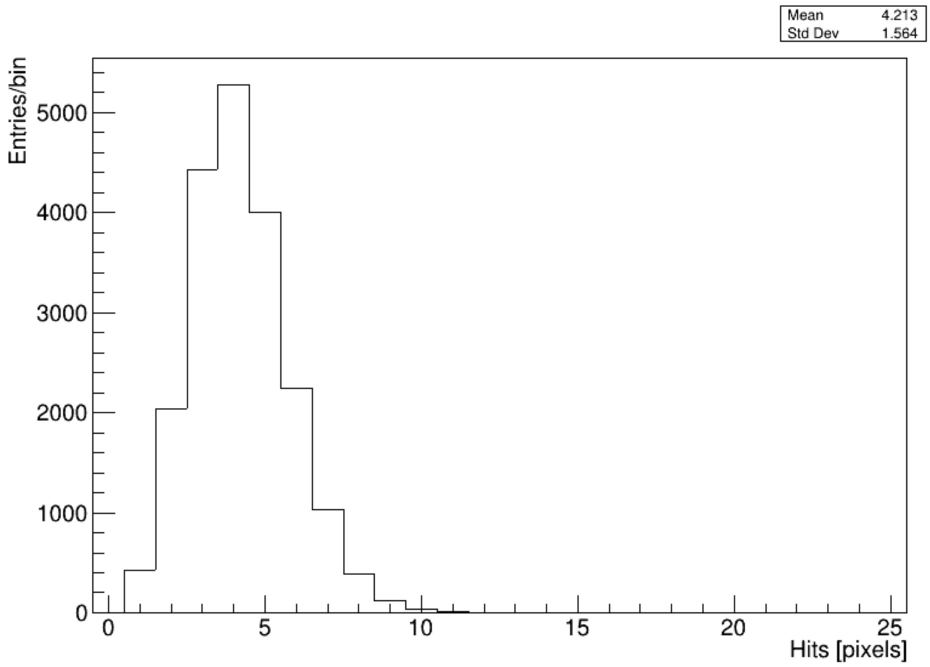

Figure 6.32: Hit multiplicity of the hit module of the first pixel layer (along the way of the beam) from a simulated run of 20000 events.

Finally, the simulation program for the CHROMini telescope can check if there is a stub in a given event. For every strip of the first 2S sensor (along the way of the beam) with ID = i, which has counted a hit, the program checks if any of the strips with ID = $i-2$, $i-1$, i, $i+1$, $i+2$ (if they exist) of the second 2S sensor have also counted a hit. If a hit match between the two 2S planes is found and its distance in the y-direction from the line which connects points A and D (as described above) is smaller than a fixed upper limit (here set to 100 μm), then the program may print out that a stub has been found in the current event. For vertical incidence of the beam and for configurations similar to the one described in this document, usually a stub is found in more than 99% of the events.

To summarize, CHROMini, a new high-rate telescope, has been commissioned at IPHC, mostly based on technology developed for the CMS experiment, thus being compatible with previously existing CMS hardware and software. Similarly to CHROMIE, it can be used for tests of front-end electronics under high particle rates and at high occupancy, to study detector performance and to monitor effects of radiation damage on silicon sensors. A standalone simulation program based on the Geant4 toolkit has been developed to predict the response of the telescope under a 25 MeV proton beam (as well as other types of particle beams). This program can be used for estimating unknown beam parameters through comparison of its output with plots from real data where some magnitudes are unknown (e.g. for the estimation of the beam diameter from the hit occupancy plot, given that the pixel size is known). There is currently a good agreement in the resolution, hit occupancy and hit multiplicity between the test beam data and the simulation results. The program could be used as a potential base for future simulations of other particle telescopes with silicon pixel sensors and organic scintillators, for

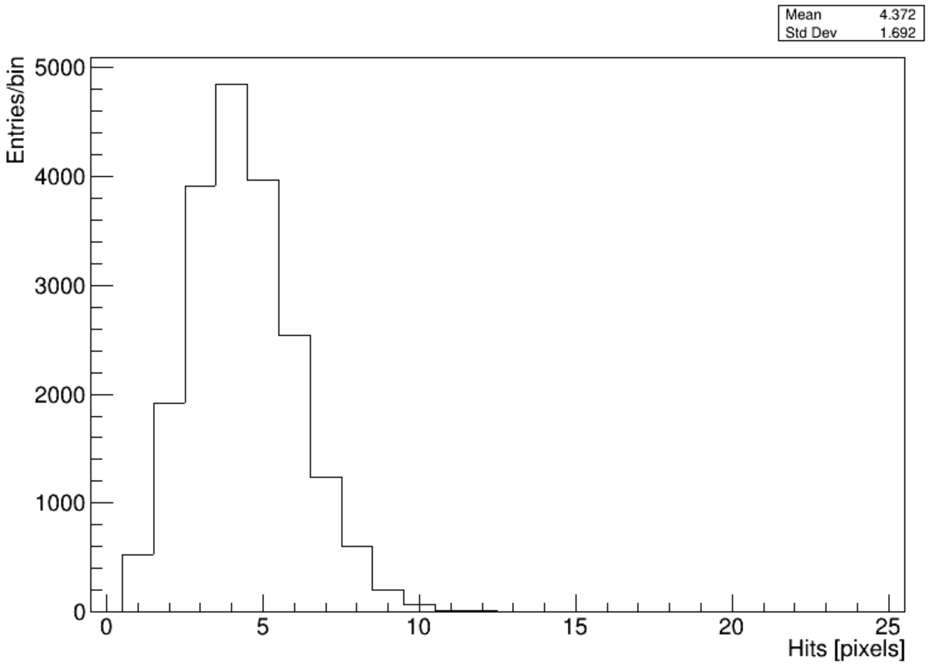

Figure 6.33: Hit multiplicity of the hit module of the second pixel layer (along the way of the beam) from a simulated run of 20000 events.

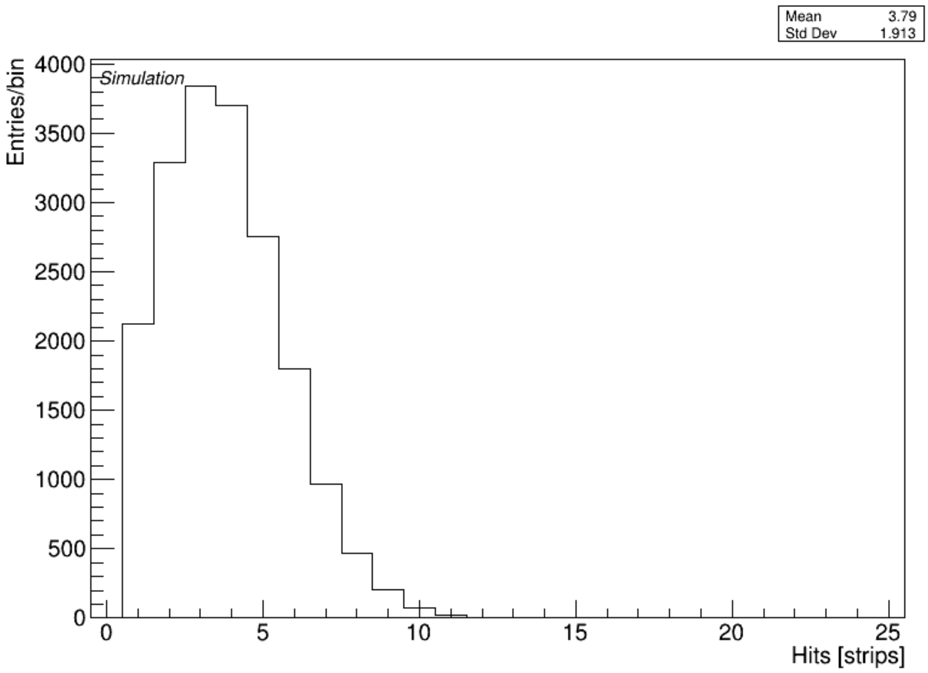

Figure 6.34: Hit multiplicity of the first 2S sensor (along the way of the beam) from a simulated run of 20000 events.

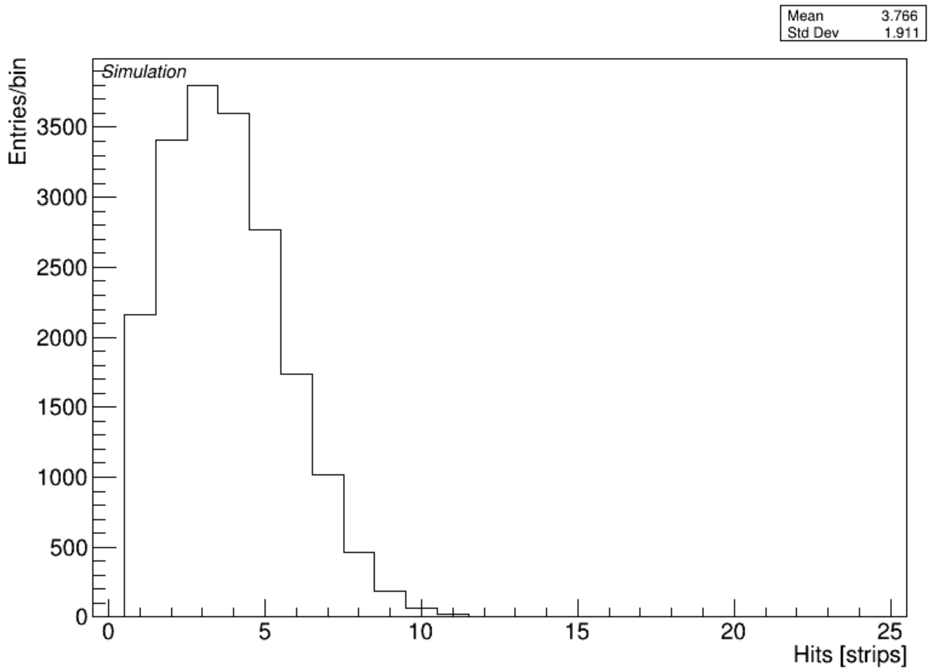

Figure 6.35: Hit multiplicity of the second 2S sensor (along the way of the beam) from a simulated run of 20000 events.

selecting the various parameters of the design (e.g. distances between planes, material thickness) in order to minimize the multiple scattering effects and optimize the resolution for low energy beams [15].

6.6 Appendix: Other outputs of the simulation

The energies deposited in the various volumes of the setup are shown in Fig. 6.36-6.44. The kinetic energies of the primary protons at the entrances and exits of the different components of the setup are presented in Fig. 6.45-6.57. The kinetic energies of the secondary particles (mainly electrons) created in the sensors of the 2S module are shown in Fig. 6.58-6.59. Secondary particles here are the particles which have sufficient energy to travel at least 100 μm from their production point. The total energies lost by primary protons in each of the two sensors of the 2S module are shown in Fig. 6.60 and 6.61, respectively. The total energy lost in a volume by a particle is the sum of the energy deposited in the volume and the kinetic energy of newly produced secondary particles. All plots are obtained from a simulated run of 20000 events with a 25 MeV proton beam.

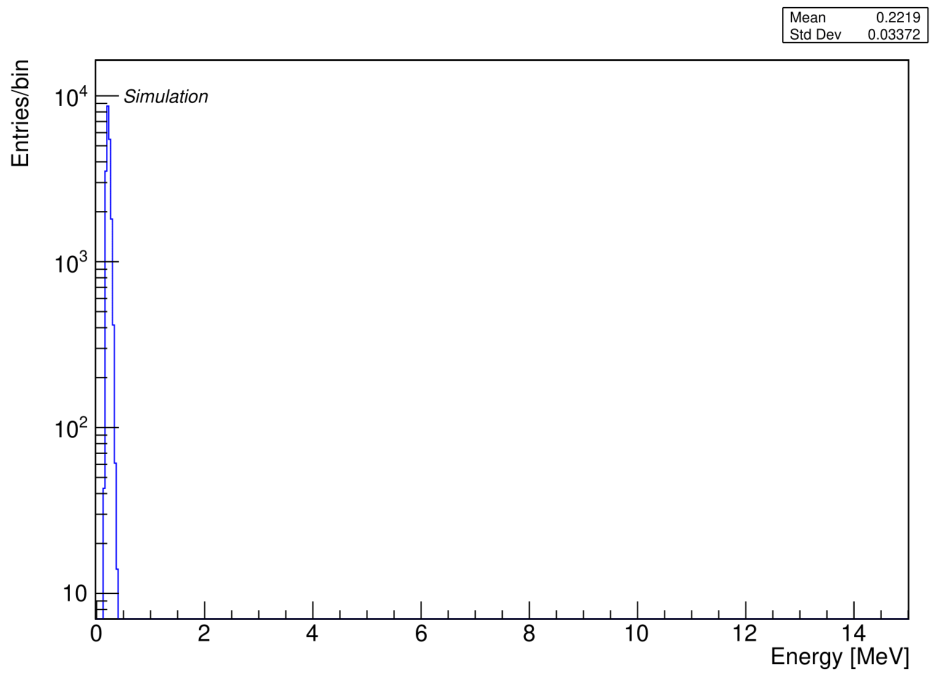

Figure 6.36: Energy deposited in the Al foil (logarithmic scale, simulation).

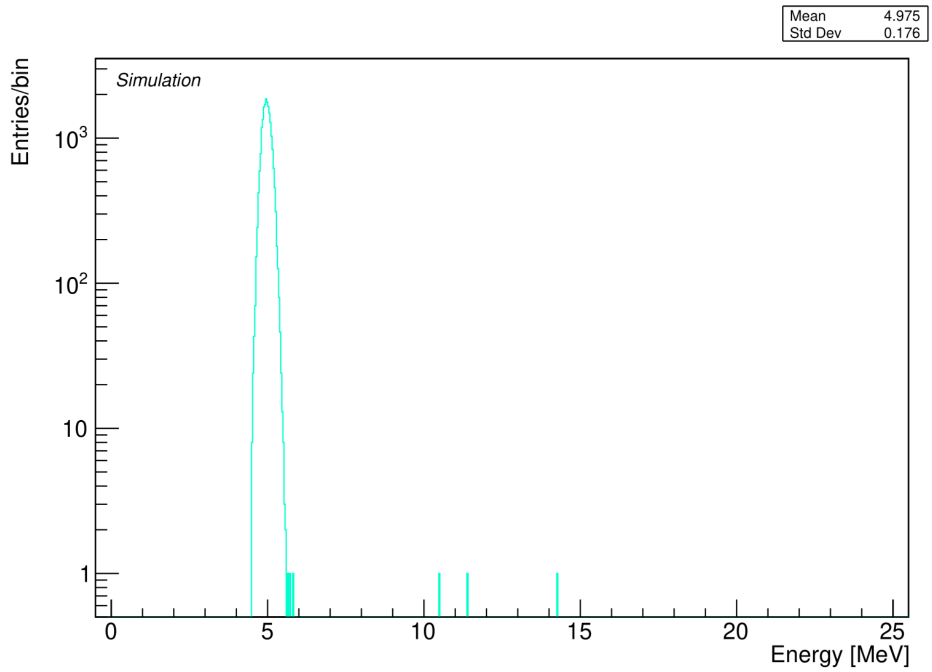

Figure 6.37: Energy deposited in the first scintillator (logarithmic scale, simulation).

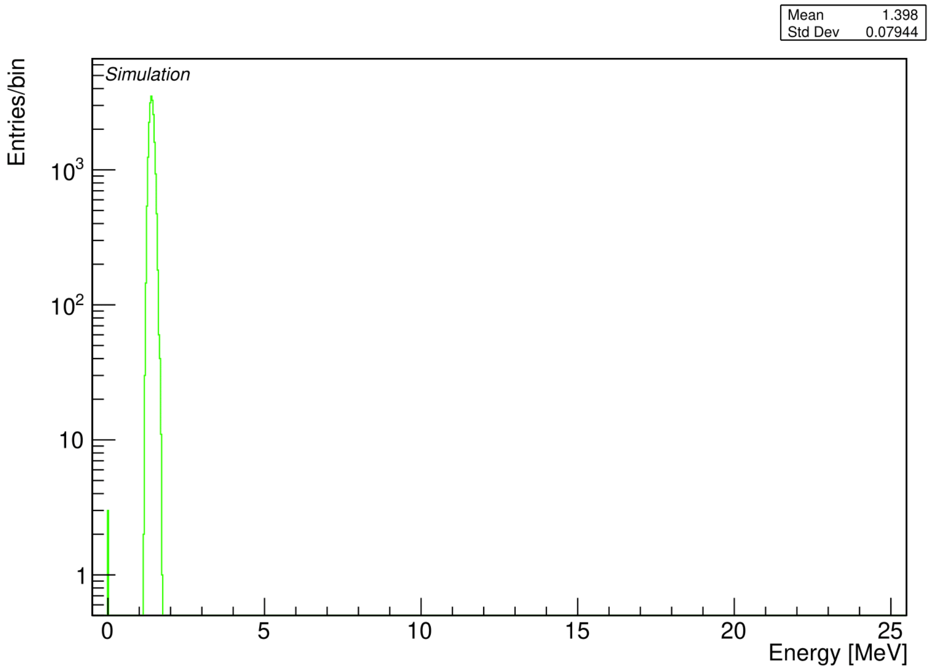

Figure 6.38: Energy deposited in the sensor of the hit module of the first pixel layer (logarithmic scale, simulation).

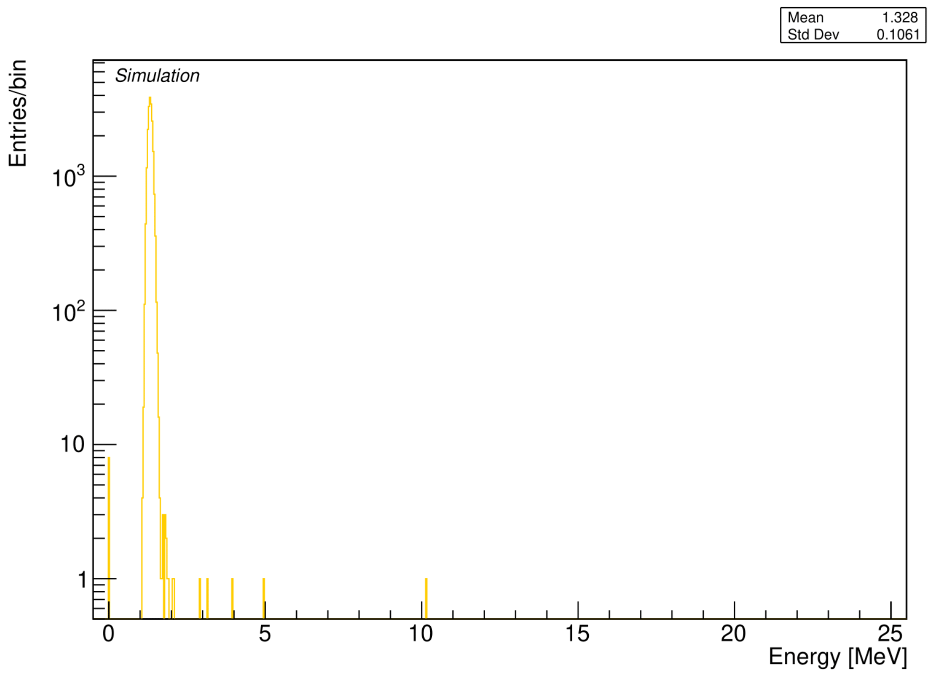

Figure 6.39: Energy deposited in the ROC of the hit module of the first pixel layer (logarithmic scale, simulation).

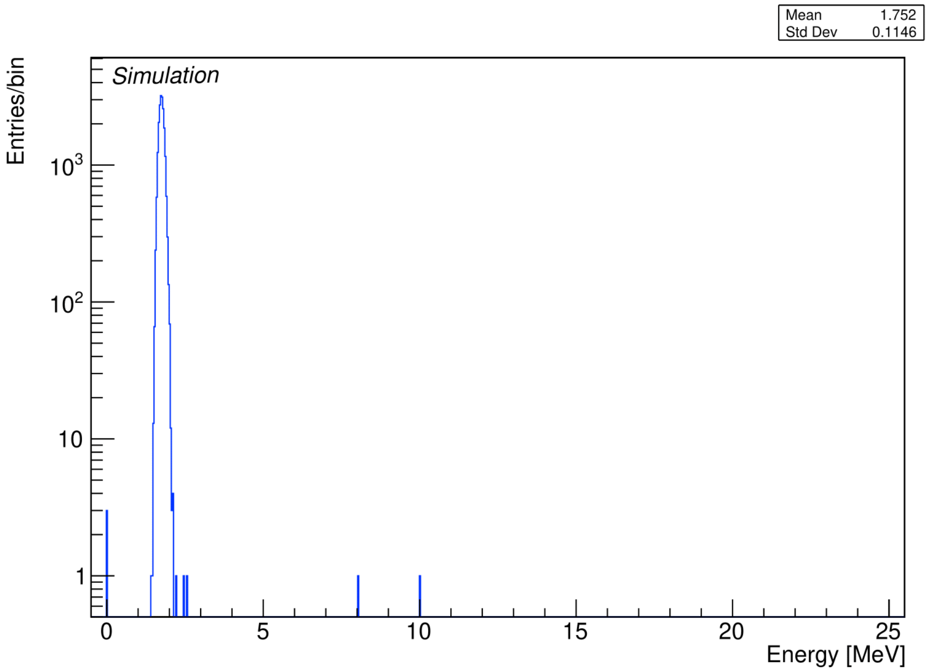

Figure 6.40: Energy deposited in the first 2S sensor (logarithmic scale, simulation).

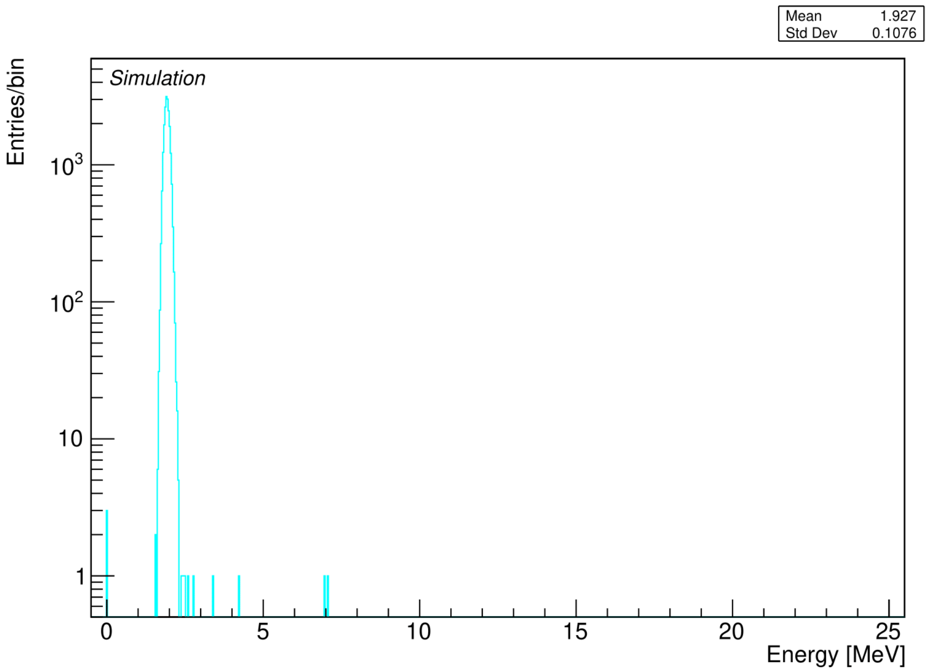

Figure 6.41: Energy deposited in the second 2S sensor (logarithmic scale, simulation).

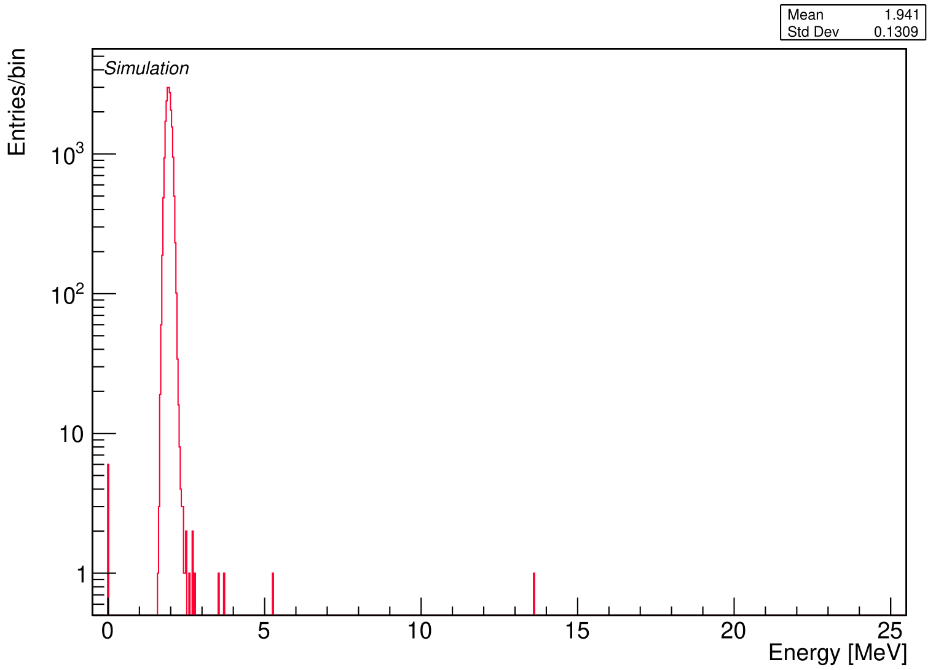

Figure 6.42: Energy deposited in the sensor of the hit module of the second pixel layer (logarithmic scale, simulation).

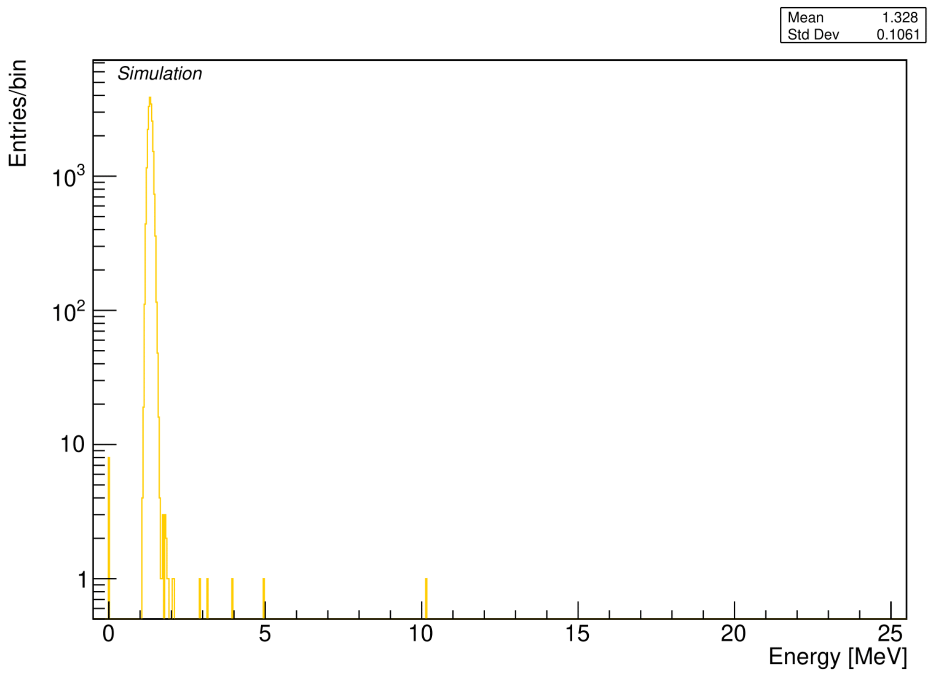

Figure 6.43: Energy deposited in the ROC of the hit module of the second pixel layer (logarithmic scale, simulation).

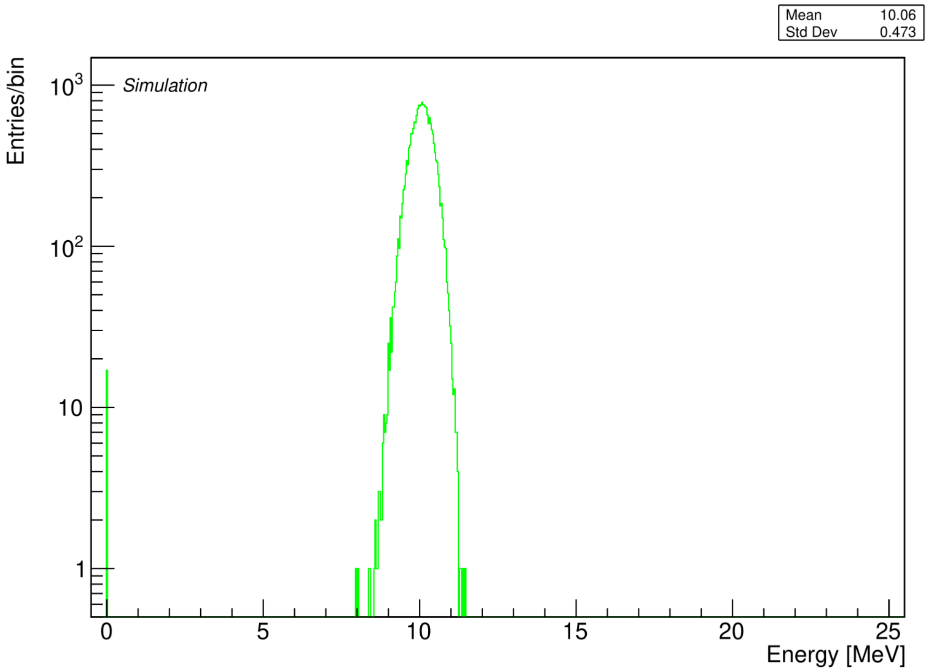

Figure 6.44: Energy deposited in the second scintillator (logarithmic scale, simulation).

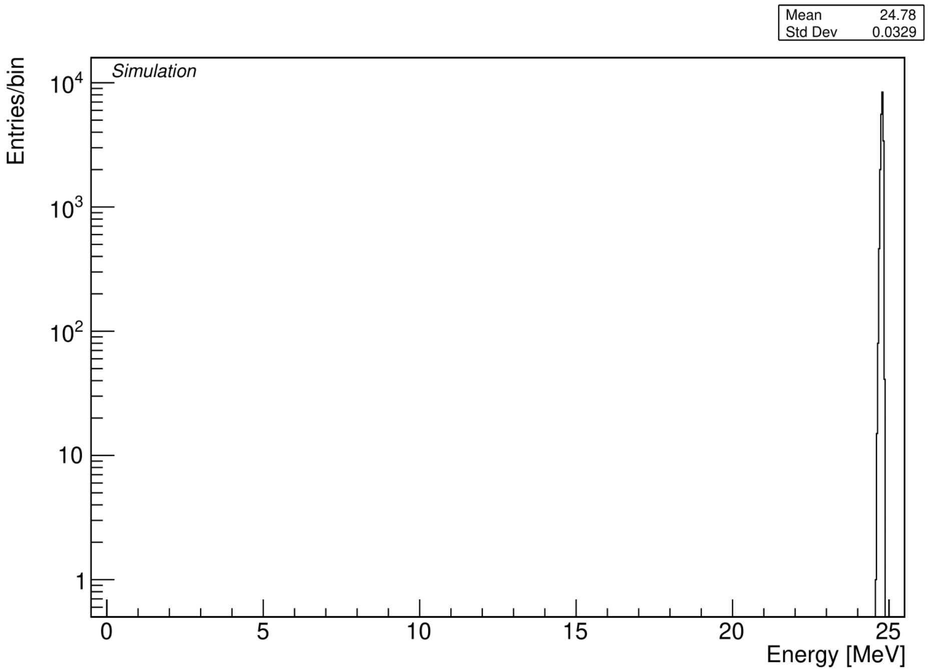

Figure 6.45: Kinetic energy of primary protons at the exit of the Al foil (logarithmic scale, simulation).

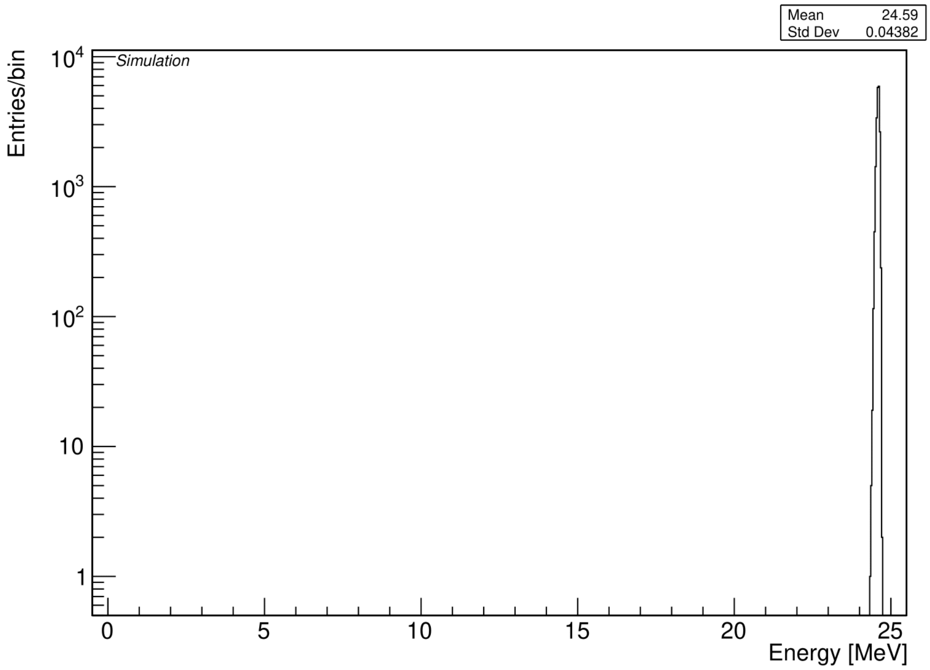

Figure 6.46: Kinetic energy of primary protons at the entrance of the first scintillator (logarithmic scale, simulation).

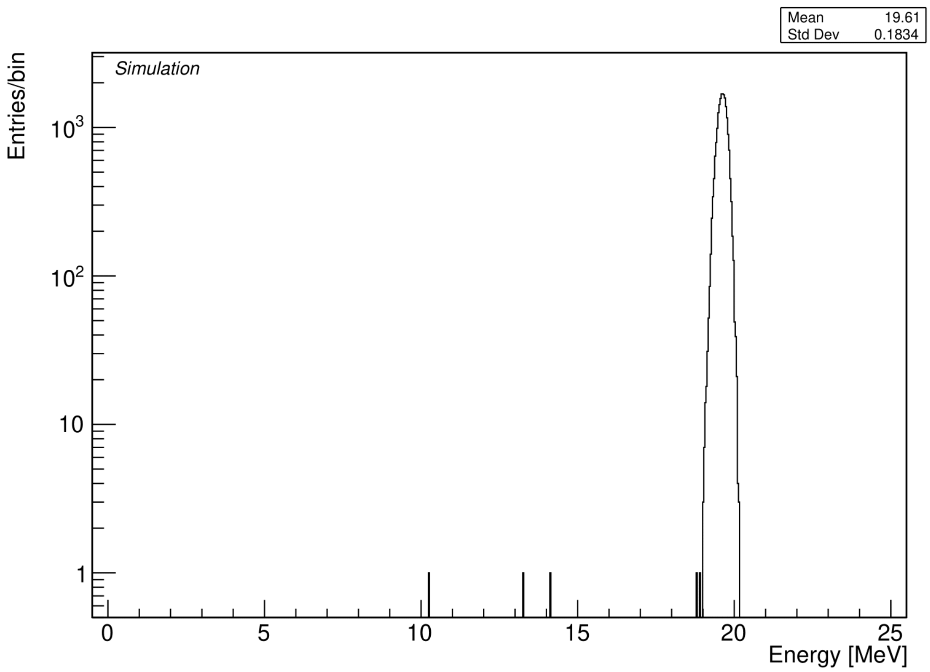

Figure 6.47: Kinetic energy of primary protons at the exit of the first scintillator (logarithmic scale, simulation).

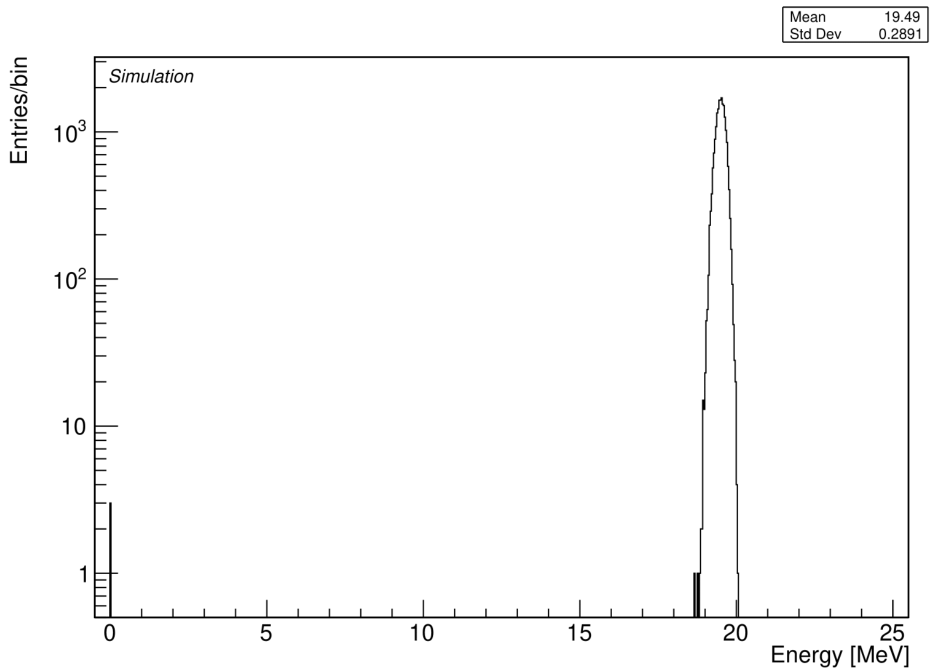

Figure 6.48: Kinetic energy of primary protons at the entrance of the first pixel layer (logarithmic scale, simulation).

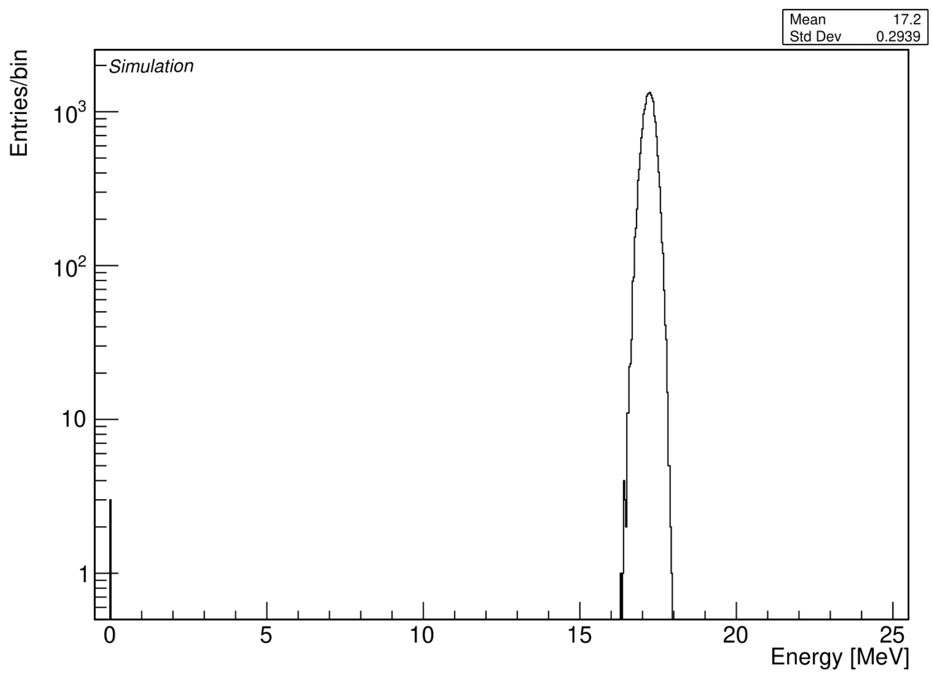

Figure 6.49: Kinetic energy of primary protons at the exit of the first pixel layer (logarithmic scale, simulation).

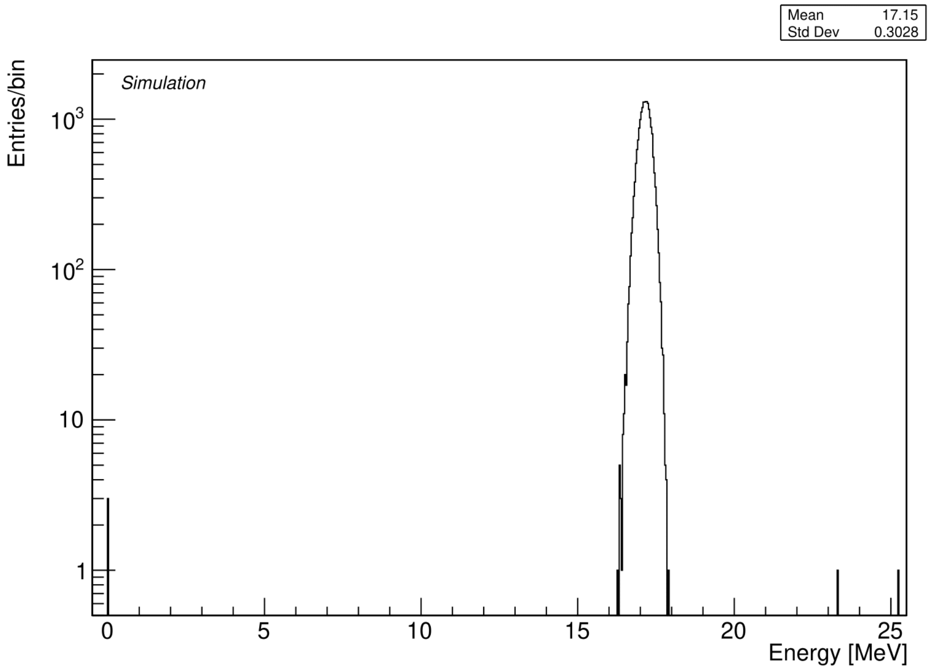

Figure 6.50: Kinetic energy of primary protons at the entrance of the first 2S sensor (logarithmic scale, simulation).

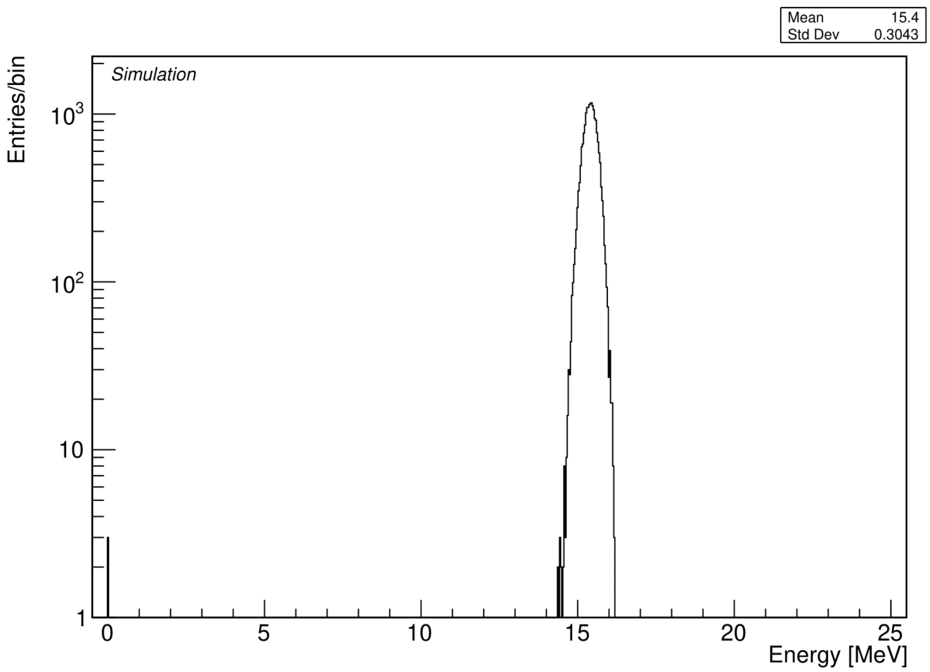

Figure 6.51: Kinetic energy of primary protons at the exit of the first 2S sensor (logarithmic scale, simulation).

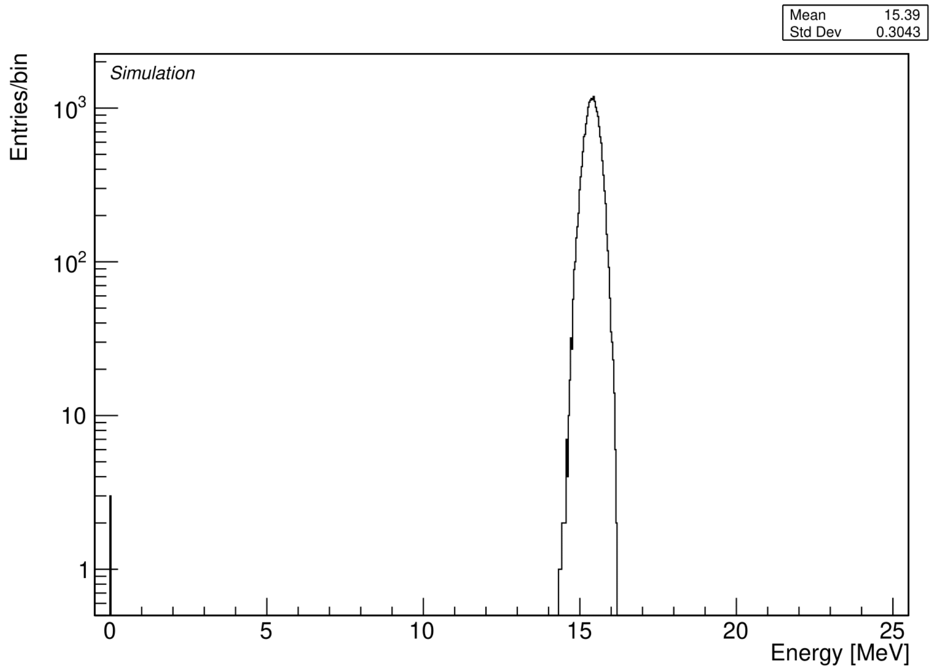

Figure 6.52: Kinetic energy of primary protons at the entrance of the second 2S sensor (logarithmic scale, simulation).

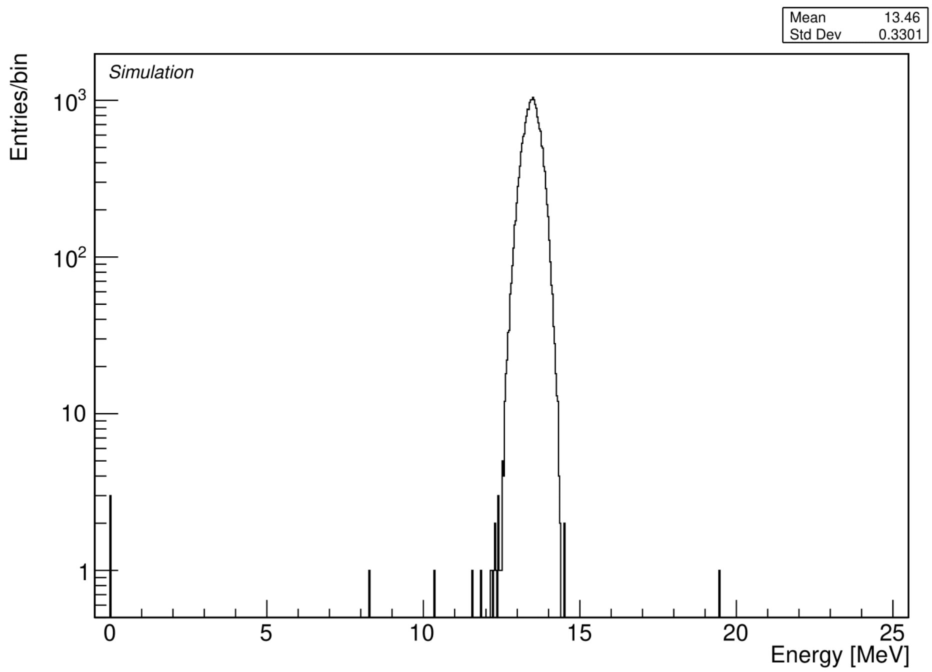

Figure 6.53: Kinetic energy of primary protons at the exit of the second 2S sensor (logarithmic scale, simulation).

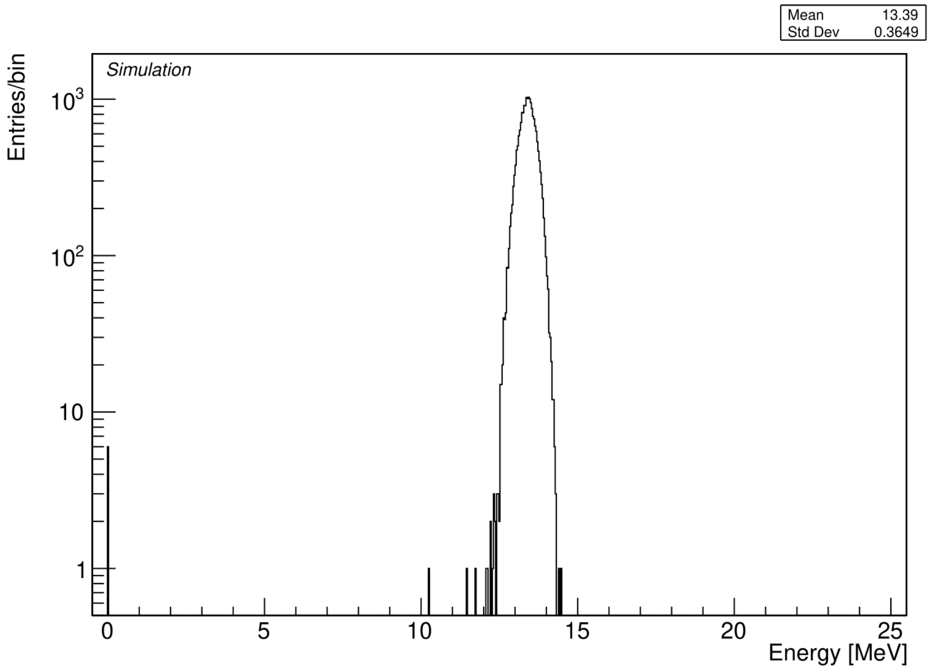

Figure 6.54: Kinetic energy of primary protons at the entrance of the second pixel layer (logarithmic scale, simulation).

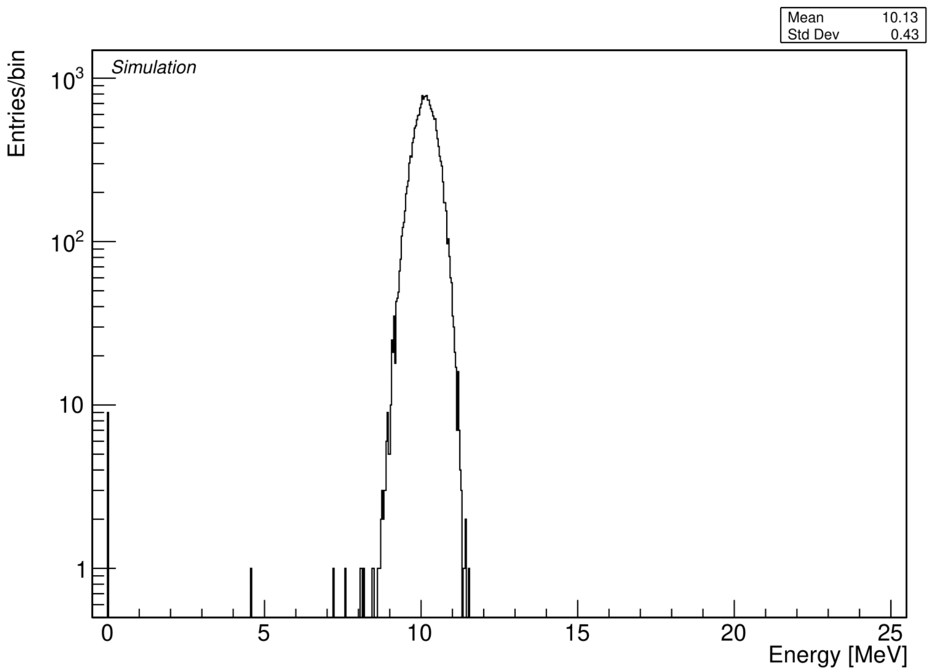

Figure 6.55: Kinetic energy of primary protons at the exit of the second pixel layer (logarithmic scale, simulation).

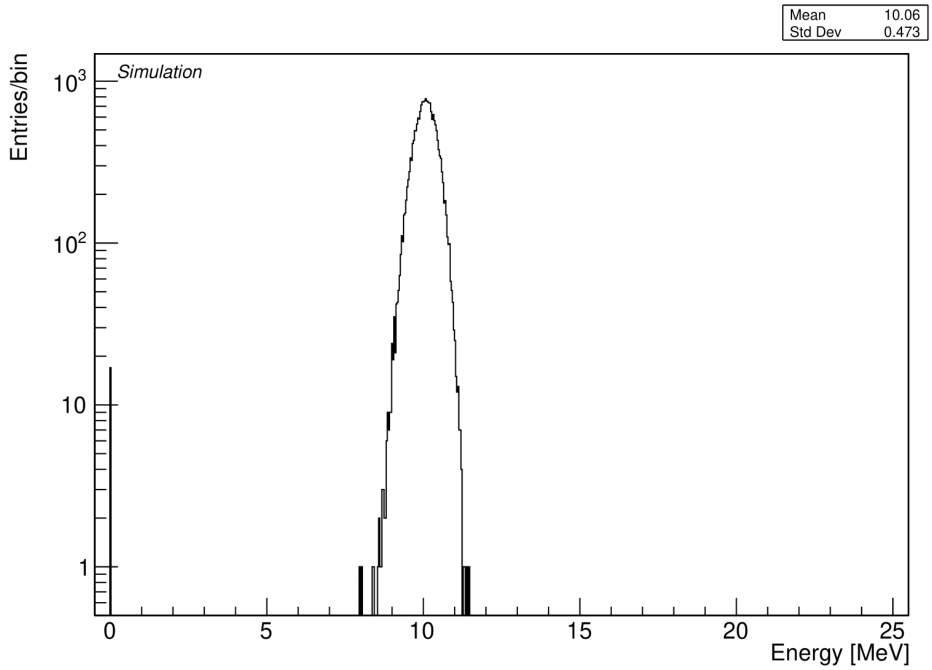

Figure 6.56: Kinetic energy of primary protons at the entrance of the second scintillator (logarithmic scale, simulation).

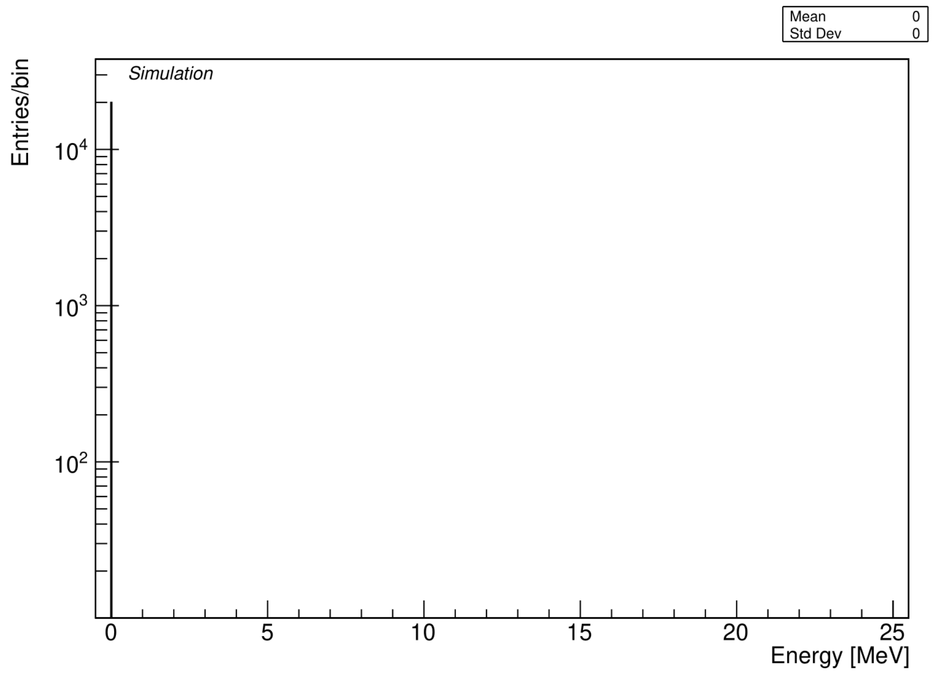

Figure 6.57: Kinetic energy of primary protons at the exit of the second scintillator (logarithmic scale, simulation).

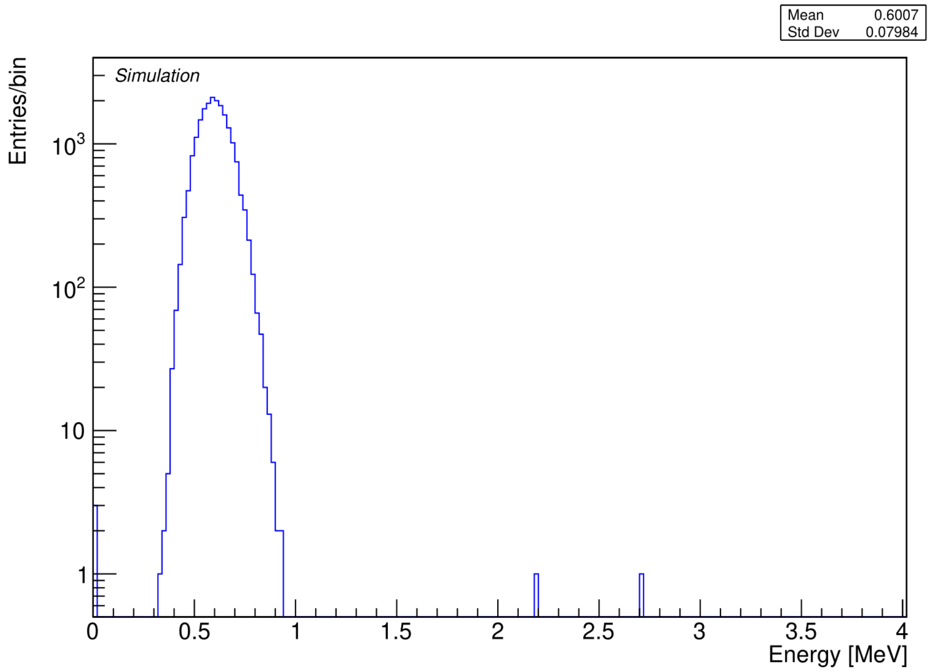

Figure 6.58: Kinetic energy of secondary particles produced in the first 2S sensor (logarithmic scale, simulation).

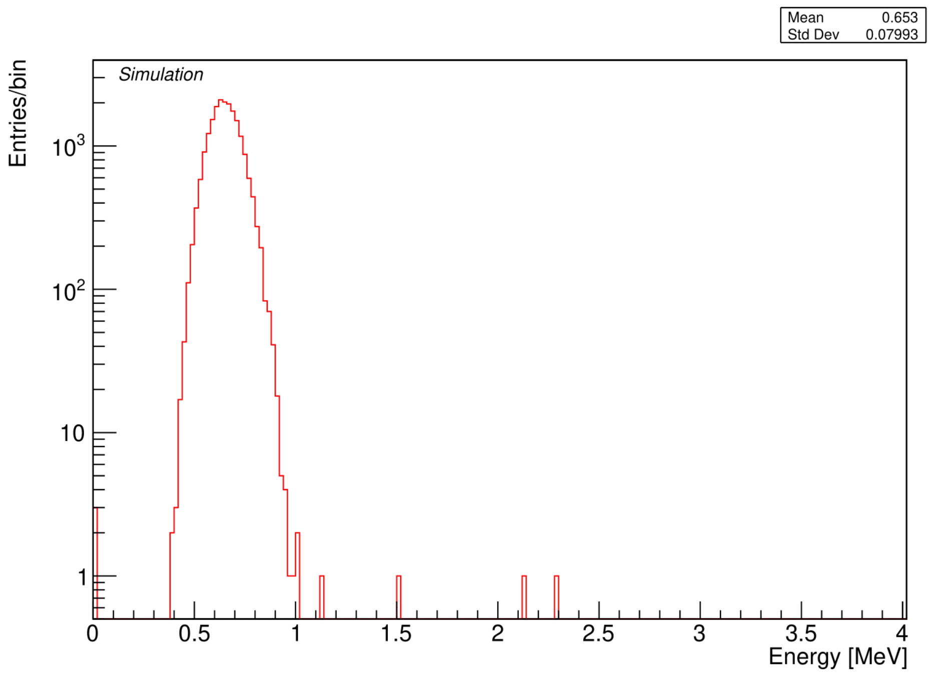

Figure 6.59: Kinetic energy of secondary particles produced in the second 2S sensor (logarithmic scale, simulation).

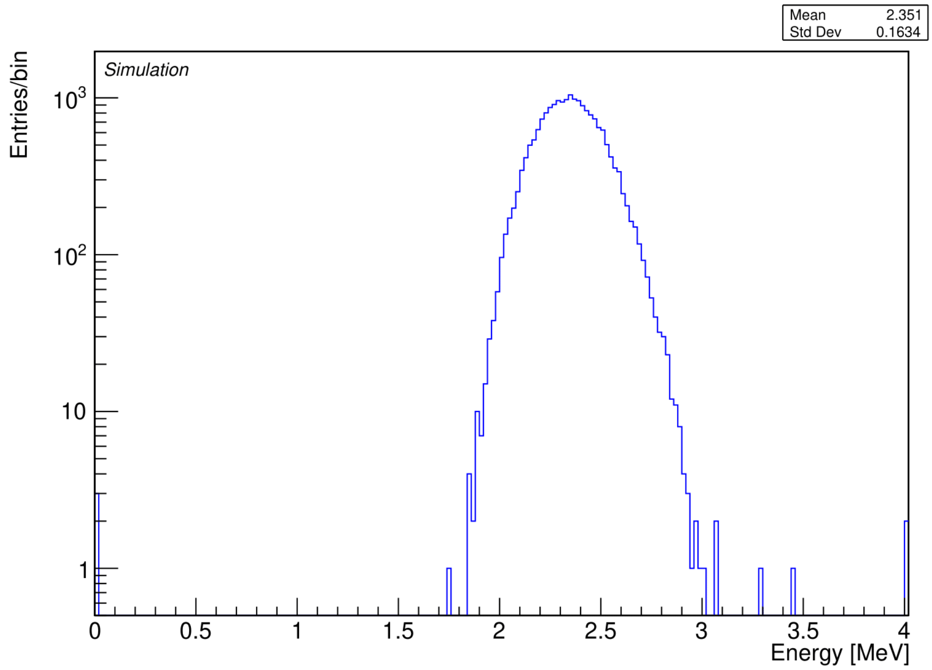

Figure 6.60: Total energy lost by the primary protons in the first 2S sensor (logarithmic scale, simulation).

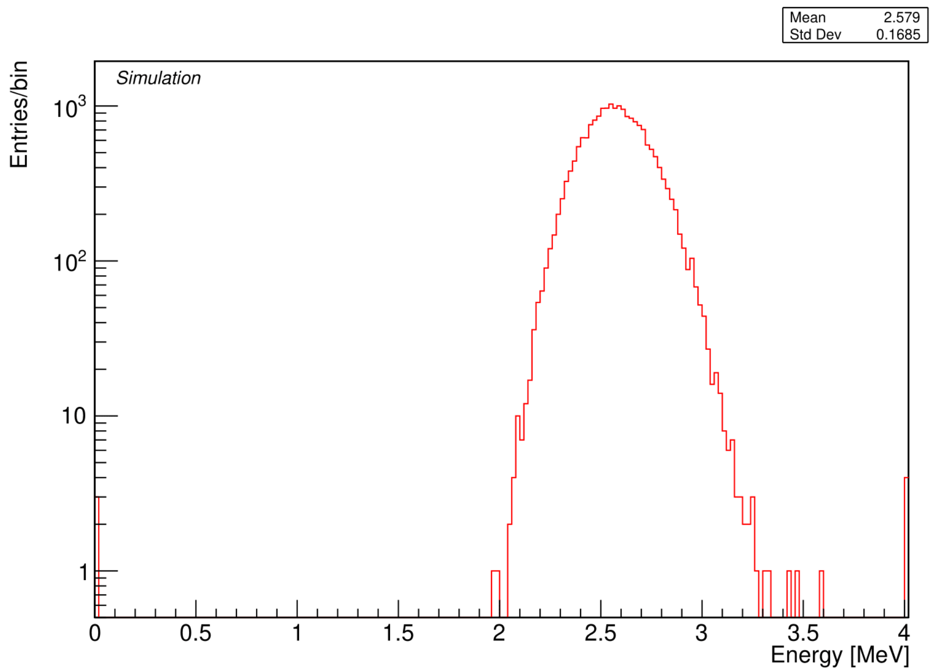

Figure 6.61: Total energy lost by the primary protons in the second 2S sensor (logarithmic scale, simulation).

Bibliography

[1] G. Apollinari et al., *High-Luminosity Large Hadron Collider (HL-LHC): Technical Design Report V. 0.1*, CERN Yellow Rep.Monogr. 4 (2017) 1-516 CERN-2017-007-M.

[2] CMS Collaboration, *The CMS experiment at the CERN LHC. The Compact Muon Solenoid experiment*, JINST 3 S08004 (2008).

[3] CMS Collaboration, *The Phase-2 Upgrade of the CMS Tracker*, CERN-LHCC-2017-009, [CMS-TDR-17-001] (2017).

[4] P. Marchand, A. Ouadi, M. Pellicioli, D. Brasse, *Cyrcé, un cyclotron pour la recherche et l'enseignement en Alsace*, L'Actualité Chimique 386 (2014) 9-14.

[5] C. Grimault, U. Goerlach, *Reference telescope for detector tests at the 25 MeV proton cyclotron CYRCé at Strasbourg*, 8th Beam Telescopes and Test Beams Workshop, 27-31 January 2020, Tbilisi State University.

[6] U. Goerlach, *Test-beam and irradiation facility for high rates and occupancies with a LHC like beam frequency of 42.5 MHz at the 25 MeV proton cyclotron CYRCé at Strasbourg*, 8th Beam Telescopes and Test Beams Workshop, 27-31 January 2020, Tbilisi State University.

[7] S. Agostinelli et al., *Geant4: A simulation toolkit*, Nucl. Instrum. Meth. A 506 (2003), 250-303.

[8] Geant4 Collaboration, *Geant4: A Simulation toolkit: Book for Application Developers*, Release 10.6, Rev4.0: December 6th, 2019.

[9] Martin Lipinski, *The Phase-1 Upgrade of the CMS Pixel Detector*, JINST 12 (2017) C07009.

[10] J.B. Birks, *Scintillations from Organic Crystals: Specific Fluorescence and Relative Response to Different Radiations*, Proc. Phys. Soc. A64: 874 (1951).

[11] S. Damache et al., *Stopping powers and energy loss straggling for MeV protons in a kapton polyimide thin film*, Nucl. Instrum. Meth. B 383 (2016).

[12] P. Alexa, A. Synytsya et al., *Raman Spectroscopy of Irradiated Tissue Samples*, Capture Gamma-Ray Spectroscopy and Related Topics: Proceedings of the Eleventh International Symposium 2-6 September, 2002 Pruhonice, Czech Republic.

[13] *NIST: Appendix for ESTAR, PSTAR, and ASTAR*, physics.nist.gov .

[14] M. Esposito et al., *Geant4-based simulations of charge collection in CMOS Active Pixel Sensors*, JINST 12 P03028 (2017).

[15] Patrick Asenov, *Performance of a simple 2-plane telescope (CHROMini) and a CMS 2S module in a 25 MeV proton beam: Comparison between data and Geant4 simulation*, 8th Beam Telescopes and Test Beams Workshop, 27-31 January 2020, Tbilisi State University.

Chapter 7

Test beam characterization of a 2S module with the DATURA telescope

The results of an analysis of test-beam data from DESY, where the stub efficiency of a 2S module is calculated for various angles of rotation of the module, are summed up in this chapter.

7.1 The EUDET-type beam telescopes and DATURA

Apart from CHROMini at IPHC, which was discussed previously, prototype 2S modules have additionally been characterized at beam tests with a EUDET-type beam telescope. The EUDET-type beam telescopes are Mimosa pixel telescopes that originated from a EUDET project before 2010, within the Integrated Infrastructure Initiative funded by the EU in the 6th Framework Programme. They provide a high-precision beam tracking ($\sim 2\,\mu$m, though at lower beam energies the track resolution deteriorates due to increasing multiple scattering), a sufficient event rate (~ 2 kHz rate at DESY) and an easy integration capability of a device under test (via pre-defined interfaces, for fast LHC-type tracking devices as well as slower rolling-shutter readout devices). In general, they are operated by the EUDAQ framework (generic DAQ framework) and analysed with EUTelescope (generic pixel telescope data analysis framework). The original EUDET beam telescope, which was modified to become the AIDA telescope, is operated at SPS beamline H6 (CERN), and several replicas have been built since then, and are nowadays located in various test beam facilities around the world (CERN, Germany, USA) [1], [2], [3].

The EUDET-type beam telescopes are equipped with six sensor planes using CMOS MIMOSA 26 monolithic active pixel devices, and the mechanics for precise positioning of the device under test (DUT) and the telescope planes in the beam (Fig. 7.1, where in the Cartesian, right-handed coordinate system chosen, the y-direction points vertically down and the z-direction along the beam direction). A programmable Trigger Logic Unit (TLU) provides trigger logic and time stamp information on particle passage. Threshold studies have shown an optimal working point of the MIMOSA 26 sensors at a sensor threshold of between five and six times their RMS noise [1], [2], [3].

Test-beam data for the 2S module characterization have been taken at the DESY II test beam facilities. The DESY II electron/positron synchrotron at the DESY site in Hamburg has a circumference of 292.8 m. Its main purpose is to act as an injector for the PETRA III storage ring. However, it also supplies beam to three test beam areas (TB21, TB22, TB24). Its dipole

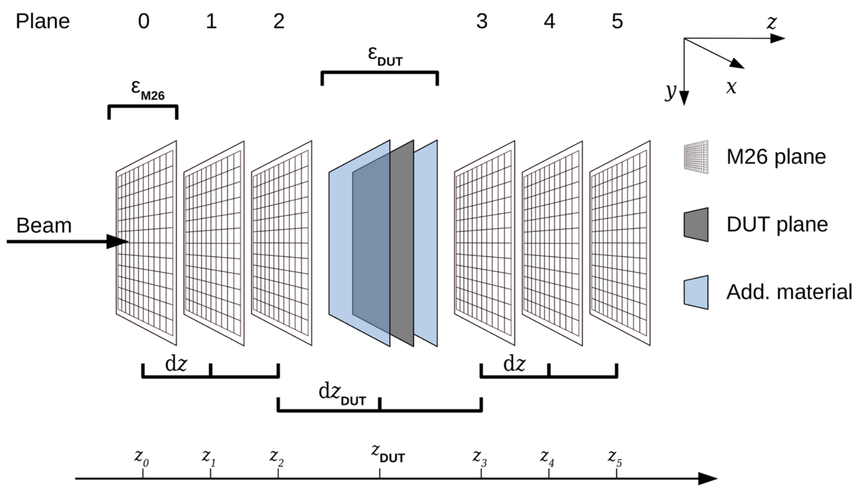

Figure 7.1: Sketch of the EUDET-type beam telescope setup and its important parameters (made by H. Jansen et al.). Planes 0 to 2 and planes 3 to 5 are referred to as upstream and downstream planes, respectively.

magnets operate in a sinusoidal ramping mode with a frequency of 12.5 Hz, and so one DESY II cycle takes 80 ms, with a bunch length of around 30 ps. The DESY-II synchrotron is equipped with movable carbon fibres, that when positioned in the beam produce bremsstrahlung photons which escape the beam line tangentially. Afterwards, the photons are converted to electron/-positron pairs on a secondary metal target. Their energy distribution reaches up to 6 GeV. This secondary electron/positron beam can be spread out thanks to a dipole magnet. Certain energy ranges of the beams reaching the experimental halls can be selected with a collimator, with an achievable rate of about 10 kHz to 100 kHz [1], [4].

The DESY Advanced Telescope Using Readout Acceleration (DATURA) at TB21 was the telescope used for beam tests with a 2S module as a DUT. Just like the other EUDET-type telescopes, DATURA, features six pixel detector planes equipped with MIMOSA 26 sensors. Each MIMOSA 26 sensor consists of pixels sized 18.4 µm × 18.4 µm, which are arranged in 1152 columns and 576 rows covering 21.2 mm × 10.6 mm. The sensors are thinned down to a thickness of about 50 µm and together with 50 µm of thin protective lightproof Kapton foil (25 µm on each side of the sensor), the total material of the six telescope planes (300 µm of silicon and 300 µm of Kapton) amounts to $\epsilon = x/X_0 = 4.8 \times 10^{-3}$, expressed as the fraction of radiation lengths. (ϵ defines the material budget of the scattering medium as the physical material thicknesses x normalized to their radiation lengths, with values of $X_0 = 93.65$ mm for silicon, $X_0 = 3.042 \times 10^5$ mm for dry air, and $X_0 = 285.6$ mm for Kapton.) The average intrinsic resolution (the average over all cluster sizes) has been measured to be 3.24 µm. The TLU features a coincidence unit with discriminator boards accepting up to four input signals. The TLU takes a trigger decision based on its four input channels and issues asynchronous triggers subsequently to connected subsystems. The telescope planes are designed to ensure that the amount of the material that the beam particles traverse remains as low as possible in order to achieve an excellent track resolution even at beam particle energies of a few GeV. The incoming charged particles traverse the telescope planes depositing energy therein. Free electron-hole-pairs are created along their path. The free carriers then drift towards the respective readout electrodes and if the collected charge surpasses a certain threshold in a given pixel, this pixel is registered. Finally, neighboring fired pixels are combined to form clusters [1], [2], [3].

The MIMOSA 26 sensors are read out with a rolling-shutter, taking 16 cycles of an 80 MHz clock per row, with all columns being read out in parallel, and at this clock frequency, the MIMOSA 26 integration time equals 115.2 μs. The expected maximum rate of detectable particles through the active area is estimated to be about 1 MHz/cm^2 [1], [2], [3].

Each pixel sensor is mounted within an aluminum jig, while three jigs are in turn mounted on each of the two aluminum telescope arms. The two telescope arms (one upstream and one downstream of the DUT) are movable along the direction of the beam in order to allow DUTs of different size to be fitted into the setup. The jigs are cooled keeping the MIMOSA 26 sensors at a constant temperature for stable operation. The entire beam telescope is placed on a rotatable frame, making it easier to achieve orientation parallel to the beam. Additionally, this frame is mounted on a robust structure for further stability and wheels that facilitate transportation [1], [2], [3].

The spatial acceptance for triggers is defined by four Hamamatsu PMT assemblies with scintillators and light guides, two in the front and two in the back of the telescope. The crossed scintillators (with a cross section of $\sim 2\,\text{cm} \times 2\,\text{cm}$) on either side of the beam telescope define a rectangular acceptance window in order to match the MIMOSA 26 sensor area [1], [2].

The modular cross-platform data acquisition framework EUDAQ for DATURA (and other EUDET-type telescopes) has been designed to allow the easy integration of other devices. It consists of entirely independent modules communicating via TCP/IP enabling a distributed data with modules running on separate machines. The main interaction point for users with the framework is the Run Control and its graphical user interface (GUI) which provides all controls necessary to the user on shift. Another important components of the system are the Log Collector (which gathers logging information from all modules and displays them in one unified logging window), the Producers (links between the EUDAQ framework and the subdetector systems such as the beam telescope, the TLU, or user DAQ systems), the Data Collector (which is responsible for the event building, i.e. the correlation of events from all subdetector systems to single global events comprising all data belonging to one trigger), the Online Monitor tool (which ensures data quality during data acquisition) and the Data Converter plug-ins (whose purpose is to perform data decoding) for every detector type attached to the Run Control [1].

7.2 The CMS November-December 2019 beam test at DESY

A test beam with 4 GeV electrons for the characterization of prototype 8CBC3 2S modules (2S front-end hybrids, each containing eight front-end CMS Binary Chips, version 3) [5] produced at the Karlsruhe Institute of Technology (KIT), the RWTH-Aachen University and the Brown University, took place in November and December 2019, at the DESY TB21 area in Hamburg (Fig. 7.2) [4]. The goals of the beam test were to achieve: a) tracking of particles in 2-3 synchronous 2S module; b) verification of the uniformity of efficiencies; c) check for inefficiencies or hit/stub duplications in the center of a 2S where the strips face each other; d) check stub finding inefficiency for tracks inclined along the strips; e) measurement of efficiency and noise hit rate versus the threshold; f) examination of the variation of noise versus operation time through the repetitions of the noise scan after several hours of data taking; g) study of the cluster width through repetitions of the angular scan at high angles; h) study the misalignment of two sensors in the modules with a very high statistics; and i) measurement of the stub correlation window. Different modes of operation were possible, such as having 3 modules between the arms of the DATURA telescope movable in the x- and y-directions, or a single module between the arms of the DATURA telescope which could be rotated about the y-axis. In this beam test and subsequent analysis the z-axis is always the axis of the beam. A FE-I4 plane from DESY was used as the reference plane needed to correct the track selection. Before the beam test, the DAQ was set up in the control room of the TB21 area. The EUDAQ was installed on a dedicated DAQ computer, EUDET and the AIDA TLU were tested, and specific EUDAQ producers for the DUTs and for environmental monitoring were prepared.

Figure 7.2: Photo of the area TB21 where the dipole magnet and DATURA are indicated.

The crew consisted of several groups from European, American and Asian universities and research centers. For each shift slot 2-3 people were assigned. Members of the CMS NCSR "Demokritos" group participated in the setup of the beam test, the shift and the stub efficiency-related analysis of the data.

Before entering the test beam area, the crew members had to undergo a safety course. They had to learn all crucial aspects related to escape routes and assembly points, behavior in case of fire, emergency OFF buttons, electrical safety and cabling, general tidiness, translation stages, ladders and bricks, test magnets, laser safety, gas safety, shipping and handling of hazardous materials, radiation safety, area interlocks and radiation warnings inside areas.

Additionally, each crew member had to learn how to initialize the test beam setup from scratch (log in to various machines, check power supply units, start operation of the MIMOSA DAQ), take data (control runs with EUDAQ, initialize/terminate runs), perform data quality monitoring (DQM) during data taking by checking various correlations, and check the temperature of the modules and the module current through the high-voltage (HV) monitor log.

Initially, a single module was commissioned in the beam area, at the center of the telescope. Noise scan results and latency scan with beam results were obtained. Afterwards, the other three modules were installed downstream. Since the readout of the telescope and the DUTs was not synchronous, several runs were spent to debug the DAQ. After some unsuccessful attempts, stable data taking conditions and synchronous data taking were achieved with two of the modules, and then the shifts started. A Vcth scan with beam was then performed (where the variable Vcth refers to the threshold settings). All test-beam data was stored on EOS, an open source distributed disk-based, low-latency storage service [6]. All runs and their details were registered in ELOG (a Web application which is used to create personal and common logbooks).

An IV curve and noise measurements for each module were taken during commissioning. During the initial runs, the beam was located with one of the modules, and threshold measurements were performed. They were followed by a Delay Locked Loop (DLL) scan to check how many times a cluster is found close to a track when selecting specific time-to-digital converter (TDC) phases. (A TDC is a a device for recognizing events and providing a digital representation of the time they occurred, and in our case it is highly programmable and based on the DLL principle.) After that, several threshold scans, horizontal scans, angular scans, scans along the strips and angular scans along the strips were performed on the modules (with voltages -300 V or -600 V). As mentioned before, since in the beginning the stubs in the 2S module did not match the hits in the data, the first days were mostly spent for debugging, but in the end the problem was resolved. A configuration of the setup is shown in Fig. 7.3.

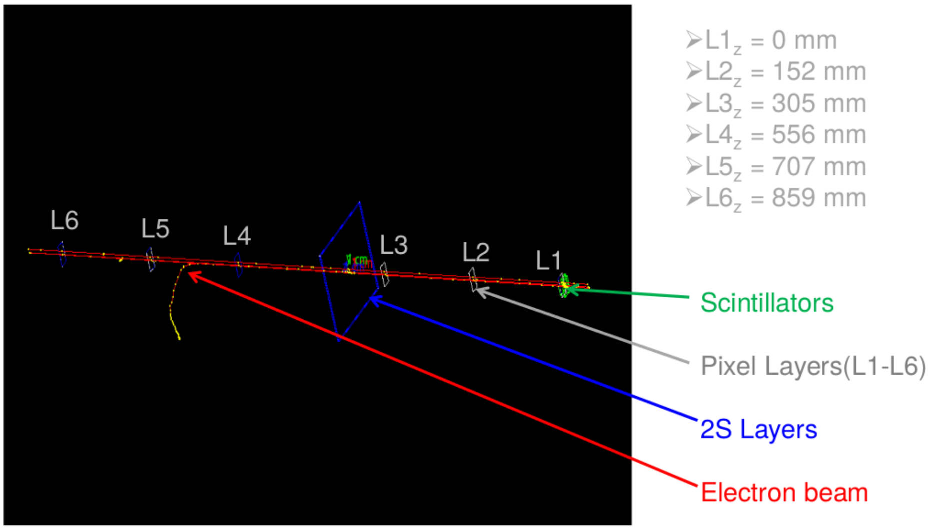

Figure 7.3: A schematic of a telescope and DUT configuration which was used during a scan along the strips. The DATURA planes, scintillators and a 2S module DUT are visible. Visualization through Geant4.

At the end of the beam test, a list of all the successful runs was made and the various runs were separated into categories.

7.3 The test-beam data analysis frameworks

The most commonly used framework for analysis of the DATURA data is EUTelescope, a library that provides tools for the offline spatial reconstruction of particle tracks. It features a close integration of the EUDAQ software framework and is based on the ILCSoft framework which provides the basic building blocks for offline analysis such as a generic data model (Linear Collider I/O, LCIO), a geometry description language (GEAR) and the central event processor (Marlin). Each task is implemented as an independent processor which is called by Marlin for every event. Every processor exposes a set of parameters to the user which can be configured and loaded at runtime via the so-called steering files in XML format. Several processors are provided by EUTelescope for Marlin, for the implementation of the algorithms which are necessary for a full track reconstruction and data analysis of test beam experiments

(Fig. 7.4). At low-energy beam lines, like the present at the DESY II test beam facility, multiple scattering is a factor which undermines the overall track resolution certainty, especially in measurements with significant DUT material budget. This is why EUTelescope provides processors implementing advanced algorithms for tracking based on the concepts of a Deterministic Annealing Filter (DAF) or General Broken Lines (GBL), which account for scattering in all material present in the beam. Furthermore, precise offline detector alignment can be performed by minimising track residuals using the EUTelescope alignment processor which utilises the Millepede-II algorithm [7]. The analysis program utilized by the NCSR "Demokritos" group for the November-December 2019 test-beam data was based on a EUTelescope-related analysis program developed by KIT.

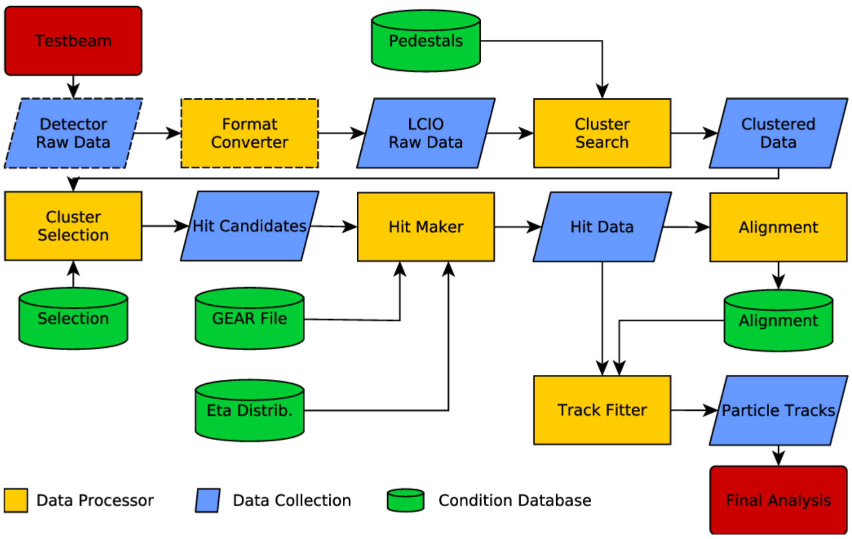

Figure 7.4: Schematic of the overall telescope data reconstruction and analysis strategy of the EUTelescope framework (by H. Jansen et al.). EUTelescope provides processors for all steps, except for the conversion of the DUT raw data, marked with a dashed outline.

While EUTelescope is the framework used by most group for the analysis of the November-December 2019 beam test, the CMS NCSR "Demokritos" group additionally used the scope2s framework developed at DESY (Daniel Pitzl's latest version). Through scope2s the telescope alignment is performed, where each sensor plane defines a local coordinate systems for its hits (columns and rows for pixels; rows for strips). In scope2s, the second telescope plane defines the global xy reference system. The beam is along the z-axis, as mentioned above, and the tracks of the primary particles are straight since there is no magnetic field present in the telescope system. The alignment is hierarchical: the 1st and 3rd telescope planes are aligned relatively to the 2nd (x- and y-shifts and rotation), the 4th and 6th telescope planes are aligned relatively to the 5th (x- and y-shifts and rotation), and the downstream triplet is aligned relatively to the upstream triplet (x-, y- and z-shifts). While for the telescope alignment the coordinates of the hits are changed (active transformations), for the DUT the coordinates of the reference frame are changed instead (passive transformations) and all corrections are applied only to the track. The intersection of the telescope tracks with the tilted DUT is calculated and transformed into DUT coordinates to allow detailed DUT studies. The alignment of the DUT itself is primarily based on profile plots and projections and for its implementation it is assumed that the 2S sensors are planar. The alignment consists of a set of shifts of axes, rotations around the beam axis and adjustments of the tilt angle and the skew angle. The method converges after a few iterations and gives good precision, consistent with the results of EUTelescope [8].

For most parameters, the stub efficiency included, the two frameworks return essentially similar values. However, one of the differences between the frameworks regards the calculation of the stub efficiency and deserves to be pointed out: a) EUTelescope compares a track directly to the stub, without any selection based on the hits, and thus examines the efficiency of the full 2S module to produce a stub for a given incident track. b) On the other hand, scope2s uses only tracks that are matched to hits in each of the sensors of the 2S module, and thus checks that the CBC stub correlation logic is working as expected. When the DUT is rotated, the displacement between the hits in the two sensors of the 2S module becomes larger, and at a certain angle the number of stubs is expected to decrease. In case that a hit is lost by one of the sensors and no stub is created, in the EUTelescope approach this would be counted as an inefficient event, while in the scope2s approach it would not be counted at all and the event wouldn't be included in the analysis [7], [8].

7.4 The stub efficiency of a 2S module

The plots related to the stub efficiency of a 2S module will be shown below. All analysis results presented here are from the AC-M1804 2S module DUT produced at RWTH, Aachen.

Our analysis for the initial angular scan of the DUT was performed using the scope2s software. The setup configuration for the first run of this scan is shown in Fig. 7.5 where the module is arranged in such a way that the y-direction is the direction along the length of the strips. The runs used in this analysis are 916-923 and 930-945 (where each run of the beam test is attached to a unique ID, and the runs with lower IDs were test and debugging runs). Every run during the angular scan corresponds to a different turn angle of the DUT. (The alignment for these runs was performed by DESY members.) For each run events are selected with a TDC phase greater than 1 and smaller than 7 (where the TDC phase varies between 0 and 7). The event selection is the following:

1. Reconstruct clusters in the six DATURA planes
2. Fit a track with the fist three DATURA planes
3. Fit a track with all the six DATURA planes
4. If a track that fulfills the above conditions is found then:
   (a) Reconstruct cluster in both DUT planes
   (b) Declare a cluster-track match if $|\Delta x_{\text{cluster-track}}| < 0.1\,\text{mm}$
   (c) Check if a stub exists, and if it does declare a stub-track match if $|\Delta x_{\text{stub-track}}| < 0.2\,\text{mm}$

After the end of each run, the number of cluster-track matches Q_1 and the number of stub-track matches Q_2 are printed out, and the stub efficiency is defined as Q_2/Q_1. For the angular scan, the stub efficiency was calculated for each run (Fig. 7.6). From the angular scan analysis with scope2s, the 50% stub efficiency of a 8CBC3 module is observed at a -16.1° DUT turn angle, and its 99% stub efficiency is observed at a -15.0° DUT turn angle, where a 0.0° DUT turn angle signifies a beam perpendicular to the DUT sensor plane.

In the 8CBC3 modules under evaluation, the gap between the two 2S sensors is 1.7 mm. (As mentioned previously, 2S modules with various sensor gaps are considered for production.)

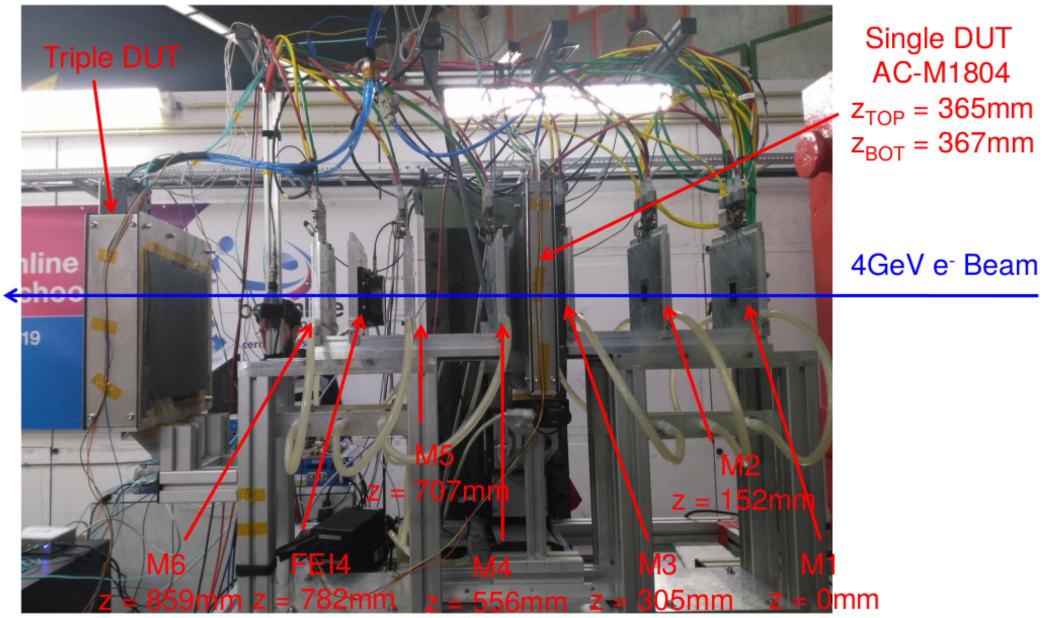

Figure 7.5: The configuration of the November-December 2019 DESY beam test setup without any rotation of the modules, where the positions of each DATURA plane and the DUT between the telescope arms are indicated. The three 2S modules after the downstream triplet (along the way of the beam) are not used in the current analysis.

For the CMS field strength of $B = 3.8\,\mathrm{T}$, the relationship between the beam incident angle (α) and the emulated transverse momentum p_T of the traversing particle for a radial position of the module (R) is given by:

$$p_T[GeV] = 0.57 \cdot \frac{R[m]}{sin(\alpha)} \tag{7.1}$$

A radius of 0.6 m (distance between the 2S module when installed in the CMS Tracker and the beam line) is used for the calculation of the effective p_T from the beam incident angle [9]. From the angular scan, the p_T turn-on threshold, for which the stub efficiency is 50%, is estimated to be 1.26 GeV (Fig. 7.7).

Both fits are performed with the FCN function, a multiparameter Fortran function on which the MINUIT package acts. In the ROOT implementation, the function FCN is defined via the MINUIT $SetFCN$ member function when a $Histogram.Fit$ command is invoked and the value of FCN will in general depend on one or more parameters [10].

The analysis for the scan along the strips of the DUT was performed using the scope2s software. The setup configuration for the first run of this scan is shown in Fig. 7.8 where the module is arranged in such a way that the x-direction is the direction along the length of the strips. The runs used in this analysis are 966-967 and 971-979, where each run during the scan along the strips corresponds to a different x-position of the DUT. (The alignment for these runs was performed by NCSR "Demokritos" members, following the alignment method for scope2s described above.) The event selection for each run and the definition of the stub efficiency are the same as those for the previous angular scan (by interchanging Δx and Δy due to the rotation of the module). For every x-position of the DUT the stub efficiency of the 8CBC3 module is observed to be $> 99\%$, the same as for run 916 (first run of angular scan for zero turn angle) as shown in Fig. 7.9.

The analysis for the angular scan along the strips of the DUT was firstly performed using

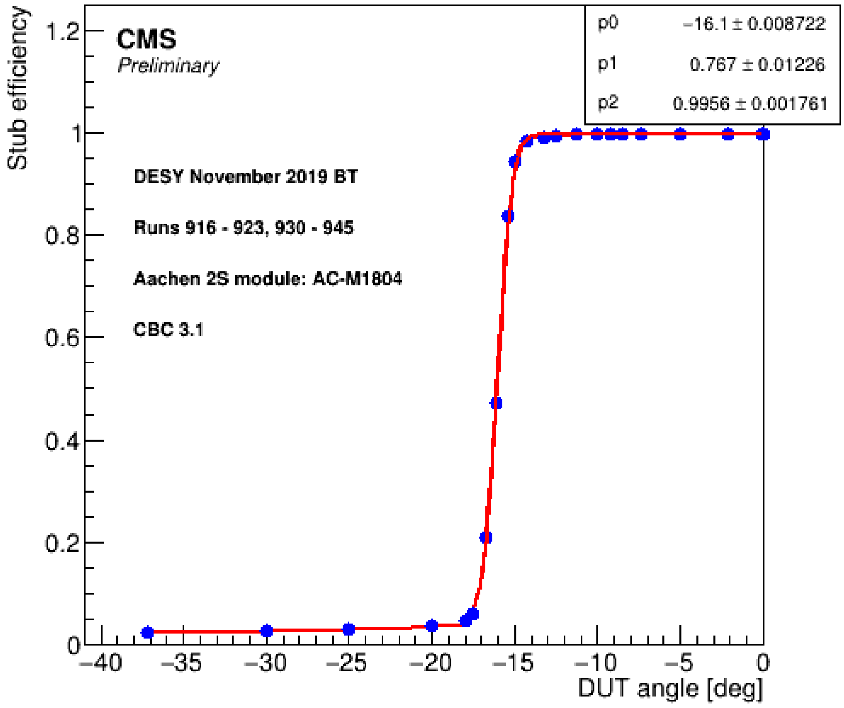

Figure 7.6: Stub efficiency of the full-size 2S module as a function of DUT turn angle measured at the DESY beam test facility during an angular scan (with rotations about the y-axis). The module is initially arranged in such a way that the y-direction is the direction along the length of the strips. The module was operated at a bias voltage of $-300\,\mathrm{V}$ and the V_{CTH} threshold value was set to 545. Fit performed using a generic FCN function where $p0$ corresponds to the DUT turn angle at 50% efficiency. Analysis performed using scope2s.

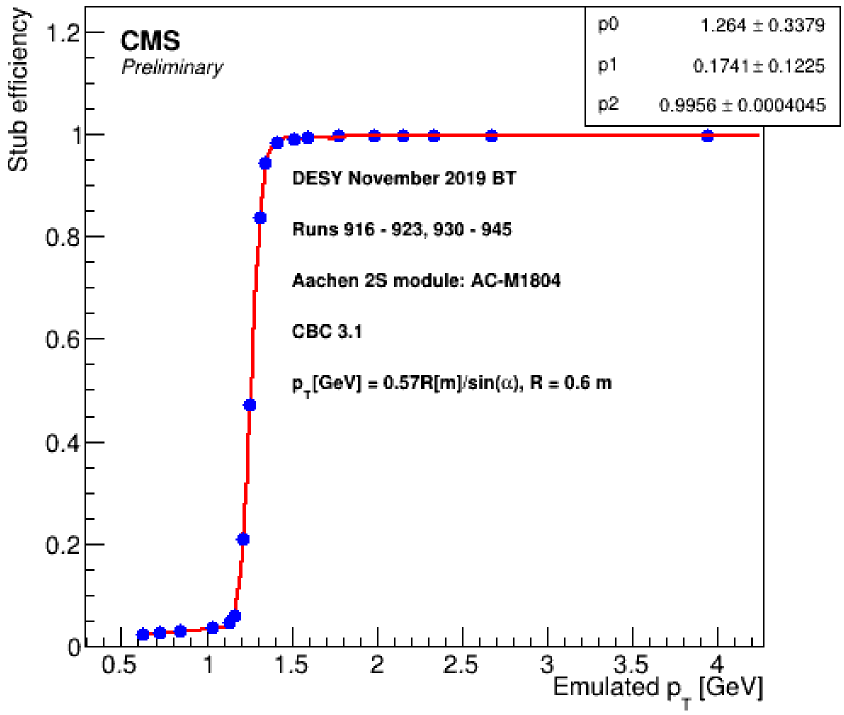

Figure 7.7: Stub efficiency of the full-size 2S module as a function of particle p_T measured at the DESY beam test facility during the angular scan (with rotations about the y-axis). The module is initially flipped in such a way that the y-direction is the direction along the length of the strips. The module was operated at a bias voltage of -300 V and the V_{CTH} threshold value was set to 545. A radius of 60 cm is used to convert the beam incident angle to effective p_T. Fit performed using a generic FCN function where $p0$ corresponds to the p_T at 50% efficiency. Analysis performed using scope2s.

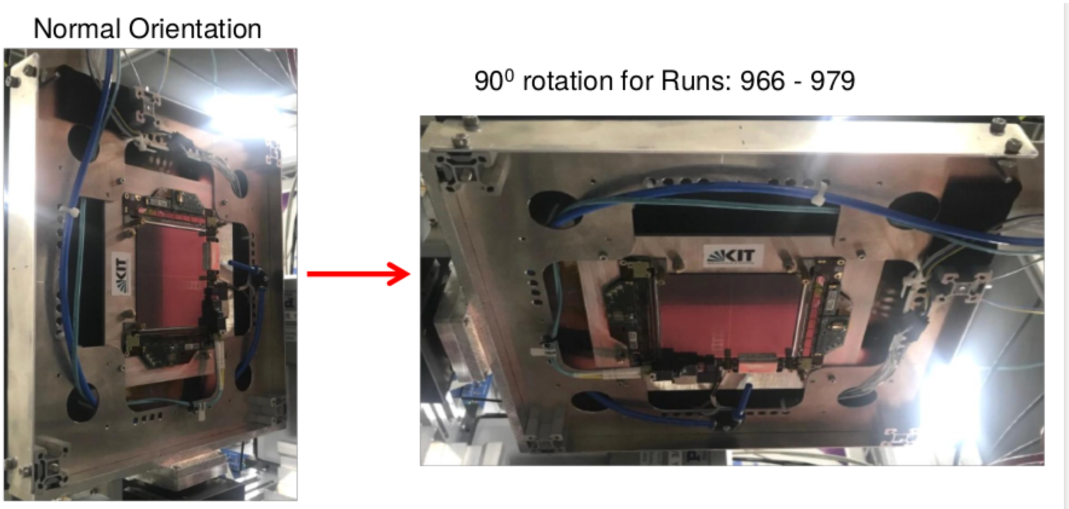

Figure 7.8: 90.0° rotation of the 2S module DUT about the z-axis, which was performed in order to measure the stub efficiency along the strips. Initially the length of the strips was along the y-axis (vertical axis), while subsequently it was along the x-axis (horizontal axis).

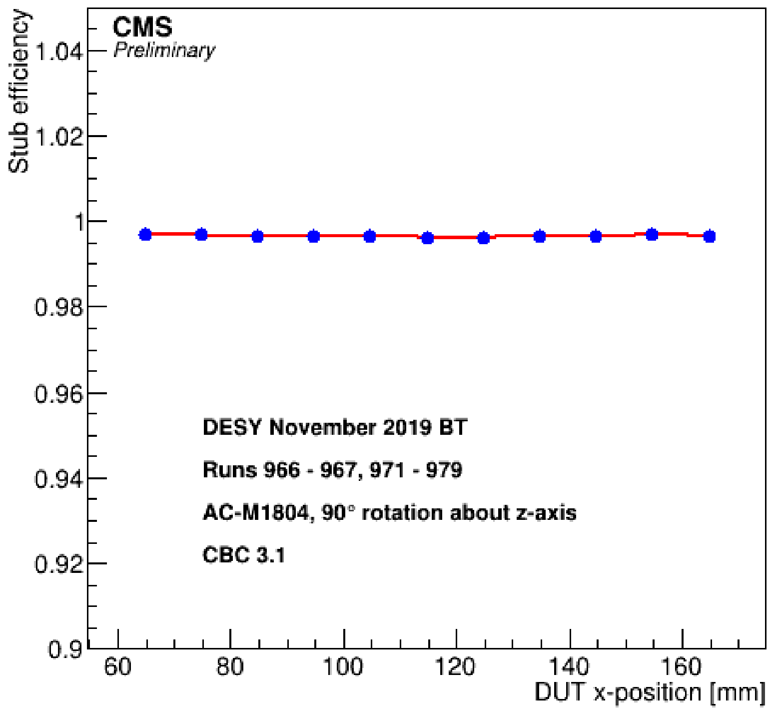

Figure 7.9: Stub efficiency of the full-size 2S module as a function of the DUT x-position measured at the DESY beam test facility during a scan along the strips (with a steady y = 47.278 mm). The module is flipped in such a way that the x-direction is the direction along the length of the strips. The module was operated at a bias voltage of -300 V and the V_{CTH} threshold value was set to 545. The stub efficiency is above 99% for each x-position. Analysis performed using scope2s.

the scope2s software. The setup configuration for the first run of this scan is the same as in Fig. 7.8 where the module is arranged in such a way that the x-direction is the direction along the length of the strips. The runs used in this analysis are 979, 980, 981, 984, 985 and 986, where each run during the scan along the strips corresponds to a different turn angle of the DUT. (The alignment for these runs was performed again by NCSR "Demokritos" members, following the alignment method for scope2s described above.) The event selection for each run and the definition of the stub efficiency are the same as those for the previous scans. The cluster-track Δy after alignment for various runs (turn angles) is shown in Fig. 7.10, and no significant variations are observed among different runs. The stub efficiency of the 8CBC3 module along the strips as function of the DUT turn angle, as calculated by scope2s, is shown in Fig. 7.11. This study indicates that the stub efficiency decreases from 99.6% for a 0.0° turn angle down to 95.7% for a 30.0° turn angle, as the DUT is scanned along its strips.

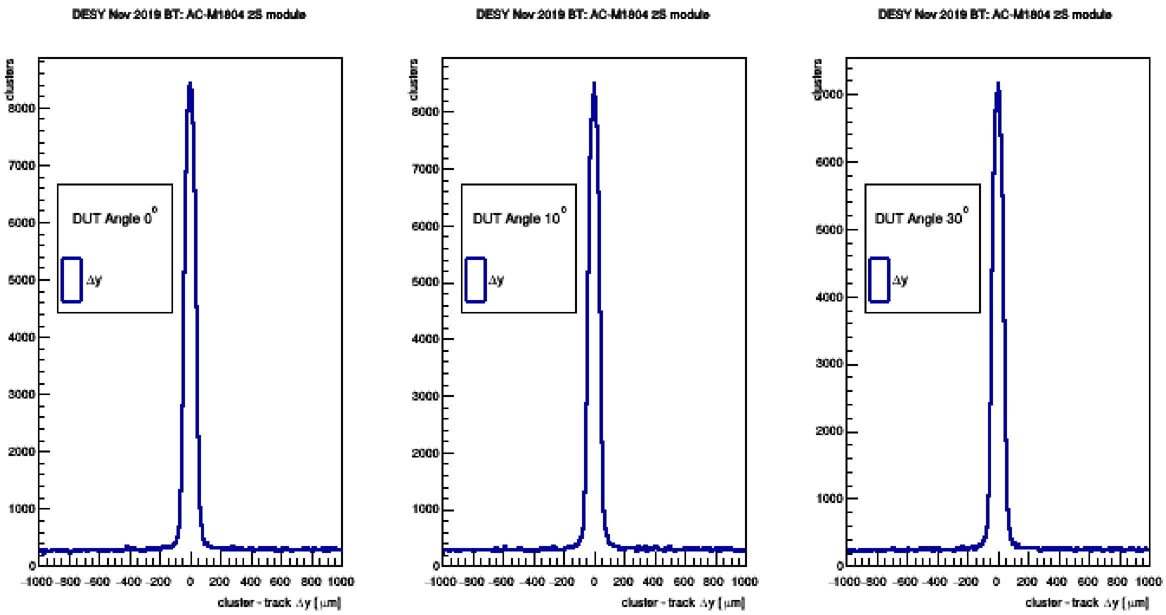

Figure 7.10: The Δy cluster-track position difference in the 2S module after alignment, for various angles of rotation. Analysis performed using scope2s.

The analysis for the angular scan along the strips of the DUT was afterwards repeated using the EUTelescope framework and an analysis script (provided by A.M. Nürnberg from KIT) for validation. The runs used in this analysis are 980, 981, 984, 985 and 986. The stub efficiency of the 8CBC3 module along the strips as function of the DUT turn angle, as calculated within the EUTelescope analysis framework, is shown in Fig. 7.12. This study indicates that the stub efficiency decreases from 99.5% for a 0.0° turn angle down to 94.2% for a 30.0° turn angle, as the DUT is scanned along its strips. The efficiencies are of the same order of magnitude as those obtained from scope2s. However, within the EUTelescope framework they are a bit lower due to the different definition of the stub efficiency.

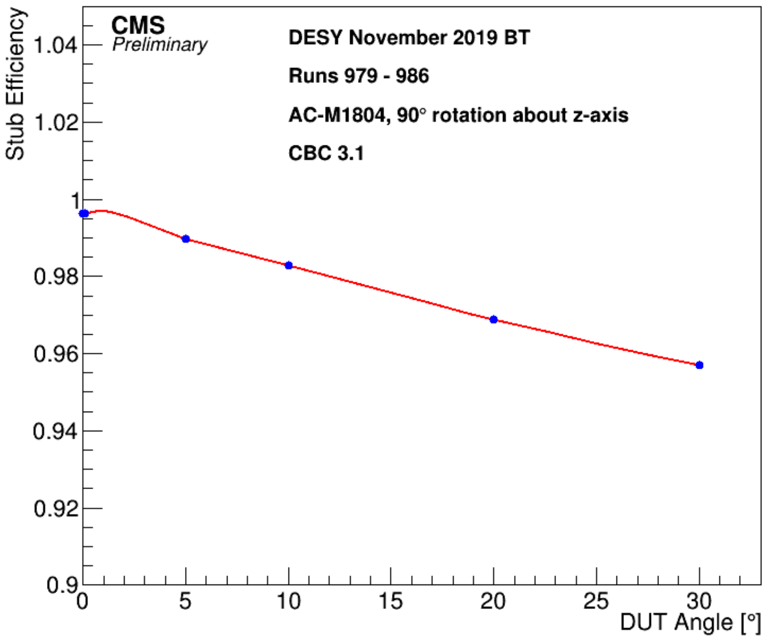

Figure 7.11: Stub efficiency along the strips of the full-size 2S module as a function of the DUT rotation angle (absolute value) measured at the DESY beam test facility during an angular scan (with a steady $x = 114.662\,\text{mm}$ and $y = 47.278\,\text{mm}$ and rotations about the y-axis). The module is flipped in such a way that at zero degrees the x-direction is the direction along the length of the strips. The module was operated at a bias voltage of $-300\,\text{V}$ and the V_{CTH} threshold value was set to 545. The stub efficiency is above 95% for each DUT rotation angle. Analysis performed using scope2s.

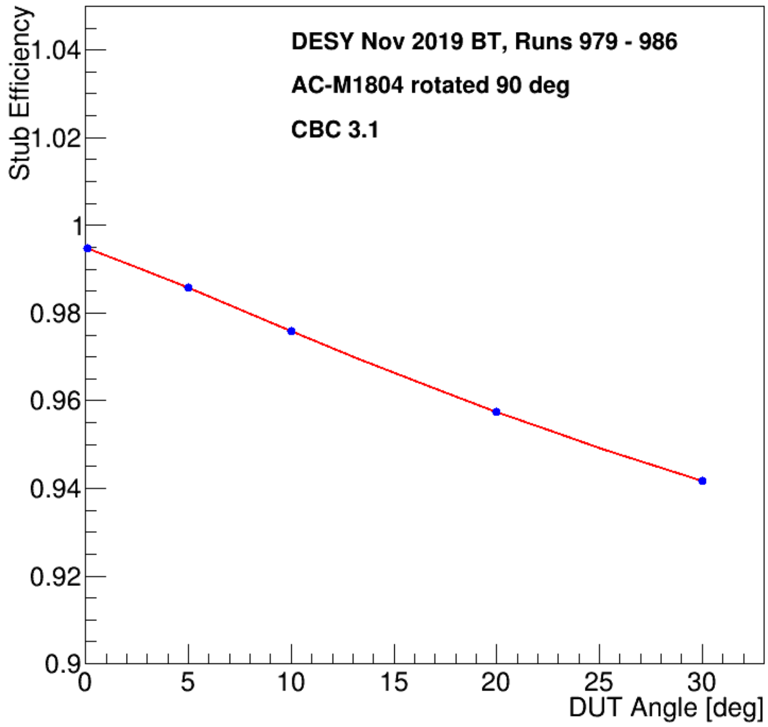

Figure 7.12: Stub efficiency along the strips of the full-size 2S module as a function of the DUT rotation angle (absolute value) measured at the DESY beam test facility during an angular scan (with a steady $x = 114.662$ mm and $y = 47.278$ mm and rotations about the y-axis). The module is flipped in such a way that at zero degrees the x-direction is the direction along the length of the strips. The module was operated at a bias voltage of -300 V and the V_{CTH} threshold value was set to 545. The stub efficiency is above 94% for each DUT rotation angle. Analysis performed using the "EUTelescope" framework and an analysis script provided by A.M. Nürnberg.

Bibliography

[1] Hendrik Jansen et al., *Performance of the EUDET-type beam telescopes*, EPJ Tech.Instrum. 3 (2016) 1, 7.

[2] Hendrik Jansen et al., *Scattering Studies with the DATURA Beam Telescope*, Springer Proc.Phys. 212 (2018) 243-250.

[3] Hendrik Jansen, *Resolution studies with the DATURA beam telescope*, 2016 JINST 11 C12031.

[4] R. Diener et al., *The DESY II Test Beam Facility*, Nucl.Instrum.Meth.A 922 (2019) 265-286.

[5] G. Blanchot et al., *Prototyping of Hybrid Circuits for the CMS Phase-2 Outer Tracker Upgrade at the HL-LHC*, PoS 370 (2020) 060.

[6] AJ Peters et al, *EOS as the present and future solution for data storage at CERN*, 2015 J. Phys.: Conf. Ser. 664 042042.

[7] Hanno Perrey, *EUDAQ and EUTelescope: Software Frameworks for Test Beam Data Acquisition and Analysis*, PoS TIPP2014 (2014) 353.

[8] *eudaq2s/tele-scope (DESY repository)*, https://stash.desy.de/projects/A/repos/eudaq2s/browse.

[9] W. Adam et al., *Beam test performance of prototype silicon detectors for the Outer Tracker for the Phase-2 Upgrade of CMS*, 2020 JINST 15 P03014.

[10] *TMinuit Class Reference*, https://root.cern.ch/doc/master/classTMinuit.html.

List of Figures

List of Tables